



**Universiteit  
Leiden**  
The Netherlands

## **Synthetic modification of fusogenic coiled coil peptides**

Crone, N.S.A.

### **Citation**

Crone, N. S. A. (2021, December 16). *Synthetic modification of fusogenic coiled coil peptides*. Retrieved from <https://hdl.handle.net/1887/3247291>

Version: Publisher's Version

License: [Licence agreement concerning inclusion of doctoral thesis in the Institutional Repository of the University of Leiden](#)

Downloaded from: <https://hdl.handle.net/1887/3247291>

**Note:** To cite this publication please use the final published version (if applicable).

# Synthetic modification of fusogenic coiled coil peptides

Proefschrift

ter verkrijging van

de graad van doctor aan de Universiteit Leiden,  
op gezag van rector magnificus prof.dr.ir. H. Bijl,  
volgens besluit van het college voor promoties  
te verdedigen op donderdag 16 december 2021

klokke 11:15 uur

door

**Nicolaas Schelto Adriaan Crone**

geboren te Almere

in 1992

# Promotiecommissie

## **Promotor**

Prof.dr. A. Kros

## **Copromotor**

Dr. A. L. Boyle

## **Overige Commissieleden**

Prof.dr. H. S. Overkleeft (voorzitter)

Prof.dr. S. A. Bonnet (secretaris)

Dr. S. J. Wezenberg

Prof.dr. G. Ashkenasy (Ben-Gurion University of Negev)

Dr. F. Thomas (Heidelberg University)

ISBN: 978-94-6421-568-7

Printed by: Ipskamp printing

All rights are reserved. No part of this thesis may be reproduced by any matter or by any means without permission from the author.

To my friends and family



# Table of Contents

<b>Chapter 1</b>	5
General introduction	
<b>Chapter 2</b>	23
Peptide-mediated liposome fusion: the effects of anchor positioning	
<b>Chapter 3</b>	47
Modulation of coiled-coil binding strength and fusogenicity through peptide stapling.	
<b>Chapter 4</b>	91
Azobenzene crosslinking for coiled-coil photoswitching	
<b>Chapter 5</b>	117
Azobenzene-based amino acids for photocontrol of coiled coil peptides	
<b>Chapter 6</b>	159
Photoswitchable $\beta$ -sheet forming peptides	
Summary and Perspectives	195
Nederlandse samenvatting	198
Curriculum Vitae	202
List of Publications	203
Acknowledgments	204





---

## General introduction

## 1.1 Peptide and protein folding

Peptides and proteins are the most abundant macromolecules encountered in living systems, and play a role in all vital cellular processes.<sup>1</sup> They are constructed from chains of amino acids, but differ in the length of the chain, with the term 'peptide' referring to chains of less than 50 residues and anything larger referred to as proteins. In order to reduce steric interference between atoms, maximise backbone hydrogen bonding interactions and facilitate favourable side-chain interactions, peptides and proteins can adopt complex three-dimensional conformations. Biological activity is often directly related to the adopted structure, with a large scientific effort dedicated to studying, predicting and controlling protein folding.<sup>2</sup>

Analysis of known protein structures have shown two dominant secondary structures; the  $\alpha$ -helix and the  $\beta$ -strand, with proteins divided into classes based on the abundance of these structural elements.<sup>3</sup> The two structures can be defined by the different angles describing the three-dimensional orientation of the amino acid around its  $\alpha$ -carbon ( $C_\alpha$ , **Figure 1.1A**). Hydrogen bonding within the same chain is maximized for  $\alpha$ -helices, with every amino acid forming a hydrogen bond to the amino acid 4 positions further in the sequence ( $i$  to  $i+4$  hydrogen bonding). The peptide chain rotates around a central axis with 3.6 residues per helix turn, resulting in a 7-amino acid sequence (called a 'heptad repeat') describing two full rotations. In contrast,  $\beta$ -structures form hydrogen bonds which can be between strands of the same, or different protein chains. These intermolecular hydrogen bonds results in multiple  $\beta$ -strands combining to form a  $\beta$ -sheet. To allow hydrogen bonding in the same sequence, these  $\beta$ -strand domains are connected via a short turn, hairpin or other structural motif;<sup>4</sup> or can bridge to separate  $\beta$ -domains in the same sequence spaced further apart. Protein self-assembly can also be driven by the formation of intermolecular  $\beta$ -sheets between  $\beta$ -structured domains in different protein chains.

The tendency of an amino acid sequence to fold as one of these two conformations depends on the order of polar (p) and hydrophobic/non-polar (n) amino acids in the sequence,<sup>5</sup> in combination with the tendency of individual amino acids to adopt either structure.<sup>6-8</sup> When polar and non-polar amino acids are directly alternated,



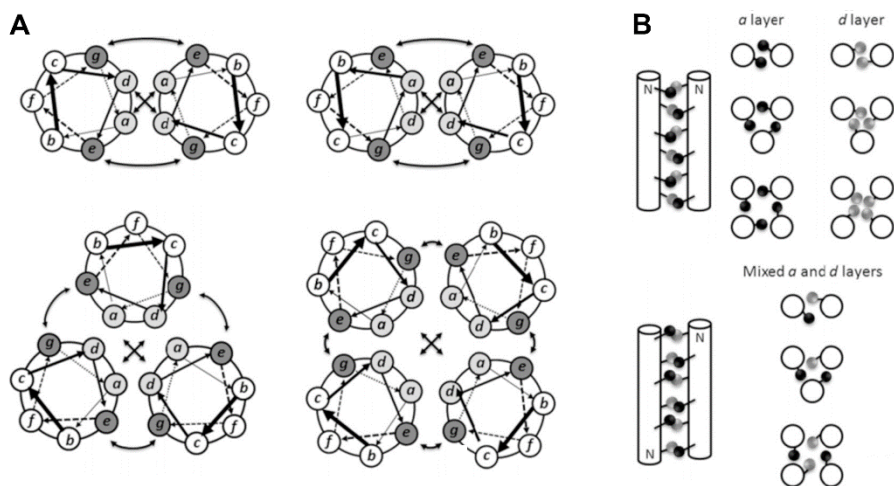


**Figure 1.2:** Helical wheel diagram of parallel dimeric (top left), anti-parallel dimeric (top right), parallel trimeric (bottom left) and parallel tetrameric (bottom right) coiled-coil peptides (A). Straight arrows indicate hydrophobic interactions, where curved arrows indicate electrostatic side-chain interactions. Packing of hydrophobic side chains according to the ‘knobs-in-holes’ configuration for parallel (top) and anti-parallel (bottom) coiled coils with up to 4 chains (B). Images adapted from Apostolovic *et al.*<sup>10</sup>

$\alpha$ -helices rotate around each other in a ‘supercoil’ structure, which reduces the effective residues per turn and allows for continuous contact of the hydrophobic amino acids. This self-assembled structure of multiple  $\alpha$ -helices is referred to as a coiled coil,<sup>11</sup> and is an abundant structural motif both within proteins and a driving force for protein oligomerization.<sup>12</sup>

In coiled-coil structures, amino acid side chains in one helix occupy empty spaces between side chains of adjacent helices, a regime which is referred to as ‘knobs-in-holes packing’.<sup>13</sup> Non-polar amino acids at positions *a* and *d* of the heptad repeat sequence, *abcdefg*, form the hydrophobic interface (**Figure 1.2A**), and packing of these side chains affects coiled-coil stability, with the size and branching also affecting the oligomer state of the coiled coil.<sup>14</sup> Switching amino acids at the *a* and *d* positions additionally determines if the coiled coil assembles in a parallel (N-termini on the same side) or anti-parallel (N-termini on opposing ends) orientation, as shown in **Figure 1.2B**. The positions *e* and *g*, flanking the hydrophobic amino acids, tend to be charged amino acids that form electrostatic interactions between different helical strands, and thereby provide pairing specificity. Finally, the other three amino acid positions are typically hydrophilic as they are solvent exposed.<sup>15</sup> These rules can be used to predict coiled-coil formation both in synthetic and

natural proteins,<sup>16-18</sup> although for pentameric and larger coiled-coils the preferred repeat sequence starts to differ.<sup>19</sup> Additionally, more variation in the sequence can be allowed for longer coiled-coil sequences, which can be used for increasing binding selectivity, introducing functional groups or introduction of an active component. A typical example of this are the asparagine residues found at position 'a' of GCN4, which promote formation of dimeric over a tetrameric coiled-coil and prevents anti-parallel or out-of-register self-assembly.<sup>20</sup>

In the last decades, coiled coils have been investigated as structural motifs in synthetic nanoparticles,<sup>21</sup> therapeutics such as vaccines,<sup>22</sup> hydrogels,<sup>23</sup> cellular delivery systems,<sup>24</sup> and synthetic biology in general.<sup>25</sup> The high binding strength, well defined structure and self-assembly, and ease of preparation via solid-phase peptide synthesis (SPPS) provide several advantages and flexibility in their application.<sup>26</sup> The use of coiled coil lipopeptides in synthetic membrane fusion has shown to be particularly effective,<sup>27</sup> using the energy associated with coiled-coil formation to drive the fusion process, and is the main focus of the work presented in this thesis.

## 1.2 Membrane fusion and SNARE proteins

Membrane fusion describes the process in which two separate (lipid) membranes combine into one continuous membrane. Fusion of membranes results in mixing of encapsulated content, when discussing fusion between vesicles, or release of content from a vesicle across a membrane. Fusion of biological membranes is a fundamental process for all living systems, ranging from continuous processes such as nutrient uptake and digestion by lysosomes to cell fusion during reproduction and the viral infection of host cells.<sup>28</sup> Due to the importance of these processes, an understanding of the membrane fusion mechanism is of direct scientific interest. For example, understanding protein-membrane interactions should allow for the development of novel therapeutics against viral infections from HIV and novel variants of SARS-CoV-2.<sup>29, 30</sup> Besides control over natural fusion processes, development of artificial fusion systems has shown potential in the fields of drug delivery, sensing, and synthetic biology.<sup>31</sup>

Combining two separate lipid bilayers into a single continuous membrane requires rearrangement of the bilayers through (non-bilayer) metastable intermediates. These intermediate states are characterized by high curvature, are energetically

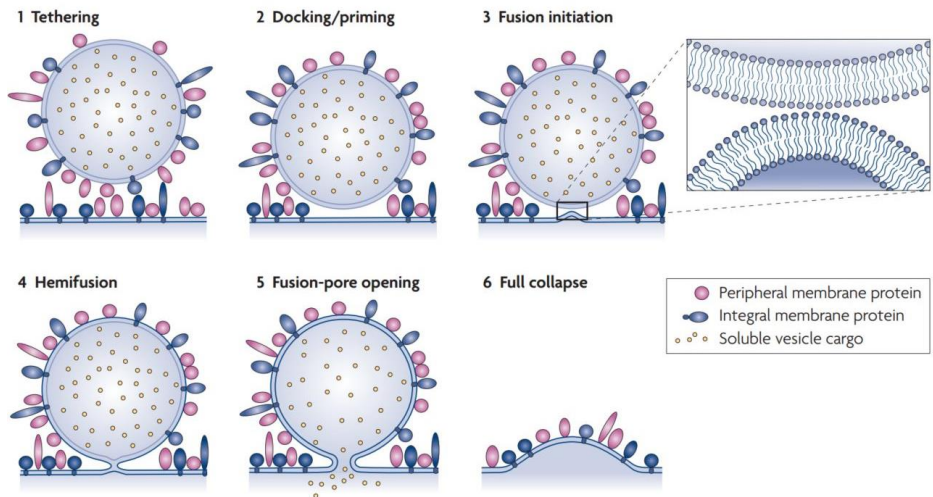


**Figure 1.3:** Fusion model of lipid membranes from two separate lipid bilayers through a hemifusion diaphragm and pore opening until the two membranes are fully mixed. First the fusing vesicle is loosely tethered to the target membrane (1), followed by increased protein binding on the membrane surface, resulting in tight binding (docking, 2) of the two membranes. Initiation of fusion (3) results in mixing of lipids and leads to the temporally stable hemifusion diaphragm (4). Finally, opening of a pore in the fusion diaphragm (5) leads to mixing of contents and expansion of the fusion pore eventually leads to a fully fused membrane (6). Although the process is shown as distinct steps, in practice they are not as clearly separated as shown schematically. Image adapted from Martens and McMahon.<sup>32</sup>

unfavourable, and therefore do not occur spontaneously. In Nature, membrane fusion proteins are thus employed by living systems to drive this process by lowering the energy barrier of the intermediates, and to control the instance and location where membrane fusion occurs.<sup>32-34</sup> The basic steps of bilayer fusion are shown in **Figure 1.3** and start with two membranes that are in close proximity, followed by closer contact called 'docking' and initiation of fusion. Rearrangement of the lipids leads to a hemifusion diaphragm, where both a double and a single bilayer are present, followed by the opening of a fusion pore and finally expansion of the pore until the membranes are fully fused. The hemifusion intermediate is deemed essential to all fusion processes, and has been shown to exist as a temporally stable state for multiple fusion systems.<sup>35, 36</sup> Initiation of fusion has long been theorized to occur through a fusion stalk intermediate,<sup>34</sup> with discussion<sup>37-39</sup> as to the exact mechanism still ongoing.

One of the best understood biological fusion processes is that involved in the release of neurotransmitters for neuronal signal transduction. Fusion of neuronal vesicles with the axonal membrane is stimulated by  $\text{Ca}^{2+}$  influx in the cell, and

results in fast release of neurotransmitters in the synaptic cleft. The process is driven by the assembly of SNARE (soluble NSF attachment protein receptor) proteins on both membranes. A functional SNARE complex is formed by the assembly of a four-helix coiled-coil complex between the two lipid membranes, and is proposed as the energetic driving force behind fusion.<sup>40-42</sup> The SNARE proteins are separated into v-SNARE or t-SNARE groups, depending on their occurrence on vesicle or target membranes. For neuronal vesicle fusion, synaptobrevin functions as the v-SNARE, whilst the other three helices of the complex originate from Syntaxin 1 and two copies of SNAP25 as t-SNARE proteins. The combination of different SNARE proteins in the formation of a SNARE complex is part of the mechanism that allows for selectivity of fusion of different cellular membranes.<sup>43</sup> A long-standing question has been how many SNARE complexes are required to successfully fuse two membranes, with some evidence showing that a single SNARE complex might even be sufficient.<sup>44</sup> However, more experimental work points towards multiple SNARE complexes in a single fusion interface,<sup>45</sup> with theoretical studies showing the speed of fusion is entropically dependent on the number of complexes.<sup>46</sup>

Although SNARE proteins provide the driving force behind fusion, a large number of other proteins are involved to regulate where and when fusion occurs. In the example of vesicle fusion in neuronal synapses, synaptotagmin-1 binds to the SNARE complex before fusion and couples the influx of  $\text{Ca}^{2+}$  to activation of the fusion process. Other regulators of SNARE-mediated fusion are members of the SM protein family (Sec1/Munc18) working together with complexins and Munc13s, Rab3, and HOPS proteins. The complex interplay between all these fusion regulators is still under investigation and several reviews discussing this matter have been published.<sup>47-51</sup> Although these proteins are called regulators of the fusion process, many have been hypothesized or shown to have an active contribution to SNARE-mediated fusion.<sup>47</sup> Active recycling of the SNARE complex is performed by the NSF protein, which binds to the fused SNARE complex in combination with multiple SNAPS and actively disassembles the proteins driven by ATP hydrolysis.<sup>49, 52</sup> After the complex has been deconstructed, the v-SNARE is recycled while the three t-SNARE proteins remain on the target membrane until the process is restarted. Together, these regulatory systems are highly efficient in their control over SNARE-mediated fusion. They facilitate the extremely fast release of neurotransmitters (signal transfer along nerve fibres can reach speeds of up to 120 m/s)<sup>53</sup>, but prevent

the energetically costly release of neurotransmitters when no trigger signal is present.

### 1.3 Synthetic mimics of biological membrane fusion

Study of SNARE-mediated fusion and the complex systems in place to regulate fusion activity have progressed in the last decades, but remain difficult because of the number of proteins involved and the multiple roles that they can perform.<sup>54</sup> Furthermore, reconstitution of the fusion machinery in model systems may lead to different results than observed in the cellular process.<sup>55</sup> Because of these reasons, and the potential applications of fusion systems discussed earlier, synthetic model systems have been prepared as mimics of SNARE-mediated fusion.<sup>56, 57</sup> The ultimate goal in developing such model systems is the same fusion efficiency and selectivity as observed in the native system, with low leakage of contents, which indicates membrane instability rather than fusion. Minimalism in design allows for deconvolution of the contributing factors to the fusion process, but a multi-component strategy is essential to obtain the required selectivity, with a minimum of one component in each membrane. Synthetic fusion systems exist that do rely on the action of a single entity, such as the pore-forming GALA peptides,<sup>58</sup> but these result in the random mixing of vesicles instead of controlled mixing of different entities. Liposomal fusion model systems can in principle be based on any strong and selective interaction, and have been demonstrated using complementary strands of single strand DNA or PNA,<sup>59, 60</sup> the hydrogen bonding interaction between cyanuric acid and melamine,<sup>61, 62</sup> the reversible covalent linkages between boronic acids and *cis*-diols,<sup>63</sup> and binding of vancomycin to the *D*-Ala-*D*-Ala peptide sequence.<sup>64, 65</sup>

#### *Coiled coil peptides as fusion mimics*

The most investigated model system for membrane fusion has been developed in the Kros group and uses coiled-coil peptides (**Figure 1.4**).<sup>27</sup> It consists of two peptides named 'E'; (EIAALEK)<sub>n</sub>, and 'K'; (KIAALKE)<sub>n</sub>, after the dominant charged amino acid in their respective sequences. These peptides are designed to form a tight-binding heterodimeric coiled-coil,<sup>66</sup> as a synthetic alternative to the tetrameric coiled-coil formed by SNARE proteins. A lipid anchor connected to the peptide through a polyethylene glycol (PEG) spacer allows for their integration into lipid membranes. Incorporating these peptides in separate lipid membranes results in their fusion upon mixing. Because of the simplicity of the system, it allows

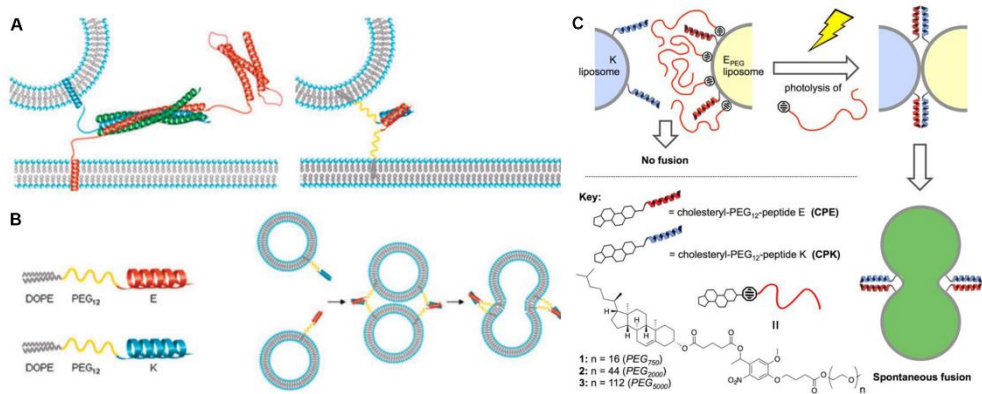


**Figure 1.4:** Schematic representation of membrane fusion mediated by coiled-coil peptides, as mimics of the biological fusion process. Comparison between the SNARE fusion complex (left) and the coiled-coil fusion system (right) (A), overview of the structure of the coiled coil lipopeptides consisting of peptide E or K connected to a lipid via a PEG spacer, and how they are incorporated in lipid vesicles (B), and how this fusion process can be controlled via the incorporation of a photolabile PEG lipid which shields the peptides from interaction (C). Images are adapted from Marsden *et al.*<sup>56</sup> and Kong *et al.*<sup>67</sup>

synthetic derivatization to determine how the structure is related to the fusion activity.

The E/K fusion system initially used phospholipids as the membrane anchor, but a study comparing different lipids revealed cholesterol as the optimal lipid anchor,<sup>68</sup> possibly because it is easier for cholesterol-peptides to disperse through the lipid membrane. Increasing the coiled-coil length, which is directly related to the binding strength, results in increased fusion with the direction of the coiled coil (N-terminal versus C-terminal anchoring) not having a significant effect.<sup>69, 70</sup> Changing the length of the PEG spacer also altered fusion efficiency, with an optimum of around 12 polyethylene glycol repeats.<sup>71</sup> Biophysical investigations of the coiled-coil fusion system have mainly focused on the disparate roles of the two peptides during the fusion process. Peptide K was shown to interact with lipid membranes, a phenomenon which originates from its structure as a positively charged amphipathic helix. This membrane interaction was theorized as one of the driving forces behind the systems fusogenicity.<sup>72, 73</sup> Further investigation showed that peptide K, both by itself and when connected to the lipid membrane, can result in altered membrane curvature, viscosity and hydration.<sup>74, 75</sup> These interactions might lower the energy required for reorganization of lipid membranes in the fusion intermediates described earlier, and thereby result in higher fusion efficiency.

Because the E/K coiled-coil is designed *de novo*, its' activity is orthogonal to normal biological processes, and its' liposomal formulation is therefore of interest as a drug delivery system. Cellular studies using the E/K fusion system have shown successful delivery of liposomal doxorubicin,<sup>76</sup> and showed promising results in zebrafish xenografts.<sup>77</sup> In other studies using giant unilamellar vesicles (GUVs) as a model system, liposomal fusion was used to effectively introduce the hydrophobic bis-(thioureido)decalin anion transporter.<sup>78</sup> Besides liposomes, the coiled-coil system could be used for delivery of mesoporous silica nanoparticles and nucleic acid lipid particles *in vitro*.<sup>79, 80</sup> The strong interactions between the E/K peptides have also resulted in other applications such as the immobilization of vesicles on a patterned surface substrate,<sup>81</sup> studying cellular exchange by forcing close proximity of cellular membranes through coiled-coil modification,<sup>82</sup> and recently the sorting of cells with magnetic beads bearing a coiled-coil functionalized dextran polymer.<sup>83</sup>

The incorporation of lipids containing a long ( $M_n = 2000$  g/mol) PEG chain proved to block the peptides from fusing lipid vesicles, by preventing coiled-coil interactions in the vesicle docking phase.<sup>84</sup> This effect was used to introduce more selectivity in the fusion process, by combining the E/K coiled-coil with a photocleavable PEG lipid to halt any fusion progress until the PEG was cleaved from the vesicle with UV light (**Figure 1.4C**).<sup>67</sup> This mechanism allowed for photoactive doxorubicin delivery in a zebrafish cancer model,<sup>85</sup> showing the potential of combining a fusion system with active components. This dePEGylation strategy could be seen as a mimic of the natural regulatory proteins involved in the control of SNARE protein activity, halting liposomal fusion until a trigger is applied. However, there is no selectivity in the interactions between PEG and the fusogenic coiled-coil peptides, resulting in the requirement for a large excess of PEG to shield the entire liposomal surface. Furthermore, a lack of reversibility in the dePEGylation prevents precise control over coiled-coil interactions, and limit its potential applications. Therefore, development of novel (photo)activation strategies for coiled-coil peptides is still of direct interest.

Together, all of this work shows not only the flexibility of the coiled-coil peptides, but also their compatibility with biological systems. Improving our understanding of the interactions of peptide E and K in membrane fusion directly leads to better drug delivery systems, but alterations to the coiled-coil that allow for increased binding, biocompatibility or introduction of other functionalities are also of general interest outside the field of membrane fusion.

## 1.4 Aims and scope of this thesis

The work presented in this thesis aims to understand the underlying mechanisms that drive coiled-coil based membrane fusion, using a synthetic investigation strategy to determine relationships between peptide structure, interactions with its binding partner and lipid membranes, and fusion of liposomal membranes. The second part of this thesis aims to introduce a light-active component in the peptide structure to gain spatiotemporal control over peptide folding and activity.

In **Chapter 2** of this thesis the effect of lipid anchor attachment location in the E/K coiled-coil fusion mechanism is investigated. The cholesterol-PEG moiety used as the membrane anchor is repositioned from the peptide terminus to the center of the peptide sequence, mimicking side-chain palmitoylation common in the natural SNARE fusion system. The new variants showed lower fusion efficiency compared to the unmodified peptides, and liposomes prepared with the new E variant were shown to be unstable and aggregate, which was attributed to the homomeric interactions of peptide E on opposing membranes. The formation of weak homomeric coiled-coils of peptide E was previously assumed to have no effect on the fusion process, however here we showed how this stabilized the peptide before the docking stage, allowing fusion to occur in a leakage-free manner.

In order to separate the effects of coiled-coil and membrane interactions on fusion efficiency, a peptide stapling strategy is used in **Chapter 3** to investigate the interactions of peptide K<sub>3</sub>. Cysteines were introduced in the peptide backbone, spaced *i* to *i+4* to span a single helical turn, and crosslinked to generate structural variants of peptide K. These stapled peptides were analysed for changes in folding, coiled-coil binding and membrane affinity, with stapling increasing coiled-coil binding through a pre-organization mechanism. Fusion assays showed a large increase in content mixing directly related to increased coiled-coil binding strength. The results in this chapter disprove the hypothesis that membrane interactions of peptide K are beneficial for fusion, and support the idea that fusion efficiency is directly related to coiled-coil binding strength.

**Chapter 4** investigates coiled-coil peptide stapling using azobenzene crosslinkers as light-switchable alternatives to the rigid crosslinkers shown to affect coiled-coil formation in **Chapter 3**. These azobenzene crosslinkers can switch between two isomers upon light irradiation, and when connected to the peptide at two positions,

this change in morphology allows for photocontrol of peptide folding. A single azobenzene crosslinker was found ineffective for controlling peptide structure in a four-heptad coiled coil, but reducing the length of the coiled coil to three heptads resulted in a larger separation between the two isomers, and shows the potential of this strategy to control coiled-coil self-assembly using light.

Because the preparation of azobenzene-crosslinked peptides in **Chapter 4** was synthetically challenging, a different strategy for coiled-coil photocontrol was investigated in **Chapter 5**, based on the incorporation of amino acids bearing an azobenzene moiety. Two azobenzene derivatives of phenylalanine were prepared, based on previous literature procedures, as well as a novel azobenzene derivative of phenylglycine. Substitution of a single isoleucine in the hydrophobic core of peptide K by these amino acids yielded peptides that could be switched between two states using UV light. The phenylglycine based photoswitch created the largest difference upon isomerization, and the mechanism of action was related to a switch in polarity of the diazene bond upon isomerization. Molecular dynamics (MD) simulations revealed the diazene of the phenylglycine based photoswitch to be positioned in the coiled-coil hydrophobic core, and demonstrated how the methylene group in phenylalanine-based photoswitches increased reorganization after isomerization. Together, these findings demonstrate the incorporation of azobenzene-based amino acids as an effective, novel method for coiled-coil photocontrol.

Disruption of hydrophobic domains, by amino acids containing an azobenzene moiety, was hypothesized as a general mechanism for peptide photocontrol. The viability of this strategy in  $\beta$ -structured peptides is investigated in **Chapter 6** of this thesis. A photoswitchable amino acid was introduced in different positions of a peptide known to self-assemble to form  $\beta$ -sheet-based fibres, and the effect of isomerization on structure and self-assembly was studied. Prepared peptides showed  $\beta$ -sheet fibre formation, with different oligomerization and self-assembly kinetics depending on the location of the photoswitch. Peptide folding and the critical aggregation concentration could be altered through light isomerization, demonstrating the application of this amino acid in the photocontrol of  $\beta$ -sheet peptides and confirming our hypothesis. To test if azobenzene isomerization can be used to control peptide activity, histidine residues were introduced and the peptides were evaluated for organocatalytic activity, demonstrating an activity which was dependent on the state of the photoswitch.

## 1.5 References

1. Nelson, D. L., Lehninger, A. L., and Cox, M. M. (2017) *Lehninger principles of biochemistry*, 7th ed., Macmillan.
2. Dill, K. A., *et al.* (2008) The protein folding problem. *Annu Rev Biophys* 37, 289-316.
3. Orengo, C. A., *et al.* (1997) CATH--a hierarchic classification of protein domain structures. *Structure* 5, 1093-108.
4. Smith, C. K., and Regan, L. (1997) Construction and Design of  $\beta$ -Sheets. *Acc. Chem. Res.* 30, 153-161.
5. Xiong, H., *et al.* (1995) Periodicity of polar and nonpolar amino acids is the major determinant of secondary structure in self-assembling oligomeric peptides. *P. Natl. Acad. Sci. USA* 92, 6349-6353.
6. Nick Pace, C., and Martin Scholtz, J. (1998) A Helix Propensity Scale Based on Experimental Studies of Peptides and Proteins. *Biophys. J.* 75, 422-427.
7. Smith, C. K., Withka, J. M., and Regan, L. (1994) A Thermodynamic Scale for the beta.-Sheet Forming Tendencies of the Amino Acids. *Biochem.* 33, 5510-5517.
8. Minor, D. L., and Kim, P. S. (1994) Measurement of the  $\beta$ -sheet-forming propensities of amino acids. *Nature* 367, 660-663.
9. Kohn, W. D., and Hodges, R. S. (1998) De novo design of  $\alpha$ -helical coiled coils and bundles: models for the development of protein-design principles. *Trends Biotech.* 16, 379-389.
10. Apostolovic, B., Danial, M., and Klok, H. A. (2010) Coiled coils: attractive protein folding motifs for the fabrication of self-assembled, responsive and bioactive materials. *Chemical Society reviews* 39, 3541-75.
11. Crick, F. H. C. (1953) The packing of  $\alpha$ -helices: simple coiled-coils. *Acta Crystallogr.* 6, 689-697.
12. Lupas, A. (1996) Coiled coils: new structures and new functions. *Trends Biochem. Sci.* 21, 375-82.
13. Walshaw, J., and Woolfson, D. N. (2003) Extended knobs-into-holes packing in classical and complex coiled-coil assemblies. *J. Struct. Biol.* 144, 349-361.
14. Woolfson, D. N. (2005) The design of coiled-coil structures and assemblies. *Adv. Protein Chem.* 70, 79-112.
15. Mason, J. M., and Arndt, K. M. (2004) Coiled coil domains: stability, specificity, and biological implications. *ChemBiochem : a European journal of chemical biology* 5, 170-6.
16. Lupas, A., Van Dyke, M., and Stock, J. (1991) Predicting coiled coils from protein sequences. *Science* 252, 1162-1164.
17. Wolf, E., Kim, P. S., and Berger, B. (1997) MultiCoil: A program for predicting two-and three-stranded coiled coils. *Protein Sci.* 6, 1179-1189.
18. Walshaw, J., and Woolfson, D. N. (2001) Socket: a program for identifying and analysing coiled-coil motifs within protein structures. *J. Mol. Biol.* 307, 1427-50.
19. Dawson, W. M., *et al.* (2021) Coiled coils 9-to-5: rational de novo design of  $\alpha$ -helical barrels with tunable oligomeric states. *Chem. Sci.* 12, 6923-6928.

20. Harbury, P. B., *et al.* (1993) A switch between two-, three-, and four-stranded coiled coils in GCN4 leucine zipper mutants. *Science* 262, 1401-7.
21. Thomas, F., *et al.* (2016) Controlling the Assembly of Coiled–Coil Peptide Nanotubes. *Angew. Chem. Int. Ed.* 55, 987-991.
22. Boato, F., *et al.* (2007) Synthetic virus-like particles from self-assembling coiled-coil lipopeptides and their use in antigen display to the immune system. *Angew. Chem. Int. Ed.* 46, 9015-8.
23. Banwell, E. F., *et al.* (2009) Rational design and application of responsive  $\alpha$ -helical peptide hydrogels. *Nat. Mater.* 8, 596-600.
24. Hakata, Y., *et al.* (2015) A novel leucine zipper motif-based hybrid peptide delivers a functional peptide cargo inside cells. *Chem. Commun.* 51, 413-6.
25. Utterström, J., *et al.* (2021) Coiled coil-based therapeutics and drug delivery systems. *Adv. Drug Del. Rev.* 170, 26-43.
26. Marsden, H. R., and Kros, A. (2010) Self-Assembly of Coiled Coils in Synthetic Biology: Inspiration and Progress. *Angew. Chem. Int. Edit.* 49, 2988-3005.
27. Robson Marsden, H., *et al.* (2009) A Reduced SNARE Model for Membrane Fusion. *Angew. Chem. Int. Edit.* 48, 2330-2333.
28. Jahn, R., Lang, T., and Südhof, T. C. (2003) Membrane fusion. *Cell* 112, 519-33.
29. Xiao, T., Cai, Y., and Chen, B. (2021) HIV-1 Entry and Membrane Fusion Inhibitors. *Viruses* 13, 735.
30. Nishima, W., and Kulik, M. (2021) Full-Length Computational Model of the SARS-CoV-2 Spike Protein and Its Implications for a Viral Membrane Fusion Mechanism. *Viruses* 13, 1126.
31. Mazur, F., and Chandrawati, R. (2021) Membrane Fusion Models for Bioapplications. *ChemNanoMat* 7, 223-237.
32. Martens, S., and McMahon, H. T. (2008) Mechanisms of membrane fusion: disparate players and common principles. *Nat. Rev. Mol. Cell Biol.* 9, 543.
33. Cohen, F. S., and Melikyan, G. B. (2004) The energetics of membrane fusion from binding, through hemifusion, pore formation, and pore enlargement. *J Membrane Biol* 199, 1-14.
34. Kozlovsky, Y., and Kozlov, M. M. (2002) Stalk model of membrane fusion: Solution of energy crisis. *Biophys J* 82, 882-895.
35. Chlanda, P., *et al.* (2016) The hemifusion structure induced by influenza virus haemagglutinin is determined by physical properties of the target membranes. *Nat. Microbiol.* 1, 16050.
36. Hernandez, J. M., *et al.* (2012) Membrane fusion intermediates via directional and full assembly of the SNARE complex. *Science* 336, 1581-1584.
37. Risselada, H. J. (2017) Membrane Fusion Stalks and Lipid Rafts: A Love-Hate Relationship. *Biophys. J.* 112, 2475-2478.
38. Risselada, H. J., Bubnis, G., and Grubmüller, H. (2014) Expansion of the fusion stalk and its implication for biological membrane fusion. *P. Natl. Acad. Sci. USA* 111, 11043-11048.

39. Kawamoto, S., and Shinoda, W. (2014) Free energy analysis along the stalk mechanism of membrane fusion. *sSoft Matter* 10, 3048-3054.
40. Weber, T., et al. (1998) SNAREpins: Minimal Machinery for Membrane Fusion. *Cell* 92, 759-772.
41. Poirier, M. A., et al. (1998) The synaptic SNARE complex is a parallel four-stranded helical bundle. *Nat. Str. Biol.* 5, 765-769.
42. Li, F., et al. (2007) Energetics and dynamics of SNAREpin folding across lipid bilayers. *Nat. Str. Mol. Biol.* 14, 890-896.
43. Furukawa, N., and Mima, J. (2014) Multiple and distinct strategies of yeast SNAREs to confer the specificity of membrane fusion. *Sci. Rep.* 4, 4277.
44. van den Bogaart, G., et al. (2010) One SNARE complex is sufficient for membrane fusion. *Nat. Str. Mol. Biol.* 17, 358-364.
45. Li, X., et al. (2019) Symmetrical organization of proteins under docked synaptic vesicles. *FEBS letters* 593, 144-153.
46. McDargh, Z. A., Polley, A., and O'Shaughnessy, B. (2018) SNARE-mediated membrane fusion is a two-stage process driven by entropic forces. *FEBS letters* 592, 3504-3515.
47. Südhof, T. C. (2013) Neurotransmitter release: the last millisecond in the life of a synaptic vesicle. *Neuron* 80, 675-90.
48. Rizo, J., and Xu, J. (2015) The Synaptic Vesicle Release Machinery. *Annu. Rev. Biophys.* 44, 339-367.
49. Baker, R. W., and Hughson, F. M. (2016) Chaperoning SNARE assembly and disassembly. *Nat. Rev. Mol. Cell Biol.* 17, 465-479.
50. Risselada, H. J., and Mayer, A. (2020) SNAREs, tethers and SM proteins: how to overcome the final barriers to membrane fusion? *The Biochemical journal* 477, 243-258.
51. Rizo, J., Jaczynska, K., and Stepien, K. P. (2021) Molecular machinery turns full circle. *eLife* 10, e70298.
52. Zhao, M., et al. (2015) Mechanistic insights into the recycling machine of the SNARE complex. *Nature* 518, 61-67.
53. Waxman, S. G. (1980) Determinants of conduction velocity in myelinated nerve fibers. *Muscle & nerve* 3, 141-150.
54. Han, J., Pluhackova, K., and Böckmann, R. A. (2017) The Multifaceted Role of SNARE Proteins in Membrane Fusion. *Front. Physiol.* 8.
55. Chen, X., et al. (2006) SNARE-mediated lipid mixing depends on the physical state of the vesicles. *Biophys J* 90, 2062-2074.
56. Marsden, H. R., Tomatsu, I., and Kros, A. (2011) Model systems for membrane fusion. *Chem. Soc. Rev.* 40, 1572-1585.
57. Kumar, P., Guha, S., and Diederichsen, U. (2015) SNARE protein analog-mediated membrane fusion. *J. Pept. Sci.* 21, 621-629.
58. Li, W., Nicol, F., and Szoka, F. C. (2004) GALA: a designed synthetic pH-responsive amphipathic peptide with applications in drug and gene delivery. *Adv. Drug Del. Rev.* 56, 967-985.

59. Sun, L., *et al.* (2018) Guiding protein delivery into live cells using DNA-programmed membrane fusion. *Chem. Sci.* 9, 5967-5975.
60. Lygina, A. S., *et al.* (2011) Transmembrane Domain Peptide/Peptide Nucleic Acid Hybrid as a Model of a SNARE Protein in Vesicle Fusion. *Angew. Chem. Int. Edit.* 50, 8597-8601.
61. Ma, M., Gong, Y., and Bong, D. (2009) Lipid Membrane Adhesion and Fusion Driven by Designed, Minimally Multivalent Hydrogen-Bonding Lipids. *J. Am. Chem. Soc.* 131, 16919-16926.
62. Marchi-Artzner, V., *et al.* (1997) Molecular recognition induced aggregation and fusion between vesicles containing lipids bearing complementary hydrogen bonding head-groups. *Chem. Comm.*, 117-118.
63. Kashiwada, A., Tsuboi, M., and Matsuda, K. (2009) Target-selective vesicle fusion induced by molecular recognition on lipid bilayers. *Chem. Commun.*, 695-697.
64. Gong, Y., *et al.* (2008) Functional Determinants of a Synthetic Vesicle Fusion System. *J. Am. Chem. Soc.* 130, 6196-6205.
65. Gong, Y., Luo, Y. M., and Bong, D. (2006) Membrane activation: Selective vesicle fusion via small molecule recognition. *J. Am. Chem. Soc.* 128, 14430-14431.
66. Litowski, J. R., and Hodges, R. S. (2002) Designing heterodimeric two-stranded alpha-helical coiled-coils - Effects of hydrophobicity and alpha-helical propensity on protein folding, stability, and specificity. *J. Biol. Chem.* 277, 37272-37279.
67. Kong, L., *et al.* (2016) Temporal Control of Membrane Fusion through Photolabile PEGylation of Liposome Membranes. *Angew. Chem. Int. Edit.* 55, 1396-1400.
68. Versluis, F., *et al.* (2013) In Situ Modification of Plain Liposomes with Lipidated Coiled Coil Forming Peptides Induces Membrane Fusion. *J. Am. Chem. Soc.* 135, 8057-8062.
69. Versluis, F., *et al.* (2013) Coiled-coil driven membrane fusion: zipper-like vs. non-zipper-like peptide orientation. *Faraday Disc.* 166, 349-359.
70. Zheng, T. T., *et al.* (2013) Controlling the rate of coiled coil driven membrane fusion. *Chem. Comm.* 49, 3649-3651.
71. Daudey, G. A., *et al.* (2017) Membrane-Fusogen Distance Is Critical for Efficient Coiled-Coil Peptide-Mediated Liposome Fusion. *Langmuir* 33, 12443-12452.
72. Rabe, M., *et al.* (2014) Membrane Interactions of Fusogenic Coiled-Coil Peptides: Implications for Lipopeptide Mediated Vesicle Fusion. *Langmuir* 30, 7724-7735.
73. Rabe, M., Zope, H. R., and Kros, A. (2015) Interplay between Lipid Interaction and Homo-coiling of Membrane-Tethered Coiled-Coil Peptides. *Langmuir* 31, 9953-9964.
74. Rabe, M., *et al.* (2016) A Coiled-Coil Peptide Shaping Lipid Bilayers upon Fusion. *Biophys. J.* 111, 2162-2175.
75. Koukalova, A., *et al.* (2018) Distinct roles of SNARE-mimicking lipopeptides during initial steps of membrane fusion. *Nanoscale* 10, 19064-19073.
76. Yang, J., *et al.* (2016) Drug Delivery via Cell Membrane Fusion Using Lipopeptide Modified Liposomes. *ACS Cent. Sci.* 2, 621-630.
77. Yang, J., *et al.* (2016) Application of Coiled Coil Peptides in Liposomal Anticancer Drug Delivery Using a Zebrafish Xenograft Model. *ACS nano* 10, 7428-35.

78. Mora, N. L., *et al.* (2016) Targeted anion transporter delivery by coiled-coil driven membrane fusion. *Chem. Sci.* 7, 1768-1772.
79. Yang, J., *et al.* (2017) Membrane Fusion Mediated Intracellular Delivery of Lipid Bilayer Coated Mesoporous Silica Nanoparticles. *Adv. Helthc. Mater.* 6, 1700759.
80. Oude Blenke, E. E., *et al.* (2016) Coiled coil interactions for the targeting of liposomes for nucleic acid delivery. *Nanoscale* 8, 8955-8965.
81. Voskuhl, J., *et al.* (2012) Immobilization of liposomes and vesicles on patterned surfaces by a peptide coiled-coil binding motif. *Angew. Chem. Int. Edit.* 51, 12616-20.
82. Poulcharidis, D., *et al.* (2017) A flow cytometry assay to quantify intercellular exchange of membrane components. *Chem. Sci.* 8, 5585-5590.
83. Shen, M.-J., *et al.* (2021) Magnetic-Activated Cell Sorting Using Coiled-Coil Peptides: An Alternative Strategy for Isolating Cells with High Efficiency and Specificity. *ACS Appl. Mater. Interfaces* 13, 11621-11630.
84. Tomatsu, I., *et al.* (2011) Influence of pegylation on peptide-mediated liposome fusion. *J. Mat. Chem.* 21, 18927-18933.
85. Kong, L., *et al.* (2020) Light-Triggered Cancer Cell Specific Targeting and Liposomal Drug Delivery in a Zebrafish Xenograft Model. *Adv. Helthc. Mater.* 9, 1901489.





---

## Peptide-mediated liposome fusion: the effects of anchor positioning

This chapter was published as an original research paper: Niek S.A. Crone, Dirk Minnee, Alexander Kros, Aimee L. Boyle, *Int. J. Mol. Sci.* **2018**, 19(1), 211.

## **Abstract**

A minimal model system for membrane fusion, comprising two complementary peptides dubbed 'E' and 'K' joined to a cholesterol anchor via a polyethyleneglycol spacer, has previously been developed in our group. This system promotes the fusion of large unilamellar vesicles and facilitates liposome-cell fusion both *in vitro* and *in vivo*. Whilst several aspects of the system have previously been investigated to provide an insight as to how fusion is facilitated, anchor positioning has not yet been considered. In this study, the effects of placing the anchor at either the N-terminus or in the center of the peptide are investigated using a combination of circular dichroism spectroscopy, dynamic light scattering, and fluorescence assays. It was discovered that anchoring the 'K' peptide in the center of the sequence had no effect on its structure, its ability to interact with membranes, or its ability to promote fusion, whereas anchoring the 'E' peptide in the middle of the sequence dramatically decreases fusion efficiency. We postulate that anchoring the 'E' peptide in the middle of the sequence disrupts its ability to form homodimers with peptides on the same membrane, leading to aggregation and content leakage.

## 2.1 Introduction

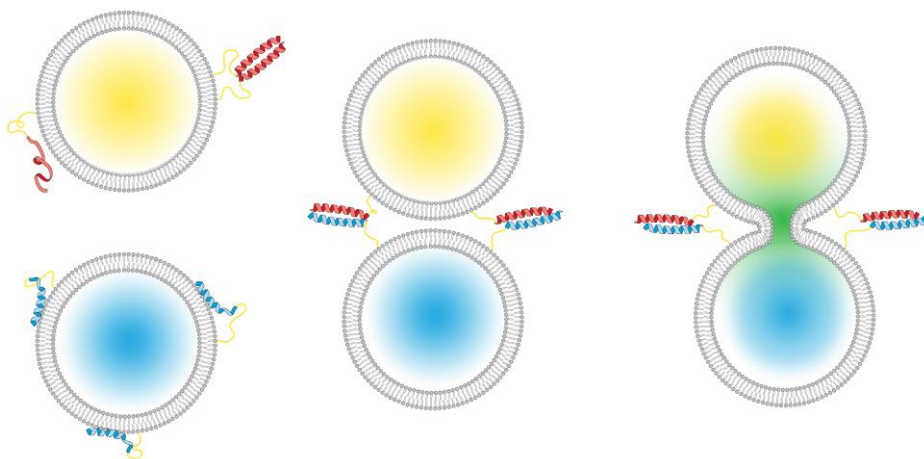
Within cells, the process of membrane fusion regulates a range of vital processes, including intracellular transport and exocytosis. In eukaryotic cells, these fusion events are regulated by a family of proteins named soluble *N*-ethylmaleimide-sensitive factor (NSF) attachment protein receptor (SNARE) proteins.<sup>1-4</sup> One specific SNARE-mediated membrane fusion process that has been widely studied in recent years is that of neurotransmitter release; neurotransmitters are packaged into vesicles functionalized with one SNARE protein and this interacts with two other SNARE proteins associated with the axonal presynaptic membrane to release neurotransmitters into the synaptic cleft.<sup>5,6</sup> This fusion process has four main steps: initially, the vesicle and axonal membranes are brought into close proximity by the three SNARE proteins from both membranes interacting to form a tetrameric coiled-coil; secondly, localized disruption of the membranes occurs; in the third step, the lipids of the outer membranes mix in a process known as hemifusion; and finally, the inner membranes mix and the contents are transferred.<sup>7</sup>

Using the natural SNARE proteins to study membrane fusion processes is clearly the most accurate way to understand more about these mechanisms, but, due to the number of proteins involved, it is often difficult to isolate the roles of specific proteins,<sup>8</sup> and some studies involving reconstituted SNAREs have failed to lead to fusion.<sup>9</sup> Developing model systems for membrane fusion may therefore be a solution to some of these issues, and in addition to providing fundamental mechanistic insights, model systems may also have application as, for example, drug delivery systems. Numerous model systems have been developed in recent years with a range of molecules, such as deoxyribonucleic acid (DNA),<sup>10-13</sup> peptide nucleic acid PNA,<sup>14, 15</sup> peptides,<sup>16-19</sup> and other small-molecule recognition complexes being employed as fusogens.<sup>20-22</sup>

In our lab, we have developed a model system for membrane fusion which comprises two complementary coiled-coil-forming peptides known as peptide E and peptide K. These peptides are named due the prevalence of glutamic acid (E) residues in peptide E (EIAALEK)<sub>n</sub> and lysine (K) in peptide K (KIAALKE)<sub>n</sub>.<sup>23-25</sup> These peptides are linked to a cholesterol anchor via a polyethylene glycol (PEG) spacer, with the lipidated peptides carrying the names CPE and CPK. This cholesterol anchors the peptides into liposomal membranes, and it has been previously

demonstrated that, when E- and K-functionalized liposome populations are mixed, efficient and leakage-free lipid- and content-mixing occurs (**Scheme 2.1**).<sup>18</sup> We have previously probed numerous aspects of this system, including the peptide length and orientation,<sup>26, 27</sup> the PEG length,<sup>28</sup> and the anchor type.<sup>29</sup> Another study examined the effect of placing the anchor at the C- or N-terminus of the peptide or at both ends to generate a doubly anchored construct. It was discovered that the end at which the peptide was anchored, or indeed the presence of two anchors, did not affect either the rate or the extent of fusion.<sup>30</sup>

In this study, we aim to probe the question of anchor positioning further by examining the effect of placing the anchor in the center of the peptide. This is of interest as the majority of SNARE proteins are held in membranes by hydrophobic transmembrane domains, but some SNARE proteins, such as SNAP-25, are tethered to the membrane via palmitoyl side-chains that are bound to cysteine residues found in the center of the protein sequence.<sup>31, 32</sup> It would therefore be interesting to modify the E and K peptides so that the anchor is found at the center of the sequence and to compare these constructs to those which are anchored via the N-termini to determine which is the more effective anchor position. This system was probed using a combination of circular dichroism (CD) spectroscopy, lipid- and



**Scheme 2.1.** A peptide-mediated model system for membrane fusion. (Left): E (red) and K (blue) peptides are incorporated into liposomes; the E peptides are either unfolded or form homodimers, and the K peptides interact with lipid membranes.<sup>33</sup> Upon mixing the two liposome populations (middle), coiled-coil heterodimers are formed between the two peptides; this brings the membranes into close proximity, which facilitates full fusion, resulting in mixing of vesicle content (right).

content-mixing fluorescence assays, tryptophan fluorescence studies, and dynamic light scattering (DLS) to determine the effects of anchor positioning on peptide structure and both the rate and extent of membrane fusion.

It was discovered that placing the anchor in the center of the peptide sequence did not have a large effect on the structure of peptide K, but decreased the helicity of peptide E, although both peptides retained the ability to form a coiled-coil upon addition of the complementary peptide. Fusion was not affected when peptide K was anchored centrally, but strongly reduced lipid- and content-mixing was observed when the E peptide was anchored in this position. An increase in content leakage and a change in liposome size over time was also observed with this construct. It is postulated that anchoring the E peptide in the center of the sequence prevents homodimer formation with peptides on the same liposome, leading to aggregation as homodimers are formed with peptides on neighbouring liposomes. This aggregation then causes the liposomes to become unstable and limits the ability of this system to effectively facilitate lipid- and content-mixing.

## 2.2 Results

### *Design of the Study*

Inspired by the way in which some SNARE proteins, such as SNAP-25, are anchored to membranes,<sup>31, 32</sup> we decided to modify our model system to generate peptide constructs which had lipid anchors in the center of the peptide sequences. To facilitate this, the glutamic acid found at the 'f' position of the second heptad of the K peptide was mutated to lysine (**Figure 2.1**). A lysine was already found at this position in the E peptide, so no sequence modification was necessary. To enable selective anchor attachment, the highly acid labile methoxytrityl (mtt) protecting group was used to protect the lysine at this position. Upon completion of the peptide synthesis, this mtt group could be selectively deprotected to allow the PEG linker and cholesteryl anchor to be attached to the terminal amine group of this lysine side-chain, generating the peptides named fCPE and fCPK (**Figure 2.1A**). The consequence of anchoring the peptide at this position is an increased overall charge, from +4 to +5 for the K peptide and from -4 to -5 for the E peptide. To negate the effect of increased charge on vesicle fusion, two control peptides were synthesized which also possessed mtt-protected lysine in this position, but in this case the lysine side-chain was acetylated after synthesis to produce the control

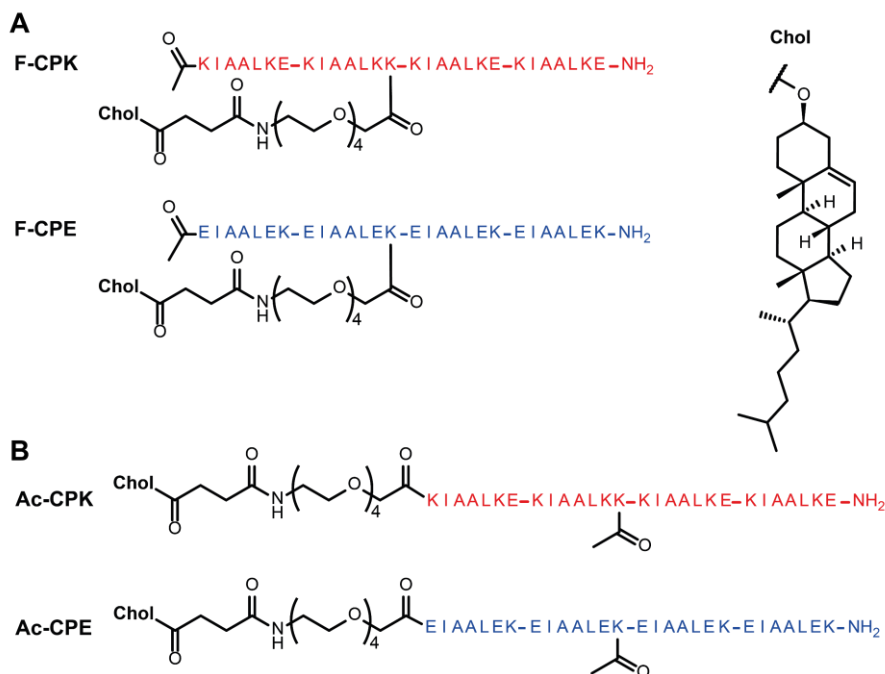


**Figure 2.1.** Structures of the cholesterol-anchored peptide constructs used in this study. The structures of fCPK and fCPE (A), and the structures of AcCPK and AcCPE (B).

peptides AcCPE and AcCPK (**Figure 2.1B**), which possessed the same charge as the fCPE and fCPK peptides.

### CD Spectroscopy

All four constructs were incorporated into liposomes and their secondary structures probed using CD spectroscopy. It is known that tethering peptides to a lipid surface can influence their secondary structure, particularly in the case of peptide K, which is required to interact with liposomes in order to facilitate fusion.<sup>33, 34</sup> As is evident from **Figure 2.2A**, both fCPK and AcCPK exhibit similar CD spectra, which show a partial helical character when tethered to liposomes; this is consistent with previous observations for CPK.<sup>33</sup> Upon addition of an equimolar amount of the complementary E peptide, the peak at 222 nm intensifies and the ratio between 208/222 nm is close to 1 (**Table 2.1**), which is indicative of coiled-coil formation. The differences in spectral shape and intensity between the two samples (fCPK + E and AcCpk + E) are negligible, indicating that anchor position does not affect the ability of the K peptide to form a coiled-coil with the E peptide. In

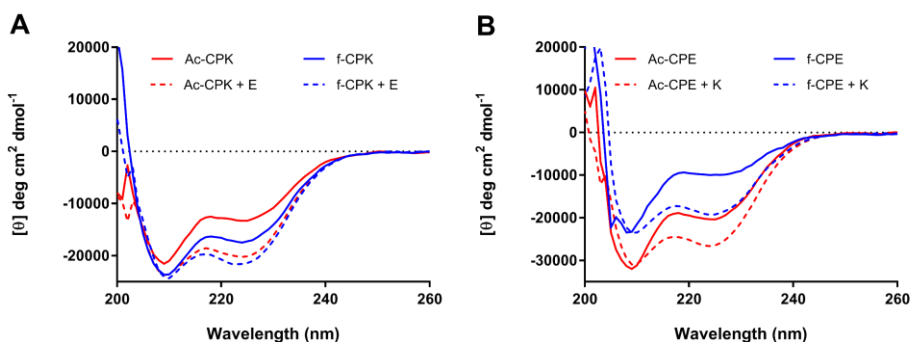


**Figure 2.2.** Circular dichroism (CD) spectra of the peptide constructs incorporated into liposomes. AcCPK (red solid line) and fCPK (blue solid line) show comparable partial helicity when incorporated into liposomes, and upon addition of E, coiled-coil species are observed with both AcCPK (red dotted line) and fCPK (blue dotted line) peptides (A); AcCPE (red solid line) and fCPE (blue solid line) are largely unfolded when incorporated into liposomes, but form coiled-coils upon K addition (red and blue dotted lines, B). [Total lipid] = 0.25 mM with 1 mol % cholesterol-anchored peptide and one equivalent E or K where stated, phosphate buffered saline (PBS), pH 7.4.

contrast, the spectra for fCPE and AcCPE, while similar in shape, show significant differences in intensity (**Figure 2.2B**). These spectra indicate that these peptides are also partially folded as  $\alpha$ -helices, and previous work reveals that this partial helicity originates from homomeric interactions between the E-peptides on the liposome surface.<sup>28, 33, 34</sup> These spectra may therefore indicate that the ability of the fCPE peptide to form these homomeric interactions is greatly reduced. Upon the addition of peptide K to both AcCPE and fCPE, more helical species are observed, indicating both peptides form heteromeric coiled-coils with peptide K.

**Table 2.1.** Molar ellipticities and helicity information for the peptides used in this study, when incorporated in monodisperse liposomes.

Peptides	$(\theta)_{222\text{nm}}$ (deg cm <sup>2</sup> dmol <sup>-1</sup> res <sup>-1</sup> )	% $\alpha$ -helix <sup>a</sup>	$(\theta)_{222\text{nm}}/(\theta)_{208\text{nm}}$
f-CPE	-9786	30%	0.42
f-CPE + K	-18,705	55%	0.84
Ac-CPE	-19,986	58%	0.64
Ac-CPE + K	-26,167	75%	0.89
f-CPK	-17,112	50%	0.75
f-CPK + E	-21,600	63%	0.94
Ac-CPK	-13,017	39%	0.62
Ac-CPK + E	-19,940	58%	0.87

<sup>a</sup> Percentage helicity was calculated from the molar ellipticity at 222 nm using previously reported methods.<sup>35</sup>

Collectively, this data indicate that the anchor position does not affect the secondary structure of the K-variants, but that the ability of the E peptide to form homomeric interactions may be disrupted when the anchor is placed in a central position. Whilst some of these intensity differences may result from concentration errors, these peptides do not contain chromophores that could be used to check for these deviations, the differences are too large to arise solely from these errors. Importantly, these data show that all of the constructs are still able to form coiled-coils effectively when the complementary peptide is added, although the overall structure is less defined when the peptides are attached to the lipid membrane (**Figure S2.1**). As coiled-coil formation is critical for liposome fusion, this indicates that, structurally, all of these constructs should be capable of promoting fusion.

### *Lipid Mixing*

To determine whether fCPE and fCPK are capable of promoting lipid-mixing, an intermediate step in the fusion process, a Förster resonance energy transfer (FRET) assay was performed. To facilitate this, 0.5 mol % of both 1,2-dioleoyl-*sn*-glycero-3-phosphoethanolamine (DOPE) with *N*-(lissamine rhodamine B sulfonyl) (DOPE-LR) and with *N*-(7-nitro-2,1,3-benzoxadiazol-4-yl) (DOPE-NBD) were incorporated into liposomes containing fCPK or AcCPK. When ~100 nm liposomes are formed, the distance between the NBD and LR fluorophores is sufficiently small that FRET occurs between the two. Upon lipid-mixing, this distance increases and FRET no longer occurs, so the emission of the NBD fluorophore can be measured and if an increase in the intensity of the emission occurs this is indicative of lipid-mixing.

**Figure 2.3A** shows a representative experiment that monitors the increase in fluorescence intensity over 1 h for the fCPK and fCPE pairing, the control peptides, and mixed combinations. From this data, it can be concluded that the AcCPE and AcCPK pairing is most efficient at lipid-mixing, with 35% lipid-mixing being observed after one hour. If one of these peptides is swapped for the centrally anchored derivative, a small decrease in lipid-mixing is observed. This decrease is negligible for the AcCPE and fCPK pairing, whereas a slightly larger decrease is observed for the AcCPK-fCPE pairing. It should be noted, however, that the extent of lipid-mixing is highly variable for this pairing (**Figure 2.3B**). All three of these combinations exhibit comparable initial rates of lipid-mixing, indicating that substituting one of the N-terminally linked peptides for a centrally anchored variant has only a small effect on the efficiency of the hemifusion process. When both fCPE and fCPK are

employed, however, a significant drop in both the rate and extent of lipid-mixing is observed, meaning that only small amounts of lipid-mixing occur when both centrally anchored peptides are employed.

### *Content Mixing*

As lipid-mixing, or hemifusion, is an intermediate step in the full fusion (content-mixing) process, it is unlikely that the fCPE–fCPK pairing will efficiently promote content-mixing, as only low levels of lipid-mixing were observed, but this was still examined. Liposomes bearing fCPE or AcCPE were loaded with a self-quenching concentration of sulforhodamine B. If content-mixing with CPK-functionalised liposomes occurs, the sulforhodamine B will dilute below its self-quenching concentration and an increase in fluorescence will be observed.

**Figure 2.4** shows that the AcCPK–AcCPE pairing is capable of promoting content-mixing with no leakage (**Figure S2.2**). After one hour, 60% content-mixing is achieved, which is comparable to the amount of content-mixing facilitated by the CPE and CPK peptides used in previous studies.<sup>27, 29</sup> The AcCPE–fCPK pairing also facilitates efficient content-mixing; both the rate and extent of mixing are comparable to the AcCPE–AcCPK pairing. The fact that both AcCPK and fCPK promote content-mixing when mixed with AcCPE is consistent with the CD data, which showed that both AcCPK and fCPK adopted partially helical structures when incorporated into liposomes and formed coiled-coils when the complementary E-peptide was added. This coiled-coil formation is the first step in the fusion process, and it is also important that the K-peptides are helical on liposomal membranes as their interaction with the liposome membranes is critical for fusion in this model system.

To confirm that fCPK and AcCPK still interact with membranes, as the CD and content-mixing data suggest, variants bearing a tryptophan (Trp) residue at their C-terminus were synthesized. Tryptophan fluorescence experiments were subsequently performed with these constructs at different peptide to lipid ratios, and these showed an increase in the intensity of the trp emission as the liposome concentration was increased (**Figure 2.5A**). A blue shift of the spectrum was also observed. Taken together, this fluorescence increase and the accompanying blue shift indicate that the trp is in a more hydrophobic environment when liposomes are present.<sup>36, 37</sup> suggesting that the peptide interacts with the liposomes. This has been observed for the original CPK variant,<sup>34, 38</sup> indicating that altering the charge

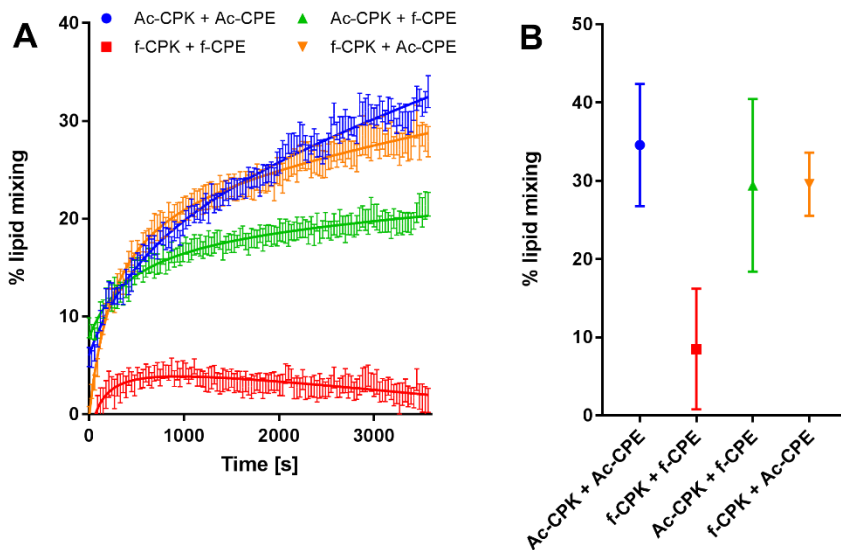


**Figure 2.3.** Lipid-mixing experiments for all combinations of fCPK, fCPE, AcCPK, and AcCPE. Representative lipid-mixing plots for: AcCPK–AcCPE (blue); fCPK–fCPE (red); AcCPK–fCPE (green); and fCPK–AcCPE (orange) with exponential fitting curves. (A) Error bars indicate the standard error of measurement between four samples. Average and standard deviation of the total % of lipid-mixing for three independent sets of experiments with: AcCPK–AcCPE (blue); fCPK–fCPE (red); AcCPK–fCPE (green); and fCPK–AcCPE (orange) lipopeptides (B). [Total lipid] = 100  $\mu$ M of DOPC:DOPE:Cholesterol, 50:25:25 mol %, with 1 mol % cholesterol-anchored peptide, PBS, pH 7.4.

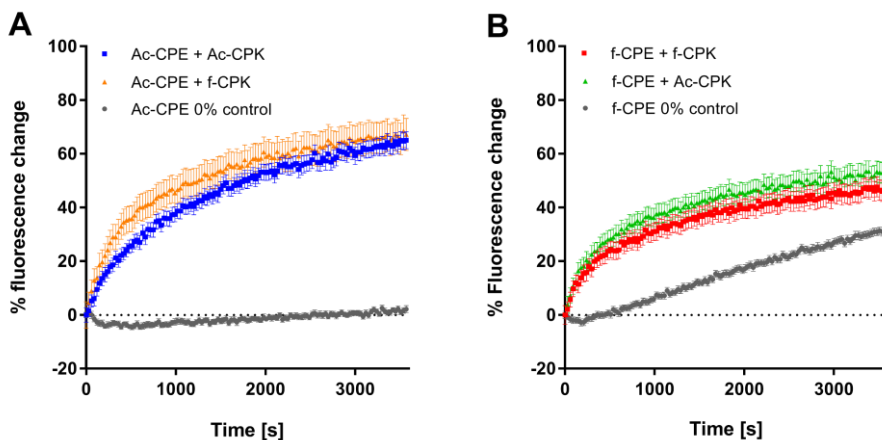


**Figure 2.4.** Content-mixing experiments for all combinations of fCPK, fCPE, AcCPK, and AcCPE. Representative content-mixing plots for: AcCPE–AcCPK (blue) and AcCPE–fCPK (orange), A; fCPE–fCPK (red) and fCPE–AcCPK (green), B. Zero percent controls represent samples of E-labelled liposomes mixed with plain liposomes. [Total lipid] = 100  $\mu$ M of DOPC:DOPE:Cholesterol, 50:25:25 mol %, with 1 mol % cholesterol-anchored peptide, PBS, pH 7.4.

of the peptide, for the AcCPK construct, coupled with changing the anchor position for fCPK, does not affect the ability of the peptide to interact with the liposome membrane.

When the fCPE construct is employed, it appears that content-mixing is observed for both the fCPE–fCPK and fCPE–AcCPK pairings, but when the 0% control is studied, a significant increase of fluorescence is also observed, indicating leakage of the dye from the fCPE liposomes (**Figure 2.4B**). The initial rate of leakage is different to the initial rate observed when fCPE is mixed with either fCPK or AcCPK, suggesting that some content-mixing may occur at first, but the final change in fluorescence for both samples with fCPE is 18% less than with the samples containing AcCPE. When leakage is accounted for (**Figure S2.2**), a relative fluorescence increase of only 17% for samples with fCPE is observed, compared to 64% for samples with AcCPE. These figures suggest that a small amount of content-mixing seems to occur with the fCPE liposomes, but this fluorescence assay cannot differentiate adequately between content-mixing and leaking, therefore it is not possible to draw firm conclusions about whether content-mixing is occurring when the fCPE variant is employed.

### Size Increase Studies

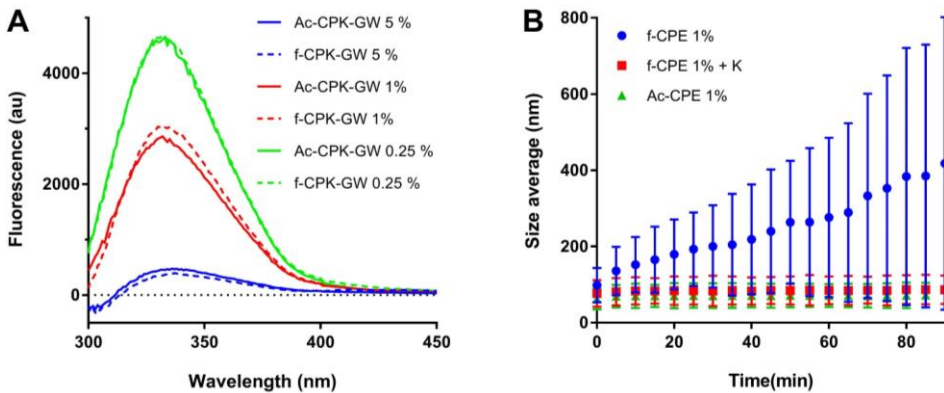


**Figure 2.5.** Liposome-dependent tryptophan fluorescence spectra for fCPK peptides (dotted lines) and AcCPK variants (solid lines) with a glycine and tryptophan on the C-terminus (A). Peptide concentration was kept constant at 2.5  $\mu\text{M}$ , and the amount of lipids was varied to create liposomes with three different peptide fractions: 5% (blue), 1% (red), and 0.25% (green). Liposome size increase monitored by dynamic light scattering (B). Size increase was monitored over 90 min for: fCPE-functionalized liposomes (blue); fCPE-functionalized liposomes with one equivalent of peptide K (red); and AcCPE-functionalized liposomes (green). Error bars indicate the 95% size distribution. [Total liposome] = 0.5 mM, PBS, pH 7.4.

To probe this unusual behaviour of fCPE further, dynamic light scattering (DLS) was employed to study the stability of the liposomes over time. Size changes of liposomes functionalized with both AcCPE and fCPE were investigated, and one equivalent of the complementary K peptide was added to fCPE-functionalized liposomes in another experiment. It is evident from **Figure 2.5B** that no significant size increase is observed for the AcCPE-functionalized liposomes, whereas the fCPE-functionalized liposomes increase in diameter from 100 nm to over 400 nm in 90 min. This change in size is accompanied by a significant change in the polydispersity of the sample, which is indicative of aggregate formation. When an equivalent of the K peptide is added to these liposomes, no size increase is observed over the same time period. Taken together, these data indicate that the size increase is likely to be due to homodimer formation between peptides anchored in different liposomes. The absence of a size increase when the K peptide is added is likely to be because EK heterodimers are formed, which are more stable than homodimers, and so the fCPE-functionalized liposomes are stabilized.

## 2.3 Discussion

We have demonstrated that changing the position of the cholesterol anchor site from the N-terminus to the center of the peptide affects E and K differently. CD spectroscopy demonstrates that both AcCPK and fCPK can interact with membranes; this is corroborated by an increase in trp fluorescence that is observed when trp-labelled derivatives of these constructs are mixed with liposomes. CD spectroscopy also revealed that both K constructs form coiled-coils when E is added. It has been demonstrated previously that both K-membrane interactions and EK-heterodimer formation are critical for effective fusion,<sup>28, 34, 38</sup> so the fact that altering the anchor position has no effect suggests that these constructs should still be capable of promoting fusion. This is demonstrated to be the case, with both AcCPK and fCPK facilitating lipid- and content-mixing when combined with AcCPE.

Different behaviour is observed for the AcCPE and fCPE derivatives. The structure of fCPE is reduced relative to both AcCPE and the free peptide E (**figure S2.1**). While AcCPE can promote leakage-free lipid- and content-mixing, reduced amounts of lipid-mixing are observed when the fCPE construct is employed, and significant leakage is observed during content-mixing when the fCPE construct is combined with either AcCPK or fCPK. An insight into what may be occurring is provided by the dynamic light scattering experiments, which show that the average particle size in a solution of fCPE-functionalized liposomes increases from 100 nm to 400 nm after

90 min. Previous studies of this system have shown that, in the absence of K, the E peptide exists primarily as a weakly associated homodimer on the surface of liposomes.<sup>33</sup> We postulate that, by anchoring the E peptide in the middle of the sequence, it is sterically prevented from forming homodimers with other peptides anchored in the same liposome. Homodimers therefore result from peptides on different liposomes interacting with each other, which leads to aggregation. This aggregation may subsequently lead to the destabilization of the liposomes, triggering content leakage, which is a phenomenon that has been observed in other peptide- and DNA-mediated fusion systems.<sup>16, 39-41</sup>

This hypothesis that f-position anchoring decreases homomeric interactions could also explain the significantly lower lipid-mixing for the fCPE–fCPK combination in comparison to fCPE–AcCPK. In our liposomal fusion model system, coiled-coil formation is the first step of the fusion process; this brings the membranes in close proximity, but the peptides are still able to dissociate, which allows peptide K to interact with opposing liposomal membranes and promote complete fusion.<sup>38</sup> Changing the anchoring position may have a significant influence on the equilibrium between associated and dissociated E and K peptides, because there is a larger thermodynamic penalty for CPE to dissociate since it cannot form a stable homodimer. At the same time, changing the lipid attachment to form fCPK could disfavour the dissociation path where peptide K enters the membrane of the liposome that it is attached to, lowering the total amount of membrane-interacting peptide further.

Future studies could focus on probing this hypothesis further: AcCPE and fCPE constructs could be incorporated into the same liposome to determine whether homodimer formation is possible between the alternatively anchored constructs, and if so, this should decrease content leakage. FRET-pair labelled versions of CPE and CPK could be synthesized to observe the interactions of these peptides when two different populations of liposomes are mixed. Another possible explanation for the high levels of content leakage observed could be that the fCPE peptides are interacting with the liposomes. This is unlikely as the peptide sequence has not been significantly changed, but this could be probed by synthesizing tryptophan-functionalized derivatives and performing tryptophan fluorescence experiments in the absence and presence of liposomes.

## 2.4 Materials and Methods

**Materials** Tentagel HL-RAM resin was obtained from Rapp Polymere (Tuebingen, Germany). Fmoc-protected amino acids and *O*-(1*H*-6-Chlorobenzotriazol-1-yl)-1,1,3,3-tetramethyluronium hexafluorophosphate (HCTU) were purchased from NovaBiochem (Amsterdam, The Netherlands). Acetic anhydride, acetonitrile, dimethylformamide (DMF), dioxane, methanol, piperidine, pyridine, and trifluoroacetic acid (TFA) were purchased from Biosolve (Valkenswaard, The Netherlands). *N,N*-Diisopropylethylamine (DIPEA) and Oxyma were purchased from Carl Roth (Karlsruhe, Germany). Cholesterol, cholesteryl hemisuccinate, Diisopropylcarbodiimide (DIC), *tert*-butanol, sulforhodamine B, sodium hydroxide, triisopropylsilane (TIPS), and trimethylphosphine (1 M in toluene) were obtained from Sigma Aldrich (Zwijndrecht, The Netherlands). Chloroform, dichloromethane (DCM), and diethyl ether were supplied by Honeywell (Meppel, The Netherlands). The compounds 1,2-dioleoyl-*sn*-glycero-3-phosphocholine (DOPC), 1,2-dioleoyl-*sn*-glycero-3-phosphoethanolamine (DOPE), 1,2-dioleoyl-*sn*-glycero-3-phosphoethanolamine-*N*-(lissamine rhodamine B sulfonyl) (DOPE-LR), and 1,2-dioleoyl-*sn*-glycero-3-phosphoethanolamine-*N*-(7-nitro-2,1,3-benzoxadiazol-4-yl) (DOPE-NBD) were all purchased from Avanti Polar Lipids (Alabaster, AL, USA). Ultrapure water was purified using a Milli-Q™ purification system from Millipore (Amsterdam, The Netherlands).

**N<sub>3</sub>-PEG<sub>4</sub>-COOH Synthesis** Ethyl 14-Azido-3,6,9,12-tetraoxatetradecan-1-oate (N<sub>3</sub>-PEG<sub>4</sub>-COOEt) was synthesized according to literature methods.<sup>42</sup> N<sub>3</sub>-PEG<sub>4</sub>-COOEt (1.64 g, 5.4 mmol) was dissolved in MeOH (25 mL). NaOH (1 M, 8 mL) was added, and the reaction was stirred overnight or until thin-layer chromatography (TLC) indicated complete conversion of the starting material. The reaction was diluted with H<sub>2</sub>O (12 mL), and the methanol was evaporated. The aqueous layer was washed with DCM (25 mL), acidified with HCl, and extracted with DCM (3 × 25 mL). After drying with Na<sub>2</sub>SO<sub>4</sub>, the solvent was removed to yield the product as a viscous liquid in quantitative yield. <sup>1</sup>H NMR (300 MHz, CDCl<sub>3</sub>) δ 10.80 (s, 1H), 4.07 (s, 2H), 3.64–3.63 (m, 2H), 3.6–3.55 (m, 12H), 3.28 (t, *J* = 6.0 Hz, 2H). <sup>13</sup>C NMR (300 MHz, CDCl<sub>3</sub>) δ 173.73, 70.82, 70.35, 70.29, 70.23, 70.17, 69.75, 50.38.

**Peptide Synthesis** Solid-phase synthesis was performed using a microwave-assisted Liberty Blue automated synthesizer from CEM (Matthews, NC, USA). Peptides were synthesized on a 0.1 mmol scale using Tentagel HL-RAM resin with a loading capacity of 0.37 mmol g<sup>-1</sup>. Fmoc deprotection was achieved using a solution

of 20% piperidine in DMF under heating at 90 °C for 1 min, followed by three washing steps. Coupling of amino acids was performed using 4 mL of coupling solution, containing 0.125 M of the respective amino acid, 0.25 M DIC as activator, and 0.125 M oxyma as base. Amino acid coupling was performed at 90 °C for 4 min.

To allow for selective deprotection and modification, mtt-protected lysine was used at position 14 of the peptide sequences. Once synthesis was complete, the peptide was first PEGylated or acylated on the N-terminus before modification of the mtt-protected lysine. The mtt-protecting group was selectively removed using DCM containing 3% TFA and 3% TIPS. Aliquots (2 mL) of this solution were added to the resin, which was shaken for 2 min before being washed with DMF. These steps were repeated until the yellow colour (indicative of the mtt-protecting group) was no longer observed. At this point, the peptides were PEGylated, reduced, lipidated, and cleaved as for the N-terminally anchored peptides.

Peptide PEGylation and lipidation was performed on resin, using two equivalents of the N<sub>3</sub>-PEG<sub>4</sub>-CH<sub>2</sub>-COOH spacer, HATU (two eq.) and DIPEA (four eq.). The resin was subsequently washed with DMF, and azide reduction was performed using trimethylphosphine (10 eq.) in 4:1 dioxane:water. After coupling, the resin was washed using 4:1 dioxane:water, DMF, and DCM. Lipidation was facilitated using cholesteryl hemisuccinate (two eq.) with HATU (two eq.) and DIPEA (four eq.). All conversions were confirmed using a Kaiser test.<sup>43</sup> The resin was washed with DMF and DCM before cleavage of the lipidated peptide construct from the resin was achieved using a 95:2.5:2.5 mixture of TFA:TIPS:water. The crude peptide was precipitated into cold diethyl ether, collected by centrifugation, redissolved in 20% acetonitrile/water, and lyophilized.

**Peptide Purification** All peptides were purified by reversed-phase HPLC using a Shimadzu system comprising two LC-8A pumps and an SPD-10AVP UV-Vis detector. Lysine-rich peptides were purified on a Kinetix Evo C18 column, and Glutamic-acid-rich peptides were purified using a Vydac protein C4 column. Eluents used were water containing 0.1% TFA (A) and MeCN with 0.1% TFA (B); all peptides were eluted using a gradient of 20–90% B over 40 min at a flow rate of 15 ml min<sup>-1</sup>. The collected fractions were examined using LCMS, (**Table S2.1**), and the fractions containing purified peptide were pooled and freeze-dried.

**Formation of Liposomes** One millimolar (1 mM) stock solutions containing DOPC:DOPE:cholesterol (50:25:25 mol %) or DOPC:DOPE:cholesterol:DOPE-

LR:DOPE-NBD (49.5:24.75:24.75:0.5:0.5 mol %) were prepared in a 1:1 (v/v) chloroform:MeOH solution. Stock solutions of the lipidated peptides were prepared at 50  $\mu$ M concentration in the same solvent system.

For the lipid-mixing assays, fluorescent liposomes containing K-lipo-peptide constructs and non-fluorescent E-lipo-peptide-containing liposomes were prepared at 500  $\mu$ M concentration with 1 mol % lipo-peptide. Lipid films were formed by evaporating the chloroform:MeOH solution under a stream of air and rehydrating the resulting film with PBS buffer. The solution was then sonicated at 55  $^{\circ}$ C for  $\sim$ 10 min to yield liposomes of  $\sim$ 100 nm diameter as assessed by dynamic light scattering (DLS) spectroscopy on a Zetasizer Nano S (Malvern instruments, Malvern, UK) with PMMA low-volume cuvettes (VWR international, Leuven, Belgium). After formulation, the solutions were diluted to the working concentration of 100  $\mu$ M. Examples of size distributions of liposomes can be found in **Figure S2.3**.

For content-mixing assays, liposomes were prepared at 500  $\mu$ M concentration with 1 mol % lipo-peptide. Liposomes functionalized with K-lipo-peptides were rehydrated with PBS and prepared in the same manner as liposomes used for lipid-mixing assays. Liposomes bearing E-lipo-peptides were rehydrated with PBS containing 20 mM sulforhodamine B. The solution was then sonicated as before, and non-encapsulated sulforhodamine B was removed by passing the liposomes down a Sephadex G25 column (GE healthcare, Eindhoven, The Netherlands). After size exclusion, liposomes were diluted to the working concentration of 100  $\mu$ M.

**Fluorescence Spectroscopy** Lipid- and content-mixing assays were performed using a TECAN infinite M1000 PRO fluorimeter at 25  $^{\circ}$ C. All experiments were performed in 96-well plates. For the lipid-mixing experiments, fluorescence intensity was measured continuously for 1 h by monitoring NBD emission at 530 nm after mixing equimolar amounts of E- and K-functionalised liposomes. The percentage of lipid-mixing between the liposomes was calculated according to Equation (1):

$$\% \text{ lipid mixing} = (F_t - F_0)/(F_{max} - F_0) \quad (1)$$

where  $F_{(t)}$  is the fluorescence intensity at time ' $t$ ',  $F_0$  is the baseline fluorescence value, which was determined by measuring the fluorescence intensity of NBD-containing, K-functionalised liposomes to which an equal amount of PBS had been added, and  $F_{max}$  is the maximum fluorescence value, which was obtained by measuring the fluorescence intensity from liposomes containing half the concentration of fluorescent lipids (i.e., 0.25 mol % each of DOPE-LR and DOPE-

NBD). For content-mixing experiments, sulforhodamine B fluorescence intensity was measured for 60 min at 580 nm after mixing non-fluorescent K-liposomes with sulforhodamine B-containing E-liposomes. Negative control liposomes were prepared from the E-liposomes mixed with an equal number of plain liposomes. The percentage fluorescence increase was calculated using Equation (2):

$$\%F = (F_t - F_0)/F_0 \quad (2)$$

where  $F_0$  is defined as the fluorescence of each sample directly after mixing of the liposomes.

**Tryptophan Fluorescence Experiments** Lipid films for the liposomes used in tryptophan fluorescence studies were prepared at a constant peptide concentration of 2.5  $\mu\text{M}$  with varying amounts of lipid stock (50:25:25 mol% DOPC:DOPE:cholesterol, 1 M total concentration) to create samples with different lipid equivalents. Tryptophan was excited at 280 nm with a 10 nm band gap, and fluorescence emission between 300 and 450 nm was collected. Each sample was measured three times with a 1 min interval, and the three spectra were averaged.

**Size Increase Experiments** Change in liposome size and size distribution were followed by DLS. Samples were measured every 5 min for 90 min at a constant temperature of 25  $^{\circ}\text{C}$ . For every time point, 10 measurements of 6 s each were performed and their values averaged. Samples were prepared at 0.5 mM lipid concentration with 1% substituted by the respective lipopeptide. The non-lipidated binding partner, one equivalent, was added to the liposomes as a 100  $\mu\text{M}$  solution.

**CD Experiments** CD spectra were measured using a JASCO J-815 CD spectrometer fitted with a Peltier temperature controller set to 25  $^{\circ}\text{C}$ . Samples were measured in quartz cuvettes with a 5 mm path length. Spectra were recorded from 260 to 190 nm at 1 nm intervals with a 1 nm bandwidth. Mean residue molar ellipticity,  $[\theta]$ , ( $\text{deg cm}^2 \text{dmol}^{-1}\text{res}^{-1}$ ) was calculated according to Equation 3:

$$[\theta] = (100 * \theta_{obs}) / (c * n * l) \quad (3)$$

where  $\theta_{obs}$  is the observed ellipticity in mdeg,  $c$  is the peptide concentration in mM,  $n$  is the number of peptide bonds, and  $l$  is the path length of the cuvette in cm. Percentage helicity was calculated from the residue molar ellipticity at 222 nm using the following Equation (4):

$$F_{helix} = ([\theta]_{222} - [\theta]_0) / ([\theta]_{max} - [\theta]_0) \quad (4)$$

With  $[\theta]_{max}$  as the maximum theoretical mean residue ellipticity, defined as  $[\theta]_{max} = [\theta]_{\infty} (n - x)/n$  for an  $n$  residue helix and  $x$  an arbitrary number of amino acids assumed not to participate in helix formation (we use three in all calculations).  $[\theta]_{\infty}$  is defined as the theoretical helicity of an infinite  $\alpha$ -helix and is temperature-dependent, defined via  $[\theta]_{\infty} = (-44,000 + 250T)$ , with  $T$  being the temperature in  $^{\circ}\text{C}$ . The minimum signal expected for a random peptide coil at 222 nm is given as  $[\theta]_0$ , and is also temperature-dependent via the following relationship  $[\theta]_0 = 2220 - 53T$ .<sup>35</sup>

## 2.5 References

1. Jahn, R., Lang, T., and Sudhof, T. C. (2003) Membrane fusion. *Cell* 112, 519-533.
2. Jahn, R., and Scheller, R. H. (2006) SNAREs - engines for membrane fusion. *Nat. Rev. Mol. Cell Biol.* 7, 631-643.
3. Weber, T., et al. (1998) SNAREpins: Minimal machinery for membrane fusion. *Cell* 92, 759-772.
4. Wickner, W., and Schekman, R. (2008) Membrane fusion. *Nat. Str. Mol. Biol.* 15, 658-664.
5. Fasshauer, D., et al. (1998) Conserved structural features of the synaptic fusion complex: SNARE proteins reclassified as Q- and R-SNAREs. *P. Natl. Acad. Sci. USA* 95, 15781-15786.
6. Sutton, R. B., et al. (1998) Crystal structure of a SNARE complex involved in synaptic exocytosis at 2.4 angstrom resolution. *Nature* 395, 347-353.
7. Chernomordik, L. V., and Kozlov, M. M. (2008) Mechanics of membrane fusion. *Nat. Rev. Mol. Cell Biol.* 15, 675-683.
8. Chen, Y. A., and Scheller, R. H. (2001) Snare-mediated membrane fusion. *Nat. Rev. Mol. Cell Biol.* 2, 98-106.
9. Chen, X. C., et al. (2006) SNARE-mediated lipid mixing depends on the physical state of the vesicles. *Biophys. J.* 90, 2062-2074.
10. Flavier, K. M., and Boxer, S. G. (2017) Vesicle Fusion Mediated by Solanesol-Anchored DNA. *Biophys. J.* 113, 1260-1268.
11. Loffler, P. M. G., et al. (2017) A DNA-Programmed Liposome Fusion Cascade. *Angew. Chem. Int. Edit.* 56, 13228-13231.
12. van Lengerich, B., et al. (2013) Individual Vesicle Fusion Events Mediated by Lipid-Anchored DNA. *Biophys. J.* 105, 409-419.
13. Meng, Z., et al. (2017) Efficient Fusion of Liposomes by Nucleobase Quadruple-Anchored DNA. *Chem. Eur. J.* 23, 9391-9396.
14. Lygina, A. S., et al. (2011) Transmembrane Domain Peptide/Peptide Nucleic Acid Hybrid as a Model of a SNARE Protein in Vesicle Fusion. *Angew. Chem. Int. Edit.* 50, 8597-8601.
15. Rabe, A., et al. (2017) Programmable fusion of liposomes mediated by lipidated PNA. *Chem. Comm.* 53, 11921-11924.

16. Kashiwada, A., *et al.* (2008) Construction of a pH-responsive artificial membrane fusion system by using designed coiled-coil polypeptides. *Chem. Eur. J.* 14, 7343-7350.
17. Kashiwada, A., *et al.* (2011) Design and Characterization of Endosomal-pH-Responsive Coiled Coils for Constructing an Artificial Membrane Fusion System. *Chem. Eur. J.* 17, 6179-6186.
18. Marsden, H. R., *et al.* (2009) A Reduced SNARE Model for Membrane Fusion. *Angew. Chem. Int. Edit.* 48, 2330-2333.
19. Meyenberg, K., *et al.* (2011) SNARE derived peptide mimic inducing membrane fusion. *Chem. Commun.* 47, 9405-9407.
20. Gong, Y., Luo, Y. M., and Bong, D. (2006) Membrane activation: Selective vesicle fusion via small molecule recognition. *J. Am. Chem. Soc.* 128, 14430-14431.
21. Kashiwada, A., Tsuboi, M., and Matsuda, K. (2009) Target-selective vesicle fusion induced by molecular recognition on lipid bilayers. *Chem. Commun.* 695-697.
22. Ma, M. M., Gong, Y., and Bong, D. (2009) Lipid Membrane Adhesion and Fusion Driven by Designed, Minimally Multivalent Hydrogen-Bonding Lipids. *J. Am. Chem. Soc.* 131, 16919-16926.
23. Litowski, J. R., and Hodges, R. S. (2001) Designing heterodimeric two-stranded alpha-helical coiled-coils: the effect of chain length on protein folding, stability and specificity. *J. Pept. Res.* 58, 477-492.
24. Litowski, J. R., and Hodges, R. S. (2002) Designing heterodimeric two-stranded alpha-helical coiled-coils - Effects of hydrophobicity and alpha-helical propensity on protein folding, stability, and specificity. *J. Biol. Chem.* 277, 37272-37279.
25. Marsden, H. R., Tomatsu, I., and Kros, A. (2011) Model systems for membrane fusion. *Chem. Soc. Rev.* 40, 1572-1585.
26. Zheng, T. T., *et al.* (2016) A non-zipper-like tetrameric coiled coil promotes membrane fusion. *RSC Adv.* 6, 7990-7998.
27. Zheng, T. T., *et al.* (2013) Controlling the rate of coiled coil driven membrane fusion. *Chem. Comm.* 49, 3649-3651.
28. Daudey, G. A., *et al.* (2017) Membrane-Fusogen Distance Is Critical for Efficient Coiled-Coil-Peptide-Mediated Liposome Fusion. *Langmuir* 33, 12443-12452.
29. Versluis, F., *et al.* (2013) In Situ Modification of Plain Liposomes with Lipidated Coiled Coil Forming Peptides Induces Membrane Fusion. *J. Am. Chem. Soc.* 135, 8057-8062.
30. Versluis, F., *et al.* (2013) Coiled-coil driven membrane fusion: zipper-like vs. non-zipper-like peptide orientation. *Faraday Disc.* 166, 349-359.
31. Gonzalo, S., Greentree, W. K., and Linder, M. E. (1999) SNAP-25 is targeted to the plasma membrane through a novel membrane-binding domain. *J. Biol. Chem.* 274, 21313-21318.
32. Hess, D. T., *et al.* (1992) The 25 kDa Synaptosomal-associated protein SNAP-25 is the major methionine-rich polypeptide in rapid axonal-transport and a major substrate for palmitoylation in adult CNS. *J. Neurosci.* 12, 4634-4641.
33. Rabe, M., Zope, H. R., and Kros, A. (2015) Interplay between Lipid Interaction and Homocooling of Membrane-Tethered Coiled-Coil Peptides. *Langmuir* 31, 9953-9964.

34. Rabe, M., *et al.* (2014) Membrane Interactions of Fusogenic Coiled-Coil Peptides: Implications for Lipopeptide Mediated Vesicle Fusion. *Langmuir* 30, 7724-7735.
35. Luo, P., and Baldwin, R. L. (1997) Mechanism of Helix Induction by Trifluoroethanol: A Framework for Extrapolating the Helix-Forming Properties of Peptides from Trifluoroethanol/Water Mixtures Back to Water. *Biochem.* 36, 8413-8421.
36. Eftink, M. R. (2006) Fluorescence Techniques for Studying Protein Structure, in *Methods of Biochemical Analysis* pp 127-205, John Wiley & Sons, Inc.
37. Lakowicz, J. R. (2006) *Principles of fluorescence spectroscopy*, Springer, New York.
38. Rabe, M., *et al.* (2016) A Coiled-Coil Peptide Shaping Lipid Bilayers upon Fusion. *Biophys. J.* 111, 2162-2175.
39. de Souza, D. L., *et al.* (2002) Membrane-active properties of alpha-MSH analogs: aggregation and fusion of liposomes triggered by surface-conjugated peptides. *BBA Biomembranes* 1558, 222-237.
40. Stengel, G., *et al.* (2008) Determinants for membrane fusion induced by cholesterol-modified DNA zippers. *J. Phys. Chem. B* 112, 8264-8274.
41. Xia, Y. Q., Sun, J. B., and Liang, D. H. (2014) Aggregation, Fusion, and Leakage of Liposomes Induced by Peptides. *Langmuir* 30, 7334-7342.
42. Shirude, P. S., Kumar, V. A., and Ganesh, K. N. (2005) BisPNA Targeting to DNA: Effect of Neutral Loop on DNA Duplex Strand Invasion by aepPNA-N7G/aepPNA-C Substituted Peptide Nucleic Acids. *Eur. J. Org. chem.*, 5207-5215.
43. Kaiser, E., *et al.* (1970) Color test for detection of free terminal amino groups in the solid-phase synthesis of peptides. *Anal. Biochem.* 34, 595-598.

## Supporting Information for Chapter 2

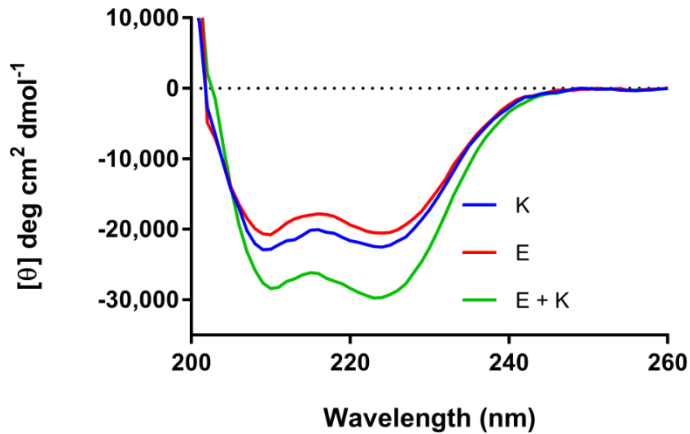


**Figure S2.1:** CD structures of the coiled-coil forming peptides E; (EIAALEK)<sub>4</sub>GW, K; (KIAALKE)<sub>4</sub>GW, and the EK coiled-coil complex without liposomes. Conditions: [2.5  $\mu\text{M}$ ] peptide, PBS pH 7.4, 25 °C.

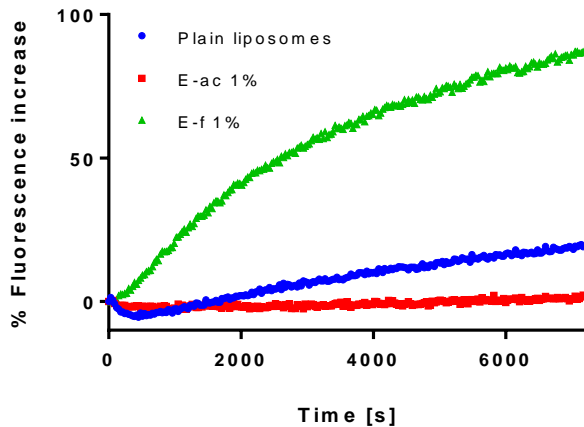


**Figure S2.2:** Leaking of sulforhodamine B from liposomes used in content mixing experiments. Liposomes [0.1 mM], comprise DOPC:DOPE:Cholesterol (50:25:25 mol%), with 20 mM Sulforhodamine B, (AcCPE, and fCPE functionalised liposomes), or 10 mM (plain liposomes) in PBS, pH 7.4.

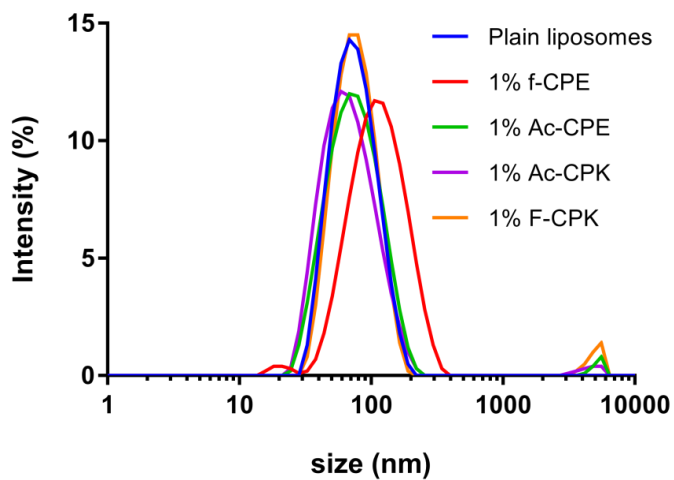


**Figure S2.3:** Size distribution by intensity of liposomes used in fusion experiments as measured using DLS. liposomes [0.5 mM], comprising DOPC:DOPE:Cholesterol (50:25:25 mol%) with 1% of the respective lipopeptide; f-CPE (Red), Ac-CPE (Green), f-CPK (yellow) and Ac-CPK (purple) in PBS at pH 7.4. Liposomes were subsequently diluted from 0.5 mM to the appropriate concentrations for CD, fluorescence, or lipid- and content-mixing experiments.

## LC-MS of purified peptides

**Table S2.1:** Overview of the calculated masses of all peptides used in this project, and the masses found by LCMS.

Peptide name	Calculated mass (Da)	Measured mass (Da)
AcCPE	$[M + 2H^+]^{2+}$ 1891.61	1890.21
	$[M + 2H^+ - \text{cholesterol}]^{2+}$ 1706.85	1705.24
	$[M + 3H^+]^{3+}$ 1261.41	1260.77
fCPE	$[M + 2H^+]^{2+}$ 1891.61	1890.00
	$[M + 2H^+ - \text{cholesterol}]^{2+}$ 1706.85	1705.94
	$[M + 3H^+]^{3+}$ 1261.41	1272.24
AcCPK	$[M + 2H^+]^{2+}$ 1889.74	1887.90
	$[M + 2H - \text{cholesterol}^+]^{2+}$ 1705.135	1702.94
	$[M + 3H^+]^{3+}$ 1260.16	1257.96
fCPK	$[M + 3H^+ - \text{cholesterol}]^{3+}$ 1137.38	1135.10
	$[M + 2H^+]^{2+}$ 1889.74	1887.50
	$[M + 2H - \text{cholesterol}^+]^{2+}$ 1705.135	1703.36
	$[M + 3H^+]^{3+}$ 1260.16	1257.77
AcCPK-GW	$[M + 3H^+ - \text{cholesterol}]^{3+}$ 1137.38	1134.50
	$[M + 2H^+]^{2+}$ 2010.29	2010.63
	$[M + 2H - \text{cholesterol}^+]^{2+}$ 1826.13	1824.69
fCPK-GW	$[M + 3H^+]^{3+}$ 1340.52	1339.51
	$[M + 2H^+]^{2+}$ 2010.29	2010.14
E <sub>4</sub> GW	$[M + 3H^+]^{3+}$ 1340.52	1339.30
	$[M + 2H^+]^{2+}$ 1661.41	1660.33
K <sub>4</sub> GW	$[M + 3H^+]^{3+}$ 1107.94	1106.59
	$[M + 2H^+ + 4 \text{ TFA}]^{2+}$ 1887.50	1886.13
	$[M + 2H^+ + 3 \text{ TFA}]^{2+}$ 1830.50	1829.33
	$[M + 3H^+ + 2 \text{ TFA}]^{3+}$ 1182.67	1182.27
	$[M + 3H^+ + \text{TFA}]^{3+}$ 1144.68	1144.60





---

Modulation of coiled-coil binding strength and  
fusogenicity through peptide stapling.

This chapter was published as an original research paper: Niek S.A. Crone, Alexander Kros, Aimee L. Boyle, *Bioconjugate Chemistry* **2020**, 31, 3, 834–843.

## **Abstract**

Peptide stapling is a technique which has been widely employed to constrain the conformation of peptides. One of the effects of such a constraint can be to modulate the interaction of the peptide with a binding partner. Here, a cysteine bis-alkylation stapling technique was applied to generate structurally isomeric peptide variants of a heterodimeric coiled-coil forming peptide. These stapled variants differed in the position and size of the formed macrocycle. C-terminal stapling showed the most significant changes in peptide structure and stability, with calorimetric binding analysis showing a significant reduction of binding entropy for stapled variants. This entropy reduction was dependent on crosslinker size and was accompanied by a change in binding enthalpy, illustrating the effects of preorganization. The stapled peptide, along with its binding partner, were subsequently employed as fusogens in a liposome model system. An increase in both lipid-, and content-mixing was observed for one of the stapled peptide variants: this increased fusogenicity was attributed to increased coiled-coil binding but not to membrane affinity; an interaction theorized to be a primary driving force in this fusion system.

### 3.1 Introduction

Intramolecular crosslinking of peptides, commonly referred to as peptide stapling, is often employed to change or constrain the secondary structure of small peptides and to induce unstructured peptides to mimic complex protein folds and protein-protein interactions (PPIs).<sup>1-4</sup> Stapling also contributes to an increased resistance to denaturation and proteolytic degradation, making it a useful technique for the modification of peptide-based therapeutics.<sup>5</sup> Hydrocarbon stapling, a technique which is based on catalyzed olefin metathesis, has seen widespread application with multiple compounds being investigated in academic, pre-clinical and clinical studies.<sup>6-10</sup>

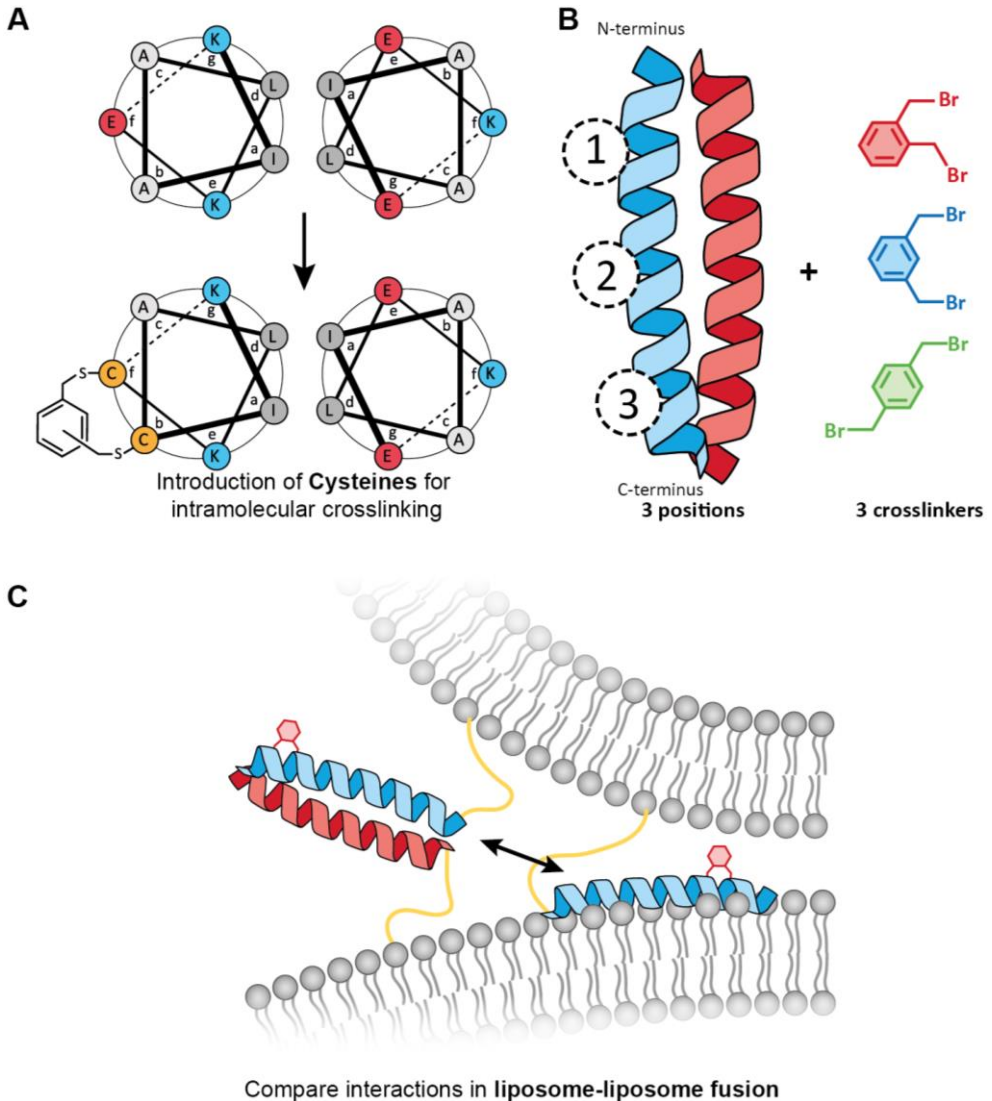
Peptide stapling techniques can be broadly divided into two categories: single- and two-component strategies. Single-component strategies incorporate amino acids that can be cross-linked selectively, or protection strategies are chosen that allow selective crosslinking. Common single-component stapling strategies include disulfide bonding,<sup>11</sup> lactam bridges,<sup>12, 13</sup> and olefin metathesis.<sup>10</sup> Two-component stapling adds a bifunctional crosslinker to bridge two amino-acid side chains; the most common techniques are based on cysteine crosslinking and triazole linkages.<sup>14-17</sup> Two-component strategies are in principle more complex than single-component strategies, but allow for a more flexible crosslinker design as it does not need to be compatible with solid-phase peptide synthesis. Although most stapling techniques are used to increase or constrain peptide helicity, systems that compare different methods are often based around short peptide sequences, and although multiple comparisons have been made,<sup>18, 19</sup> the ideal crosslinking technique is still open to debate.<sup>20</sup>

The  $\alpha$ -helix secondary structure motif has been mimicked using stapled peptides due to its common occurrence in proteins, and therefore its potential as a PPI mimic.<sup>21</sup> Coiled coils, which are protein-folding motifs comprising two or more  $\alpha$ -helices, are intrinsically helical and therefore techniques commonly used for the stapling of helices should permit modulation of coiled-coil interactions. Indeed, Rao *et al.* has shown lactam bridges can be used to generate short, helical, cFos binding peptides,<sup>22</sup> and Haney and Horne have used oxime crosslinking to generate stapled variants of the GCN4-p1 coiled-coil domain.<sup>23</sup> More recently, Wu *et al.* used a bis-triazole stapling technique to increase peptide binding to the polymerase  $\alpha$

accessory factor ctf4,<sup>15</sup> and Lathbridge and Mason showed that lactam-bridged heptapeptides can be used for the *de novo* design of a coiled-coil binding peptide.<sup>24</sup>

Together, these studies provide methods for the crosslinking of coiled-coil or coiled-coil-binding peptides, but it is unclear which method would prove most effective when applied to a different coiled-coil system. The size of the macrocycle formed varies significantly between the different cross-linking techniques, as do the polar and hydrophobic interactions of the crosslinkers in question. Interactions of the asymmetric oxime moiety with different amino acid side chains resulted in different binding strengths when the crosslinker was reversed in Haney and Horne's method. This necessitated the preparation and evaluation of both variants, and indicates oxime crosslinking effectiveness is dependent on amino acid composition.

The choice of crosslinking technique was therefore not obvious when attempting to modulate the behavior of the heterodimeric coiled coil used in our group, consisting of two peptides with a triple heptad repeat sequence of opposing charge, used as components of a membrane fusion model system.<sup>25</sup> The position of the crosslinker and the macrocycle size were deemed the most influential characteristics in the previously mentioned crosslinking strategies, therefore we wanted to evaluate both of these criteria independently for our system. The most favorable candidates could then be used to test the effect of structural changes on coiled-coil-based membrane fusion. One stapling strategy that attracted our attention was developed by the DeGrado lab, and is based on the alkylation of cysteine using dibromoxylenes.<sup>26</sup> The advantage of this system lies in the rigidity provided by the aromatic ring, allowing precise spacing between the two thiol moieties by selecting one of the three different structural isomers of dibromoxylene: *ortho*; *meta*; and *para*, **Scheme 3.1**. In the original study *meta*-xylene showed the most promise as a crosslinker, and further investigations in the same group have therefore focused on this variant.<sup>27, 28</sup> Other recent investigations have also predominantly used the *meta* derivative,<sup>29, 30</sup> and when a comparison was made between the isomers, only short or unstructured peptides were used. This means the question of whether, for a helical or coiled-coil peptide, *meta*-xylene is indeed the best crosslinking moiety is unanswered. Therefore, to probe the effect of stapling on coiled-coil peptides, we elected to investigate dibromoxylene crosslinking of cysteine's, employing all three structural isomers in order to elucidate the role of crosslinker size and its effect on structure and activity.



**Scheme 3.1.** The peptide stapling strategy used in this paper. (A) Two solvent-exposed amino acids are replaced with cysteine and crosslinked using a xylene moiety. (B) The relative positioning of three different crosslinking sites and the structures of the dibromoxylene crosslinkers investigated in this project. (C) A schematic representation of the studied membrane fusion interactions; coiled-coil formation and membrane insertion.

The fusion system developed in our lab is inspired by naturally occurring SNARE (soluble NSF attachment protein receptors) proteins,<sup>31</sup> and consists of a pair of complementary peptides. These peptides are dubbed E and K, and form a heterodimeric coiled-coil that has been attached to lipid membranes via a PEG spacer and lipid anchor.<sup>32</sup> Like SNARE proteins this model system promotes the fusion of

lipid membranes, and it can be facily modified to study the process of membrane fusion via structure-activity relationships.<sup>33</sup> It has recently been discovered that these two peptides play different roles in the fusion process.<sup>34</sup> The interactions of the K peptide with lipid membranes have been hypothesized as an important factor in membrane fusion efficiency.<sup>35</sup> Membrane interactions can occur simultaneously with formation of the coiled-coil domain in a membrane fusion interface (as visualized in **Scheme 3.1C**), therefore a fine balance between the two must be achieved. In addition, both membrane binding and coiled-coil formation depend on the peptides adopting a helical structure; we believe stapling should allow for the generation of peptides with varied helical structures, which will in turn affect coiled-coil formation and membrane binding interactions. Studying the effects of modulating the membrane interactions and coiled-coil binding affinity will generate insights into the importance of both factors in membrane fusion.

In this study, a library of nine stapled peptides was prepared by modifying peptide K via cysteine alkylation. These stapled K-peptide derivatives exhibited systematic variations in helicity and thermal stability, as observed by circular dichroism (CD) spectroscopy. The coiled-coil binding thermodynamics were studied using isothermal titration calorimetry (ITC) and it was discovered that increased coiled-coil binding is based on a preorganization effect. These observed changes in structure and binding dynamics were heavily dependent on the location of the staple and the choice of crosslinker. In lipid-, and content-mixing experiments a significant change in fusogenicity was measured for selected stapled peptides, which was attributed to the altered coiled-coil interaction strength.

## 3.2 Results and Discussion

### *Stapled Peptide Design*

The starting point for structural modification is one peptide of a three-heptad heterodimeric coiled-coil pair first reported by Litowski and Hodges.<sup>36</sup> The two peptides are named after the abundance of either glutamic acid (Glu, E) or lysine (Lys, K) respectively, and each peptide contains a C-terminal glycine and either tyrosine or tryptophan as a fluorescent reporter, giving rise to E<sub>3</sub>GY and K<sub>3</sub>GW. To facilitate stapling two amino acids in peptide K<sub>3</sub>GW were modified to cysteine, spaced *i* to *i*+4 to best match a single  $\alpha$ -helical turn. Amino acids that are involved in electrostatic (positions *e* and *g*) or hydrophobic (positions *a* or *d*) interactions

were not varied to ensure the stapled peptides retained the same stabilizing coiled-coil interactions as the parent peptides.

Three different variants were generated each with the cysteines, and therefore the staple, in a different heptad, shown in **Table 3.1**. Each of these positional variants was stapled with *ortho*-, *meta*-, and *para*-dibromoxylene generating a library of nine stapled peptides. When referring to these stapled peptide variants, a notation which reflects the position and type of crosslinker is used, for example K<sub>3</sub>GW-1M signifies the crosslinker is in the first heptad and the *meta* variant has been employed.

**Table 1.** Sequences of the coiled-coil parent peptides and cysteine-containing variants.

Peptide	Sequence				
	<i>g</i>	<i>abcdefg</i>	<i>abcdefg</i>	<i>abcdefg</i>	<i>a</i>
E <sub>3</sub> GY	E	IAALEKE	IAALEKE	IAALEKG	Y
K <sub>3</sub> GW	K	IAALKEK	IAALKEK	IAALKEG	W
K <sub>3</sub> GW-1	K	ICALKCK	IAALKEK	IAALKEG	W
K <sub>3</sub> GW-2	K	IAALKEK	ICALKCK	IAALKEG	W
K <sub>3</sub> GW-3	K	IAALKEK	IAALKEK	ICALKCG	W

### Secondary structure analysis

CD spectroscopy was employed to determine the secondary structure of the stapled peptide variants; the effects of both stapling location and the size of the crosslinker can be clearly observed, **Figure 3.1** & **Figure S3.1**. Peptide stapling close to the C-terminus (K<sub>3</sub>GW-3 variants) showed the largest increase in  $\alpha$ -helicity for all three xylenes, whereas modification in the second heptad (K<sub>3</sub>GW-2 variants) showed the lowest increase. Notably, when *para*-xylene was used as the crosslinker in the second heptad, the overall peptide helicity was reduced, **Figure 3.1B**, showing *para*-xylene is too large to form an ideal  $\alpha$ -helix. The N-terminal positions (K<sub>3</sub>GW-1 variants) all show a moderate increase in helicity, largely independent of staple size, confirming the previously observed trend for hydrocarbon stapling to be most effective at peptide termini.<sup>37</sup> Using temperature-dependent CD spectroscopy, an increase in melting temperature ( $T_m$ ) could be determined for the stapled peptide variants, as shown in **Figure 3.2** and **Figure S3.2**,

with the change in  $T_m$  closely following the observed changes in helicity. C-terminal modification showed the largest increase in melting temperature, with the *ortho*-xylene crosslinker yielding the most stable peptides over all three peptide variants, followed by the *meta*-xylene crosslinker. All stapled peptides interacted with  $E_3GY$ , showing typical coiled-coil spectra as is evident in **Figure 3.1C** and **Figure S3.1**. C-terminal stapling showed the highest helicity, while the N-terminal stapled peptides did not have increased coiled-coil helicity compared to the staples located in the central heptad.

In contrast to the stapled peptides in isolation, *meta*-xylene-modified peptides show the most  $\alpha$ -helical structure as a coiled coil. *Ortho*-xylene stapled peptides

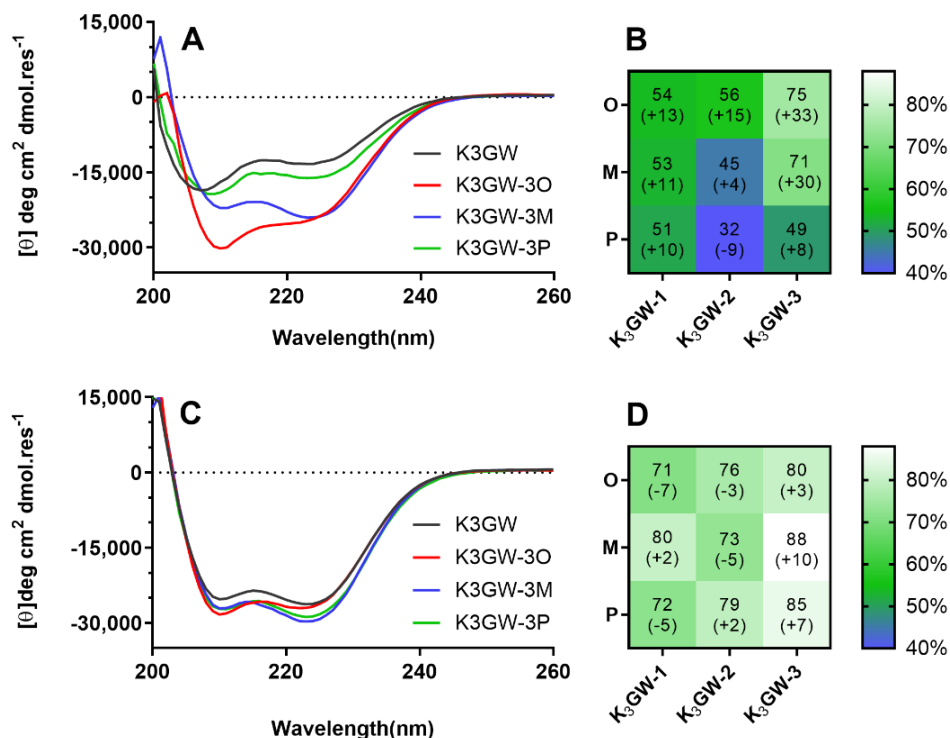


**Figure 3.1.** CD spectra of stapled peptides. (A) CD spectra of C-terminal stapled peptides, (B) heat map of the percentage of peptide helicity for all stapled variants and the change in helicity compared to  $K_3GW$  in brackets, (C) CD spectra of the C-terminal stapled peptides mixed with peptide  $E_3GY$  to form a coiled coil, and (D) heat map of average peptide helicity of all stapled peptides when combined with peptide  $E_3GY$  and the change in helicity compared to the coiled-coil with  $K_3GW$  in brackets. Total peptide concentration is 50  $\mu M$ , spectra were recorded at 20 °C in pH 7.4 PBS buffer.

had the largest increase in  $T_m$  for all three positions (**Figure 3.2**), and the trends in coiled-coil stability are similar to those observed for the single peptides, with an average increase in  $T_m$  of 4.9 °C for the stapled peptides, (**Table S3.1**) and 4.8 °C for their coiled coils, (**Table S3.2**). *Meta*-xylene was previously shown to have the largest increase in helicity in small unstructured peptides,<sup>26</sup> but in the E/K system *ortho*-xylene stapled variants yielded the highest single-peptide helicity and largest increase in  $T_m$  for both the peptides and their respective coiled-coils. Because it is possible that stapling affects coiled-coil interactions without changing peptide helicity as observed via the thermal unfolding experiments, the effect of peptide stapling on coiled-coil binding was further investigated using isothermal titration calorimetry (ITC).

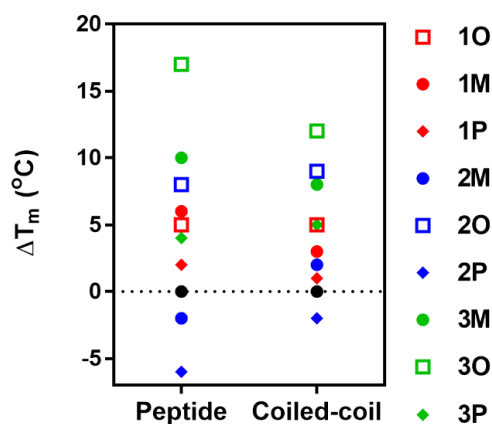


**Figure 3.2.** Change in peptide (left) and coiled-coil (right) melting temperature for stapled peptides in comparison to  $K_3GW$  as determined via CD spectroscopy. Total peptide concentration is 50  $\mu M$  C in pH 7.4 PBS buffer, spectra were recorded from 5 to 95 °C and are shown in **Figure S3.2**.

### *Binding thermodynamics of stapled coiled-coils*

Direct determination of the dissociation constant ( $K_d$ ) and enthalpy of binding ( $\Delta H_b$ ), and therefore calculation of the free energy ( $\Delta G_b$ ) and entropy of binding ( $\Delta S_b$ ) is possible using ITC (**Figure S3.3**), allowing investigation of peptide interactions independent of peptide structure.<sup>38</sup> The results shown in **Figure 3.3** and **Table S3.3** show that, in general, coiled-coil binding of peptides  $K_3GW$  and  $E_3GY$  is strongly enthalpically favored but entropically unfavored. The effect of enthalpy can be explained via the formation of amide hydrogen bonds and electrostatic interactions upon folding of the peptide.

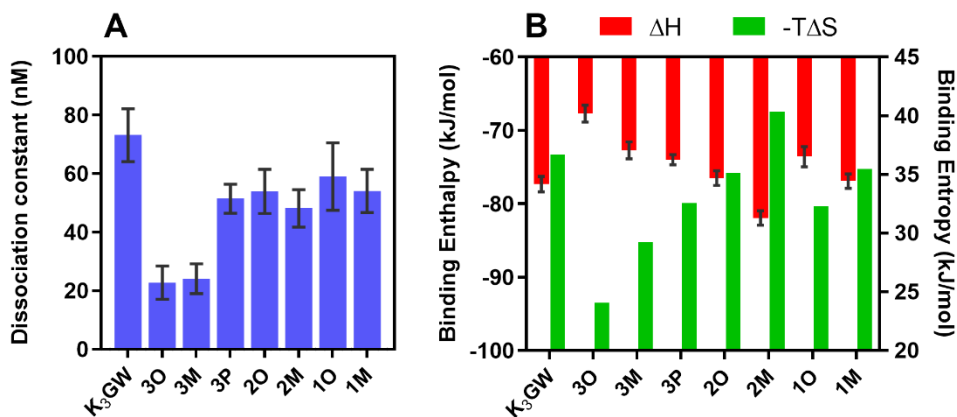


**Figure 3.3.** Thermodynamic binding parameters of K<sub>3</sub>GW and its stapled derivatives in complex with E<sub>3</sub>GY, determined via ITC. Error bars show the fitting error to a single-binding site model for both (A) the dissociation constant, and (B) the binding enthalpy ( $\Delta H$ ). The entropy ( $-T\Delta S$ ) is calculated from these parameters, and no error bars are drawn.

When the C-terminally-stapled variants of peptide K<sub>3</sub>GW are analyzed, the K<sub>d</sub> is decreased from 73 nM to 22 and 24 nM for the 3O and 3M variants respectively, and to 51 nM for the 3P variant. A large decrease in  $\Delta S_b$  was observed and was directly related to the size of the implemented staple. *Ortho*-xylene stapling at the C-terminus reduced the effect of entropy upon binding from 37 to 24 kJ/mol, a reduction of 35%. At the same time, an increase in the  $\Delta H_b$  from -77 to -68 kJ/mol was observed, counteracting the observed entropic effects and leading to the conclusion that the mechanism of peptide stapling relies on a preorganization effect. Through conformational restriction, the peptide is preorganized in a helical conformation which reducing the entropic effects on binding, but the potential energy that is gained upon formation of an  $\alpha$ -helix is also lost. Although the K<sub>d</sub> for the C-terminal *ortho*-, and *meta*-xylene stapled peptides are comparable, the  $\Delta S_b$  is more favorable for the *ortho* variant, explaining the large differences in T<sub>m</sub> observed for these two peptides. At all three stapling positions, the *ortho* variants show a reduced effect of entropy upon binding compared to the *meta* variants, which is likely caused by the smaller size of the *ortho* crosslinker. A smaller crosslinker restricts the maximum distance between the two helical turns, and therefore limits the number of possible conformations that the peptide can assume.

Recently, Miles *et al.* screened hydrocarbon-stapled peptides as protein-protein interaction (PPI) mimics against Bcl-x<sub>L</sub>/Mcl-1 and observed similar changes in the

$\Delta H_b$  and  $\Delta S_b$  for their stapled peptides, however they observed an overall increase in  $\Delta G_b$ .<sup>39</sup> Binding kinetics determined via a surface plasmon resonance (SPR) assay showed that the binding of their PPI mimic could best be explained via an induced fit mechanism, where the PPI can interact via multiple binding modes. Restricting the potential conformations of the peptide through the introduction of a staple reduced the number of possible binding modes, and therefore increased the overall  $K_d$  of the system. The E/K peptides used in this paper are designed, and experimentally confirmed to form heterodimeric coiled-coils exclusively.<sup>40</sup> As there is only one binding mode the observed changes in structure and stability, as determined via CD, show a direct correlation with the binding thermodynamics in ITC: C-terminal stapling using *ortho* and *meta*-xylene is the most effective way to increase the binding strength of coiled-coil peptides.

#### *Membrane interactions of peptide K3GW are perturbed by peptide stapling*

The effectiveness of E/K-based membrane fusion is partially attributed to the membrane interactions of peptide K, which are theorized to induce membrane curvature and therefore accelerate the transition from membrane docking to hemifusion.<sup>41</sup> The interactions of peptide K with lipid membranes are based on a lysine snorkeling mechanism, which describes the hydrophobic amino acids in the 'a' and 'd' positions inserting in a lipid membrane, helped by the favorable electrostatic interactions between lysine's and the phosphate groups of the lipid membrane.<sup>42</sup> This is a reversible process that can only happen when the peptide folds into an amphipathic helix and all the hydrophobic amino acids are positioned on the same face. Peptide stapling, which changes the overall peptide conformation, is therefore theorized to have an effect on membrane binding. The membrane partition coefficient ( $K_p$ ) of the stapled K variants was assayed via tryptophan fluorescence titration experiments, and the results are shown in **Figure 3.4**. Membrane binding is either comparable to unmodified K<sub>3</sub>GW or was increased up to a factor of two, and did not show any correlation to the location of the staple or to the overall helicity of the peptide (**Figure S3.4**). The difference in partition coefficient between K<sub>3</sub>GW-3O and K<sub>3</sub>GW-3M is striking, as the value is almost half for the *ortho* variant despite the helicity of the two being very similar. This shows that the addition of a hydrophobic crosslinking moiety between the 'b' and 'f' positions does not increase the membrane affinity of amphiphilic  $\alpha$ -helical peptides in a structure-dependent manner, and leads to the hypothesis that peptide K<sub>3</sub>GW does not bind to liposomal membranes as a highly structured  $\alpha$ -helix.

CD experiments were performed with the C-terminal stapled peptides in the presence of liposomes, and this data showed a reduced ellipticity at 222 nm, and a high 208/222 nm ratio (see **Figure S3.6**). This indicates that the peptides are less  $\alpha$ -helical in the presence of liposomes, which supports this hypothesis. If partitioning from the aqueous phase into the membrane is assumed to require partial unfolding of the peptide helix, the difference in binding strength between the *ortho* and *meta* variants can also be explained by the smaller size of the *ortho* crosslinker, which restricts the ability of the peptide to unfold.

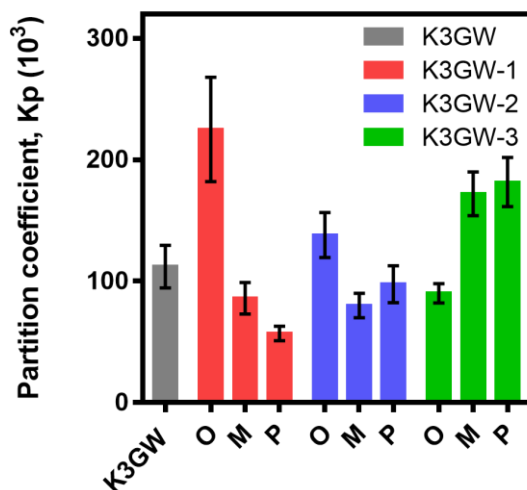


**Figure 3.4.** Partition coefficient of peptides with liposome membranes. Partition was measured via tryptophan fluorescence titration at 20 °C in pH 7.4 PBS buffer. Error bars represent the error in fitting of  $K_p$ . Values and fitting of the titration data can be found in **Table S3.4** and **Figure S3.5**.

#### *Lipid- and content-mixing is increased for C-terminal stapled peptides*

Complete fusion of two lipid-membrane-enclosed spaces will result in homogenous mixing of the lipids in the inner and outer leaflets, as well as mixing of the inner contents. In a liposomal system this process can be studied via the incorporation of chromophores into the lipid bilayer or on the inside of the liposomes.

Fusion of these liposomes with non-labeled liposomes will result in a fluorescence change which can be quantified to compare the peptide fusogenicity. Lipopeptides were prepared which contained cholesterol and a polyethyleneglycol (PEG<sub>4</sub>) spacer at the N-terminus, facilitating membrane anchoring.<sup>43</sup> Stapled peptides K<sub>3</sub>GW-30

and  $K_3GW-3M$  were selected for fusion studies because these gave rise to the largest structural and thermodynamic changes. Moreover, their binding strength is comparable but their partition coefficient differs by a factor of two therefore by testing both, and comparing them to unmodified  $K_3GW$ , the effect of both coiled-coil binding strength and membrane binding on fusogenicity can be determined. The lipopeptides were prepared using a novel on-resin stapling technique enabled by the use of 4-Methoxytrityl (Mtt) protected cysteine, full details are available in the materials and methods section. These peptides were tested for fusogenicity together with the lipidated variant of  $E_3GY$  (structures can be found in **Scheme S3.1**).

Lipid mixing was quantified using a Förster resonance energy transfer (FRET) pair incorporated in the lipid membrane, the results are shown in **Figure 3.5A**. The amount of lipid mixing observed was comparable for  $K_3GW$  and  $K_3GW-3M$  at a 1% peptide concentration, while the  $K_3GW-3O$  variant showing increased lipid mixing six minutes after the start of the experiment. This indicates that docking of the liposomes occurs at the same speed, but more lipid mixing occurs for the  $K_3GW-3O$

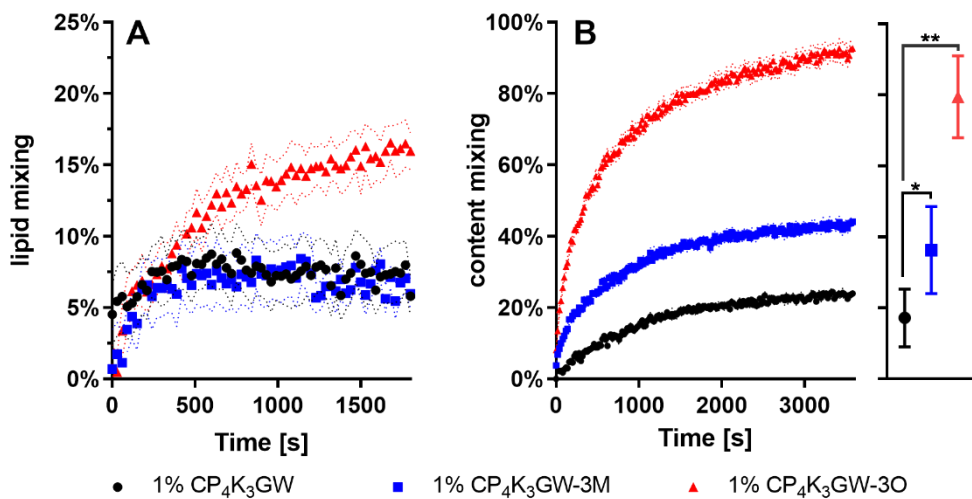


**Figure 3.5.** (A) Lipid mixing and (B) content mixing experiments of liposomes decorated with stapled peptides. Graphs show the change in mixing over time, and the standard deviation between 4 samples followed simultaneously. The dot bar graph (right) represents the average content mixing and deviation over 3 separate experiments. Experiments were performed at 500  $\mu$ M total lipid concentration in pH 7.4 PBS at 20 °C. Fusion experiments were performed at 1% lipopeptide concentration and fluorescence was normalized against 0% and 100% control samples.

variant. As the absolute amount of lipid mixing was low, the same experiment was also performed with 2% of the lipopeptides, which doubled the amount of lipid mixing observed while retaining the same trends (**Figure S3.7**).

Content mixing experiments when performed properly are the best measure for complete fusion of two lipid membranes. The membrane-impermeable sulforhodamine B (SrB) dye was employed as a fluorescent reporter and showed significant increases in fusion for both stapled peptide variants, **Figure 3.5B**, with the K<sub>3</sub>GW-3M variant doubling the amount of content mixing compared to K<sub>3</sub>GW (from 17.1% to 36.2%). The K<sub>3</sub>GW-3O variant produced an even larger increase; up to 93% content mixing was observed after 60 minutes, with an average of 79.5%. This is surprising, since there was no observed difference between K<sub>3</sub>GW and the K<sub>3</sub>GW-3M variant during lipid mixing experiments. An immediate difference between the three peptides is observed at the start of the experiment, which is not the case for lipid mixing, raising the concern that the stapled peptide variants might be destabilizing the liposomes and cause leakage of SrB across the lipid membranes. Plain liposomes and liposomes modified with 1% lipidated E<sub>3</sub>GY were tested for leakage but did not show significant differences (**Figure S3.8**), indicating that the stapled peptides do not destabilize the liposomal membranes.

#### *Insights into the mechanism of coiled-coil based membrane fusion*

Membrane fusion occurs in multiple stages, starting with the docking of two membranes to create a membrane fusion interface, followed by hemifusion which results in the mixing of the outer lipid leaflets, and proceeding via the formation of a fusion pore to complete fusion of the two liposomes, meaning their contents are exchanged.<sup>33</sup> Both lipid- and content-mixing experiments showed increased fusogenicity for the lipidated K<sub>3</sub>GW-3O peptide, with increased content mixing also observed for the K<sub>3</sub>GW-3M variant. Differences in lipid-mixing amount are obvious after six minutes, indicating that the rates of initial docking and outer leaflet mixing is comparable for the three peptides. Because complete fusion of the liposomes, as judged by content mixing, is increased significantly for the K<sub>3</sub>GW-3O variant, the observed difference in lipid mixing is most likely caused by an increased mixing of the inner leaflet lipids. The increased coiled-coil binding strength observed via ITC, could explain the increase in fusion except for the fact that K<sub>3</sub>GW-3O and K<sub>3</sub>GW-3M are dissimilar in their fusogenicity, yet they have a comparable K<sub>d</sub>. The K<sub>3</sub>GW-3O and K<sub>3</sub>GW-3M stapled peptides differ in their effects of entropy on coiled-coil binding and the strength of their membrane interactions, which are both increased

for  $K_3GW-3M$ . The  $K_d$  of coiled-coil formation is dependent on the association and dissociation rate constants, which show different behavior in temperature dependent stopped-flow experiments of coiled-coil peptides.<sup>44</sup> The dissociation rate was shown to be more dependent on temperature, and therefore had a much larger entropic component than the rate of association. The stapled peptide variants tested have a decreased entropic binding component, and should therefore also show a lower rate of dissociation. In a membrane fusion interface, dissociation of the coiled-coil is most likely followed by either another peptide binding event, or by the insertion of peptide K into the lipid membrane. A decrease in the dissociation rate should therefore result in an increase in the rate of fusion, although the total amount of fusion observed is not expected to change.

For SNARE-mediated membrane fusion it is known that multiple protein complexes are required to drive fusion of a single vesicle, and the likelihood of fusion occurring is dependent on the number of protein complexes at the fusion interface.<sup>45, 46</sup> This cooperativity is likely also necessary for our coiled-coil based system, and any interactions that influence the amount of coiled-coils that can be co-assembled around a fusion interface will influence the amount of fusion observed. In this case, both  $K_3GW-3O$  and  $K_3GW-3M$  show increased binding and lowered binding entropy, and therefore increased fusion via a lower dissociation rate. For  $K_3GW-3M$  this difference is less significant, and is likely to be partially counteracted by the increased membrane affinity of the peptide. This is a competitive interaction in the formation of the coiled-coil complex, and an interaction which can provide a pathway for dissipation of the free peptide after dissociation of the coiled coil.<sup>41</sup> In this manner, the total number of peptide complexes that are formed around a membrane fusion interface is reduced, and no increase in membrane fusion is observed. This reasoning can also be applied to homomeric peptide interactions, which could provide a pathway for dissipation of the lipopeptide away from the fusion interface. A CD titration was performed with  $K_3GW$  and the  $K_3GW-3O$  and  $K_3GW-3M$  analogues to test for homodimerization (**Figure S3.9** and **Table S3.5**), but the dimerization constant was found to be comparable for all variants, and weak enough that this should not be considered an important part of the fusion mechanism. This mechanistic understanding derived from the observed differences between the two stapled peptide variants will require further confirmation in different systems and experiments.

### 3.3 Conclusions

We have employed a cysteine bisalkylation stapling technique to generate a series of nine structurally isomeric  $\alpha$ -helical peptides that can form a heterodimeric coiled-coil when mixed with their binding partner. CD and ITC experiments showed that both stapling location and choice of staple affected the properties of the resulting peptides and coiled-coil complexes, with the largest increase in structure, binding and stability observed for peptides stapled close to the C-terminus with *ortho*-xylene. Binding strength is increased via a pre-organization mechanism, which consists of a large reduction of the unfavored entropic binding component, combined with a negative change in binding enthalpy. *Ortho*-, and *meta*-xylene crosslinkers resulted in similar coiled-coil binding strengths, although *ortho*-xylene reduced the effect of entropy the most. This effect was true for all three stapling sites and is due to the smaller size of the *ortho*-xylene crosslinker. Although there may be some dependence on amino acid composition, we conclude that *ortho*-xylene is the best crosslinker to stabilize helical peptides, despite *meta*-xylene being widely employed to date.

The effect of stapling on peptide-membrane partitioning was determined, and showed a two-fold difference between stapled peptide variants, although no direct correlation to location or staple type could be made. Lipopeptides of K<sub>3</sub>GW-3M and K<sub>3</sub>GW-3O were prepared via a novel on-resin stapling method. These peptides were tested in lipid-, and content-mixing experiments, and large increases in fusogenicity for the K<sub>3</sub>GW-3O variant were observed. K<sub>3</sub>GW-3M also showed significantly increased content mixing, but exhibited a similar amount of lipid mixing to the parent peptide. We theorize that these differences in fusogenicity can be explained via reduced dissociation; increasing coiled-coil interactions without increasing lipid membrane interactions allows accumulation of more coiled-coil pairs at the fusion interface and therefore increases membrane fusion.

### 3.4 Experimental

Tentagel resin was purchased from Rapp Polymere. Dimethylformamide (DMF), piperidine, pyridine, acetic anhydride, trifluoroacetic acid (TFA) and acetonitrile (MeCN) were supplied from Biosolve. N,N-diisopropylethylamine (DIPEA) and Oxyma were purchased from Carl Roth. Dichloromethane (DCM) and diethyl ether were supplied by Honeywell. HBTU and all protected amino acids except Fmoc-Cys(mtt)-OH were purchased from Novabiochem. All other chemicals were

purchased from Sigma Aldrich. Ultrapure water was obtained from a MILLI-Q™ water purification system. Peptide concentration was established via absorption at 280 nm, determined using a CARY-300 UV-Vis spectrophotometer.

**Peptide synthesis and purification** All peptides were synthesized on solid phase using a CEM liberty blue automated, microwave-assisted, peptide synthesizer. Peptides were prepared on a 0.1 mmol scale using Tentagel HL RAM resin with a loading of 0.39 mmol/g. Fmoc deprotection was performed using 20% piperidine in DMF at 90°C for 60 seconds. Amide coupling was achieved using 5 eq. of protected amino acid, 5 eq. DIC as activator and 5 eq. Oxyma as activator base, heated at 95°C for 240 seconds. Acetylation of the peptide N-terminus after automated synthesis was performed using an excess of acetic anhydride and pyridine in DMF.

Lipidated peptides were made on resin via the coupling of 2.5 equivalents of N<sub>3</sub>-PEG<sub>4</sub>-COOH (see supplementary methods for synthesis details), with 2.5 eq of HBTU and 5 eq. of DIPEA in DMF for 2 hours at room temperature. After washing the resin with DMF, the azide was reduced using 10 eq. of PME<sub>3</sub> (1 M in toluene), with 4:1 dioxane:water as solvent for 2.5 hours. After the reaction was finished, the resin was washed thoroughly with 4:1 dioxane:water, MeOH and DMF. Lipidation was achieved using 2 eq. of cholesteryl hemisuccinate, 2 eq. of HBTU and 4 eq. of DIPEA in 1:1 DMF:DCM, and this lipidation step was performed twice to achieve complete conversion. After the final coupling the resin was washed with DMF, MeOH, and DCM, dried under vacuum, and the peptide was cleaved using a 92.5:2.5:2.5:2.5 mixture of TFA:TIPS:EDDT:water for 1 hour, after which the peptide was precipitated in cold diethyl ether, collected via centrifugation and lyophilized.

All peptides were purified by HPLC on a Shimadzu system consisting of two KC-20AR pumps and an SPD-20A or SPD-M20A detector equipped with a Kinetix Evo C18 column. Eluents consisted of 0.1% TFA in water (A) and 0.1% TFA in MeCN (B), with all peptides eluted using a gradient of 20-90% B over 35 minutes, with a flow rate of 12 mL/min. Collected fractions were checked for purity via LCMS, with the pure fractions being pooled and lyophilized. LC-MS spectra were recorded using a Thermo Scientific TSQ quantum access MAX mass detector connected to an Ultimate 3000 liquid chromatography system fitted with a 50x4.6 mm Phenomenex Gemini 3 μm C18 column.

**Peptide stapling** Intramolecular crosslinking was achieved by dissolving the peptide in a 1:1 mixture of MeCN:H<sub>2</sub>O containing 10 mM NH<sub>4</sub>HCO<sub>3</sub> up to a peptide

concentration of 500  $\mu$ M. TCEP, 1 eq. was added as a 10 mM stock solution, and the reaction was stirred for 1 hour, followed by addition of 1.2 eq. of the dibromoxylene crosslinker (50 mM in DMF) and reacted for 3 hours. The reaction was quenched by the addition of 5% acetic acid, and purified using preparative HPLC. For the lipidated peptides, the crosslinking was performed on solid phase. In short; Cysteines protected with Mtt were incorporated into the peptide, and after automated synthesis these protecting groups were removed by incubating the resin with 2% TFA, and 3% TIS in DCM for 2 minutes, followed by washing the resin with DCM twice. This was repeated until no more color appeared when a small amount of the resin was mixed with TFA. Crosslinking was achieved by addition of 1.5 eq. of the crosslinker and 2.5 eq. of DIPEA in 1:1 DMF:TFE, and incubating this reaction for 3 hours. On resin stapling was usually performed before lipidation.

**Circular dichroism measurements.** CD spectra were recorded on a JASCO J-815 CD spectrometer fitted with a Peltier temperature controller. Unless otherwise specified, samples were measured at 20 °C in a quartz cuvette with a 2 mm path length. Spectra were recorded from 190 to 260 nm at 1 nm intervals, with a bandwidth of 1 nm, with the final spectrum consisting of the average of 5 sequentially recorded spectra. The mean residue molar ellipticity ( $\theta$ , deg cm<sup>2</sup> dmol.res<sup>-1</sup>) was calculated according to equation 1:

$$[\theta] = (100 * [\theta]_{obs}) / (c * n * l) \quad (1)$$

With  $[\theta]_{obs}$  representing the observed ellipticity in mdeg, c the peptide concentration in mM, n the number of peptide bonds and l the path length of the cuvette in cm. The fraction of  $\alpha$ -helical peptide could be calculated from the MRE using equation 2:

$$F_{helix} = ([\theta]_{222} - [\theta]_0) / ([\theta]_{max} - [\theta]_0) \quad (2)$$

With the maximum theoretical mean residue ellipticity,  $[\theta]_{max}$ , defined as  $[\theta]_{max} = [\theta]_{\infty} (n - x) / n$  for a helix with n residues and x a number of amino acids assumed not to participate in helix formation (in this case 3).  $[\theta]_{\infty}$  is defined as the theoretical helicity of an infinite  $\alpha$ -helix and is temperature dependent, defined via  $[\theta]_{\infty} = (-44000 + 250T)$ , with T being the temperature in °C. The minimal expected absorbance at 222 nm for a random coil is defined in  $[\theta]_0$ , which is also temperature dependent via the relationship  $[\theta]_0 = 2220 - 53T$ .

**Tryptophan fluorescence titration.** Fluorescence was measured in 96 well plates using a TECAN Infinite M1000 Pro microplate reader. Liposomes of the composition 2:1:1 DOPC:DOPE:Cholesterol were prepared at a 10 mM concentration via extrusion in PBS buffer, using an Avanti mini extruder with 100 nm polycarbonate membranes. Titration series of liposomes in PBS buffer were prepared with concentrations between 25 and 3750  $\mu\text{M}$ , with the peptide concentration held constant at 2.5  $\mu\text{M}$ . Samples were prepared in 96 well plates, and after 60 minutes of incubation a fluorescence spectrum was taken between 300 and 450 nm. The maximum fluorescence of each sample was plotted as a fold increase of the fluorescence of the peptide without liposomes present, and fitted against equation 3 to determine the partition constant:

$$F = 1 + (F_{max} - 1) * (K_p * X) / (55.3 + K_p * X) \quad (3)$$

Where the normalized fluorescence,  $F$ , is dependent on the maximum fluorescence when all peptide is bound to the membrane  $F_{max}$ , molar partition coefficient  $K_p$ , the lipid concentration  $X$  and the concentration of water which is assumed to be constant at 55.3 M. Experimental data of 3 separate experiments was fitted to equation 3 using the least-squares method to yield the partition coefficient, and the standard error of fitting.

**Isothermal titration calorimetry.** ITC measurements were performed on a Malvern MicroCal PEAQ-ITC automated calorimeter. In a standard experiment, the measurement cell contained 200  $\mu\text{L}$  of 10  $\mu\text{M}$  peptide K and the syringe was filled with E<sub>3</sub>GY at 100  $\mu\text{M}$  concentration, with both peptides dissolved in PBS. The syringe content was added in 21 injections of 1.9  $\mu\text{L}$  at 120s intervals, except the first injection which was 0.5  $\mu\text{L}$ . The reference power was set at 2.0  $\mu\text{Cal}/\text{sec}$ , and experiments were performed at 25 °C. The data was analyzed with the Microcal PEAQ-ITC analysis software, and fitted to a single binding site model to generate the thermodynamic binding parameters. The experiment was repeated on 3 separate occasions, and the experimental results with the lowest reduced chi-squared value are represented in this paper.

**Lipid and content mixing experiments** Liposomes with the lipid composition 2:1:1 DOPC:DOPE:Cholesterol were used at a 500  $\mu\text{M}$  concentration, where 1% of the lipids was substituted with the respective lipopeptide. Lipid films were prepared via evaporation of lipid and lipopeptide stock solutions in 1:1  $\text{CHCl}_3$ :MeOH under a stream of nitrogen, followed by high vacuum for at least 2 hours. The lipid films

were rehydrated via vortex mixing with PBS buffer and sonication for 5 minutes at 55 °C in a Branson 2510 bath sonicator. The liposomes were checked for size and polydispersity (PDI) via DLS (Malvern Zetasizer Nano S), and sonicated for a second time if the PDI was larger than 0.25. Lipid mixing was assayed via the incorporation of 0.5% DOPE-NBD (1,2-dioleoyl-sn-glycero-3-phosphoethanolamine-N-(7-nitro-2-1,3-benzoxadiazol-4-yl)) and 0.5% DOPE-LR (1,2-dioleoyl-sn-glycero-3-phosphoethanolamine-N-(lissamine rhodamine B sulfonyl)) in the lipid membranes of the CPK-containing liposomes. 100 µL of fluorescent CPK-containing liposomes were mixed with 100 µL of non-fluorescent CPE-decorated liposomes, and the emission of NBD at 530 nm was followed over time. Each experiment included a positive control consisting of liposomes at a 500 µM concentration and 0.25% of both DOPE-LR and DOPE-NBD, and a negative control where the fluorescent liposomes were combined with liposomes without CPE. The standard deviation was calculated on the average of 4 separate measurement samples, and the experiment was repeated at least 3 times.

Content mixing was assayed via the incorporation of 10 mM Sulforhodamine B in the hydration buffer of CPE-decorated liposomes. After sonication, the unincorporated rhodamine was removed using an Illustra NAP-25 size-exclusion column. For each experiment, 100 µL of sulforhodamine-containing CPE-liposomes were mixed with 100 µL CPK-containing liposomes, and the fluorescence of sulforhodamine followed over time at 585 nm. The value was normalized via referencing a positive control consisting of liposomes containing 5 mM sulforhodamine B prepared in the same manner and a negative control where the fluorescent CPE liposomes were combined with plain liposomes. The standard deviation was calculated on the average of 4 separate measurement samples, and the experiment was repeated at least 3 times.

Change in fluorescence was measured in 96 well plates using a TECAN Infinite M1000 Pro microplate reader. The percentage of lipid and content mixing was calculated using the following formula (Equation 4):

$$\% \text{ mixing} = (F_t - F_0) / (F_{max} - F_0) \quad (4)$$

Where  $F_t$  is the fluorescence at time  $t$ , and  $F_0$  and  $F_{max}$  are the fluorescence of the negative and positive controls at the same time point. Processing of fluorescence data and one-way ANOVA analysis was performed in GraphPad Prism 8.1.1.

### 3.5 Acknowledgements

I gratefully acknowledge Professor Nathaniel I. Martin and Ioli Kotsogianni from the Institute of Biology (IBL) at Leiden University for access to, and technical assistance with, the ITC measurements.

### 3.6 References

1. Pelay-Gimeno, M., *et al.* (2015) Structure-Based Design of Inhibitors of Protein-Protein Interactions: Mimicking Peptide Binding Epitopes. *Angew. Chem. Int. Edit.* 54, 8896-8927.
2. Klein, M. (2017) Stabilized helical peptides: overview of the technologies and its impact on drug discovery. *Expert Opin. Drug. Dis.* 12, 1117-1125.
3. Hill, T. A., *et al.* (2014) Constraining Cyclic Peptides To Mimic Protein Structure Motifs. *Angew. Chem. Int. Edit.* 53, 13020-13041.
4. Siegert, T. R., *et al.* (2016) Analysis of Loops that Mediate Protein-Protein Interactions and Translation into Submicromolar Inhibitors. *J. Am. Chem. Soc.* 138, 12876-12884.
5. Nilsson, A., Lindgren, J., and Karlstrom, A. E. (2017) Intramolecular Thioether Crosslinking to Increase the Proteolytic Stability of Affibody Molecules. *Chembiochem : a European journal of chemical biology* 18, 2056-2062.
6. Walensky, L. D., *et al.* (2004) Activation of apoptosis in vivo by a hydrocarbon-stapled BH3 helix. *Science* 305, 1466-1470.
7. Walensky, L. D., and Bird, G. H. (2014) Hydrocarbon-Stapled Peptides: Principles, Practice, and Progress. *J. Am. Chem. Soc.* 57, 6275-6288.
8. Wang, C., *et al.* (2018) Discovery of Hydrocarbon-Stapled Short alpha-Helical Peptides as Promising Middle East Respiratory Syndrome Coronavirus (MERS-CoV) Fusion Inhibitors. *J. Med. Chem.* 61, 2018-2026.
9. Carvajal, L. A., *et al.* (2018) Dual inhibition of MDMX and MDM2 as a therapeutic strategy in leukemia. *Sci. Transl. Med.* 10.
10. Cromm, P. M., Spiegel, J., and Grossmann, T. N. (2015) Hydrocarbon Stapled Peptides as Modulators of Biological Function. *ACS Chem. Biol.* 10, 1362-1375.
11. Gongora-Benitez, M., Tulla-Puche, J., and Albericio, F. (2014) Multifaceted Roles of Disulfide Bonds. Peptides as Therapeutics. *Chem. Rev.* 114, 901-926.
12. Shepherd, N. E., *et al.* (2006) Modular alpha-helical mimetics with antiviral activity against respiratory syncytial virus. *J. Am. Chem. Soc.* 128, 13284-13289.
13. Khoo, K. K., *et al.* (2011) Lactam-Stabilized Helical Analogues of the Analgesic mu-Conotoxin KIIIA. *J. Med. Chem.* 54, 7558-7566.
14. Kawamoto, S. A., *et al.* (2012) Design of Triazole-Stapled BCL9  $\alpha$ -Helical Peptides to Target the  $\beta$ -Catenin/B-Cell CLL/lymphoma 9 (BCL9) Protein-Protein Interaction. *J. Med. Chem.* 55, 1137-1146.
15. Wu, Y. T., *et al.* (2017) Targeting the Genome-Stability Hub Ctf4 by Stapled-Peptide Design. *Angew. Chem. Int. Edit.* 56, 12866-12872.

16. Peraro, L., *et al.* (2017) Diversity-Oriented Stapling Yields Intrinsically Cell-Penetrant Inducers of Autophagy. *J. Am. Chem. Soc.* 139, 7792-7802.
17. Fairlie, D. P., and Dantas de Araujo, A. (2016) Stapling peptides using cysteine crosslinking. *Peptide Science* 106, 843-852.
18. de Araujo, A. D., *et al.* (2014) Comparative alpha-Helicity of Cyclic Pentapeptides in Water. *Angew. Chem. Int. Edit.* 53, 6965-6969.
19. Tian, Y., *et al.* (2017) Effect of Stapling Architecture on Physicochemical Properties and Cell Permeability of Stapled alpha-Helical Peptides: A Comparative Study. *ChemBiochem : a European journal of chemical biology* 18, 2087-2093.
20. Lau, Y. H., *et al.* (2015) Peptide stapling techniques based on different macrocyclisation chemistries. *Chem. Soc. Rev.* 44, 91-102.
21. Henchey, L. K., Jochim, A. L., and Arora, P. S. (2008) Contemporary strategies for the stabilization of peptides in the alpha-helical conformation. *Curr. Opin. Chem. Biol.* 12, 692-697.
22. Rao, T., *et al.* (2013) Truncated and Helix-Constrained Peptides with High Affinity and Specificity for the cFos Coiled-Coil of AP-1. *Plos One* 8.
23. Haney, C. M., and Horne, W. S. (2013) Oxime Side-Chain Cross-Links in an -Helical Coiled-Coil Protein: Structure, Thermodynamics, and Folding-Templated Synthesis of Bicyclic Species. *Chem. Eur. J.* 19, 11342-11351.
24. Lathbridget, A., and Mason, J. M. (2019) Combining Constrained Heptapeptide Cassettes with Computational Design To Create Coiled-Coil Targeting Helical Peptides. *ACS Chem. Biol.* 14, 1293-1304.
25. Robson Marsden, H., *et al.* (2013) Controlled liposome fusion mediated by SNARE protein mimics. *Biomat. Sci.* 1, 1046-1054.
26. Jo, H., *et al.* (2012) Development of alpha-Helical Calpain Probes by Mimicking a Natural Protein-Protein Interaction. *J. Am. Chem. Soc.* 134, 17704-17713.
27. Acharyya, A., *et al.* (2019) Exposing the Nucleation Site in alpha-Helix Folding: A Joint Experimental and Simulation Study. *J. Phys. Chem. B* 123, 1797-1807.
28. Wu, H. F., *et al.* (2018) Design of a Short Thermally Stable -Helix Embedded in a Macrocycle. *ChemBiochem : a European journal of chemical biology* 19, 902-906.
29. Iqbal, E. S., *et al.* (2019) A new strategy for the in vitro selection of stapled peptide inhibitors by mRNA display. *Chem. Commun.* 55, 8959-8962.
30. Diderich, P., *et al.* (2016) Phage Selection of Chemically Stabilized alpha-Helical Peptide Ligands. *ACS Chem. Biol.* 11, 1422-1427.
31. Sudhof, T. C., and Rothman, J. E. (2009) Membrane Fusion: Grappling with SNARE and SM Proteins. *Science* 323, 474-477.
32. Marsden, H. R., *et al.* (2009) A Reduced SNARE Model for Membrane Fusion. *Angew. Chem. Int. Edit.* 48, 2330-2333.
33. Marsden, H. R., Tomatsu, I., and Kros, A. (2011) Model systems for membrane fusion. *Chem. Soc. Rev.* 40, 1572-1585.

34. Koukalova, A., *et al.* (2018) Distinct roles of SNARE-mimicking lipopeptides during initial steps of membrane fusion. *Nanoscale* 10, 19064-19073.
35. Rabe, M., Zope, H. R., and Kros, A. (2015) Interplay between Lipid Interaction and Homocoiling of Membrane-Tethered Coiled-Coil Peptides. *Langmuir* 31, 9953-9964.
36. Litowski, J. R., and Hodges, R. S. (2002) Designing heterodimeric two-stranded alpha-helical coiled-coils - Effects of hydrophobicity and alpha-helical propensity on protein folding, stability, and specificity. *J. Biol. Chem.* 277, 37272-37279.
37. Green, B. R., *et al.* (2013) Cyclic analogs of galanin and neuropeptide Y by hydrocarbon stapling. *Bioorgan. Med. Chem.* 21, 303-310.
38. Pierce, M. M., Raman, C. S., and Nall, B. T. (1999) Isothermal titration calorimetry of protein-protein interactions. *Meth. Enzymol.* 19, 213-221.
39. Miles, J. A., *et al.* (2016) Hydrocarbon constrained peptides - understanding preorganisation and binding affinity. *Chem. Sci.* 7, 3694-3702.
40. Lindhout, D. A., *et al.* (2004) NMR solution structure of a highly stable de novo heterodimeric coiled-coil. *Biopolymers* 75, 367-375.
41. Rabe, M., *et al.* (2016) A Coiled-Coil Peptide Shaping Lipid Bilayers upon Fusion. *Biophys. J.* 111, 2162-2175.
42. Pluhackova, K., *et al.* (2015) Spontaneous Adsorption of Coiled-Coil Model Peptides K and E to a Mixed Lipid Bilayer. *J. Phys. Chem. B.* 119, 4396-4408.
43. Versluis, F., *et al.* (2013) In Situ Modification of Plain Liposomes with Lipidated Coiled Coil Forming Peptides Induces Membrane Fusion. *J. Am. Chem. Soc.* 135, 8057-8062.
44. Bosshard, H. R., *et al.* (2001) Energetics of coiled coil folding: The nature of the transition states. *Biochem.* 40, 3544-3552.
45. McDargh, Z. A., Polley, A., and O'Shaughnessy, B. (2018) SNARE-mediated membrane fusion is a two-stage process driven by entropic forces. *FEBS letters* 592, 3504-3515.
46. Mostafavi, H., *et al.* (2017) Entropic forces drive self-organization and membrane fusion by SNARE proteins. *P. Natl. Acad. Sci. USA* 114, 5455-5460.

## Supporting Information for Chapter 3

### Circular Dichroism

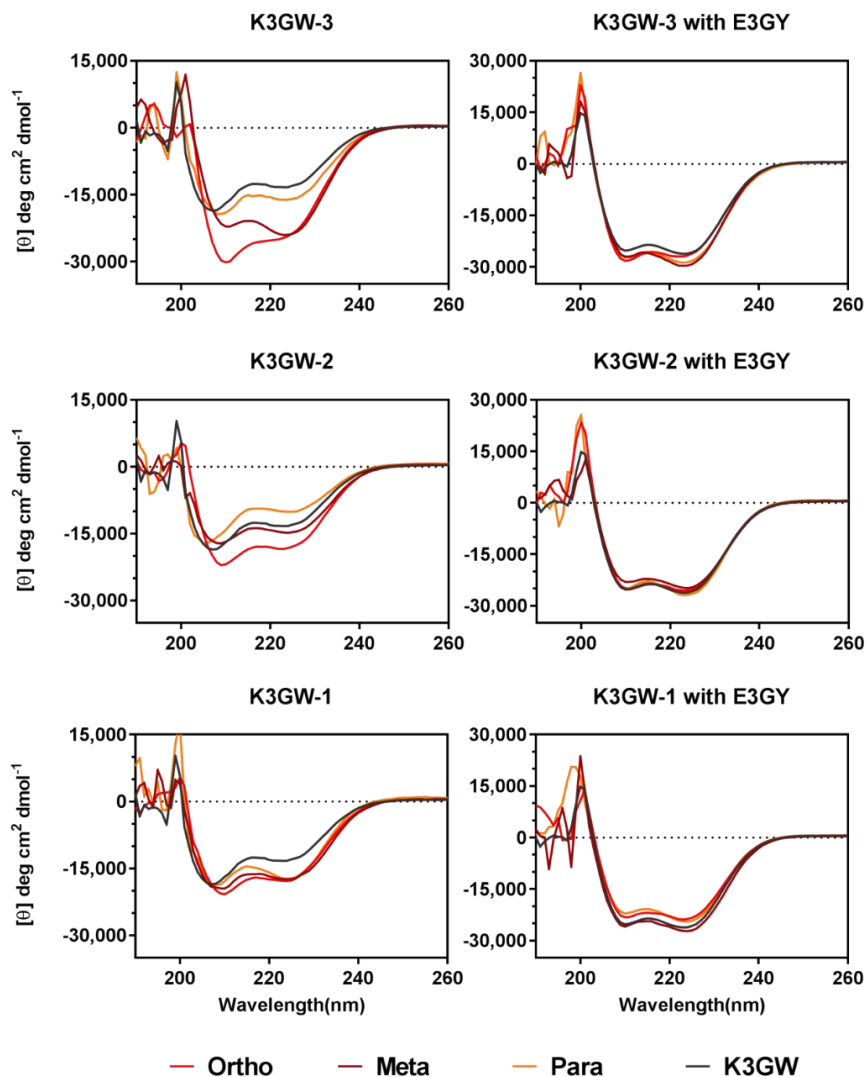


**Figure S3.1:** CD spectra of xylene stapled peptide variants by themselves (left) and in combination with E<sub>3</sub>GY (right). Peptides were dissolved at a total concentration of 50  $\mu\text{M}$  in PBS at pH 7.4, and spectra were measured at 20°C.

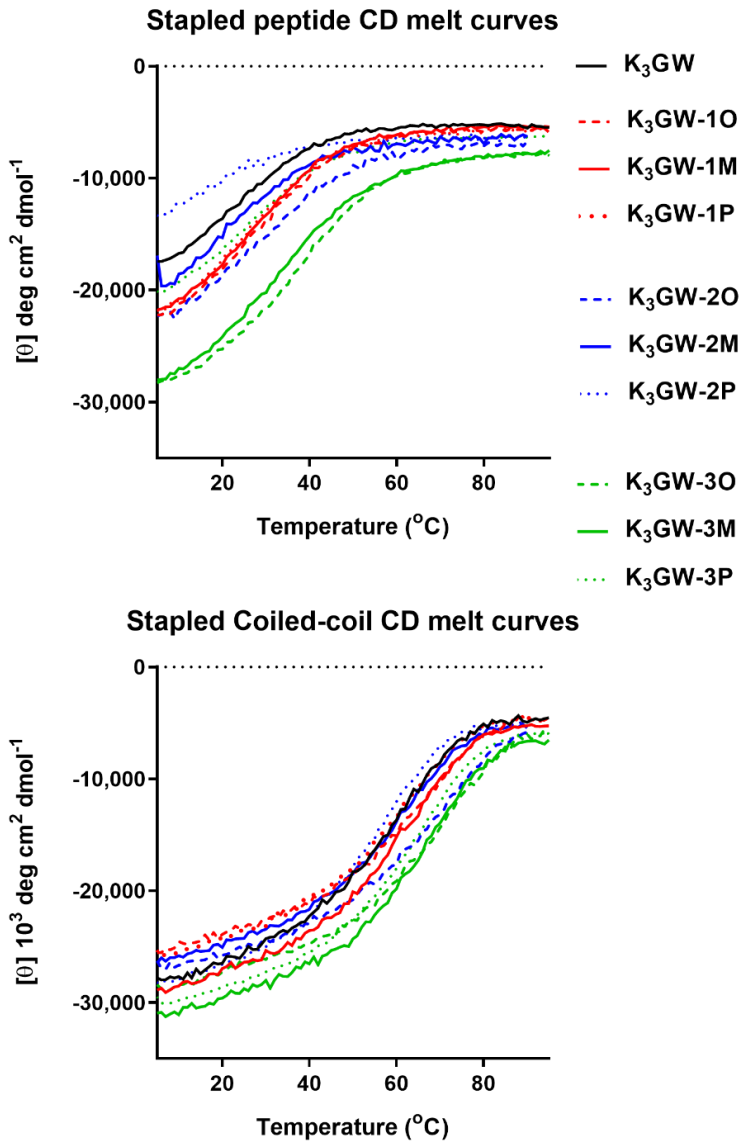


**Table S3.1:** CD spectroscopy results for peptide K<sub>3</sub>GW and its stapled derivatives.

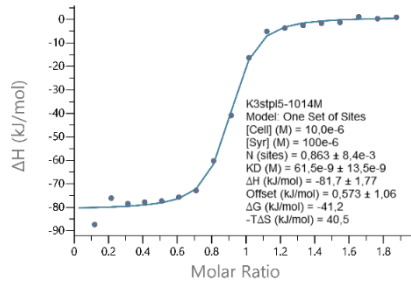
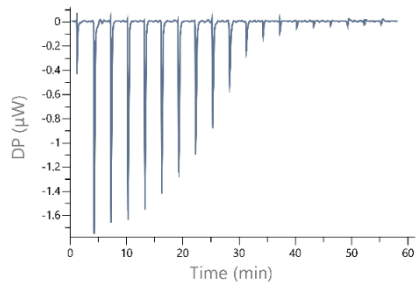
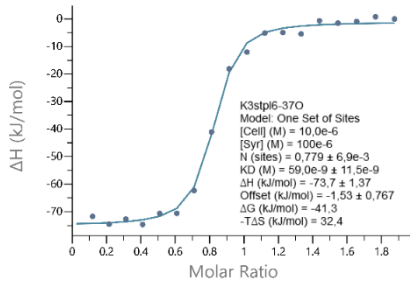
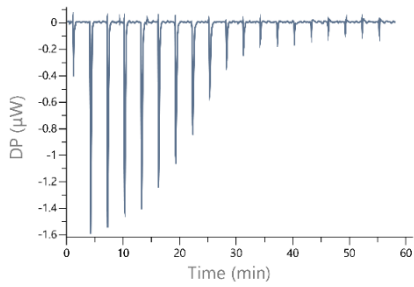
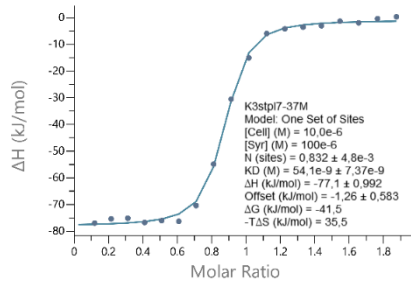
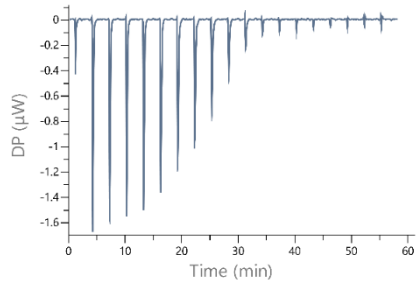
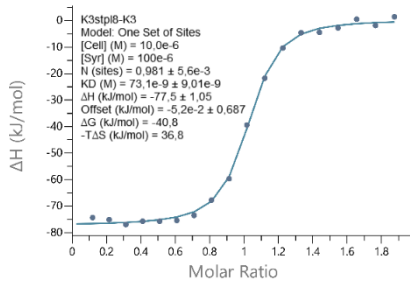
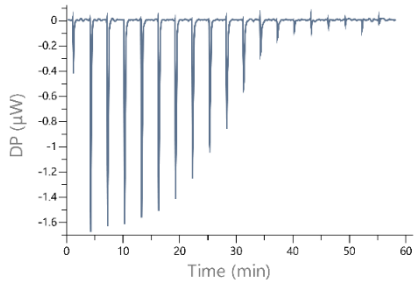
Peptide	[ $\Theta$ ] <sub>222nm</sub> (deg cm <sup>2</sup> dmol <sup>-1</sup> )	[ $\Theta$ ] <sub>222nm</sub> /[ $\Theta$ ] <sub>208nm</sub>	Helicity (%)	T <sub>m</sub> (°C)
K <sub>3</sub> GW	-13247	0.72	41%	22
K <sub>3</sub> GW-1O	-17662	0.89	54%	27
K <sub>3</sub> GW-1M	-17255	0.89	53%	28
K <sub>3</sub> GW-1P	-16898	0.90	51%	24
K <sub>3</sub> GW-2O	-18408	0.86	56%	30
K <sub>3</sub> GW-2M	-14607	0.85	45%	20
K <sub>3</sub> GW-2P	-9949	0.63	32%	16
K <sub>3</sub> GW-3O	-24980	0.89	75%	39
K <sub>3</sub> GW-3M	-23790	1.18	71%	32
K <sub>3</sub> GW-3P	-16109	0.84	49%	26

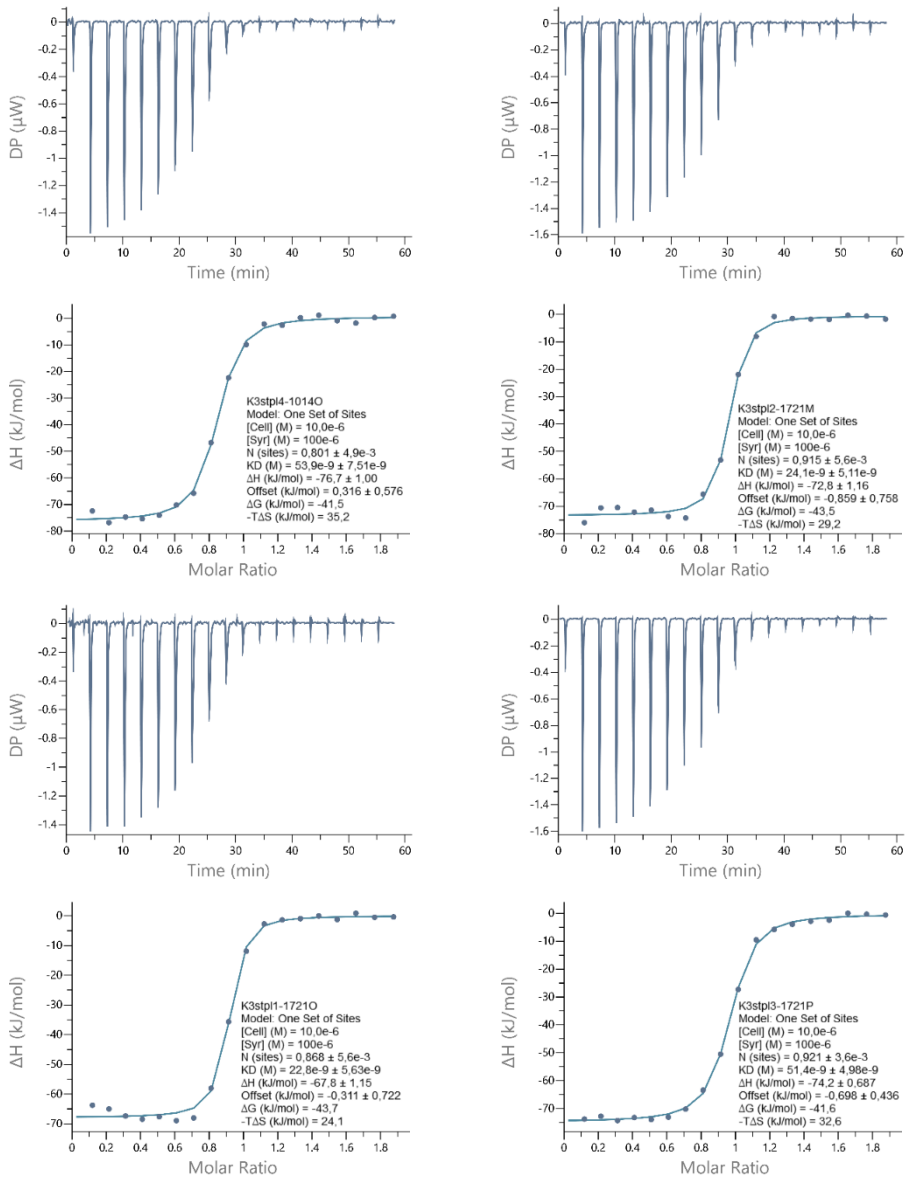
**Table S3.2:** Measured characteristics of peptide K<sub>3</sub>GW and its stapled variants as a coiled coil with peptide E<sub>3</sub>GY, determined via CD spectroscopy.

Peptide	[ $\Theta$ ] <sub>222nm</sub> (deg cm <sup>2</sup> dmol <sup>-1</sup> )	[ $\Theta$ ] <sub>222nm</sub> /[ $\Theta$ ] <sub>208nm</sub>	Helicity (%)	T <sub>m</sub> (°C)
K <sub>3</sub> GW	-26080	1.13	78%	60
K <sub>3</sub> GW-1O	-23722	1.13	71%	65
K <sub>3</sub> GW-1M	-26946	1.13	80%	63
K <sub>3</sub> GW-1P	-24179	1.19	72%	61
K <sub>3</sub> GW-2O	-25466	1.13	76%	69
K <sub>3</sub> GW-2M	-24500	1.16	73%	62
K <sub>3</sub> GW-2P	-26712	1.17	79%	58
K <sub>3</sub> GW-3O	-27006	1.04	80%	72
K <sub>3</sub> GW-3M	-29608	1.22	88%	68
K <sub>3</sub> GW-3P	-28577	1.14	85%	65

*Isothermal Titration Calorimetry***Table S3.3:** Binding thermodynamics of peptide K<sub>3</sub>GW and its stapled variants as a coiled coil with peptide E<sub>3</sub>GY, determined via isothermal titration calorimetry .

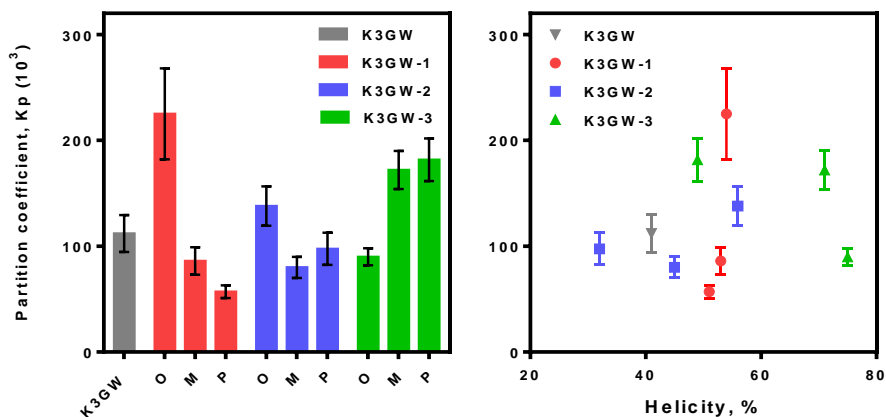
Peptide	N sites	K <sub>d</sub> (nM)	ΔH (kJ/mol)	ΔG (kJ/mol)	-TΔS (kJ/mol)	R. Chi-Sqr. (kcal/mol) <sup>2</sup>
K <sub>3</sub> GW	0.98	73.1 +/- 9.0	-77.3 +/- 1.1	-40.7	36.7	0.11
K <sub>3</sub> GW-1O	0.78	59 +/- 11.5	-73.6 +/- 1.4	-41.2	32.3	0.21
K <sub>3</sub> GW-1M	0.83	54.1 +/- 7.4	-76.9 +/- 1.0	-41.5	35.5	0.11
K <sub>3</sub> GW-2O	0.80	53.9 +/- 7.5	-76.5 +/- 1.0	-41.5	35.1	0.12
K <sub>3</sub> GW-2M	0.83	48.1 +/- 6.4	-81.9 +/- 1.0	-41.8	40.3	0.12
K <sub>3</sub> GW-3O	0.87	22.7 +/- 5.7	-67.7 +/- 1.2	-43.5	24.1	0.20
K <sub>3</sub> GW-3M	0.92	24.1 +/- 5.1	-72.7 +/- 1.2	-43.5	29.2	0.20
K <sub>3</sub> GW-3P	0.92	51.4 +/- 5.0	-74.0 +/- 0.7	-41.6	32.6	0.06





**Figure S3.3:** ITC binding curves of K<sub>3</sub>GW and stapled variants with binding partner E<sub>3</sub>GY.

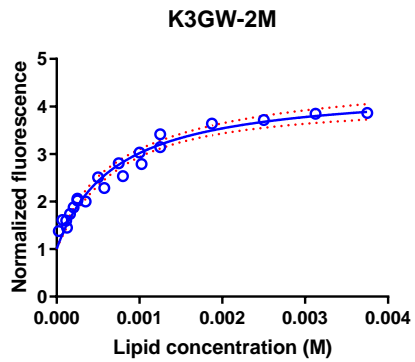
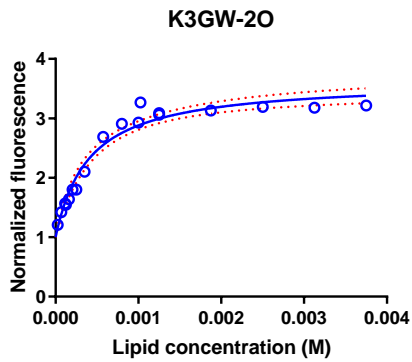
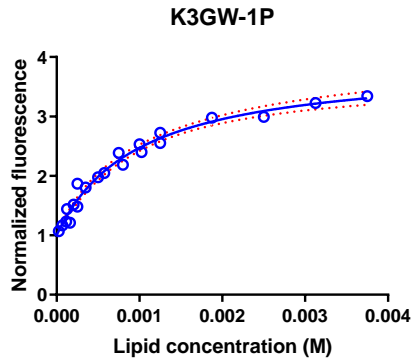
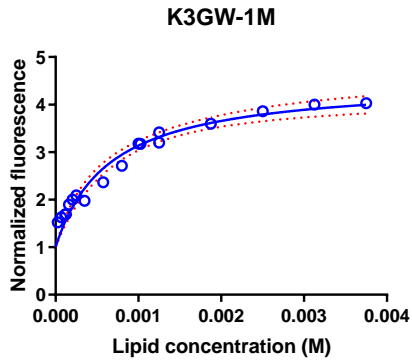
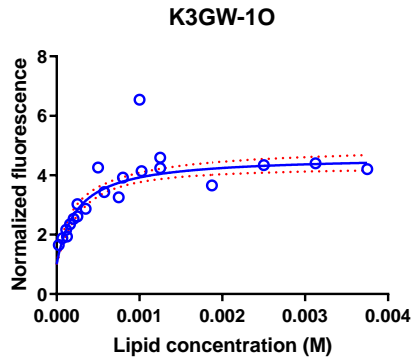
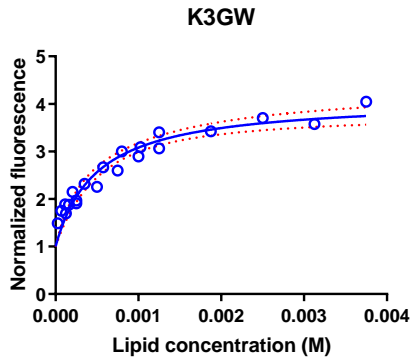
## Tryptophan fluorescence experiments

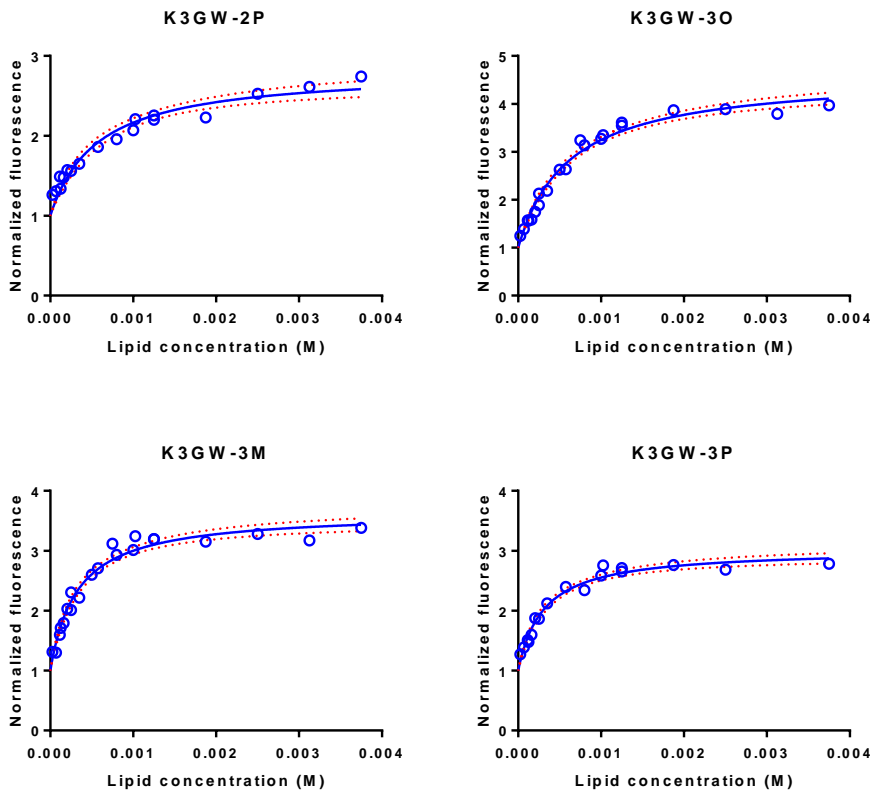


**Figure S3.4:** Overview of the membrane partition coefficient of stapled peptide variants (left) and membrane partition set against peptide helicity (right) as determined via CD spectroscopy. Error bars represent the standard error of fitting.

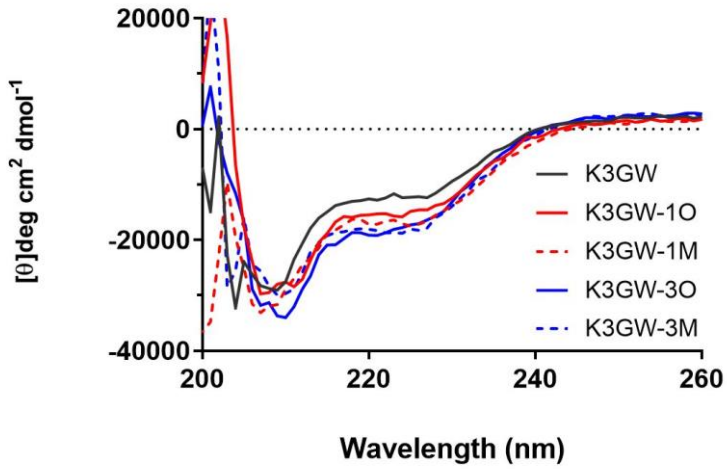
**Table S3.4:** Membrane binding affinity determined via tryptophan fluorescence for peptide K<sub>3</sub>GW and its stapled derivatives. The shown values are derived from the fitted curves shown in Figure S3.5.

Peptide	$K_p$ ( $10^3$ )	$R^2$	$\Delta G$ (KJ/Mol)	$\Delta\Delta G$ (KJ/Mol)
K <sub>3</sub> GW	112	0.93	-28.80	-
K <sub>3</sub> GW-1O	225	0.88	-30.53	-1.73
K <sub>3</sub> GW-1M	86	0.96	-28.15	0.65
K <sub>3</sub> GW-1P	57	0.98	-27.13	1.67
K <sub>3</sub> GW-2O	137.8	0.96	-29.32	-0.51
K <sub>3</sub> GW-2M	80	0.96	-27.97	0.83
K <sub>3</sub> GW-2P	97.5	0.95	-28.46	0.34
K <sub>3</sub> GW-3O	90	0.98	-28.26	0.54
K <sub>3</sub> GW-3M	172	0.97	-29.87	-1.06
K <sub>3</sub> GW-3P	181.7	0.97	-30.00	-1.20



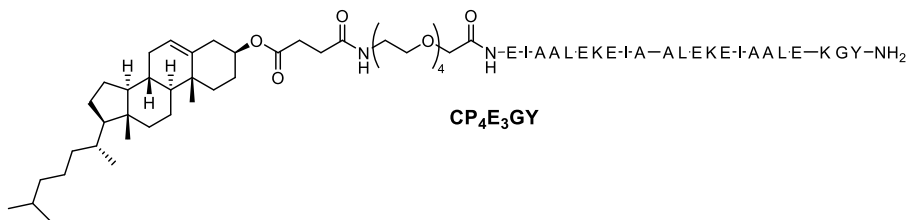


**Figure S3.5:** Fitting curves used to determine the membrane partition coefficient ( $K_p$ ) of the stapled peptides. Red dotted lines represent the 95% confidence interval of the fit.

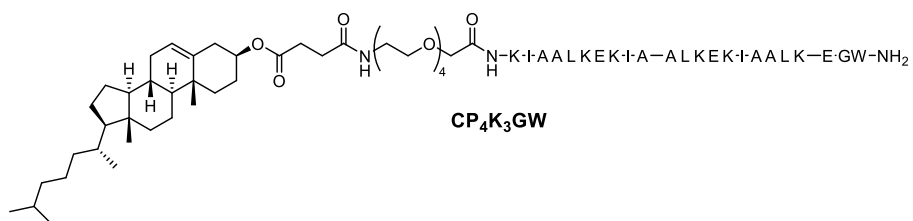
*CD spectra with liposomes*

**Figure S3.6:** CD spectra of stapled peptides when combined with liposomes. Peptide concentration is 10  $\mu\text{M}$ , liposomes are at a 1 mM lipid concentration and consist of DOPC:DOPE:Cholesterol in a 2:1:1 ratio. All spectra were measured in PBS in a 10 mm quartz cuvette at 25 °C.

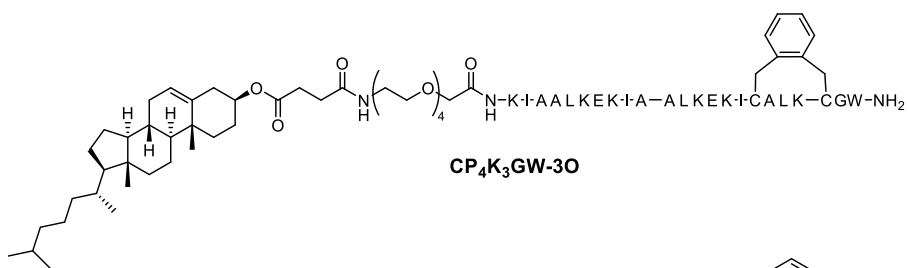
## Lipidated peptide structures



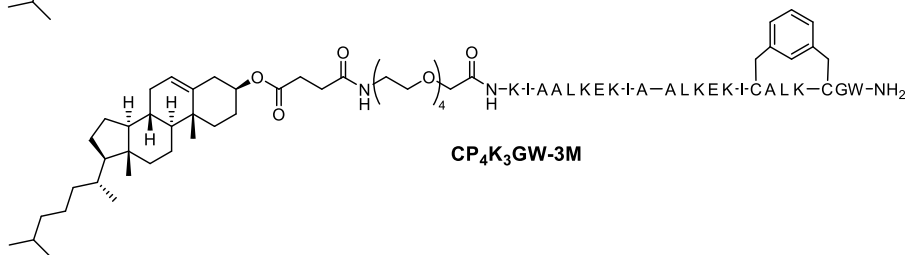
CP<sub>4</sub>E<sub>3</sub>GY



CP<sub>4</sub>K<sub>3</sub>GW

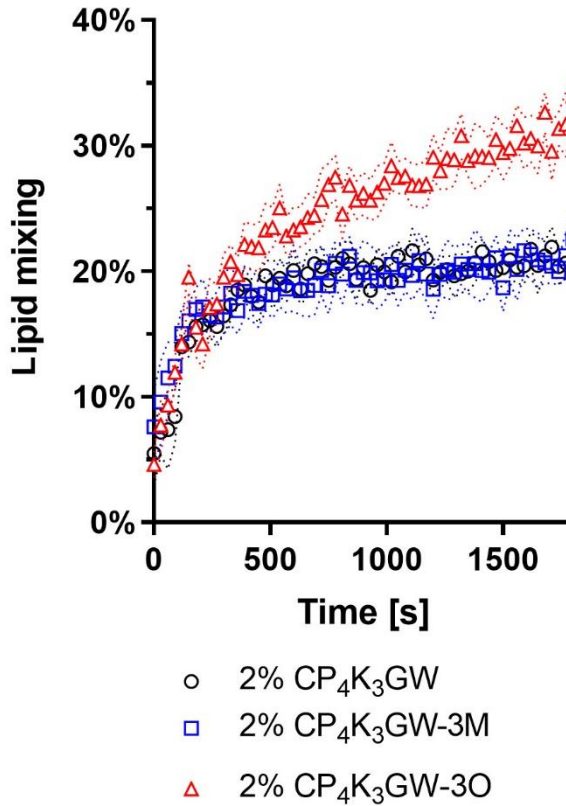


CP<sub>4</sub>K<sub>3</sub>GW-30



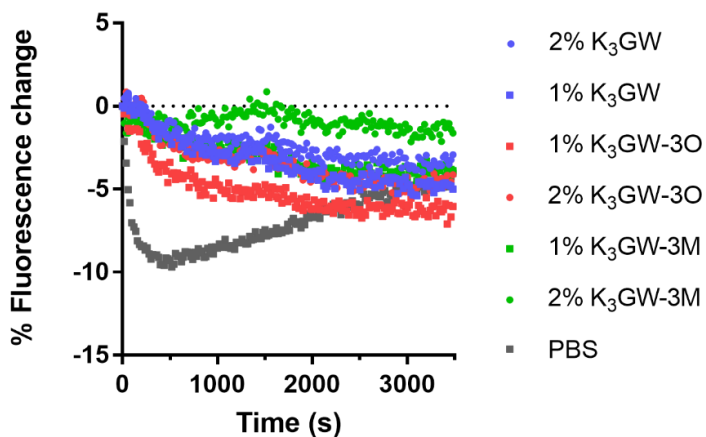
CP<sub>4</sub>K<sub>3</sub>GW-3M

**Scheme S3.1:** Structures of lipidated peptides used for membrane fusion studies in this manuscript.

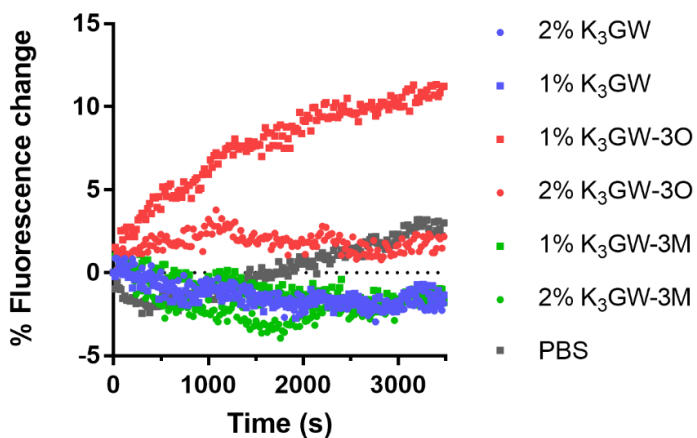
*Lipid and content mixing control experiments*

**Figure S3.7:** Lipid mixing experiments performed with 2% lipopeptides in the liposomal membranes. Graphs show the change in mixing over time, and the standard deviation between 4 samples followed simultaneously. Experiments were performed at 500  $\mu$ M total lipid concentration in pH 7.4 PBS at 20 °C. Observed fluorescence was normalized against 0% and 100% control samples.

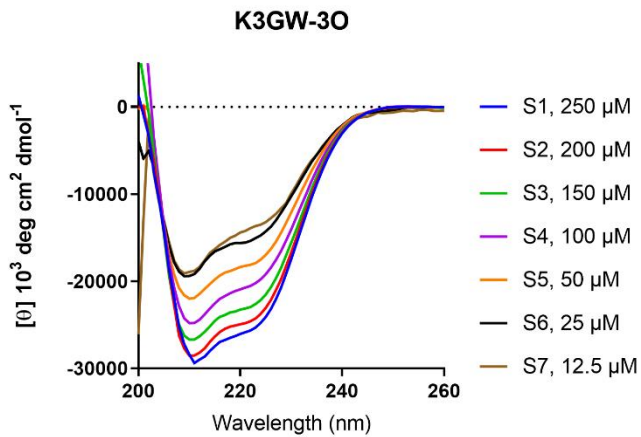
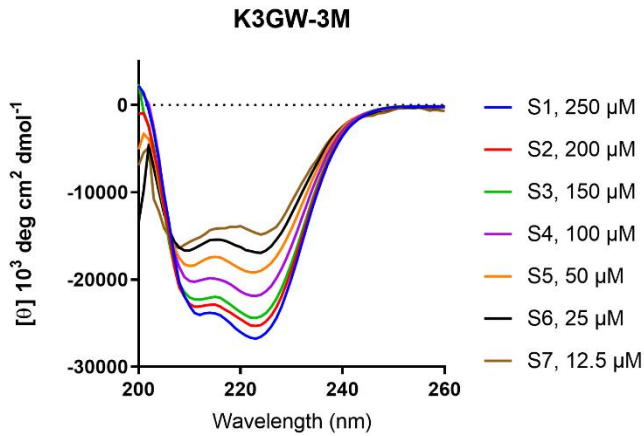
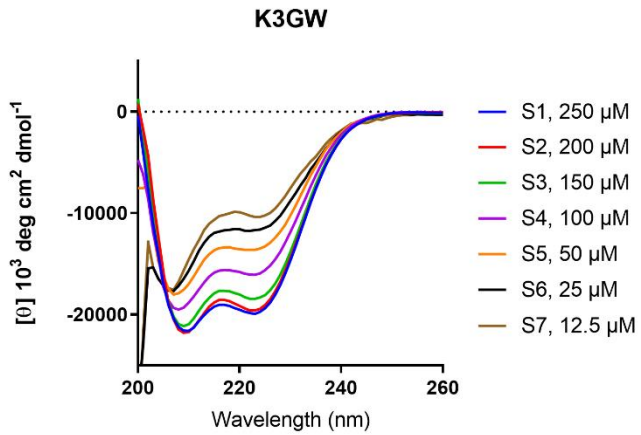
### SrB leakage from plain liposomes



### SrB leakage from 1% CP<sub>4</sub>E<sub>3</sub>GY liposomes



**Figure S3.8:** Sulforhodamine B leakage experiments for stapled peptide variants. Liposomes (500  $\mu$ M lipid concentration) filled with sulforhodamine B were combined with acylated variants of peptide K<sub>3</sub>GW at concentrations similar to those used in content mixing experiments, and change in absolute fluorescence was observed over time. No peptide was added to the samples labelled 'PBS'.

*Homodimerization of stapled peptides*

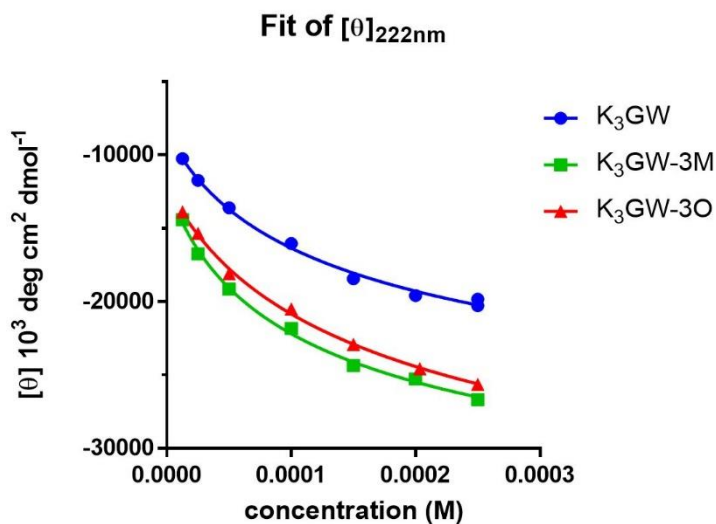


**Figure S3.9:** CD titration of peptide K<sub>3</sub>GW, K<sub>3</sub>GW-3M, and K<sub>3</sub>GW-3O to determine homodimer formation of these peptide (top), and the extrapolated absorbance at 222 nm plotted against the concentration (bottom). Spectra were recorded at 25 °C in PBS buffer.

**Table S3.5:** Results of a non-linear fit of the CD ellipticity data shown in Figure S3.9 to determine the peptide affinity constant ( $K_a$ ) of homodimer formation.  $[\theta]_m$  and  $[\theta]_d$  are fitted constants and represent the CD ellipticity values of the peptide as a monomer and a dimer respectively.

Peptide	$[\theta]_m$ $10^3 \text{ deg cm}^2 \text{ dmol}^{-1}$	$[\theta]_d$ $10^3 \text{ deg cm}^2 \text{ dmol}^{-1}$	$K_a (10^3)$	$R^2$
<b>K3GW</b>	-8434	-33396	3.41	0.995
<b>K3GW-3O</b>	-12010	-39808	4.57	0.997
<b>K3GW-3M</b>	-12056	-43076	2.76	0.998

*Fitting procedure for homodimer formation*

To calculate the peptide homodimerization from the CD spectra, the following chemical equilibria and equations are employed:



$$K_d = \frac{[P_m]^2}{[P_d]} \quad (S2)$$

$$[P_t] = [P_m] + 2[P_d] \quad (S3)$$

where  $P_m$  and  $P_d$  represent the monomer and dimer concentration, and  $P_t$  the total peptide concentration.

From this Equation S4 can be derived:

$$[P_d] = \frac{[P_m]^2}{K_d} \quad [P_t] = [P_m] + \frac{2[P_m]^2}{K_d} \quad (S4)$$

And a solution for  $P_m$  is shown as Equation S5:

$$[P_m] = \frac{K_d}{4} \left( -1 + \sqrt{1 + \frac{8[P_t]}{K_d}} \right) \quad (S5)$$

The equation for the measured absorbance  $\theta$  as a function of the absorbance of the peptide as a monomer ( $\theta_m$ ) and dimer ( $\theta_d$ ), which are constants, is as follows:

$$\theta = \frac{[P_m][\theta_m] + 2[P_d][\theta_d]}{[P_t]} \quad (S6)$$

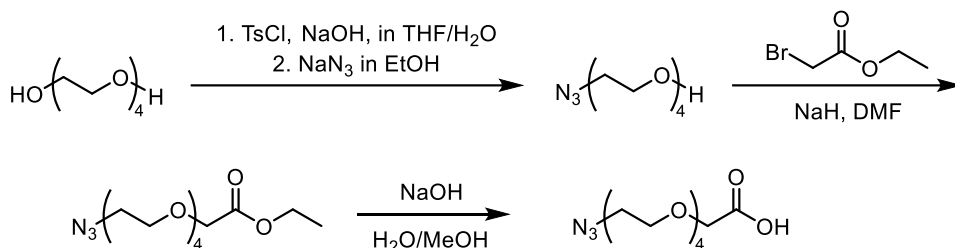
Combining S6 with S4 gives us the following:

$$\theta = \frac{[P_m][\theta_m] + \frac{2[P_m]^2}{K_d}[\theta_d]}{[P_t]} \quad (S7)$$

Using this equation combined with the equation above for  $P_m$ , the binding curve of the peptides can be fitted.

### Synthesis of $N_3$ -PEG<sub>4</sub>-COOH

The synthetic route to produce the polyethylene glycol crosslinker used in the preparation of lipopeptides is shown in scheme S3.2.



**Scheme S3.2:** Synthetic scheme for the preparation of linker  $N_3$ -PEG<sub>4</sub>-COOH.

### Preparation of O-(2-azidoethyl)-triethylene glycol (N<sub>3</sub>-PEG<sub>4</sub>)

A 250-mL round bottom flask equipped with a magnetic stirring bar was charged with tetraethylene glycol (50.9 g, 262 mmol, 10 eq) in 10 mL tetrahydrofuran. An aqueous solution (10 mL) containing sodium hydroxide (1.68 g, 42 mmol, 1.6 eq) was added to the flask, and p-toluenesulfonyl chloride (5 g, 26.2 mmol, 1 eq) dissolved in 30 mL tetrahydrofuran (THF) was added dropwise over 3h to the mixture maintained at 0 °C. The reaction was diluted with ice-cold water (150 mL) and extracted with 3 x 100 mL dichloromethane. The combined organic layers were washed with 2 x 300 mL of water and once with 100 mL of brine, dried over  $\text{MgSO}_4$ , filtered, and concentrated to yield a clear oil (9.2 g, 26.2 mmol, quantitative yield). Sodium azide (4.3 g, 65.5 mmol, 2.5 eq,) was added to the tosylate intermediate, and the mixture was dissolved in absolute ethanol (200 mL). The reaction was stirred under reflux overnight, cooled to room temperature, and then diluted with water (150 mL). The mixture was concentrated by rotary evaporation to approximately 150 mL, and the product was extracted into ethyl acetate (3 x 150 mL), dried with  $\text{MgSO}_4$ , filtered, and concentrated to yield a faint yellow liquid (5.1 g, 23.3 mmol, 89% yield over two steps).  $^1\text{H NMR}$  (300 MHz,  $\text{CDCl}_3$ )  $\delta$  3.63 (d,  $J = 4.9$  Hz, 12H), 3.59 – 3.54 (m, 2H), 3.40 – 3.31 (m, 2H), 2.69 (s, 1H).  $^{13}\text{C NMR}$  (75 MHz,  $\text{CDCl}_3$ )  $\delta$  72.54, 70.74, 70.71, 70.64, 70.40, 70.09, 61.75, 50.71.

**Preparation of 14-azido-3,6,9,12-tetraoxatetradecanoic acid (N<sub>3</sub>-PEG<sub>4</sub>-COOH)**

To a dry flask, NaH was added (60% suspension in mineral oil, 0.56 g, 14 mmol, 1.4 eq), and 10 mL dry THF was added to suspend the powder. The reaction was temperature controlled with a water bath and N<sub>3</sub>-PEG<sub>4</sub> was added (2,17 g, 10 mmol) in 10 mL dry THF. To the reaction ethyl-bromoacetate (1,67 mL, 15 mmol, 1.5 eq) in 10 mL THF was added dropwise over the course of 30 minutes. The addition funnel was cleaned with a further 5 mL HF, which was also added. The reaction was heated to 50 °C and stirred overnight. The reaction was quenched by dropwise addition of ice-cold 90% EtOH/H<sub>2</sub>O, and the mixture neutralized to pH 7. The solvent was removed via rotary evaporation, the product dissolved in H<sub>2</sub>O, 30 mL and extracted with EtOAc (3 x 30 mL). The solvent was removed yielding a yellowish oil, which was purified via column chromatography using 1:1 Et<sub>2</sub>O:ethyl acetate and solvent was removed to yield 903 mg (3 mmol, 30% yield) of an off-white oil. 700 mg (2,3 mmol) of the alkylated PEG was dissolved in 5 mL 96% EtOH, 1,5 mL 5M NaOH was added and the mixture was heated at reflux for 90 minutes. The ethanol was evaporated, the mixture diluted with 8 mL H<sub>2</sub>O and washed with 2 x 20 mL DCM. Afterwards, the aq. layer was acidified with acetic acid and extracted with 4 x 20 mL DCM, the organic layers were combined and washed with 10 mL brine, dried with Na<sub>2</sub>SO<sub>4</sub> and the solvent removed under vacuum, to yield 640 mg of an off-white oil (quantitative yield). <sup>1</sup>H NMR (300 MHz, CDCl<sub>3</sub>) δ 4.07 (s, 2H), 3.70 – 3.47 (m, 14H), 3.33 – 3.23 (t, *J* = 12 Hz, 2H). <sup>13</sup>C NMR (75 MHz, CDCl<sub>3</sub>) δ 173.73, 70.81, 70.35, 70.29, 70.23, 70.17, 69.75, 68.17, 50.38.

## LC-MS of purified peptides

**Table S3.6:** Overview of the calculated masses of all peptides used in this chapter, and the masses found by LCMS.

Peptide name	Calculated mass (Da)	Measured mass (Da)
<b>K<sub>3</sub>GW-1O</b>	[M + 2H <sup>+</sup> ] <sup>2+</sup> 1336.77	1335.80
<b>K<sub>3</sub>GW-1M</b>	[M + 2H <sup>+</sup> ] <sup>2+</sup> 1336.77	1335.31
<b>K<sub>3</sub>GW-1P</b>	[M + 2H <sup>+</sup> ] <sup>2+</sup> 1336.77	1335.10
<b>K<sub>3</sub>GW-2O</b>	[M + 2H <sup>+</sup> ] <sup>2+</sup> 1336.77	1336.06
<b>K<sub>3</sub>GW-2M</b>	[M + 2H <sup>+</sup> ] <sup>2+</sup> 1336.77	1335.57
<b>K<sub>3</sub>GW-2P</b>	[M + 2H <sup>+</sup> ] <sup>2+</sup> 1336.77	1335.71
<b>K<sub>3</sub>GW-3O</b>	[M + 2H <sup>+</sup> ] <sup>2+</sup> 1336.77	1335.59
<b>K<sub>3</sub>GW-3M</b>	[M + 2H <sup>+</sup> ] <sup>2+</sup> 1336.77	1336.01
<b>K<sub>3</sub>GW-3P</b>	[M + 2H <sup>+</sup> ] <sup>2+</sup> 1336.77	1335.71
<b>K<sub>3</sub>GW</b>	[M + 2H <sup>+</sup> ] <sup>2+</sup> 1283.27	1281.77
<b>E<sub>3</sub>GY</b>	[M + 2H <sup>+</sup> ] <sup>2+</sup> 1272.69	1271.70
<b>CP<sub>4</sub>-E<sub>3</sub>GY</b>	[M + 2H <sup>+</sup> ] <sup>2+</sup> 1601.94	1602.13
	[M + 2H-cholesterol <sup>+</sup> ] <sup>2+</sup> 1417.24	1417.01
<b>CP<sub>4</sub>-K<sub>3</sub>GW</b>	[M + 2H <sup>+</sup> ] <sup>2+</sup> 1612.03	1612.06
	[M + 2H-cholesterol <sup>+</sup> ] <sup>2+</sup> 1427.33	1427.22
<b>CP<sub>4</sub>-K<sub>3</sub>GW-3O</b>	[M + 2H <sup>+</sup> ] <sup>2+</sup> 1666.51	1666.21
	[M + 2H-cholesterol <sup>+</sup> ] <sup>2+</sup> 1481.81	1481.51
<b>CP<sub>4</sub>-K<sub>3</sub>GW-3M</b>	[M + 2H <sup>+</sup> ] <sup>2+</sup> 1666.51	1666.35
	[M + 2H-cholesterol <sup>+</sup> ] <sup>2+</sup> 1481.81	1481.65







---

Azobenzene crosslinking for coiled-coil  
photoswitching

## **Abstract**

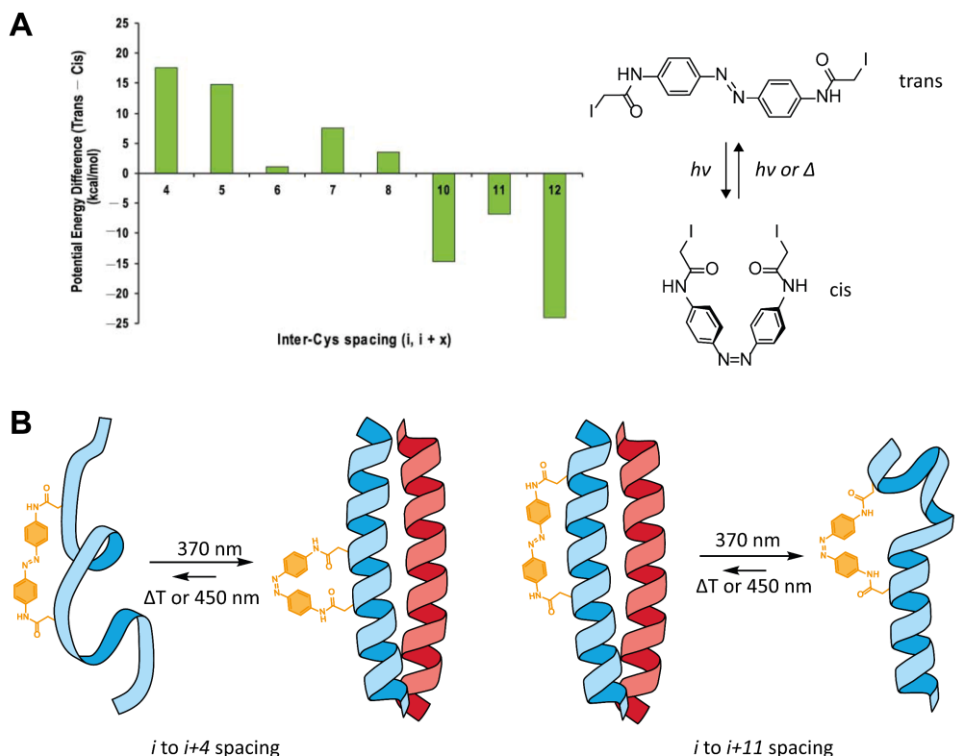
Azobenzene-based intramolecular crosslinkers have been shown to allow control over peptide structure through photoisomerization of the azobenzene. This crosslinking strategy was applied to a coiled-coil system previously used for membrane fusion, with the aim of introducing control in that system. Photocontrol over peptide structure could be achieved, but after combining the peptide with its complementary binding partner only a minimal difference between the initial dark and irradiated state was observed. Reducing the length of the peptide to three heptads increased the effect of the azobenzene crosslinker on peptide structure, yielding a heterodimeric coiled-coil that could be switched from 46% helicity in the dark state to 64% helicity in the light state. For further studies, alternative (synthetic) methods of crosslinking should be investigated as yields of the azobenzene-crosslinked products were low, and more effective switching of peptide structure leads to increased control over peptide activity.

## 4.1 Introduction

Coiled-coil motifs can be designed to self-assemble with high affinity and selectivity.<sup>1</sup> These properties have given them an important role in the field of synthetic biology and self-assembled nanomaterials.<sup>2-4</sup> The range of applications for coiled-coil peptides can be broadened by integrating specific, external triggers for their self-assembly. Specifically, active control over coiled-coil formation in the liposomal membrane fusion system developed in our group should allow control over its activity. This system consists of a heterodimeric coiled-coil that, when attached to separate lipid membranes via a cholesterol anchor and polyethylene glycol (PEG) spacer, shows membrane fusion in a manner similar to naturally occurring SNARE-proteins.<sup>5, 6</sup> The coiled-coil peptides are named 'E' and 'K', based on the dominant charged amino acid in their sequence. For applications in drug delivery, improving upon the existing coiled-coil fusion systems via the incorporation of external stimuli should allow precisely controlled release of carrier molecules across lipid membranes.

Stimuli-responsive systems can change their behaviour in response to an alteration in chemical or physical conditions. Specifically the binding of metal ions,<sup>7</sup> change in pH,<sup>8</sup> redox chemistry,<sup>9</sup> and enzymatic alteration of amino acids,<sup>10</sup> have been used to generate chemoresponsive coiled-coil peptides and proteins. Chemical control over self-assembly often requires precise control over experimental conditions, which is easy to achieve in laboratory settings, but does not translate well to bioactive systems. Due to the requirement for biocompatibility in combination with selectivity and ease of use, light is a popular alternative to chemical input when designing a responsive system.<sup>11</sup> The integration of a photoactive molecular switch also has the advantage of being reversible, either optically or thermally, and is therefore a common method of generating photoactive systems.<sup>12, 13</sup>

Azobenzenes are one of the most widely used photoactive switches, changing in structure upon isomerization between the planar *trans* isomer and the twisted *cis* isomer across the diazene bond (**Scheme 4.1A**). Under dark conditions, the azobenzene is predominantly *trans*, which is the most thermodynamically favoured isomer, but the ratio of isomers can be altered via light isomerization. The ratio of isomers after light irradiation depends on the quantum yield of the *trans-cis* and *cis-trans* isomerization and their extinction coefficients at the wavelength used for



**Scheme 4.1:** Azobenzene based crosslinker for the photocontrol of peptide structure and the effect of crosslinker spacing on the difference in calculated peptide folding energy when switching between *cis* and *trans* isomers (A). Images adapted from Flint *et. al.*<sup>14</sup> Schematic representation of incorporating photoactive crosslinkers in a heterodimeric coiled-coil system (B). Depending on spacing between the attachment points of the crosslinker, either the light or the dark state can be expected to show the highest coiled-coil characteristics.

isomerization. Both of these properties can be influenced by substituents on the aromatic rings of the azobenzene. In general, the *cis* conformation is the predominant isomer when light corresponding to the  $\pi$ - $\pi^*$  absorption band is used for isomerization, while the *trans* isomer is dominant with light corresponding to the  $n$ - $\pi^*$  transition.<sup>15</sup> The isomerization changes the relative position of substituents placed on the azobenzene rings. End-to-end distance between substituents placed on the azobenzene shows a large change in distance in the *trans* conformation compared to the *cis* isomer. This change in end-to-end distance has been used successfully for the control of biomolecule activity.<sup>16-18</sup>

The group of Woolley extensively used azobenzene based bifunctional crosslinkers (**Scheme 4.1A**) to generate photoresponsive peptides. For example, they were able

to photocontrol the helicity of a short 16-amino acid peptide via intramolecular crosslinking of two cysteine residues.<sup>19</sup> By changing the inter-cysteine spacing the difference in peptide folding energy between the *trans* and *cis* isomers of the crosslinker could be altered (**Scheme 4.1A**). This allowed both states to be the predominantly folded state depending on cysteine spacing, showing the versatility of this crosslinking strategy.<sup>14</sup> Many alterations to this system have been made to change linker size, absorption maximum, relaxation time and solubility to tune the system for different biochemical applications, but the central mechanism of function remains the same.<sup>20-24</sup>

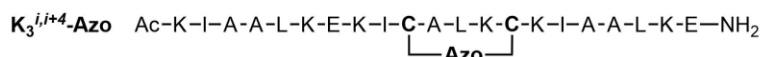
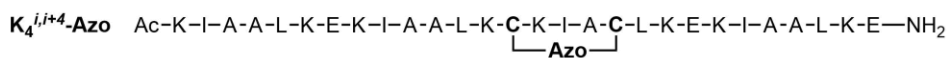
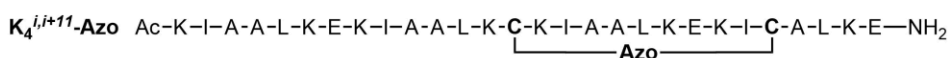
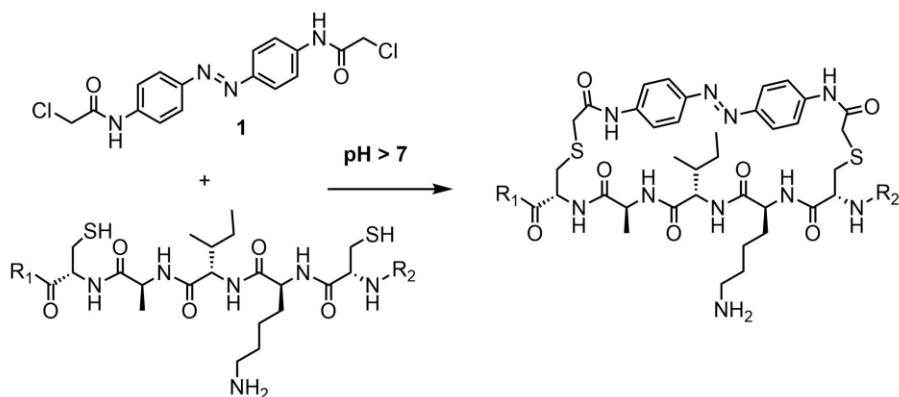
The prospect of using photoswitchable crosslinkers in coiled-coil motifs has been investigated previously, specifically in controlling the activity of basic leucine zipper proteins (bZIPs). The DNA-binding homodimeric GCN4-bZIP was modified with an azobenzene-based crosslinker and showed an increase from 40% to 90% DNA binding when isomerized with light, demonstrating changes in structure-dependent activity.<sup>25</sup> The transcription factor Fos was also shown to have altered activity when macrocyclized using an azobenzene crosslinker. Normally an equilibrium between the more stable Fos/Jun heterodimeric bZIP and less stable Jun/Jun homodimeric bZIP is observed; this equilibrium could be shifted using the photoactive XAFosW variant, resulting in significant differences between the irradiated and dark adapted state which were visualized using a luciferase reporter *in vitro*.<sup>26</sup> Recently, bifunctional azobenzene crosslinking was also used for intermolecular crosslinking of a short (14 amino acid) homodimeric coiled-coil peptide, which allowed for significant changes in peptide structure between the two isomers.<sup>27</sup>

In this chapter we aim to bridge the design of photocontrolled  $\alpha$ -helices and coiled-coil proteins through the incorporation of a photoactive crosslinker in one of the helices of a synthetic heterodimeric coiled (**Scheme 4.1B**), which should in turn allow photocontrolled activation of membrane fusion. Both 'turning on', and 'turning off' coiled-coil formation by light irradiation are shown, and depend on the spacing of crosslinking sites, with the overall effectiveness of photoswitching being dependent on the length of the coiled-coil motif.

## 4.2 Results and Discussion

### *Peptide and crosslinker synthesis*

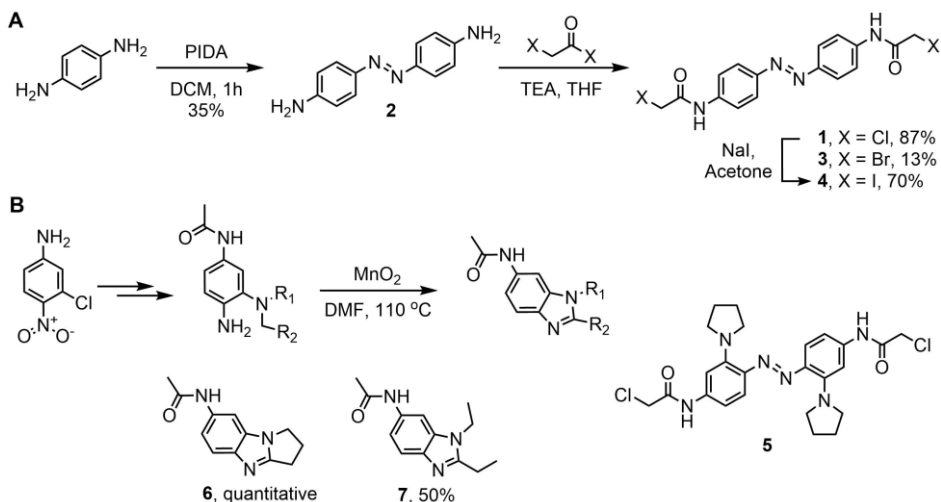
Two variants of the fusogenic peptide K<sub>4</sub> were prepared for crosslinking via Fmoc-based SPPS(**Scheme 4.2**), incorporating two cysteine modifications which should



**Scheme 4.2:** General reaction scheme for the preparation of azobenzene-crosslinked peptides, and the sequences of the three crosslinked peptides discussed in this chapter.

allow thiol-halogen exchange with the crosslinker at neutral pH. Cysteines were positioned in the coiled-coil backbone at the centre of the peptide sequence with an  $i$  to  $i+4$  or  $i$  to  $i+11$  spacing, as this has previously been demonstrated to be optimal for helical control of this type of crosslinker.<sup>14</sup> The  $i$  to  $i+4$  spaced variant is designed to fold into a helical structure when the azobenzene crosslinker is in its *cis* isomer, while the  $i$  to  $i+11$  spacing is expected to yield the most helical peptide with the crosslinker in the *trans* conformation. Azobenzene based crosslinkers were prepared according to previously published literature procedures.<sup>19</sup> In short, 1,4-diaminobenzene was oxidized to 4,4'-diamino-azobenzene (**2**), which was reacted with chloroacetyl chloride to yield crosslinker **1** in 87% yield (reaction scheme shown in **Scheme 4.3A**). The dibromo-variant **3** could be prepared in the same manner as **1** using bromoacetyl bromide, with the diiodo variant **4** prepared through a Finkelstein substitution of **1** with sodium iodide.

An attempt was also made to synthesize the previously published azobenzene crosslinker **5** (starting from 4-nitro-3-chloroaniline, **Scheme 4.3B**) containing two pyrrolidine moieties positioned *ortho* to the diazene, which was shown to have a very fast thermal *cis* to *trans* isomerization and red-shifted absorption bands.<sup>21</sup>



**Scheme 4.3:** Synthesis of azobenzene crosslinkers **1**, **3** and **4**, (A) and the attempted synthesis of crosslinker **5** showing efficient conversion of ortho-aminoalkanes to benzimidazoles (B).

Preparation of this crosslinker according to the literature procedure was deemed unsuitable, since the published yield was only 2% for oxidation of the aniline intermediate. Different reaction conditions were tested to oxidize 4-amino-3-(pyrrolidyl)acetanilide to the respective azobenzene. Conditions that formed the desired product were not found, but when manganese dioxide was used as the oxidant in DMF, an alternative reaction was observed that yielded the cyclized benzimidazole product **6** exclusively. The same conditions oxidized 4-amino-3-(diethylamino)acetanilide to benzimidazole **7** in 50% yield, showing that this reaction occurs generally for this class of compounds and these conditions might be of interest for further study into their potential synthetic application. Because no novel oxidative methods were encountered that yielded the azobenzene in good yields, the synthesis of crosslinker **5** was not pursued further.

Crosslinking of cysteine substituted peptides  $K_4^{i,i+11}$ -Azo and  $K_4^{i,i+4}$ -Azo was attempted with crosslinker **1** following literature protocols relying on thiol-halogen exchange under basic conditions (pH 7.6-8.2, **Scheme 4.2**). These conditions make use of a low peptide concentration to favour the intramolecularly crosslinked product over intermolecular crosslinking. The followed protocols generally require peptides in an unstructured state, relying on high concentrations of chemical denaturants and organic solvents to keep the hydrophobic crosslinker dissolved during the synthesis.<sup>28</sup> The  $i$  to  $i+4$  crosslinked variant additionally requires the azobenzene crosslinker to be in the *cis* conformation for successful incorporation,

adding illumination steps in the synthetic protocol since the *trans* isomer is thermodynamically the most stable. These protocols proved to be low-yielding and the reaction mixtures were difficult to purify, resulting in low (<2%) yield of both peptides after optimization of reaction time and illumination steps.

#### *Photoswitching and structural analysis of photoactive K<sub>4</sub> derivatives*

The crosslinked peptides were assumed to be in thermal equilibrium after purification and work-up, which was supported by their UV-Vis spectra showing mostly the *trans* isomer (**Figure 4.1A**). Isomerization of the azobenzene crosslinker could be achieved by irradiation with 375 nm or 385 nm light, as shown by the disappearance of the strong absorption maximum at 367 nm. These spectra are comparable to those of Flint *et al.*, which demonstrated mostly the *trans* isomer if the sample was dark adapted, transitioning to 80% of the *cis* isomer upon illumination.<sup>14</sup> Thermal relaxation of the *cis* isomer back to the *trans* conformation could also be studied in this manner and the thermal half-life of the *cis* state was determined to be 14 minutes for K<sub>4</sub><sup>*i,i+11*</sup>-Azo (**Figure S4.2**), which is close to previously published half-life for this crosslinker, and 9.1h for K<sub>4</sub><sup>*i,i+4*</sup>-Azo (**Figure 4.1B** and **4.1C**). This 40x difference in relaxation half-life is stark, in previous work only a 3x increase half-life was observed when comparing *i* to *i+4* with *i* to *i+11* spacing. The observed difference in half-life can likely be attributed to the different functions of the *cis* state in the folded helix, resulting in a geometric constraint.

The folding of peptide K<sub>4</sub> in an  $\alpha$ -helical conformation is energetically favoured, with the photoswitchable crosslinker providing an energetic constraint which prevents the peptide from folding completely in the 'inactive' state (*trans* for K<sub>4</sub><sup>*i,i+4*</sup>-Azo, *cis* for K<sub>4</sub><sup>*i,i+11*</sup>-Azo). In turn, the peptide is applying a force on the crosslinker when the peptide is unfolded. The transition states of *trans*-azobenzene photoisomerization has experimentally been shown to decay in less than a picosecond,<sup>29</sup> multiple orders of magnitude faster than the potential folding speed of  $\alpha$ -helical peptides and proteins.<sup>30</sup> Consequently, during the transition state the peptide can be viewed as constant and applying a structural constraint to the azobenzene crosslinker. Thermal isomerization of the azobenzene occurs via Rotation or Inversion,<sup>15</sup> which decreases the likelihood of the transition state resulting in the *trans* isomer. For K<sub>4</sub><sup>*i,i+4*</sup>-Azo this results in a significantly increased half-life of the *cis* state, where for peptide K<sub>4</sub><sup>*i,i+11*</sup>-Azo this would most likely affect the quantum yield of the *trans* to *cis* photoisomerization.

To determine the effect of crosslinking and isomeric state on peptide structure, circular dichroism (CD) spectra were recorded of azobenzene crosslinked K<sub>4</sub><sup>*i,i+11*</sup>-Azo

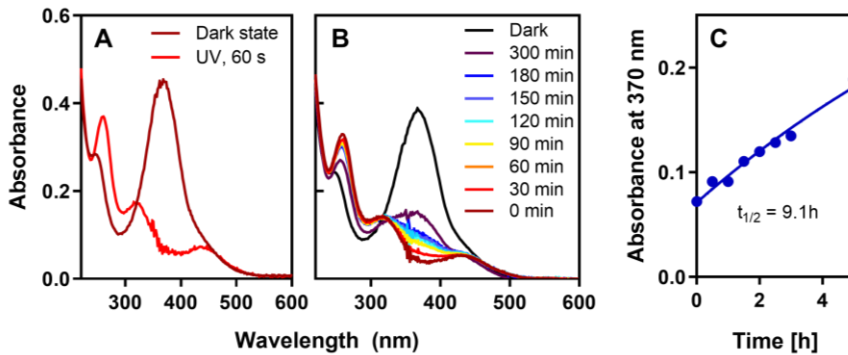


**Figure 4.1:** UV-Vis spectra showing the *cis* to *trans* isomerization under UV light (A), thermal back-relaxation of peptide  $K_4^{i,i+4}$ -Azo (B) and the fitting of this thermal relaxation (C). Peptide concentration is 50  $\mu$ M in PBS, illumination performed with 375 nm light.

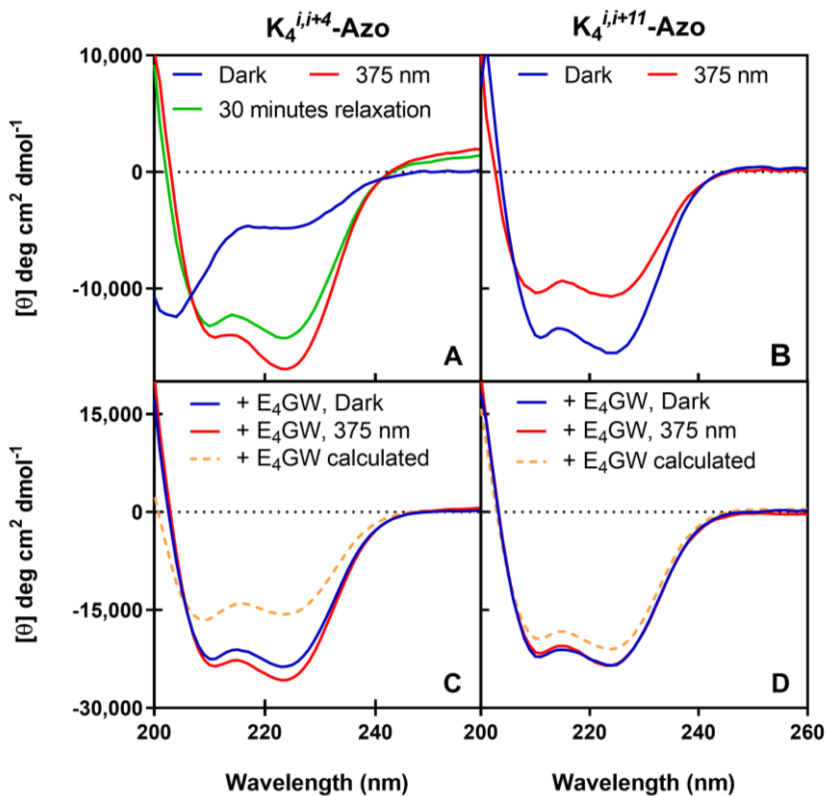


**Figure 4.2:** CD spectra of  $K_4$  peptide variants crosslinked with azobenzenes. CD measurements are shown for peptide  $K_4^{i,i+4}$ -Azo (A) and peptide  $K_4^{i,i+11}$ -Azo (B) and their respective complexes with peptide  $E_4GW$  (C and D). Spectra are measured at 25  $\mu$ M peptide concentration in PBS at pH 7.4, with samples either kept in the dark before measurements, or illuminated for 3 minutes with 375 nm light. Calculated coiled-coil spectra are for the less folded azobenzene isomer (*Trans* isomer for  $K_4^{i,i+4}$ -Azo, C; *Cis* isomer for  $K_4^{i,i+11}$ -Azo, D).

and  $K_4^{i,i+4}$ -Azo both individually and as a coiled-coil in combination with peptide  $E_4GW$ ; results of these experiments can be seen in **Figure 4.2** and **Table 4.1**.  $K_4^{i,i+4}$ -Azo showed a random-coil structure in the initial dark state (**Figure 4.2A**), which changed to a coiled-coil like structure upon irradiation with 375 nm light. In combination with peptide  $E_4GW$ , a folded coiled-coil structure was observed for both isomers, varying from 68% average  $\alpha$ -helicity in the initial dark state to 71% average  $\alpha$ -helicity after light irradiation. As expected, the response of peptide  $K_4^{i,i+11}$ -Azo to photoisomerization was inverted, showing a coiled-coil structure which decreased from 45% to 33% average  $\alpha$ -helicity when the azobenzene was switched to the *cis* isomer (**Figure 4.2B**, **Table 4.1**). Like the *i* to *i+4* variant, differences between the initial dark and irradiated state were minimal for the coiled coil of  $K_4^{i,i+11}$ -Azo with  $E_4GW$ . A clear difference can be observed between the measured coiled-coil spectra for both peptides, and the expected curves calculated by combining their independent CD absorption spectra (dashed yellow lines, **Figure 4.2C & 4.2D**) in the dark. This increase in helicity shows coiled-coil formation, which has not been hampered by incorporation of the crosslinker in both isomeric states.

The CD experiments clearly demonstrate the premise on which the peptides were designed is indeed correct: intramolecular cysteine crosslinking using azobenzene allows for control of peptide helicity. Positioning of cysteines *i* to *i+4* shows very effective switching between an unfolded and folded helix (33% increase in average  $\alpha$ -helicity) upon light irradiation, where cysteine positioning *i* to *i+11* allows for unfolding of the peptide when illuminated with light, although the difference is reduced with a 12% decrease in average  $\alpha$ -helicity. These results do not translate as well to the coiled-coils, where differences between the two isomers are small for both peptides. From these CD spectra we can conclude that the geometric constraint applied by the crosslinker in the 'unfolded' state applies an energy penalty for  $\alpha$ -helical folding. This energy penalty is larger than the folding energy of peptide K or formation of the K/K homodimer, but not larger than the energy associated with formation of the E/K heterodimeric coiled-coil. The difference in energy for the formation of the homodimer is multiple orders of magnitude lower (**Chapter 3** of this thesis) so this result is not surprising, but the observed small difference between the two isomers as a coiled-coil makes these peptides unsuitable for photocontrol of membrane fusion. To increase the difference between the two isomers, either the applied constraint needs to be amplified, or the energy of coiled-coil formation needs to be decreased to increase the effect of a single crosslinker on coiled-coil formation. Because three heptad variants of the E/K coiled-coil have already been well studied and have a lower binding energy due

to the reduction in peptide length,<sup>31, 32</sup> we decided to pursue azobenzene crosslinked variants of that system to achieve successful coiled-coil switching.

#### *Synthesis and study of photoswitchable peptide $K_3^{i,i+4}$ -Azo*

The preparation of four heptad repeat, azobenzene crosslinked peptides was inefficient, therefore other methods were explored in the preparation of a three-heptad variant. A variant of peptide  $K_3$  containing cysteines spaced  $i$  to  $i+4$  in the second heptad was chosen (**Scheme 4.2**) in order to optimize coupling efficiency. Different buffering conditions, solvent additives, choice and equivalents of crosslinker, illumination and reaction time were tested to increase the yield of crosslinked product with negligible improvements (**Table S4.1**). Because crosslinker **1** seemed to precipitate from solution quickly after addition started, we hypothesized the solubility of the azobenzene crosslinkers was the major bottleneck in this reaction. To overcome this, two different approaches were pursued: liquid phase coupling of the crosslinker with unprotected peptides in organic solvents, and on-resin coupling of the crosslinker to the peptide after cysteine protecting groups were selectively removed. Liquid-phase coupling was attempted with crosslinkers **1**, **3** and **4** in DMF or DMSO using DIPEA as base and showed either no reaction, or a complex mixture of products with high molecular weights, indicative of unselective crosslinking of the peptides. Coupling of the azobenzene on resin seemed to proceed well, and the desired product was a major component of the crude peptide product obtained after TFA cleavage of the peptide from the solid support; however, yields after cleavage were very low and during HPLC purification a large amount of crude material seemed to elute without giving distinguishable peaks. This leads to the conclusion that the desired products are not stable under the acidic cleavage conditions. Therefore, these two methods are not suitable for the large-scale preparation of these crosslinked peptides. Nevertheless, enough of the desired  $K_3^{i,i+4}$ -Azo product was isolated to analyse its viability as a photoswitching system.

The CD spectra of peptide  $K_3^{i,i+4}$ -Azo shows a mostly unfolded structure initially (**Figure 4.3A** and **Table 4.1**, 22% average  $\alpha$ -helicity), which is reduced by a further 4% when isomerized to the *cis* state with 375 nm light. When this peptide is combined with its binding partner  $E_3$ GW, a clear increase in signal is observed showing absorbance bands characteristic for helical structures. A significant difference is observed between the dark adapted and irradiated state, showing an increase in average  $\alpha$ -helicity from 46% to 64%, with the ratio of  $\theta_{208\text{nm}}/\theta_{222\text{nm}}$  showing distinctive coiled-coil characteristics in the *cis* state. Photoisomerization

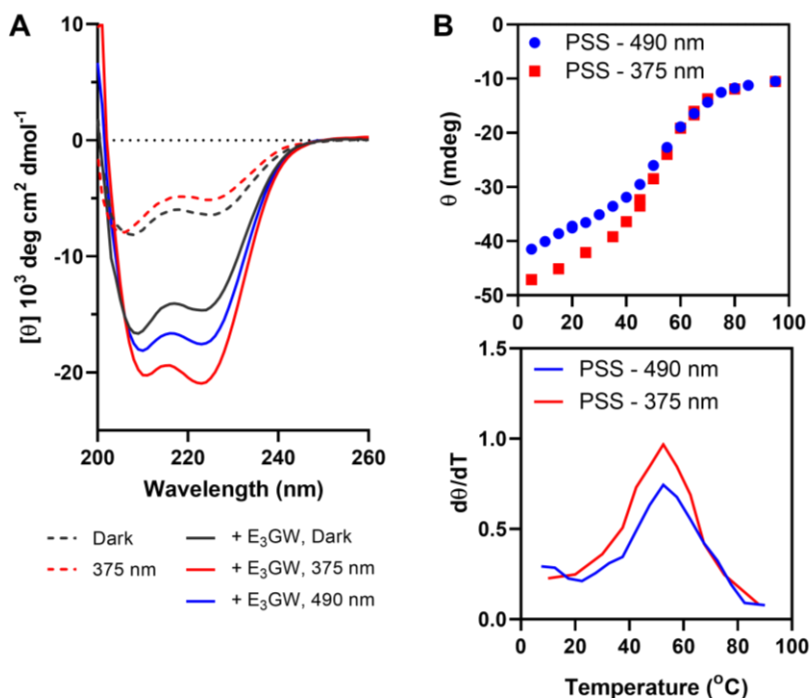


**Figure 4.3:** CD spectra showing the differences in folding for peptide  $K_3^{i,i+4}$ -Azo independently and as a coiled-coil with peptide E<sub>3</sub>GW at different photostationary states. (A) Melt curves of the coiled-coil after isomerization with either 375 nm or 490 nm light (B, top graph) and the first order derivative of these melt spectra (B, bottom graph). Spectra were recorded in PBS buffer at pH 7.4, with 50  $\mu\text{M}$  total peptide concentration.

back to the *trans* isomer can be achieved using 490 nm light, with the UV absorption of the azobenzene switching back 89% of the dark state (see **Figure S4.1**). The CD spectrum recorded after illumination with 490 nm light shows a higher degree of folding than would be expected from the combined spectra observed for the dark state and PSS at 375 nm. This suggests the coiled-coil formation of these crosslinked peptides could be partially cooperative, or contain non-dimeric intermediates that overall show a higher degree of folding than observed for the initial dark state.

Thermal denaturation experiments comparing two photostationary states (**Figure 4.3B**, **Figure S4.3**) shows the melting behaviour is only distinct in the lower temperature range. The melting point is the same for both photostationary states, indicating comparable entropic contributions to the binding affinity. Peptide  $K_3^{i,i+4}$ -Azo shows significantly better coiled-coil photoswitching than the four-heptad equivalent, with 18% difference in  $\alpha$ -helicity compared to 3% difference between the dark and light states. This difference between states is counteracted

**Table 4.1.** Molar ellipticity and helicity for the crosslinked derivatives of peptide K, as observed by CD.

Peptides	$(\theta)_{222\text{nm}}$ (deg cm <sup>2</sup> dmol <sup>-1</sup> res <sup>-1</sup> )	% $\alpha$ -helix <sup>a</sup>	$(\theta)_{222\text{nm}}/$ $(\theta)_{208\text{nm}}$
K <sub>4</sub> <sup>i,i+4</sup> -azo, dark	-4,790	17%	0.50
K <sub>4</sub> <sup>i,i+4</sup> -azo, 375nm	-16,927	50%	1.31
K <sub>4</sub> <sup>i,i+4</sup> -azo + E <sub>4</sub> GW, dark	-23,485	68%	1.15
K <sub>4</sub> <sup>i,i+4</sup> -azo + E <sub>4</sub> GW, 375nm	-24,550	71%	1.16
K <sub>4</sub> <sup>i,i+11</sup> -azo, dark	-15,211	45%	1.31
K <sub>4</sub> <sup>i,i+11</sup> -azo, 375nm	-10,572	33%	1.07
K <sub>4</sub> <sup>i,i+11</sup> -azo+ E <sub>4</sub> GW, dark	-23,116	67%	1.19
K <sub>4</sub> <sup>i,i+11</sup> -azo+ E <sub>4</sub> GW, 375nm	-23,264	68%	1.21
K <sub>3</sub> <sup>i,i+4</sup> -azo dark	-6,293	22%	0.77
K <sub>3</sub> <sup>i,i+4</sup> -azo 375nm	-4,981	18%	0.67
K <sub>3</sub> <sup>i,i+4</sup> -azo + E <sub>3</sub> GW, dark	-14,599	46%	0.88
K <sub>3</sub> <sup>i,i+4</sup> -azo + E <sub>3</sub> GW, 375nm	-21,001	64%	1.11
K <sub>3</sub> <sup>i,i+4</sup> -azo + E <sub>3</sub> GW, 490nm	-17,505	54%	1.00

<sup>a</sup> Percentage helicity was calculated from the molar ellipticity at 222 nm using Equation 2 (see materials and methods).

by a decrease in overall helicity of the irradiated state of peptide K<sub>3</sub><sup>i,i+4</sup>-Azo, which indicates total fusion rates will likely be lower for this variant. If the peptide is still effective in this application remains to be determined. For this investigation, a different peptide crosslinking protocol than the one set out in this chapter will be required, due to the low yields of the crosslinking reaction.

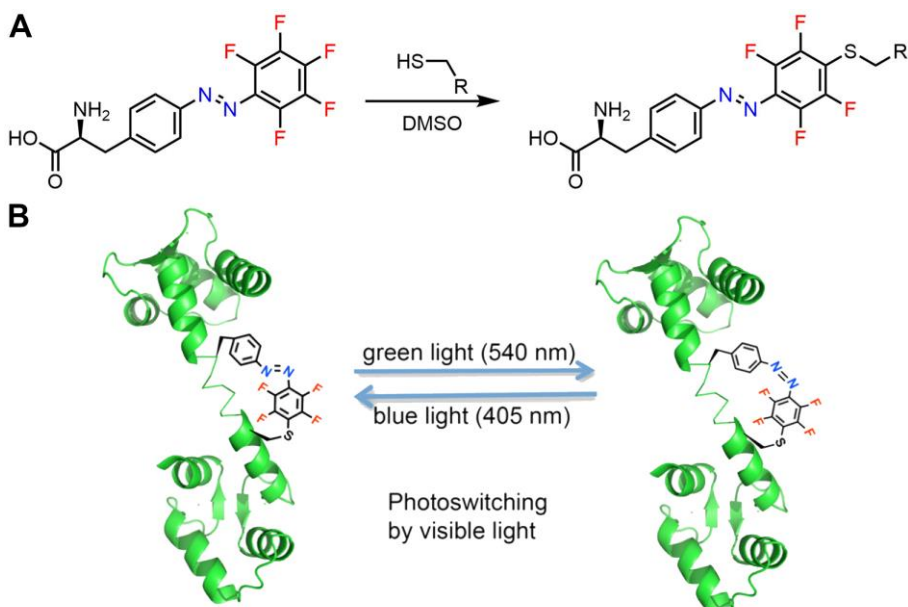
### 4.3 Conclusions and outlook

Azobenzene crosslinker **1** was successfully prepared according to literature procedures, and attempts to prepare azobenzene crosslinker **5** revealed an interesting side-reaction that produced benzimidazoles from *ortho*-(alkylamino)-anilines. Since benzimidazoles are commonly used motifs, a novel mild condition for their generation would be of synthetic interest and should therefore be pursued further.

Variants of peptide K<sub>3</sub> or K<sub>4</sub> crosslinked with **1** could be photoisomerized effectively and showed clear differences in structure either individually, for the four heptad sequences, or as a coiled-coil for the three-heptad variant. This demonstrates how binding strength affects structural control of photoswitchable crosslinkers, and shows previous optimization of cysteine spacing in single helices extends to coiled-

coil motifs.<sup>14</sup> The structural differences show the feasibility of using photocontrol over coiled-coil structure in applications that would benefit from mediation of coiled-coil binding strength.

The methods used in this chapter for the preparation of photoswitchable peptides using crosslinkers **1**, **3** or **4** are not optimal due to low yields. Other methods should therefore be explored to continue with this line of research. Specifically, the azobenzene-derivative of phenylalanine published by Hoppmann *et al.*<sup>33</sup> (**Scheme 4.4A**) would appear to be a suitable alternative. This amino acid contains a thiol-reactive pentafluorophenyl ring which is reactive to nucleophilic aromatic substitution (S<sub>N</sub>Ar) by thiols under mild conditions. Incorporation of this amino acid omits the first reaction step of bi-reactive crosslinkers such as **1**, which negates any problems related to solubility. The crosslinker of Hoppmann *et al.* showed good reactivity towards S<sub>N</sub>Ar by cysteine thiols and was successfully incorporated in the Calmodulin (CaM) protein by genetic code expansion (**Scheme 4.4B**). Photoisomerization of the azobenzene allowed control over the interactions of the crosslinked CaM protein with neuronal nitric oxide synthase, a CaM-binding protein, showing this crosslinking strategy as effective for this model system.



**Scheme 4.4:** Reaction of 4-(pentafluorophenyl)azo-L-phenylalanine with free thiols via nucleophilic aromatic substitution (A), and the application of this amino acid in the photomodulation of Calmodulin (B). Images adapted from Hoppmann *et al.*, 2015.<sup>33</sup>

If the alternative crosslinker suggested above shows the same capability of controlling coiled-coil structure as the azobenzene crosslinker tested in this chapter, it would be interesting to try generating lipidated variants of these photoswitching peptides to test the hypothesis that this strategy can be used for photocontrolled membrane fusion.

#### 4.4 Materials and Methods

Fmoc-protected amino acids were purchased from Novabiochem (Amsterdam, The Netherlands). Acetic anhydride ( $\text{Ac}_2\text{O}$ ), acetonitrile (MeCN), dimethylformamide (DMF), piperidine, pyridine, trifluoroacetic acid (TFA) and tetrahydrofuran (THF) were purchased from Biosolve (Valkenswaard, The Netherlands). Oxyma was purchased from Carl Roth (Karlsruhe, Germany). *p*-phenylenediamine, triethylamine, (diacetoxyiodo)-benzene, chloroacetyl chloride, bromoacetyl bromide, sodium iodide, *N,N'*-diisopropylcarbodiimide (DIC) and 1,2-Bis(2-mercaptoethoxy)-ethane (EODT) were purchased from Sigma Aldrich (Zwijndrecht, The Netherlands). Manganese dioxide ( $\text{MnO}_2$ ) was purchased from Alfa Aesar (Kandel, Germany). Chloroform, dichloromethane (DCM), ethyl acetate (EtOAc), ethanol and diethyl ether ( $\text{Et}_2\text{O}$ ) were supplied by Honeywell (Meppel, The Netherlands). All reagents were used as purchased. Ultrapure water was purified using a Milli-Q™ purification system from Millipore (Amsterdam, The Netherlands). NMR spectra were recorded on a Bruker AV-400 (400 MHz) or AV-300 (300 MHz) spectrometer. Chemical shift values are reported in ppm relative to the solvent signal (for  $^1\text{H}$ : DMSO  $\delta = 2.50$ , MeOH  $\delta = 3.31$ ; for  $^{13}\text{C}$ : DMSO  $\delta = 39.52$ , MeOH  $\delta = 49$ ), with multiplicity (*s* = singlet, *d* = doublet, *dd* = doublet of doublets, *t* = triplet, *q* = quartet, *m* = multiplet), coupling constants *J* (Hz) and relative integration.

**Peptide Synthesis and purification** Peptides were prepared via Fmoc-based SPPS on a 0.1 mmol scale using a Liberty Blue (CEM corporation) microwave-assisted synthesizer. Synthesis was performed using Tentagel S resin (Rapp Polymere, Tuebingen, Germany) with a loading of 0.23 mmol/g. Fmoc deprotection was performed with 20% piperidine at 87 °C for 1 minute and amino acid coupling was achieved using 5 equivalents of Fmoc-protected amino acid, DIC and Oxyma pure at 87 °C for 4 minutes. After synthesis, peptides were acetylated using  $\text{Ac}_2\text{O}$  and pyridine in DMF, and cleaved from the solid support using TFA containing 2.5% each of water, TIS and EODT as scavengers. After 90 minutes peptides were precipitated in cold  $\text{Et}_2\text{O}$ , dried under a stream of air, and lyophilized. Peptides were purified using reversed-phase HPLC on a Shimadzu system consisting of two KC-20AR pumps

and an SPD-20A or SPD-M20A detector, equipped with a Kinetix Evo C18 column. Purification was achieved using non-linear gradients from 10-90% MeCN in H<sub>2</sub>O with 0.1% TFA as buffering agent. Purity was confirmed via LC-MS on a Thermo Scientific TSQ quantum access MAX mass detector connected to an Ultimate 3000 LC system fitted with a 50x4.6 mm Phenomenex Gemini 3 μm C18 column. Pure fractions were pooled and lyophilized to yield the peptides as a dry powder.

**Azobenzene coupling** The coupling of crosslinker **1** to double-cysteine peptides was performed by first dissolving the peptides in 50% 10 mM pH 8.0 phosphate buffer/MeCN, at 500 μM peptide concentration, followed by addition of 1.5 eq. TCEP (10 mg/mL stock solution). After 30 minutes, crosslinker **1** was dissolved in DMSO (5 mg/mL), illuminated with 375nm light to isomerize the azobenzene, and 1.5 eq. of the crosslinker is added dropwise to the peptide solution. This is repeated 3 times, for a total of 4.5 eq. of crosslinker. After 2 hours the reaction is illuminated with 375 nm light for 10 minutes to isomerize the azobenzene, then left to react overnight. The reaction was stopped by treating it with 5% TFA, centrifuged to remove any solids and purified over HPLC.

**UV-Vis spectroscopy** Absorption spectra were measured on an Agilent Cary-300 spectrophotometer with a scanning speed of 600 nm/min and a switchover between the visible and ultraviolet lamp at 350 nm. Samples were measured in quartz cuvettes with a path length of 10 mm and baseline corrected using a blank sample of the same solvent used for sample preparation. During measurement, samples were kept at room temperature (20 °C) using an Agilent Cary temperature controller.

**CD Spectroscopy** Circular dichroism spectra were recorded on a JASCO J-815 spectrometer fitted with a Peltier temperature controller. Spectra were recorded in a 2 mm quartz cuvette at 20 °C, with peptides dissolved in PBS at pH 7.4 unless otherwise specified. A wavelength range from 190-260 nm was used, with 1 nm intervals and a scanning speed of 100 nm/min, with the final spectrum consisting of the average of 5 sequentially recorded spectra, and spectra were baseline corrected using individually recorded spectra of the same buffer used for sample preparation. The mean residue molar ellipticity ( $\theta$ , deg cm<sup>2</sup> dmol.res<sup>-1</sup>) was calculated according to equation 1:

$$[\theta] = (100 * [\theta]_{obs}) / (c * n * l) \quad (1)$$

With  $[\theta]_{\text{obs}}$  representing the observed ellipticity in mdeg,  $c$  the peptide concentration in mM,  $n$  the number of peptide bonds and  $l$  the path length of the cuvette in cm. The fraction of  $\alpha$ -helical peptide could be calculated from the MRE using equation 2:

$$F_{\text{helix}} = ([\theta]_{222} - [\theta]_0) / ([\theta]_{\text{max}} - [\theta]_0) \quad (2)$$

With the maximum theoretical mean residue ellipticity,  $[\theta]_{\text{max}}$ , defined as  $[\theta]_{\text{max}} = [\theta]_{\infty} (n - x) / n$  for a helix with  $n$  residues and  $x$  a number of amino acids assumed not to participate in helix formation (in this case 3).  $[\theta]_{\infty}$  is defined as the theoretical helicity of an infinite  $\alpha$ -helix and is temperature dependent, defined via  $[\theta]_{\infty} = (-44000 + 250T)$ , with  $T$  being the temperature in  $^{\circ}\text{C}$ . The minimal expected absorbance at 222 nm for a random coil is defined in  $[\theta]_0$ , which is also temperature dependent via the relationship  $[\theta]_0 = 2220 - 53T$ .

**Sample illumination** High-power single chip LEDs were purchased from Roithner Laser (Vienna, Austria) from the H2A1 series. LEDs were mounted on an aluminum back plate for heat dissipation, and powered at 350 mA current using a driver built in-house. For illumination the LED was placed parallel to the side of the cuvette at a distance of 5 mm, centered to the width and height of the sample.

### *Organic synthesis*

Synthesis of **2** was adapted from the procedure of Ma *et al.*,<sup>34</sup> and the synthesis of cross-linkers was based on previous work.<sup>19</sup>

**4,4'-Diaminoazobenzene (2):** To a solution of 3.24 g p-phenylenediamine (30 mmol) in 175 mL DCM was added (diacetoxyiodo)-benzene (9.77 g, 30.3 mmol) under vigorous stirring and an immediate colour change to amber then black was observed. After 1h, the mixture was purified by silica column chromatography. The product was eluted using a gradient of 5 to 30% EtOAc in DCM and solvent was removed under reduced pressure to yield 1.11 g (5.23 mmol, 35%) of the product as a red, micro-crystalline powder. <sup>1</sup>H NMR (400 MHz, DMSO-*d*<sub>6</sub>)  $\delta$  7.53 (d,  $J = 8.7$  Hz, 4H), 6.63 (d,  $J = 8.7$  Hz, 4H), 5.75 (s, 4H). <sup>13</sup>C NMR (101 MHz, DMSO-*d*<sub>6</sub>)  $\delta$  151.00, 143.14, 123.81, 113.4

**4,4'-Di(chloroacetamido)azobenzene (1):** Diaminoazobenzene (200 mg, 0.94 mmol) was dissolved in 10 mL dry THF and cooled to 5  $^{\circ}\text{C}$ . Triethylamine (400  $\mu\text{L}$ , 2.85 mmol) and chloroacetyl chloride (250  $\mu\text{L}$ , 3.07 mmol) were added and the reaction was stirred for 20 minutes. The reaction was diluted with 30 mL cold water,

the precipitate that formed was filtered off and washed 3 times with 20 mL water. The precipitate was removed from the filter with 150 mL hot acetone, and solvent was removed under reduced pressure to yield 298 mg (0.82 mmol, 87%) of the product as a brown coloured powder.  $^1\text{H NMR}$  (400 MHz,  $\text{DMSO-}d_6$ )  $\delta$  10.65 (s, 1H), 7.88 (d,  $J = 8.5$  Hz, 1H), 7.81 (d,  $J = 8.6$  Hz, 1H), 4.31 (s, 1H).  $^{13}\text{C NMR}$  (101 MHz,  $\text{DMSO-}d_6$ )  $\delta$  165.07, 148.00, 141.20, 123.55, 119.63.

**4,4'-Di(bromoacetamido)azobenzene (3):** Diaminoazobenzene (228 mg, 1.08 mmol) was dissolved in 15 mL dry THF and cooled to 5 °C. Triethylamine (450  $\mu\text{L}$ , 3.23 mmol) and bromoacetyl bromide (400  $\mu\text{L}$ , 4.06 mmol) in 5 mL THF were added, resulting in an immediate precipitate. The reaction was stirred for 10 minutes, followed by quenching with 20 mL 1:1 EtOH/ $\text{H}_2\text{O}$ . The precipitate was filtered off and washed 3 times with 20 mL 1:1 EtOH/ $\text{H}_2\text{O}$ . The precipitate was removed from the filter with 100 mL hot acetone, and solvent was removed under reduced pressure to yield 63 mg (0.14 mmol, 13%) of the product as a brown solid.  $^1\text{H NMR}$  (400 MHz,  $\text{DMSO-}d_6$ )  $\delta$  10.73 (s, 2H), 7.88 (d,  $J = 8.5$  Hz, 4H), 7.80 (d,  $J = 8.6$  Hz, 4H), 4.09 (s, 4H).  $^{13}\text{C NMR}$  (101 MHz,  $\text{DMSO-}d_6$ )  $\delta$  165.26, 148.00, 141.32, 123.57, 119.54, 30.38.

**4,4'-Di(iodoacetamido)azobenzene (4):** Sodium iodide (272 mg; 1.81 mmol; 7 eq.) was dissolved in a 4 mL mixture of 25 % dry THF and dry acetone. This solution was added to 60 (0.16 mmol) mg of 4,4'-di(chloroacetylamino)azobenzene and stirred under argon and protected from light for 20 hours. The reaction mixture was filtered and the solvent was evaporated under reduced pressure resulting in a brown/yellow solid. The crude product was dissolved in 2 mL of THF and cold water was added until precipitation formed. The suspension was filtered and the residue dissolved in acetone. Evaporation of the solvent yielded in 68 mg of the desired product (0.124 mmol, 70%) as a brown solid.  $^1\text{H NMR}$  (400 MHz,  $\text{DMSO-}d_6$ )  $\delta$  10.72 (d,  $J = 41.7$  Hz, 2H), 7.82 (d,  $J = 28.4$  Hz, 8H), 3.87 (s, 4H).  $^{13}\text{C NMR}$  (101 MHz,  $\text{DMSO-}d_6$ )  $\delta$  167.10, 154.14, 147.86, 123.54, 119.36, 39.52, 1.41

**N-(2,3-dihydro-1H-pyrrolo[1,2-a]benzimidazol-6-yl)acetamide (6):** In a 10 mL pressure vial, 11 mg 4-amino-3-(pyrrolidyl)phenyl-acetamide (0.05 mmol) and 45 mg  $\text{MnO}_2$  (0.52 mmol; 10 eq.) was combined with 2 mL dry DMF. The vial was sealed and the reaction mixture was stirred at 110 °C for 20 hours. After all of the amine had reacted according to TLC, the mixture was filtered over Celite and the filter washed with DMF. After the solvent was evaporated under reduced pressure, the crude product was purified by silica column chromatography which yielded 11 mg

of product **6** (quantitative yield).  $^1\text{H NMR}$  (400 MHz, MeOD- $d_4$ )  $\delta$  7.92 (d,  $J$  = 1.9 Hz, 1H), 7.47 (d,  $J$  = 8.7 Hz, 1H), 7.13 (dd,  $J$  = 8.7, 2.0 Hz, 1H), 4.14 (t,  $J$  = 7.1 Hz, 2H), 3.03 (t,  $J$  = 7.6 Hz, 2H), 2.78 – 2.69 (m, 2H), 2.15 (s, 3H).  $^{13}\text{C NMR}$  (101 MHz, MeOD- $d_4$ )  $\delta$  171.54 (s), 145.40 (s), 142.75 (s), 134.88 (s), 119.20 (s), 116.39 (s), 103.36 (s), 44.01 (s), 27.02 (s), 24.13 (s), 23.77 (s). **TOF-MS**:  $[\text{M}+\text{H}]^+$  = 216.1135; calculated  $[\text{M}+\text{H}]^+$  = 216.1059

**N-(1-ethyl-2-methyl-1H-benzo[d]imidazol-6-yl)acetamide (7)**: In a 10 ml pressure vial, 10 mg N-(4-amino-3-(diethylamino)phenyl)acetamide, 0.05 mmol, and 40 mg  $\text{MnO}_2$  (0.50 mmol, 10 eq.) were combined with 2 ml dry DMF. The vial was sealed and stirred for 20 hours at 110 °C. After all of the amine had reacted, according to TLC, the mixture was filtered over Celite and the filter was washed with DMF. After the solvent was evaporated under reduced pressure, the crude product was purified by silica column chromatography, which yielded 5 mg (0.025, 50%) of product **6**.  $^1\text{H NMR}$  (300 MHz, MeOD- $d_4$ )  $\delta$  7.97 (d,  $J$  = 1.5 Hz, 1H), 7.46 (d,  $J$  = 8.6 Hz, 1H), 7.15 (dd,  $J$  = 8.6, 1.8 Hz, 1H), 4.23 (q,  $J$  = 7.3 Hz, 2H), 2.59 (s, 3H), 2.16 (s, 3H), 1.40 (t, 3H).

## 4.6 References

1. Lapenta, F., *et al.* (2018) Coiled coil protein origami: from modular design principles towards biotechnological applications. *Chem. Soc. Rev.* 47, 3530-3542.
2. Marsden, H. R., and Kros, A. (2010) Self-Assembly of Coiled Coils in Synthetic Biology: Inspiration and Progress. *Angew. Chem. Int. Edit.* 49, 2988-3005.
3. Wu, Y. Y., and Collier, J. H. (2017) alpha-Helical coiled-coil peptide materials for biomedical applications. *WIREs Nanomed Nanobiotechnol.* 9, e1424.
4. Utterström, J., *et al.* (2021) Coiled coil-based therapeutics and drug delivery systems. *Adv. Drug Del. Rev.* 170, 26-43.
5. Marsden, H. R., Tomatsu, I., and Kros, A. (2011) Model systems for membrane fusion. *Chem. Soc. Rev.* 40, 1572-1585.
6. Robson Marsden, H., *et al.* (2013) Controlled liposome fusion mediated by SNARE protein mimics. *Biomater. Sci.* 1, 1046-1054.
7. Dublin, S. N., and Conticello, V. P. (2008) Design of a selective metal ion switch for self-assembly of peptide-based fibrils. *J. Am. Chem. Soc.* 130, 49-51.
8. Zimenkov, Y., *et al.* (2006) Rational design of a reversible pH-responsive switch for peptide self-assembly. *J. Am. Chem. Soc.* 128, 6770-6771.
9. GarciaEcheverria, C. (1996) Disruption of coiled coil formation by methionine oxidation. *Bioorg. Med. Chem. Lett.* 6, 229-232.
10. Szilak, L., Moitra, J., and Vinson, C. (1997) Design of a leucine zipper coiled coil stabilized 1.4 kcal mol<sup>-1</sup> by phosphorylation of a serine in the e position. *Protein Sci.* 6, 1273-1283.

11. Ankenbruck, N., *et al.* (2018) Optochemical Control of Biological Processes in Cells and Animals. *Angew. Chem. Int. Edit.* 57, 2768-2798.
12. Szymanski, W., *et al.* (2013) Reversible Photocontrol of Biological Systems by the Incorporation of Molecular Photoswitches. *Chem. Rev.* 113, 6114-6178.
13. Pianowski, Z. L. (2019) Recent Implementations of Molecular Photoswitches into Smart Materials and Biological Systems. *Chem. Eur. J.* 25, 5128-5144.
14. Flint, D. G., *et al.* (2002) Using an azobenzene cross-linker to either increase or decrease peptide helix content upon trans-to-cis photoisomerization. *Chem. Biol.* 9, 391-397.
15. Bandara, H. M. D., and Burdette, S. C. (2012) Photoisomerization in different classes of azobenzene. *Chem. Soc. Rev.* 41, 1809-1825.
16. Beharry, A. A., and Woolley, G. A. (2011) Azobenzene photoswitches for biomolecules. *Chem. Soc. Rev.* 40, 4422-4437.
17. Mart, R. J., and Allemann, R. K. (2016) Azobenzene photocontrol of peptides and proteins. *Chem. Commun.* 52, 12262-12277.
18. Zhu, M. Y., and Zhou, H. C. (2018) Azobenzene-based small molecular photoswitches for protein modulation. *Org. Biomol. Chem.* 16, 8434-8445.
19. Kumita, J. R., Smart, O. S., and Woolley, G. A. (2000) Photo-control of helix content in a short peptide. *P. Natl. Acad. Sci. USA* 97, 3803-3808.
20. Zhang, Z. H., *et al.* (2003) A water-soluble azobenzene cross-linker for photocontrol of peptide conformation. *Bioconjugate Chem.* 14, 824-829.
21. Sadovski, O., *et al.* (2009) Spectral Tuning of Azobenzene Photoswitches for Biological Applications. *Angew. Chem. Int. Edit.* 48, 1484-1486.
22. Chi, L., Sadovski, O., and Woolley, G. A. (2006) A blue-green absorbing cross-linker for rapid photoswitching of peptide helix content. *Bioconjugate Chem.* 17, 670-676.
23. Beharry, A. A., Sadovski, O., and Woolley, G. A. (2008) Photo-control of peptide conformation on a timescale of seconds with a conformationally constrained, blue-absorbing, photo-switchable linker. *Org. Biomol. Chem.* 6, 4323-4332.
24. Samanta, S., *et al.* (2013) Photoswitching Azo Compounds in Vivo with Red Light. *J. Am. Chem. Soc.* 135, 9777-9784.
25. Woolley, G. A., *et al.* (2006) Reversible photocontrol of DNA binding by a designed GCN4-bZIP protein. *Biochem.* 45, 6075-6084.
26. Zhang, F. Z., *et al.* (2010) Photocontrol of Coiled-Coil Proteins in Living Cells. *Angew. Chem. Int. Edit.* 49, 3943-3946.
27. Torner, J. M., and Arora, P. S. (2021) Conformational control in a photoswitchable coiled coil. *Chem. Commun.* 57, 1442-1445.
28. Yasuike, N., *et al.* (2019) Intramolecular cross-linking of proteins with azobenzene-based cross-linkers. *Method. Enzymol.* 624, 129-149.
29. Fujino, T., Arzhantsev, S. Y., and Tahara, T. (2001) Femtosecond Time-Resolved Fluorescence Study of Photoisomerization of trans-Azobenzene. *J. Phys. Chem. A* 105, 8123-8129.
30. Kubelka, J., Hofrichter, J., and Eaton, W. A. (2004) The protein folding 'speed limit'. *Curr. Opin. Chem. Biol.* 14, 76-88.

31. Robson Marsden, H., *et al.* (2009) A Reduced SNARE Model for Membrane Fusion. *Angew. Chem. Int. Edit.* 48, 2330-2333.
32. Litowski, J. R., and Hodges, R. S. (2002) Designing heterodimeric two-stranded alpha-helical coiled-coils - Effects of hydrophobicity and alpha-helical propensity on protein folding, stability, and specificity. *J. Biol. Chem.* 277, 37272-37279.
33. Hoppmann, C., *et al.* (2015) In Situ Formation of an Azo Bridge on Proteins Controllable by Visible Light. *J. Am. Chem. Soc.* 137, 11218-11221.
34. Ma, H., *et al.* (2012) Organocatalytic oxidative dehydrogenation of aromatic amines for the preparation of azobenzenes under mild conditions. *Tetrahedron Letters* 68, 8358-8366.

## Supporting Information for Chapter 4

### UV-Vis Spectra

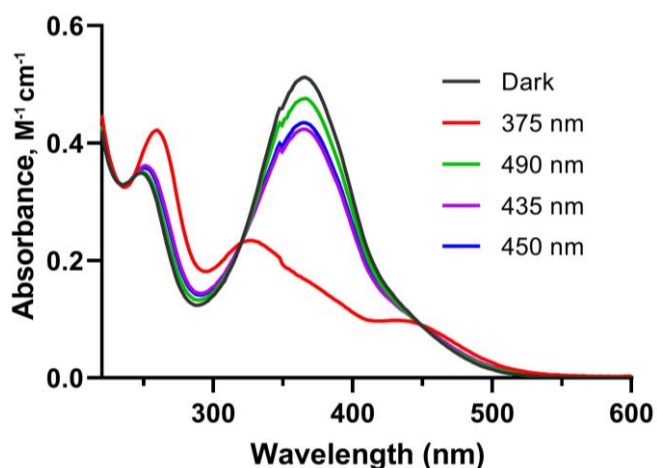


**Figure S4.1:** UV-Vis spectra at different photostationary states of peptide K<sub>3</sub><sup>i,i+4</sup>-Azo showing successful switching between *cis*-, (375 nm) and *trans*-dominant (490 nm) photostationary states. Spectra were measured at 50 μM peptide concentration in PBS buffer, pH 7.4.

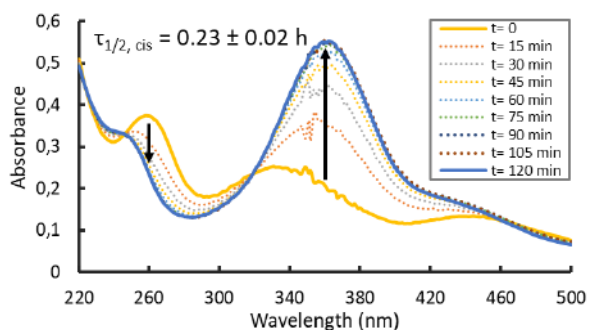


**Figure S4.2:** UV-Vis spectra showing the *cis* to *trans* relaxation of peptide K<sub>4</sub><sup>i,i+11</sup>-Azo, 35 μM in PBS, pH 7.4. The peptide solution was irradiated with 385 nm light before relaxation was measured at a constant temperature of 25 °C. Figure adapted from the Msc. Thesis of Wessel Verbeet.

## CD Spectra

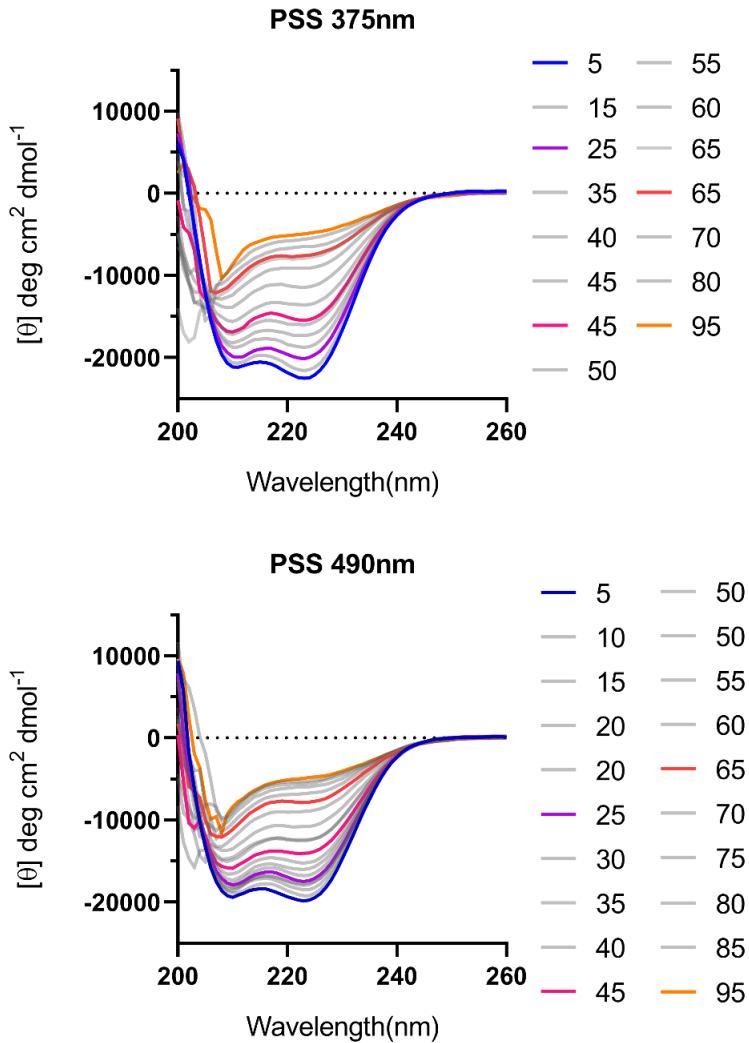


**Figure S4.3:** CD spectra at different temperatures (in °C) for the coiled-coil between peptide  $K_3^{i,i+4}$ -Azo and  $E_3$ GY at 50  $\mu$ M total peptide concentration in PBS, pH 7.4. The peptide solution was irradiated with either 375 nm (top) or 490 nm (bottom) light long enough to reach the photostationary state before each measurement.

**Table S4.1:** Deviations from the azobenzene crosslinking protocol, and the effect on reaction outcome. Crosslinked products indicate any peptide product that has increased in mass and has an absorption band around 370 nm as observed during HPLC analysis/purification. No change indicates similar results to the crosslinking method in the materials and methods section of **Chapter 4**.

<b>Conditions</b>	<b>Effect</b>
Using NH <sub>4</sub> HCO <sub>3</sub> or Tris buffer instead of phosphate	No change was observed
Changing peptide concentration (350 μM to 2 mM).	No change was observed
Varying the amount of crosslinker between 1.2 to 6 equivalents	Slight increase in the amount of crosslinked products, larger amounts prevent effective illumination of the sample.
Using 2M Guanidine as denaturant	Work-up was very difficult, no significant changes in yields
Using 40-60% of MeCN, DMSO, DMF, THF or ethanol as co-solvents	Slight increase in crosslinking, but increased difficulty in work-up, especially for DMF/DMSO.
Varying TCEP between 1 and 5 equivalents	No change was observed
Increasing temperature up to 50 °C	Reduced yields/more side products observed
Continuous addition of crosslinker 1 over 2 hours	No change was observed
Continuous illumination of sample for 2 hours	No change was observed
Using azobenzene crosslinker 3 or 4 to increase reactivity	Reduced yields / more side-products were observed.
Using Pyridine / 1-methylimidazole as catalysts	A decrease in peptide coupling was observed
Adding 1,2 eq. of cyclodextrin (α or β) to solubilize the azobenzene crosslinker	No change was observed

*LC-MS of purified peptides***Table S4.2:** Overview of the calculated masses of all peptides used in this project, and the masses found by LCMS.

Peptide name	Calculated mass (Da)	Measured mass (Da)
<b>E<sub>4</sub>GW</b>	[M + 2H <sup>+</sup> ] <sup>2+</sup> 1661.41	1660.89
	[M + 3H <sup>+</sup> ] <sup>3+</sup> 1107.94	1106.94
<b>E<sub>3</sub>GW</b>	[M + 2H <sup>+</sup> ] <sup>2+</sup> 1284.20	1284.28
	[M + 3H <sup>+</sup> ] <sup>3+</sup> 856.47	856.23
<b>K<sub>4</sub><sup>i-i+11</sup>-Azo</b>	[M + 2H <sup>+</sup> ] <sup>2+</sup> 1687.48	1686.85
	[M + 3H <sup>+</sup> ] <sup>3+</sup> 1124.65	1124.13
<b>K<sub>4</sub><sup>i-i+4</sup>-Azo</b>	[M + 2H <sup>+</sup> ] <sup>2+</sup> 1686.48	1688.11
	[M + 3H <sup>+</sup> ] <sup>3+</sup> 1124.65	1125.27
<b>K<sub>3</sub><sup>i-i+4</sup>-Azo</b>	[M + 2H <sup>+</sup> ] <sup>2+</sup> 1311.76	1309.06





---

## Azobenzene-based amino acids for photocontrol of coiled coil peptides

This chapter is in preparation as an original research paper: Niek S.A. Crone, Niek v. Hilten, Alex v.d. Ham, Aimee L. Boyle, Alexander Kros, **2021**.

## Abstract

Coiled coil peptides have been under investigation as binding motifs in synthetic biology and biomaterials, with active control over their self-assembly allowing for a wider range of applications. To introduce photocontrol in coiled-coil assembly, three azobenzene-containing amino acids were prepared and incorporated into the hydrophobic core of the heterodimeric coiled coil formed between peptide 'K<sub>3</sub>', (KIAALKE)<sub>3</sub> and peptide 'E<sub>3</sub>' (EIAALEK)<sub>3</sub>. Two amino acids (**APhe1** and **APhe2**) were based on phenylalanine, differing in the presence of a carboxylic acid group, and have previously shown to allow photomodulation of protein activity. When incorporated in peptide K<sub>3</sub>, binding to peptide E<sub>3</sub>GY changed upon *trans* to *cis* isomerization, with the two variants differing in the most folded state. The third azobenzene-containing amino acid, **APgly**, is a novel design based on phenylglycine, and showed comparable absorption bands and isomerization to the phenylalanine based amino acids. When **APgly** was incorporated in the coiled-coil, a 4.7-fold decrease in folding constant was observed upon *trans* to *cis* isomerization, the largest difference for all three amino acids. Removal of the methylene group was theorized to position the diazene closer to the hydrophobic amino acids and reduce the possible rotations of the amino acid, with molecular dynamics simulations supporting these hypotheses. Combined, these results show **APgly** as a novel photoswitchable amino acid for the photocontrol of coiled-coil assembly. The introduction of **APgly** in existing coiled-coil based biomaterials should therefore allow for control over activity related to coiled-coil formation.

## 5.1 Introduction

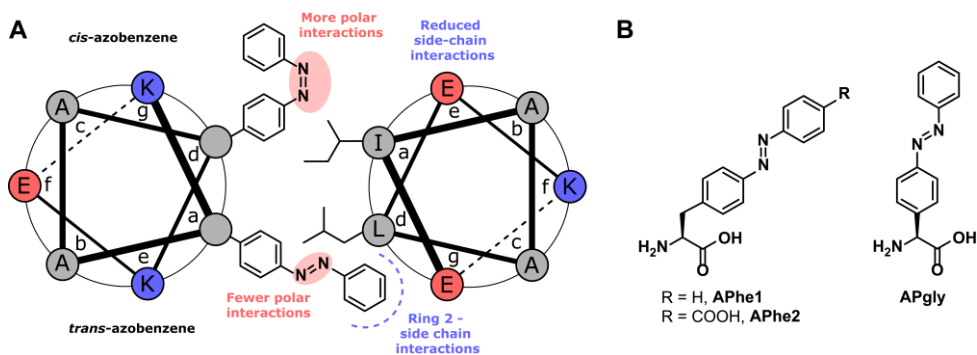
In **Chapter 4**, the photocontrol of coiled-coil peptide assembly was investigated via intramolecular cyclization using an azobenzene-based crosslinker. This cyclization-based strategy affects peptide structure by providing an energetic constraint on the length of the crosslinked region, and by design does not interact with the amino acid side chains taking part in coiled-coil formation.<sup>1</sup> Because the crosslinking strategy proved to be a major bottleneck in the preparation of photoactive peptides, alternative methods were sought. Therefore, in this chapter, the incorporation of azobenzene-based amino acids into the hydrophobic positions of coiled-coil peptides is investigated as a novel method for coiled-coil photocontrol.

Single amino acid modifications in the hydrophobic domain of coiled-coil forming peptides have been investigated both to aid understanding of coiled-coil assembly, and to introduce selectivity or functionality. For example, the group of Hodges investigated substitution at the 'a' position of a cysteine-crosslinked homotrimeric system,<sup>2</sup> and, in a separate study, the role of the 'd' position in a crosslinked homodimeric peptide.<sup>3</sup> The two positions showed a different preference for amino acids, with the general trend being that hydrophobic amino acids stabilize, and polar or charged amino acids destabilize, coiled-coil formation relative to alanine. When comparing aromatic amino acids, phenylalanine and tyrosine are well tolerated but the large double ring system of tryptophan does not provide higher stability compared to alanine. Acharya *et al.* performed single amino acid substitutions in the basic leucine zipper protein VBP, and observed changes in the Gibbs free energy of binding of up to 9.2 kcal/mol by substituting opposing amino acids in the 'a' position.<sup>4, 5</sup> Although not all possible amino acids were investigated, the same trend was observed as previously shown by the group of Hodges, and the effect remained when both chains were substituted. The role of asparagine in the hydrophobic core has also been investigated, because it is a common feature in natural coiled-coil peptides, and is useful to control peptide oligomerization although at a cost of overall stability of the coiled coil.<sup>6, 7</sup> To introduce a response to an external trigger, redox switching of methionine residues in the hydrophobic core has been investigated and results in disruption of the coiled coil,<sup>8</sup> and substitution of hydrophobic amino acids for histidine residues leads to self-assembly which is dependent on pH or metal ion coordination in a trimeric coiled-coil system.<sup>9-11</sup> This previous work on hydrophobic core modifications suggests that

the incorporation of azobenzene-based amino acids, which change structure and polarity via *cis/trans* isomerization through light illumination (see **Chapter 4**), should allow for control over coiled-coil assembly.

Phenylazo-phenylalanine (**APhe1**, **Scheme 5.1**) was one of the first published amino acids containing an azobenzene moiety,<sup>12</sup> and has been incorporated into synthetic peptides and into protein structures via genetic code expansion.<sup>13</sup> To date, **APhe1** and structural derivatives have been used to control enzyme dimerization necessary for catalytic activity,<sup>14, 15</sup> the DNA binding strength of the CAP transcription factor by destabilization of its cAMP binding site,<sup>13</sup> incorporation into superfolder green fluorescent protein,<sup>16</sup> and allosterically reducing the protein-ligand binding strength in chemiluminescent luciferase or subunit interaction in imidazole glycerol phosphate synthase.<sup>17, 18</sup> Derivatives of **APhe1** containing reactive sites for the generation of intramolecular crosslinked proteins have also been studied for control over helical folding,<sup>19, 20</sup> similar to the crosslinking strategy investigated in the previous chapter. Since its incorporation into peptides and proteins has been demonstrated to be straightforward, the potential ability of **APhe1** derivatives to control coiled-coil assembly would provide a novel method for the introduction of photoswitching into a wide variety of natural and synthetic coiled-coil systems already under investigation.<sup>21, 22</sup>

To test whether azobenzene-based amino acids can be used to control coiled-coil folding, peptides incorporating three structurally diverse non-natural amino acids were prepared by solid phase peptides synthesis (SPPS). Two of the amino acids were derived from L-phenylalanine, namely **APhe1** and **APhe2**, and these differ in



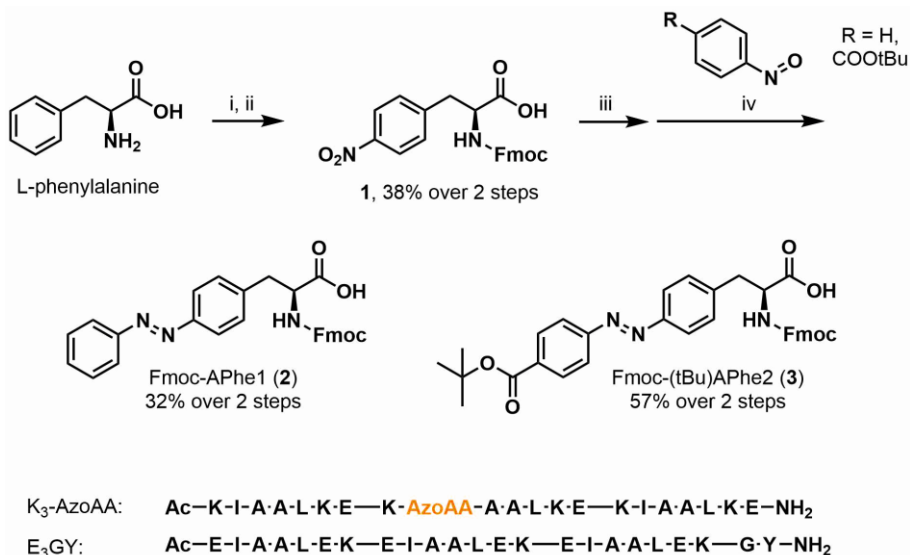
**Scheme 5.1:** Hypothesized interactions of azobenzene in the coiled-coil hydrophobic core (A), and the three azobenzene based amino acids investigated in this chapter for the control over coiled-coil self-assembly (B).

the presence of a carboxylic acid group *para* to the diazene group for **APhe2** (**Scheme 5.1B**). The carboxylic acid present in **APhe2** is theorized to introduce electrostatic repulsion with the opposing glutamic acid residue, destabilizing the coiled coil when the azobenzene is in the *trans* conformation. Switching electrostatic interactions has been investigated previously via enzymatic serine phosphorylation,<sup>23</sup> and allowed both stronger and weaker interactions after phosphorylation depending on the design.<sup>24</sup> Besides azobenzene derivatives of L-phenylalanine, the azobenzene derivative of L-phenylglycine was prepared (**APgly**, **Scheme 5.1B**), with the expectation that this amino acid would result in a better incorporation in the hydrophobic core compared to **APhe1** due to the absence of a methylene group. The three azobenzene-based amino acids were incorporated into a dimeric coiled-coil which is used in our group as a SNARE protein mimic.<sup>25</sup> This coiled-coil system consists of peptide 'K<sub>3</sub>', (KIAALKE)<sub>3</sub> and peptide 'E<sub>3</sub>' (EIAALEK)<sub>3</sub>, which self-assemble into a dimeric parallel coiled-coil with high binding affinity.<sup>26</sup> After incorporation in peptide K<sub>3</sub>, **APgly** showed the largest difference in coiled-coil binding upon *trans* to *cis* isomerization, with a 4.65 fold decrease in the folding constant. Molecular dynamics (MD) simulations of **APhe1** and **APgly** in the coiled coil show more rearrangement of the **APhe1** azobenzene after isomerization, and support **APgly** as a better switch for coiled-coil photocontrol.

## 5.2 Results and Discussion

### *Peptides containing azobenzene derivatives of phenylalanine.*

Photoswitchable amino acids based on phenylalanine were prepared following literature procedures (**Scheme 5.2**),<sup>14</sup> with the 9-fluorenylmethoxy-carbonyl (Fmoc) protecting group on the  $\alpha$ -amine to facilitate use in SPPS. Fmoc-4-nitro-L-phenylalanine, **1**, was prepared from L-phenylalanine via nitration and Fmoc-protection, or was purchased commercially. Subsequently the nitro group of **1** was reduced to the respective aniline with Zn powder and ammonium chloride, followed by a Mills reaction with nitrosobenzene to yield N <sup>$\alpha$</sup> -fmoc-4-(phenylazo)-L-phenylalanine, **2**. The same procedure was followed for the preparation of protected **APhe2**, utilizing *tert*-butyl-4-nitrosobenzoate in the Mills reaction resulting in product **3**. The *tert*-butyl ester is used to prevent side reactions during SPPS, and is removed by the acidic peptide cleavage conditions to yield the carboxylic acid. Derivatives of peptide K<sub>3</sub> (sequence shown in **Scheme 5.2**) were prepared via SPPS, with the isoleucine at position 9 replaced with **APhe1** or **APhe2**.



**Scheme 5.2:** Reaction scheme for the preparation of azobenzene containing amino acids based on phenylalanine (top) and amino acid sequences of peptides prepared in this chapter (bottom). AzoAA refers to APhe1, APhe2 or APgly. Reagents and conditions: (i)  $\text{HNO}_3, \text{H}_2\text{SO}_4$ ; (ii) Fmoc-chloride,  $\text{NaHCO}_3$ ; (iii) Zn powder,  $\text{NH}_4\text{Cl}, \text{EtOH}$ ; (iv)  $\text{AcOH}$ .

The UV absorption spectra of the two peptides were very similar (**Figure 5.1A**), with a slight redshift for the absorption bands of **APhe2** (335 nm,  $\epsilon = 9,480 \text{ M}^{-1} \text{ cm}^{-1}$ ) compared to **APhe1** (327 nm,  $\epsilon = 10,020 \text{ M}^{-1} \text{ cm}^{-1}$ ). Both amino acids could be isomerized to the *cis* conformation with 340 nm light, as observed by the disappearance over time of the strong absorption peak (**Figure S5.1**). *Cis* to *trans* isomerization from the 340 nm photostationary state (PSS) could be achieved efficiently with 435 nm light (**Figure 5.1B**). After plotting the change in intensity of the absorption maximum in the dark-adapted state, a larger difference after 340 nm irradiation is observed for **APhe1**, indicating this amino acid is isomerized to the *cis* conformation more completely by 340 nm light, or the *cis* conformer of **APhe2** has a stronger absorption band (**Figure 5.1C**). Back isomerization from *cis* to *trans* with 435 nm light is slightly more efficient for **APhe2**, resulting in 98% of the absorption maximum observed in the dark state, compared to 92% for **APhe1**.

The structure of the  $\text{K}_3$  peptides and coiled coils was studied via CD spectroscopy to determine the effect of phenylalanine-based photoswitches on peptide folding. Peptide  $\text{E}_3\text{GY}$  was used as binding partner, since the tyrosine can be used to accurately determine peptide concentration. Both  **$\text{K}_3\text{-APhe1}$**  and  **$\text{K}_3\text{-APhe2}$**  peptides were mostly unstructured by themselves, and able to form coiled coils in

combination with E<sub>3</sub>GY (Figure 5.2), with only marginal differences in structure between the dark adapted and 340 nm irradiated states. Because no obvious differences in structure were observed after irradiation, thermal denaturation experiments were performed to determine whether the binding affinity was dependent on sample irradiation. For this, CD melting curves measured at different concentrations were fitted to a coiled-coil binding model (Figure S5.2 and Figure S5.3).<sup>27</sup> The best fit was achieved for a dimeric coiled coil over other oligomeric states, and important parameters from this fitting are shown in Table 5.1.

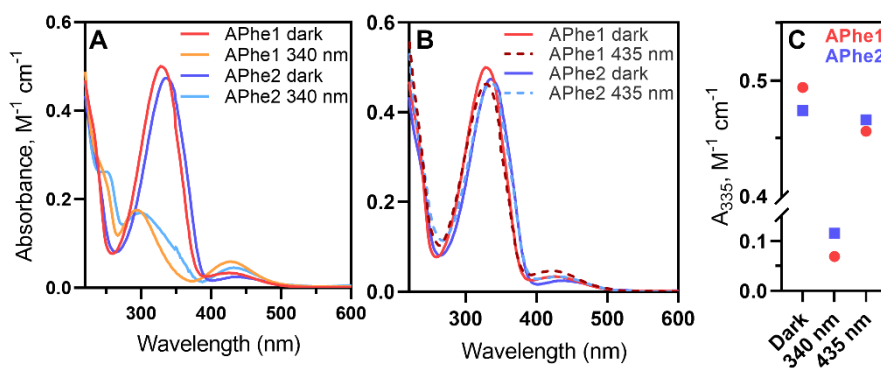


**Figure 5.1:** UV spectra of peptide K<sub>3</sub> with position 9 changed for APhe1 or APhe2, showing spectra for the dark-adapted peptide and after *trans* to *cis* isomerization with 340 nm light (A). Spectra after *cis* to *trans* isomerization using 435 nm light (B), and an overview of the absorbance at 335 nm for the dark adapted, 340 nm PSS and 435 nm PSS (C). [Peptide] = 50 μM in PBS buffer.

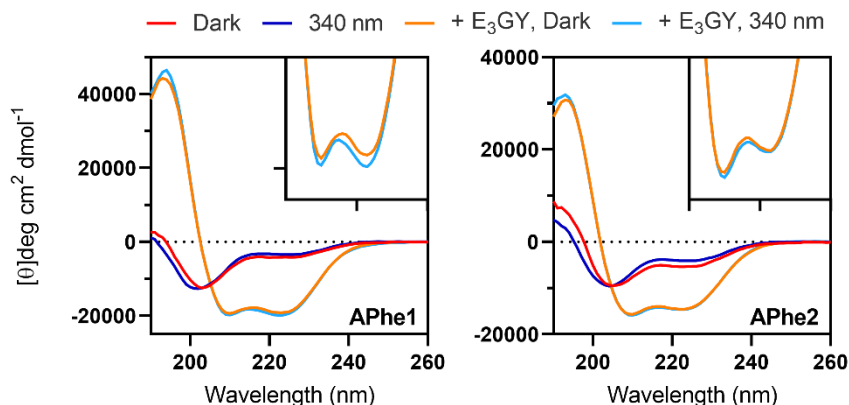


**Figure 5.2:** CD spectra of peptide K<sub>3</sub> with the 9<sup>th</sup> amino acid changed for APhe1 or APhe2, showing both the dark adapted and 340 nm irradiated states, as well as spectra with and without binding partner E<sub>3</sub>GY. All samples were measured in 10 mM phosphate containing 2 mM NaCl, with [peptide] = 50 μM.

**Table 5.1:** Fit results of CD thermal unfolding curves from **APhe1**-, or **APhe2**-containing  $K_3$  as a coiled-coil with  $E_3GY$ . A complete list of fitting parameters and confidence intervals can be found in **Table S5.1**.

Parameter	$K_3$ - <b>APhe1</b> Dark	$K_3$ - <b>APhe1</b> 340nm	$K_3$ - <b>APhe2</b> dark	$K_3$ - <b>APhe2</b> 340nm
$\Delta H^{\circ a}$ (kJ mol <sup>-1</sup> )	224.7	261.4	175.0	259.0
$T^{\circ a}$ (°C)	123	114.1	142.5	102.1
$\Delta C_p^b$ (kJ mol <sup>-1</sup> K <sup>-1</sup> )	1.69	2.46	1.07	2.65
$K_f$ (M <sup>-1</sup> ) <sup>c</sup>	9.19 10 <sup>5</sup>	7.09 10 <sup>5</sup>	2.18 10 <sup>5</sup>	3.26 10 <sup>5</sup>
$K_u$ (μM) <sup>c</sup>	<b>1.09</b>	<b>1.41</b>	<b>4.58</b>	<b>3.07</b>
Dark/340nm PSS		1.30		0.67

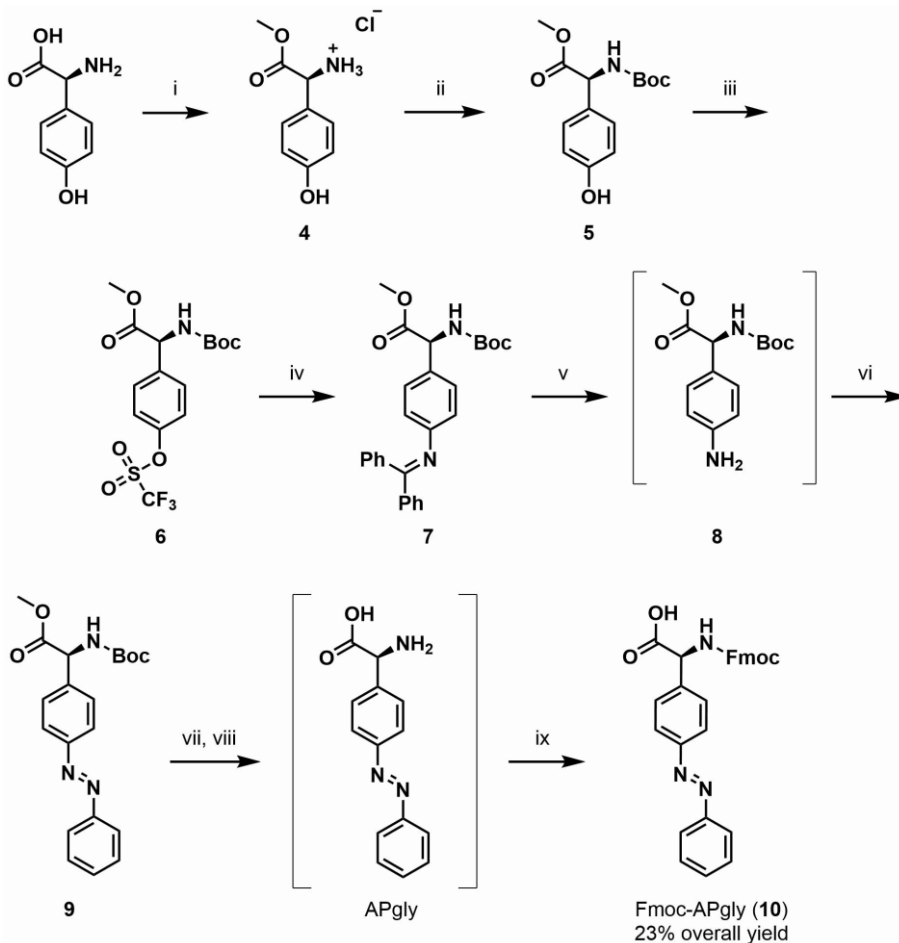
<sup>a</sup>  $\Delta H^{\circ}$  and  $T^{\circ}$  are the enthalpy and the temperature where  $\Delta G = 0$  and  $K_U = K_F = 1$ . <sup>b</sup>  $\Delta C_p$  is the change in heat capacity upon unfolding. <sup>c</sup> Binding model at 20 (°C).

Photoisomerization of  $K_3$ -**APhe1** using 340 nm light resulted in an increase in the unfolding constant  $K_u$ , from 1.09 to 1.41 μM, showing reduced coiled-coil binding in the irradiated state. The opposite was observed for  $K_3$ -**APhe2**, where irradiation yielded a reduction in  $K_u$  from 4.58 to 3.07 μM, revealing the 340 nm irradiated state to contain the most stable coiled-coil. The carboxylic acid group in **APhe2** is intended to increase electrostatic repulsion with glutamic acid residues of  $E_3$  in the *trans* conformation, resulting in the *cis* conformation as the most stable coiled-coil. Contrary to our expectations, the *cis* isomer of  $K_3$ -**APhe1** was not the most stable state, showing that the bulk of the *trans* azobenzene moiety is better accommodated in the hydrophobic positions of the coiled-coil, than the increased polarity of the diazene in the *cis* conformation. In summary, incorporation of **APhe1** and **APhe2** in the coiled-coil hydrophobic core was successful, but the design of these amino acids needs to be improved since the difference in coiled-coil formation between the dark state and 340 nm PSS was small.

Given the small differences observed for the peptides modified with azo derivatives of phenylalanine, a different amino acid structure was designed. Removal of the methylene group from **APhe1** results in a phenylglycine derivative that was theorized to position the diazene closer to the side chain of hydrophobic amino acids in the 'a' and 'd' positions, and increase the effect of photoisomerization. Amino acid 4-(azophenyl)phenylglycine (**APgly**, **Scheme 5.1**) was chosen to test this theory due to its structural simplicity.

*Synthesis and peptide incorporation of 4-(Azophenyl)phenylglycine*

Synthesis of N-fmoc-4-(phenylazo)-L-phenylglycine (Fmoc-APgly, **10**, Scheme 5.3) follows the same general route as the synthesis of azobenzene derivatives of phenylalanine; preparation of the *para*-substituted aniline followed by a Mills reaction with nitrosobenzene to yield the azobenzene. Preparation of the aniline requires an alternative method, since nitration of phenylglycine does not yield the *para*-nitrated product, and preparation of the 4-nitro variant via a Strecker



**Scheme 5.3:** Synthetic scheme for the preparation of Fmoc-APgly from 4-hydroxyphenylglycine. Reagents and conditions: (i) MeOH,  $\text{SOCl}_2$ , 0 °C to RT, 95%; (ii)  $\text{Boc}_2\text{O}$ , TEA, MeCN, 93%; (iii)  $\text{Tf}_2\text{O}$ , TEA, DCM, -20 °C to RT, 98% (88% from 5); (iv) Benzophenone imine, *rac*-BINAP,  $\text{Pd}(\text{OAc})_2$ ,  $\text{Cs}_2\text{CO}_3$ , PhMe, 100 °C, 65%; (v)  $\text{NH}_4\text{HCO}_2$ , 10% Pd/C, MeOH, 60 °C; (iv) Nitrosobenzene, AcOH, 74% over 2 steps; (vii) LiOH,  $\text{H}_2\text{O}/\text{THF}$ ; (viii) TFA, DCM; (ix) Fmoc-chloride,  $\text{NaHCO}_3$ ,  $\text{H}_2\text{O}/\text{THF}$ , 63% over 3 steps.

synthesis is not effective.<sup>28</sup> Therefore, amination of the respective aryl triflate (**6**) was deemed the most effective route, since the 4-hydroxy precursor is readily available. This route was tried and ultimately effective in the amination of **6** in sufficient quantities, from which **10** could be prepared following the procedure described below.

Methylation of 4-hydroxy-L-phenylglycine to form ester **4** was followed by amine protection with Boc anhydride to yield the double protected amino acid **5**, followed by installation of the aryl triflate to form intermediate **6** in high yields. Initially the use of zinc trimethylsilylamide as an ammonia equivalent was attempted in the palladium-catalysed amination of **6**,<sup>29</sup> but the use of benzophenone imine proved much more effective, producing intermediate **7** in 65% yield.<sup>30</sup> The imine was then reduced to yield aniline **8**, followed directly by the Mills reaction to form azobenzene **9**. Ester hydrolysis and Boc deprotection yielded APgly, which was Fmoc-protected to yield product **10**. The final three steps could be performed in good (63%) overall yield, however attempts to simplify the procedure in the form of a one-pot procedure resulted in a sharp reduction in product yield. The overall yield of **10** from 4-hydroxy-L-phenylglycine is good (23% over 9 steps), yet the atom efficiency could be improved as most steps concern protecting group manipulation. Since only mildly basic conditions are used for the conversion of **5** to **9**, for the larger scale synthesis of **10** the amination of Fmoc-protected phenylglycine-4-triflate would be worth investigating, as it would eliminate 4 synthetic steps.

As azobenzene photoswitches based on phenylglycine have not been reported, the photoswitching behaviour of Fmoc-APgly (**10**) was analysed, as displayed in **Figure 5.3**. High-pressure liquid chromatography (HPLC) separation of **10** dissolved in MeCN and kept under dark conditions, showed predominantly the *trans* (94.2 ± 0.2%) isomer, which switches to predominantly *cis* (91.3 ± 0.6%) when irradiated with 340 nm light (**Figure 5.3C**). The largest proportion of *trans* to *cis* isomers achieved via photoisomerization was after irradiation with 385 nm light (83.2 ± 0.2% *trans*), although higher wavelengths showed very similar distributions. No difference was observed in the proportions of isomers when **10** was directly illuminated with 435 nm light, or first isomerized to be *cis*-dominant with 340 nm light followed by illumination with 435 nm light, as is expected for the PSS. Relaxation after irradiation with 340 nm light was tracked over time (**Figure 5.3B**), and showed proportional decline of the *cis* isomer and increase in *trans* isomer,

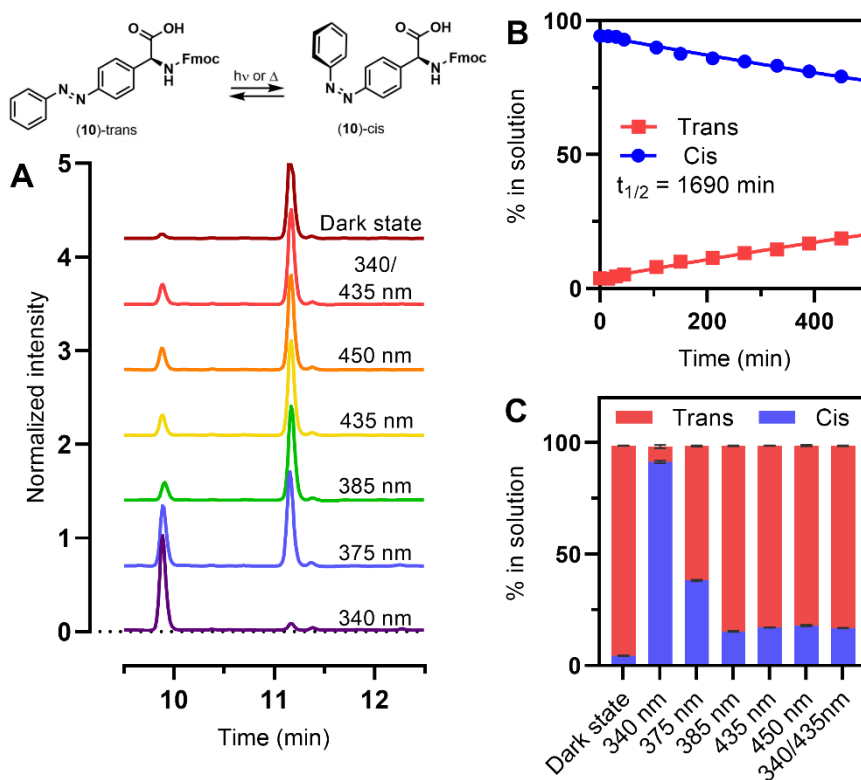


**Figure 5.3:** HPLC traces of Fmoc-APgly, showing the chromatogram of the compound after irradiation with different wavelengths of light (A), thermal relaxation back from *cis* to *trans* (B), and the percentage of the *trans* and *cis* isomers in solution at the different photostationary states (C). All illuminations and relaxation studies were performed in MeCN at 20 °C.

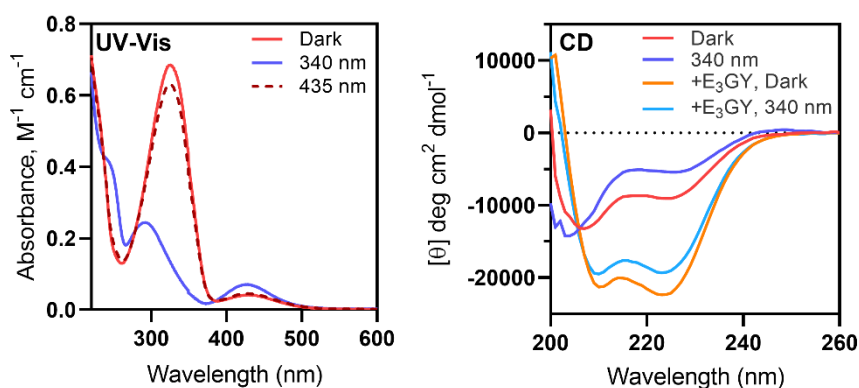


**Figure 5.4:** UV-Vis (left) and CD (right) spectra of peptide  $K_3$ -APgly during photoswitching. Spectra are recorded with samples that were dark adapted, or irradiated with light until no changes could be observed. Spectra were recorded at 20 °C in PBS with [peptide] = 50  $\mu M$ .

**Table 5.2:** Fit results of CD thermal unfolding curves from **K<sub>3</sub>-APgly** as a coiled-coil with E<sub>3</sub>GY. A complete list of fitting parameters and confidence intervals can be found in **Table S5.2**.

Coiled-coil system	K <sub>3</sub> -APgly dark	K <sub>3</sub> -APgly 340nm
$\Delta H^{\circ a}$ (kJ mol <sup>-1</sup> )	285.2	236
T <sup>ob</sup> (°C)	113.0	110.5
$\Delta C_p$ (kJ mol <sup>-1</sup> K <sup>-1</sup> )	2.80	2.15
K <sub>f</sub> (M <sup>-1</sup> ) <sup>c</sup>	1.38 x 10 <sup>6</sup>	2.97 x 10 <sup>5</sup>
K <sub>u</sub> (μM) <sup>c</sup>	<b>0.72</b>	<b>3.37</b>
<b>Dark/340nm PSS</b>		4.65

<sup>a</sup>  $\Delta H^{\circ}$  and T<sup>o</sup> are the enthalpy and the temperature where  $\Delta G = 0$  and  $K_u = K_f = 1$ . <sup>b</sup>  $\Delta C_p$  is the change in heat capacity upon unfolding. <sup>c</sup> Binding model at 20 (°C).

with a half-life of 1690 minutes ( $\approx$  28 h), comparable to reported half-lives for **APhe1** (1600 min) and **APhe2** (2100 min).<sup>14</sup> Incorporation of **10** in K<sub>3</sub> was achieved using normal Fmoc-SPPS methods. UV-Vis Spectra of **K<sub>3</sub>-APgly** in PBS showed a strong absorbance band at 325 nm (**Figure 5.4**,  $\epsilon = 13,700 \text{ M}^{-1} \text{ cm}^{-1}$ ) that disappeared upon irradiation with 340 nm light, demonstrating *trans* to *cis* isomerization, accompanied by an increase in the absorbance at 428 nm. Irradiation of the sample with 435 nm light resulted in 92% of the dark absorbance at 325 nm, showing effective *cis* to *trans* isomerization. The observed absorbance values in UV-Vis are in agreement with the isomeric ratios observed with HPLC (**Figure 5.3A**), demonstrating that **APgly** incorporation in peptides does not affect isomerization. CD spectra of **K<sub>3</sub>-APgly** showed a partially folded helix in the dark, that becomes less structured when irradiated with 340 nm light. Addition of binding partner E<sub>3</sub>GY led to a well-folded coiled-coil, that also showed a reduction in signal upon isomerization. The difference in folding between dark adapted and irradiated samples is much larger for peptide K<sub>3</sub> containing **APgly**, than it was for either of the phenylalanine derivatives, showing that the azobenzene is better positioned for coiled-coil photocontrol in the **APgly** derivative. The effect of isomerization on coiled-coil binding strength was again determined using thermal denaturation titration experiments (**Figure S5.4**), with fitting parameters shown in **Table 5.2** and **Table S5.2**. The coiled-coil formed by **K<sub>3</sub>-APgly** and E<sub>3</sub>GY was determined to have a K<sub>u</sub> of 0.72 μM in the dark, which increased to 3.37 μM after photoisomerization. This equates to a 4.65-fold reduction in binding affinity for **K<sub>3</sub>-APgly** by isomerization of the azobenzene to the *cis* dominant state.

The difference between the dark and 340 nm adapted state is larger for **K<sub>3</sub>-APgly** than was observed for either of the peptides that incorporated the phenylalanine derivatives, and the overall highest folding constant was also observed for this peptide. When comparing **APgly** isomerization to amino acid substitution at position 'a' studied by the group of Hodges,<sup>2</sup> the change in binding energy is similar to substitution of alanine by a polar (Ser) or basic (Lys) side chain.

For the potential application of **K<sub>3</sub>-APgly** in an active (fusion) system, stability of the photoswitch to repeated light exposures (photocycling) is an important characteristic. A solution of **K<sub>3</sub>-APgly** was illuminated repeatedly first with 340 nm, followed by 435 nm light, and the switching monitored via the UV absorbance band at 325 nm (**Figure 5.5** and **Figure S5.5**). The azobenzene consistently yielded the same absorption maxima during 6 cycles, demonstrating cycling of photostationary states with minimal deviation. Finally, the peptide was irradiated to the 340 nm PSS and allowed to thermally relax, showing 65% recovery in 69 hours. This thermal relaxation is 1.6 times slower ( $t_{1/2} = 46\text{h}$ ) than observed for **10** in MeCN, which can be explained by the increased dielectric constant of the solvent.<sup>31</sup>

### Molecular simulations

In the previous experiments we have shown that incorporation of an azobenzene amino acid in the hydrophobic core of the **K<sub>3</sub>/E<sub>3</sub>** coiled-coil yields more effective

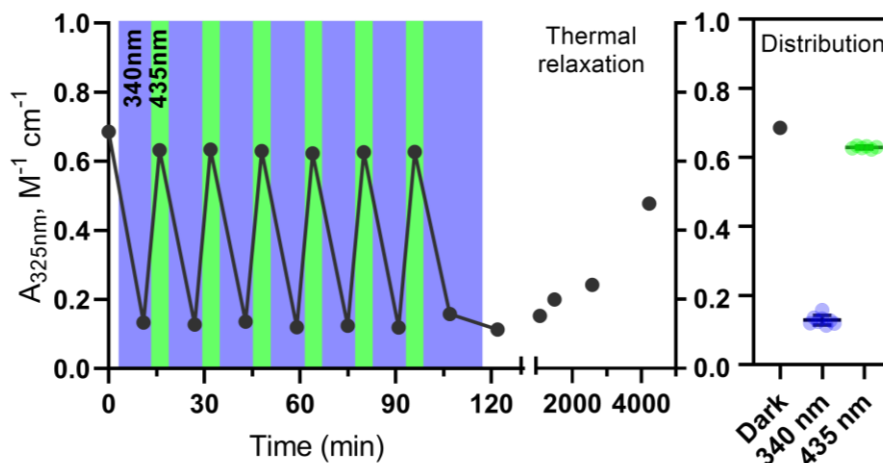


**Figure 5.5:** Photocycling of **K<sub>3</sub>-APgly** between the dark adapted, 340 nm and 435 nm PSS (left), thermal relaxation of the peptide after thermal cycling (middle) and distribution of the absorbance in the different states during cycling (right). Absorbance at 325nm is plotted (full spectra are displayed in **Figure S5.5**), measurements were performed at 20 °C in PBS with [Peptide] = 50 μM.

photoswitching when it is derived from phenylglycine then from phenylalanine. To understand how one methylene group affects azobenzene interactions, molecular models of **K<sub>3</sub>-APgly** and **K<sub>3</sub>-APhe1** were prepared. These models were based on the NMR structure of the K<sub>3</sub>/E<sub>3</sub> coiled-coil,<sup>32</sup> but with the Ile residue at position 9 replaced by a geometry optimized model of the synthetic amino acids in the *cis* or *trans* conformations. 500 ns MD simulations of these initial helical models were performed, with all 4 peptides showing a mostly stable helical coiled-coil structure during the simulations (**Figure S5.6**), although some unfolding at the termini was observed.

Snapshots from these MD simulations, displaying the azobenzene-amino acid and all side chains of peptide E<sub>3</sub> within 5 Å of that residue are shown in **Figure 5.6**. For both peptides, the azobenzene is shown to be close to the hydrophobic amino acids (Leu5, Ile9, Leu12) in the 'a' and 'd' positions, as well as adjacent amino acids (Ala4, Glu8) in the 'g' and 'c' positions. Both azobenzene amino acids extend outside of hydrophobic core, therefore shielding of the azobenzene outer phenyl group (as viewed from the backbone, and referred to as 'Ring 2') from the surrounding water by amino-acid side chains will have an impact on coiled-coil stability. The snapshot of *cis* **K<sub>3</sub>-APgly** places the diazo group in the same position as in the *trans* conformation, with ring 2 rotated towards peptide K. The opposite is observed in the snapshots of **K<sub>3</sub>-APhe1**, where the diazene group is in a different position relative to K<sub>3</sub> and ring 2 is still able to interact with amino acids in peptide E<sub>3</sub>.

Because snapshots are not representative of the entire simulations, the average change in distance between the azobenzene and the amino acids of E<sub>3</sub> over all simulations was determined (**Figure 5.7** and **Figure S5.8**). Distance changes to the diazene, ring 1 and ring 2 were plotted separately, since different interactions are expected for these groups. Both the diazene and ring 2 of **APhe1** show a negative distance change for amino acids close to the C-terminus, indicating closer positioning to those groups in the *cis* conformation, which changes to positive values when moving through the sequence. A normalized change in distance  $\leq -0.2$  or  $\geq 0.2$  was deemed 'significant' in order to compare the different groups and photoswitches. More significant distance changes are observed for ring 2, which is expected since it is further away from the isomerized diazene, and therefore any rotation is amplified. All amino acids in the 'a', 'c', 'd' and 'g' positions of E<sub>3</sub> show significant changes in distance to **APhe1**, with the other three positions also showing some significant changes. The apparent crossover point observed in the

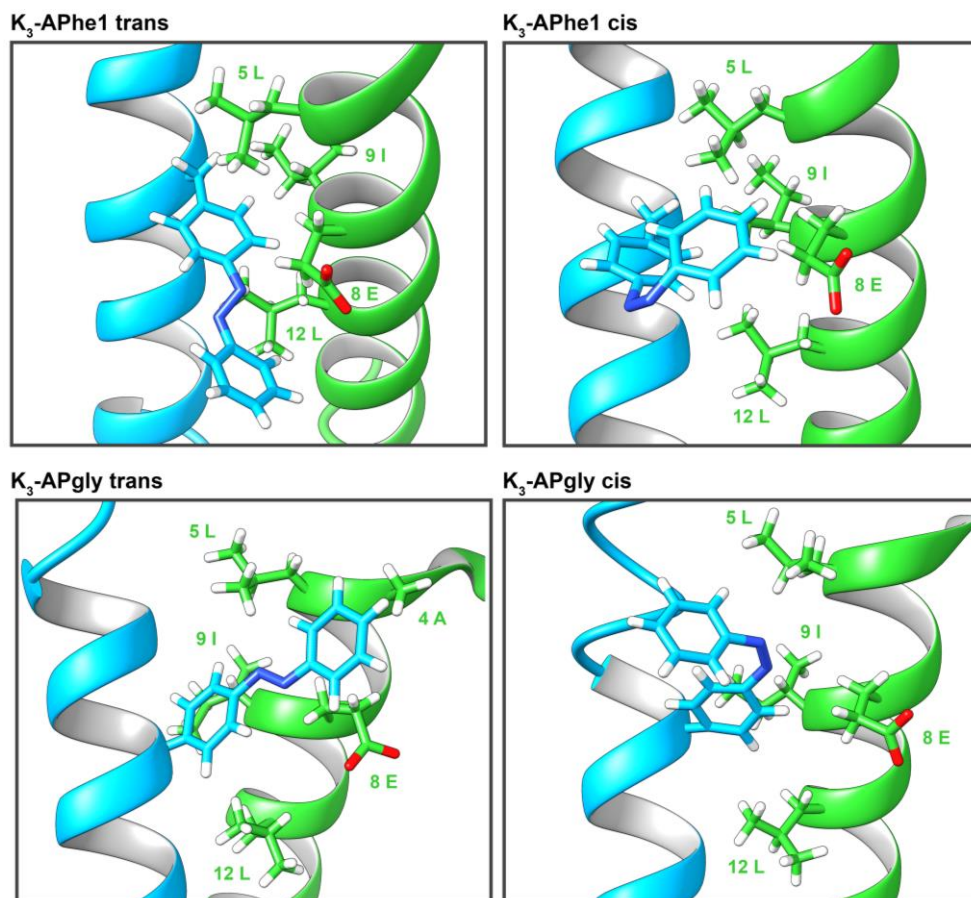


**Figure 5.6:** Snapshot from MD simulations of the coiled coil between peptide K<sub>3</sub> (blue) and E<sub>3</sub> (green), with peptide K<sub>3</sub> containing the photoswitchable amino acid **APhe1** or **APgly** in the *trans* or *cis* conformation. Peptides backbones are shown as a cartoon, with the photoswitch and all amino acid side chains of peptide E<sub>3</sub> within 5 Å displayed as sticks. Representative snapshots were chosen based on a similar RMSD from an ideal helix. Complete images are shown in **Figure S5.7**.

distance change graphs, combined with significant changes in distance upon **APhe1** isomerization for nearly all amino acids suggests reorganization after isomerization, where the azobenzene can move to a different conformation to accommodate the *cis* isomer. This is supported by the distance change for ring 1 (**Figure S5.8**), which shows the same general distribution of distance change throughout the sequence.

Peptide **K<sub>3</sub>-APgly** shows the largest change in distance for Leu side chains in the 'd' position of the heptad repeat sequence of E<sub>3</sub>, and to the Glu side chain at position 8. There are more distinct changes in distance to side chains in the 'a' and 'c' positions,

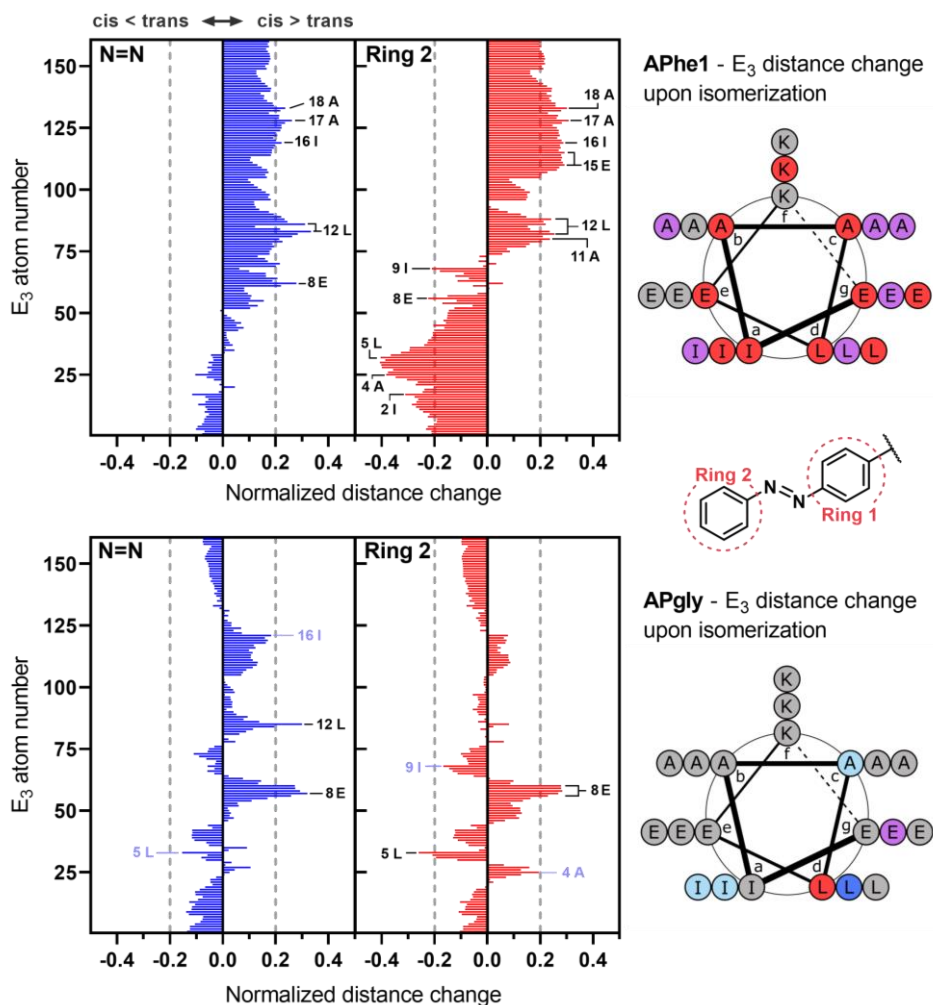


**Figure 5.7:** Normalized change in distance upon photoisomerization between the non-hydrogen atoms in peptide E<sub>3</sub> and the azobenzene diazene or ring 2 (left) during MD simulations, and helical wheel diagrams of peptide E<sub>3</sub> indicating the positions of the amino acids with significant changes in distance (right). Change in distance upon *trans* to *cis* isomerization of the azobenzene is normalized to the *trans* simulations, with positive values indicating more distance in the *cis* simulations. Distances are averaged over 3 simulations of 500 ns. Dotted lines indicate an arbitrary cut-off for significance of 0.2, with amino acids of interest marked light blue if their value falls below this line. Amino acids in the helical wheel diagram are coloured to indicate significant differences to the diazo group (blue), ring 2 (red), or both (purple), with amino acids of interest which fall below the cut-off also coloured light blue.

but these fall outside of the significance threshold that we use for comparison and have been marked with a lighter colour in **Figure 5.7**. Isomerization to *cis* is expected to result in repulsion of the diazene by hydrophobic side chains, which is

observed in the increased distance for Leu12 and Glu8, which are directly opposite the azobenzene in the coiled coil. After isomerization, ring 2 of **APgly** shows positioning close to amino acid side chains of  $K_3$  (**Figure S5.9**), which stabilizes the *cis* conformation. Overall, the photoswitch of **K<sub>3</sub>-APgly** shows changes in distance with the amino acids that are already closely positioned in the *trans* conformation, indicating the changes in distance can be attributed to the rotation around the diazene bond after isomerization.

If we generalize the structures in the MD snapshots with the changes in distance shown in **Figure 5.7**, the effect of isomerization on the coiled-coil folding constant observed in the previous section can be explained. Upon *trans* to *cis* isomerization, the diazene group becomes more polar resulting in unfavourable interactions if it is positioned in the hydrophobic core, and with both azobenzene amino acids, a general increase in distance to the diazene is observed. **APhe1** has two bonds between  $C_\alpha$  and the azobenzene moiety, which allows for more degrees of freedom to reposition the azobenzene after isomerization compared to **APgly**, which can only change position via a single rotation and deviation from the optimal bond angles. The extra rotational freedom in **APhe1** results in a decreased effect of the diazene polarity on coiled-coil stability through repositioning of the azobenzene. This repositioning also allows ring 2 to keep interacting with (different) hydrophobic side chains from peptide  $E_3$ , which is not possible for **K<sub>3</sub>-APgly**. Both of these factors decrease the differences in binding strength between the two isomeric states of **APhe1**, and explain why **APgly** shows the largest difference in coiled-coil binding upon isomerization.

### 5.3 Conclusions

Two azobenzene derivatives of phenylalanine, **APhe1** and **APhe2**, were prepared and incorporated into the hydrophobic core of Peptide  $K_3$ . Both peptides showed good photoswitching behaviour, but azobenzene isomerization had only a moderate effect on coiled-coil interactions with binding partner  $E_3GY$ . The 340 nm irradiated (*cis* dominant) state of **K<sub>3</sub>-APhe1** showed a 1.3-fold decrease in  $K_f$  compared to the dark (*trans* dominant) state. Peptide **K<sub>3</sub>-APhe2** showed the opposite behaviour, increasing the  $K_f$  by 1.5-fold, which can be attributed to the repulsion between the glutamic acid side chains and the carboxylic acid group of **APhe2**. A novel azobenzene amino acid, **APgly**, was synthesized based on L-phenylglycine and showed effective photoswitching between the *cis* and *trans* states as the Fmoc-protected amino acid in MeCN. When incorporated in peptide

$K_3$ , **APgly** also showed stability to photocycling under aqueous conditions, and exhibited a 1.6-fold slower relaxation from the 340 nm PSS. CD experiments demonstrated a difference in folding between the dark and irradiated states, and thermal melting experiments revealed a coiled-coil  $K_f$  that was reduced 4.65-fold after isomerization with 340 nm light. Combined with the highest overall  $K_f$  in the dark state, **APgly** is the superior amino acid for coiled-coil photoswitching compared to both phenylalanine derivatives.

To better understand the interactions of the azobenzene amino acid in the coiled coil, MD simulations of **K<sub>3</sub>-APhe1** and **K<sub>3</sub>-APgly** with binding partner  $E_3$  were performed. These simulations showed more distance changes between the *cis* and *trans* isomers of **APhe1** than was observed for **APgly**, indicative of a rearrangement of the amino acid after isomerization. Positioning of the **APgly** diazene group close to the centre of the hydrophobic coiled-coil interface, combined with less rearrangement of the azobenzene after isomerization makes **APgly** the more effective photoswitch for functional coiled-coil motifs and assemblies.

## 5.4 Methods

Fmoc-protected amino acids and fmoc chloride were purchased from Novabiochem (Amsterdam, The Netherlands). Acetic anhydride ( $Ac_2O$ ), acetonitrile (MeCN), dimethylformamide (DMF), piperidine, pyridine,  $NaHCO_3$ , trifluoroacetic acid (TFA) and tetrahydrofuran (THF) were purchased from Biosolve (Valkenswaard, The Netherlands). Oxyma pure was purchased from Carl Roth (Karlsruhe, Germany). Acetic acid ( $AcOH$ ), ammonia, ammonium chloride, ammonium formate, benzophenone imine, 2,2'-Bis(diphenylphosphino)-1,1'-binaphthalene (*rac*-BINAP), 1,2-bis(2-mercapto-ethoxy)-ethane (EDDT), cesium carbonate, di-*tert*-butyl decarbonate ( $Boc_2O$ ), fmoc-4-nitro-L-phenylalanine, 4-hydroxy-L-phenylglycine, lithium hydroxide, nitrosobenzene, *N-N'*-diisopropylcarbodiimide (DIC), oxone, palladium acetate, palladium on carbon (Pd/C, 10%), L-phenylalanine, tert-butyl 4-aminobenzoate, thionyl chloride, triethylamine (TEA), trifluoromethanesulfonic anhydride ( $Tf_2O$ ) and zinc powder were purchased from Sigma Aldrich (Zwijndrecht, The Netherlands). Chloroform, dichloromethane (DCM), diethyl ether ( $Et_2O$ ), ethyl acetate (EtOAc), ethanol (EtOH), methanol (MeOH), pentane, petroleum ether (PE), sodium sulfate and toluene were supplied by Honeywell (Meppel, The Netherlands). All reagents were used as purchased. Ultrapure water was purified using a Milli-Q™ purification system from Millipore (Amsterdam, The Netherlands).

**Peptide synthesis** was performed via Fmoc-based SPPS, on a CEM Liberty Blue microwave-accelerated peptide synthesizer. Peptides were prepared on a 0.1 mmol scale using Tentagel S RAM resin (0.22 mmol/g). 5 equivalents each of amino acid, Oxyma pure and DIC, the latter two of which were coupling reagents were heated at 90 °C for 4 minutes to facilitate coupling. Deprotection was achieved with 20% piperidine in DMF heated to 90 °C for 1 minute. Between deprotection and peptide coupling 3 DMF washes were performed, with a single washing step between the coupling and deprotection steps. Azobenzene amino-acids **2**, **3** and **10** were coupled manually, using 2.5 equivalents of amino acid, 2.5 equivalents of HATU and 5 equivalents DIPEA in DMF for 2-3 hours. After the last Fmoc deprotection, the N-terminus was acylated using 5 mL/mmol each of Ac<sub>2</sub>O and pyridine in DMF, for 5 minutes. The resin was washed 3 times with DMF, MeOH and DCM followed by air-drying. Cleavage of peptide was achieved performed with TFA (8 mL) containing 2.5% water and 2.5% TIS for 1 hour, followed by precipitation of the product in Et<sub>2</sub>O. The product was collected via centrifugation (4000 rpm, 10 minutes), the organic layer removed and the product resuspended in water for direct purification or lyophilization.

Peptides were purified using reverse-phase HPLC on a Shimadzu system consisting of two KC-20AR pumps and an SPD-20A or SPD-M20A detector fitted with a 21.2x150 mm Phenomenex Kinetix Evo C18 column. A nonlinear gradient from 10-90% MeCN in water was used, with 0.1% TFA as the ion-pair reagent, at a flow rate of 12 ml/min. Collected fractions were checked via analytical HPLC, pooled and lyophilized twice to yield the dry products. MS characterization of purified peptides can be found in **Table S5.4**.

#### *Analytical methods*

**LC-MS analysis** was performed on a Thermo Scientific TSQ quantum access MAX mass detector connected to an Ultimate 3000 liquid chromatography system fitted with a 50x4.6 mm Phenomenex Gemini 3 μm C18 column. LC-MS spectra were recorded using a linear gradient of 10%-90% MeCN in H<sub>2</sub>O + 0.1% TFA.

**Analytical HPLC** was performed using a Shimadzu Prominence-*i* LC-2030C 3D system fitted with a 4.6x50 mm Phenomenex Kinetix Evo C18 column. The isomeric ratio of **10** was quantified using a linear gradient of 10-90% MeCN in water containing 0.1% TFA as buffer. For each measurement, 2 μL of a 200 mM solution of **10** was injected, and measurements were repeated 3 times for accuracy.

**UV-Vis** spectra were measured on an Agilent Cary-300 spectrophotometer fitted with an Agilent temperature controller. Spectra were measured at 20 °C in a 1 cm quartz low-volume cuvette, using a scanning speed of 200 nm/min. Spectra were baseline corrected using a blank measurement with the same solvent used for sample preparation.

**CD** spectra were recorded on a Jasco J-815 CD spectrometer fitted with a Peltier temperature controller. Spectra were recorded in a 2 mm quartz cuvette at 20 °C using either PBS or low-salt buffer (2 mM NaCl, 10 mM phosphate) at pH 7.4. Spectra were recorded between 190 and 280 nm with 1 nm intervals, at a scan rate of 100 nm/min with 5 subsequent spectra averaged to minimize noise. The mean residue molar ellipticity ( $\theta$ , deg cm<sup>2</sup> dmol.res<sup>-1</sup>), was calculated using equation 1:

$$[\theta] = (100 * [\theta]_{obs}) / (c * n * l) \quad (1)$$

Where  $[\theta]_{obs}$  represents the observed ellipticity in mdeg,  $c$  represents the peptide concentration in mM,  $n$  the number of peptide bonds and  $l$  the path length of the cuvette in cm. Thermal melting curves were generated by recording  $\theta_{222nm}$  between 5 and 90 °C, at a speed of 1 °C/min. If irradiated samples were used, samples were reilluminated every 30 minutes. Melting curves were measured at 4 different concentrations and fitted using the Fitdis software package.<sup>27</sup>

**Sample illumination** at 340 nm was achieved using a Thorlabs M340F3 Fiber-coupled LED powered by a T-Cube driver at 1000 mA. For all other wavelengths, high-power single chip LEDs were purchased from Roithner Laser (Vienna, Austria) from the H2A1 series. LEDs from Roithner Laser were mounted on an aluminum back plate for heat dissipation, and powered at 350 mA current using a driver built in-house. For illumination the LED was placed parallel to the side of the cuvette at a distance of 5 mm, and centered to the width and height of the sample.

### *Molecular simulations*

**Geometry Optimization:** Input geometries of the amino acids for the MD simulations were obtained by geometry optimization performed using the Amsterdam Density Functional (ADF2019.302)<sup>33-35</sup> software package, using the BLYP functional with D3(BJ) dispersion correction,<sup>36, 37</sup> and a TZ2P basis set, which is of triple- $\zeta$  quality for all atoms and has been improved by two sets of polarization functions. The accuracies of the fit scheme (Zlm fit) and the integration grid (Becke

grid) were set to VERYGOOD. All structures were verified to be at the stationary point by the absence of negative frequencies.

**Force field parametrization:** A new atom type NX was introduced to the AMBER-96 force field<sup>38</sup> for the diazo nitrogen atoms in **APgly** and **APhe1**. Bond lengths, angles and dihedral angles for this new atom type were derived from DFT calculated optimized geometries, and are displayed in **table S5.3**. Force constants from similar existing atom type combinations were adapted. For the production runs, a high force constant ( $1000 \text{ kJ mol}^{-1} \text{ rad}^{-2}$ ) was used to restrain the cis/trans dihedral angle.

**System setup:** The NMR structure of the  $E_3/K_3$  coiled-coil heterodimer was retrieved from the protein data bank (PDB, ID: 1U0I).<sup>32</sup> Ile9 of peptide K was mutated manually to **APgly** or **APhe1** and solvated with TIP3P water<sup>39</sup> in a  $5 \times 5 \times 5 \text{ nm}^3$  simulation box. After steepest descent energy minimization, the system was equilibrated for 500 ps with and, subsequently, without position restraints on the protein atoms. For each system, three independent production runs of 500 ns were performed with pseudorandom initial velocities.

**Simulation details:** All molecular dynamics (MD) simulations were performed with GROMACS 2019.3.<sup>40</sup> A 1 fs time step was used. Constant temperature (300K,  $\tau_T = 0.1 \text{ ps}$ ) and pressure (1 bar,  $\tau_P = 2 \text{ ps}$ ) were maintained by the velocity rescaling thermostat<sup>41</sup> and the Berendsen barostat,<sup>42</sup> respectively. The system's compressibility was set to  $4.5 \cdot 10^{-5} \text{ bar}^{-1}$ . Neighbour lists were recalculated every 100 steps with a cut-off of 1 nm using the Verlet cut-off scheme.<sup>43</sup> Particle-mesh Ewald (PME)<sup>44</sup> electrostatics (0.11 nm grid) and Van der Waals interactions are shifted such that they switch off at the cut-off distance (1 nm)

### *Organic Synthesis*

**Protocol A, general method for the reduction of nitrophenylalanine:** Fmoc-4-nitro-L-phenylalanine was dissolved in absolute EtOH (150 mL/g), combined with ammonium chloride (5 eq.) and Zn dust (4 eq.), and the reaction refluxed for 2 hours. After evaporation of solvent, the resulting solids were combined with EtOAc and excess 1 M HCl, the phases separated and the aqueous layer extracted twice with ethyl acetate. The two organic layers were combined, washed with deionized water, and dried with anhydrous  $\text{Na}_2\text{SO}_4$ . Solvent was evaporated under reduced pressure, yielding Fmoc-(4-amino)-L-phenylalanine that was used without further purification.

**4-tert-Butyl-nitrosobenzoate:** 4-Amino tert-butyl benzoate (765 mg, 3.96 mmol) was dissolved in 10 mL DCM and combined with Oxone (1263 mg, 8.29 mmol) in 13 mL H<sub>2</sub>O, and the mixture was stirred vigorously under reflux for 20 hours. The layers were separated, and the aqueous layer extracted with an additional 20 mL DCM. The combined organic layers were washed sequentially with 10 mL 1M HCl, 10 mL half-saturated NaHCO<sub>3</sub> and 10 mL brine, dried over Na<sub>2</sub>SO<sub>4</sub>, and solvent was removed to yield the crude product. The product was purified via column chromatography (Et<sub>2</sub>O/C<sub>5</sub>H<sub>12</sub>) to yield 220 mg of the product as bright green needles (1.06 mmol, 27%) that were used directly in the Mills reaction. <sup>1</sup>H NMR (500 MHz, CDCl<sub>3</sub>) δ 8.23 (d, J = 8.7 Hz, 2H), 7.91 (d, 2H), 1.62 (s, 9H). <sup>13</sup>C NMR (126 MHz, CDCl<sub>3</sub>) δ 164.78, 164.47, 137.28, 130.94, 130.65, 123.51, 120.47, 82.53, 28.25.

**N-Fmoc-4-nitro-L-phenylalanine (1):** To a solution of L-phenylalanine (4.96 g, 30 mmol) dissolved in H<sub>2</sub>SO<sub>4</sub> (95%, 22.5 mL) and cooled over ice was added 4.2 mL nitrating solution (prepared by mixing 2.8 mL of 60% HNO<sub>3</sub> and 2.2 mL 95% H<sub>2</sub>SO<sub>4</sub> on ice) dropwise over 3.5 hours. The solution was neutralized with ammonia solution (25%) added dropwise until pH 6 was achieved and precipitate observed. The precipitate was collected by filtration and washed with 5 x 30 mL water. After drying, 3.5 g (55%) of 4-nitrophenylalanine was collected as an off-white solid. This intermediate (1.05 g, 5.00 mmol) was dissolved in a mixture of 20 mL 0.5 M Na<sub>2</sub>CO<sub>3</sub>, 13 mL acetone, 13 mL deionized water and 49.6 mg dodecyl sulfate and cooled over ice. A solution of Fmoc-chloride (1.32 g, 5.1 mmol) in 10 mL acetone was added dropwise to the reaction, and it was left to stir overnight at room temperature. The reaction was quenched by dilution into 300 mL cold water and addition of 5 mL, 2 M HCl. The precipitate was filtered and redissolved in 100 mL, 0.5 M Na<sub>2</sub>CO<sub>3</sub>. The mixture was allowed to stir at 70 °C for 1 hour, after which the white precipitate was filtered out and the filtrate was collected and acidified to pH < 3 with 2 M HCl. The precipitate was collected and dried to yield 1.5 g of a white solid (69%, 38% over two steps). <sup>1</sup>H NMR (400 MHz, DMSO-d<sub>6</sub>) 8.15 (d, 2H), 7.89 (d, J = 7.6 Hz, 2H), 7.80 (d, J = 8.7 Hz, 1H), 7.62 (dd, J = 7.5, 2.7 Hz, 2H), 7.56 (d, J = 8.5 Hz, 2H), 7.41 (t, J = 7.4 Hz, 2H), 7.30 (q, J = 7.4 Hz, 2H), 4.32 – 4.13 (m, 4H), 3.25 (dd, J = 13.8, 4.4 Hz, 1H), 3.02 (dd, J = 13.8, 10.8 Hz, 1H). LC-MS RT = 7.57 min, m/z = 178.47 (calc Fm<sup>+</sup> = 179.09), 454.61 (calc [1 + Na<sup>+</sup>]<sup>+</sup> = 455.12), 470.00 (calc [1 + K<sup>+</sup>]<sup>+</sup> = 471.10).

**Preparation of N-fmoc-(4-phenylazo)-L-phenylalanine, APhe1 (2):** Fmoc-4-nitrophenylalanine (1.34 g, 3.11 mmol) was reduced according to protocol A (see above), resulting in 1.04 g crude Fmoc-4-aminophenylalanine. The intermediate

was dissolved in 60 mL AcOH, before nitrosobenzene (350 mg, 3.27 mmol, 1.25 eq.) dissolved in 5 mL AcOH was added and the solution left for 20 hours. The product was precipitated by addition of the reaction mixture to 250 mL H<sub>2</sub>O, and collected via filtration. The crude product was redissolved in EtOAc, dried with Na<sub>2</sub>SO<sub>4</sub>, filtered and solvent evaporated. The solids were purified via column chromatography (dry loading, DCM/MeOH + 0.5% AcOH) and removal of solvents yielded 478 mg (0.97 mmol, 32% over 2 steps) of pure product as a brown powder. <sup>1</sup>H NMR (500 MHz, DMSO-d<sub>6</sub>) 7.89 - 7.85 (m, 4H), 7.82 (d, J = 8.3 Hz, 3H), 7.66 - 7.54 (m, 5H), 7.50 (d, J = 8.4 Hz, 2H), 7.38 (q, J = 7.9 Hz, 2H), 7.28 (dt, J = 14.9, 7.4 Hz, 2H), 4.30 - 4.24 (m, 1H), 4.21 (d, J = 6.1 Hz, 2H), 4.19 - 4.13 (m, 1H), 3.21 (dd, J = 13.8, 4.4 Hz, 1H), 2.99 (dd, J = 13.8, 10.7 Hz, 1H). <sup>13</sup>C NMR (126 MHz, DMSO) 173.14, 155.96, 151.99, 150.65, 143.77, 143.71, 142.06, 140.69, 140.68, 131.39, 130.24, 129.48, 127.61, 127.59, 127.05, 125.25, 125.19, 122.47, 120.10, 65.61, 55.22, 46.57, 36.32. LC-MS RT = 7.85 (cis), 8.90 (trans) min, m/z = 178.54 (calc Fm<sup>+</sup> = 179.09), 513.31 (calc [2 + Na<sup>+</sup>]<sup>+</sup> = 514.17).

**Preparation of N-fmoc-L-(4-(4'-tert-Butoxycarbonyl)phenylazo)phenylalanine, (3):** Fmoc-(4-nitro)-L-phenylalanine (2.02 mmol, 874 mg) was reduced according to general protocol A to yield 732 mg of Fmoc-(4-amino)-L-phenylalanine. The solids were dissolved by heating in 70 mL AcOH, and after it had returned to room temperature, 560 mg tert-Butyl-4-nitrosobenzoate was added (2.71 mmol) dissolved in 5 mL AcOH, and the reaction stirred for 20 h. Another 220 mg (1.06 mmol) of the nitrosobenzene was added to drive the reaction to completion, and the reaction stirred for another 20 h. The product was precipitated in 250 mL H<sub>2</sub>O, collected via filtration, redissolved in acetone and the solvent was removed via rotary evaporation. The crude product was purified via column chromatography (PE/Et<sub>2</sub>O + 1% AcOH) and solvent removed to yield 675 mg (1.14 mmol, 56% over two steps) of the pure product as a red semi-crystalline material. <sup>1</sup>H NMR (400 MHz, CDCl<sub>3</sub>): δ 8.12 (d, J = 8.5 Hz, 2H), 7.89 (dd, J = 11.5, 8.3 Hz, 4H), 7.76 (d, J = 7.6 Hz, 2H), 7.55 (d, J = 7.2 Hz, 2H), 7.39 (t, J = 7.4 Hz, 2H), 7.33 - 7.28 (m, 4H), 5.30 (d, J = 8.1 Hz, 1H), 4.83 - 4.71 (m, 1H), 4.51 - 4.47 (m, 1H), 4.39 (dd, J = 10.7, 6.8 Hz, 1H), 4.21 (t, J = 6.9 Hz, 1H), 3.26 (ddd, J = 45.1, 13.9, 5.8 Hz, 2H), 1.63 (s, 9H). <sup>13</sup>C NMR (101 MHz, CDCl<sub>3</sub>): δ 177.31, 165.40, 155.83, 154.93, 151.86, 143.84, 143.70, 141.47, 139.65, 133.84, 130.56, 130.38, 127.90, 127.23, 125.17, 125.11, 123.52, 122.63, 120.16, 81.71, 67.20, 54.58, 47.25, 37.82, 28.33. LC-MS RT = 8.79 (cis), 9.81 (trans) min, m/z = 178.47 (calc Fm<sup>+</sup> = 179.09), 591.25 (calc [3 + H<sup>+</sup>]<sup>+</sup> = 592.24), 613.35 (calc [3 + Na<sup>+</sup>]<sup>+</sup> = 614.23).

**4-Hydroxy-L-phenylglycine methyl ester (4):** Thionyl chloride (13.0 mL, 184 mmol, 9 eq.) was added dropwise to a suspension of 4-hydroxy-L-phenylglycine (3.39 g, 20.3 mmol) in 100 mL dry MeOH temperature controlled at 20 °C, over the course of 30 minutes. The clear solution was stirred overnight, and all liquid was evaporated under reduced pressure. The resulting oil was mixed with 50 mL Et<sub>2</sub>O to yield an off-white precipitate, which was filtered and washed with 2x 50 mL Et<sub>2</sub>O. The residue was dried under vacuum to yield 4.33 g of 4-hydroxy-phenylglycine methyl ester hydrochloride (19.9 mmol, 98%). <sup>1</sup>H NMR (400 MHz, DMSO): δ 9.98 (s, 1H), 8.98 (s, 3H), 7.28 (d, *J* = 8.6 Hz, 2H), 6.84 (d, *J* = 8.6 Hz, 2H), 5.09 (s, 1H), 3.69 (s, 3H), 3.38 (s, 1H). <sup>13</sup>C NMR (101 MHz, DMSO): δ 169.26, 158.60, 129.64, 122.61, 115.70, 54.90, 53.02.

**N-Boc-4-hydroxy-L-phenylglycine methyl ester (5):** A solution was prepared of 4-hydroxy-phenylglycine methyl ester (**4**, 1.11 g of the HCl salt, 5.11 mmol) in dry MeCN (70 mL) containing TEA (0.75 mL 5.39 mmol, 1.06 eq). Boc<sub>2</sub>O (1.30 g, 5.96 mmol, 1.17 eq) was dissolved in 20 mL dry MeCN and added dropwise to the phenylglycine solution, and the solution stirred overnight. The solvent was evaporated and remaining solids redissolved in 50 mL DCM, which was subsequently washed with 25 mL 1M H<sub>3</sub>PO<sub>4</sub>, 50 mL H<sub>2</sub>O and 25 mL brine. The organic layer was dried with Na<sub>2</sub>SO<sub>4</sub> and the solvent evaporated. The crude product was purified via filtration through a plug of silica (eluent: EtOAc) and the solvent was removed to yield 1.33 g (4.71 mmol, 93%) of product as a white solid. <sup>1</sup>H NMR (400 MHz, DMSO): δ 9.50 (s, 1H), 7.62 (d, *J* = 7.9 Hz, 1H), 7.20 – 7.13 (m, 2H), 6.75 – 6.65 (m, 2H), 5.05 (d, *J* = 7.9 Hz, 1H), 3.59 (s, 3H), 1.38 (s, 9H). <sup>13</sup>C NMR (101 MHz, DMSO): δ 171.91, 157.25, 155.20, 129.10, 126.64, 115.19, 78.42, 57.10, 52.00, 28.19.

**N-Boc-4-(trifluoromethanesulfonate)-L-phenylglycine methyl ester (6):** N-boc-4-hydroxy-L-phenylglycine methyl ester (1.41 g, 5.02 mmol) was dissolved in 25 mL DCM and combined with 1 mL (7.5 mmol, 1.5 eq.) TEA. The reaction was cooled to -20 °C and Tf<sub>2</sub>O (0.83 mL, 4.92 mmol, 0.98 eq.) was added in portions. After 30 minutes, the reaction was allowed to heat to room temperature and left to stir for 4 hours. The reaction was diluted with another 20 mL DCM and washed with 20 mL 0.5M HCl, 20 mL H<sub>2</sub>O and 20 mL brine. The organic layer was dried over Na<sub>2</sub>SO<sub>4</sub>, the solvent was removed and the product purified over a silica column (Et<sub>2</sub>O/C<sub>5</sub>H<sub>12</sub>) to yield 1.825 g of a clear oil (4.42 mmol, 98% yield relative to Tf<sub>2</sub>O, 88% relative to **5**). The oil could be turned into a solid via dissolution in pentane and removal of the

solvent.  $^1\text{H NMR}$  (500 MHz,  $\text{CDCl}_3$ ):  $\delta$  7.47 (d,  $J = 8.7$  Hz, 2H), 7.30 – 7.23 (m, 2H), 5.77 – 5.61 (m, 1H), 5.37 (d,  $J = 7.2$  Hz, 1H), 3.75 (s, 3H), 1.43 (s, 8H).  $^{13}\text{C NMR}$  (126 MHz,  $\text{CDCl}_3$ ):  $\delta$  170.93, 154.76, 149.45, 137.93, 129.17, 121.92, 118.25(d,  $J_{CF} = 161$  Hz), 80.72, 56.89, 53.21, 28.40, 27.80.  $^{19}\text{F NMR}$  (471 MHz,  $\text{CDCl}_3$ ):  $\delta$  -72.86.

**N-Boc-4-((diphenylmethylene)-amino)-L-phenylglycine methyl ester (7):**  $\text{Cs}_2\text{CO}_3$  (460 mg, 1.4 mmol, 1.4 eq), N-Boc-(4-trifluoromethanesulfonate)-L-phenylglycine methyl ester (**6**, 413 mg, 1.03 mmol) and benzophenone imine (210  $\mu\text{L}$ , 1.25 mmol, 1.21 eq) were placed in an oven-dried schlenk reaction vessel, and the flask was placed under a nitrogen atmosphere.  $\text{Pd}(\text{OAc})_2$  (15.5 mg, 0.07 mmol, 7%) and *rac*-BINAP (95 mg, 0.15 mmol, 15%) were combined in a separate vial, placed under nitrogen, and combined with 4 mL toluene and 2.5  $\mu\text{L}$   $\text{H}_2\text{O}$  (0.14 mmol, 14%) and heated to 85  $^\circ\text{C}$ . After 2 minutes the color of the catalyst solution had changed to bright red, transferred to the reaction flask and the reaction stirred at 100  $^\circ\text{C}$  for 20h. After cooling to RT, the liquid phase of the reaction was transferred to a separatory funnel, the solids washed 3x with 10 mL  $\text{Et}_2\text{O}$ , and this liquid also combined in the funnel. The organic layers were extracted with 2x 20 mL  $\text{H}_2\text{O}$ , dried with  $\text{Na}_2\text{SO}_4$  and the solvent removed. The product purified over silica column ( $\text{Et}_2\text{O}/\text{C}_5\text{H}_{12}$ ) and dried under high vacuum to yield 296 mg of a light-yellow solid (0.66 mmol, 65% yield).  $^1\text{H NMR}$  (500 MHz,  $\text{CDCl}_3$ ):  $\delta$  7.72 (d,  $J = 7.0$  Hz, 2H), 7.46 (t,  $J = 7.3$  Hz, 1H), 7.39 (dd,  $J = 8.3, 6.8$  Hz, 2H), 7.25 (d,  $J = 8.1$  Hz, 4H), 7.14 – 7.07 (m, 4H), 6.69 (d,  $J = 8.4$  Hz, 2H), 5.39 (d,  $J = 7.5$  Hz, 1H), 5.19 (d,  $J = 7.5$  Hz, 1H), 3.68 (s, 3H), 1.43 (s, 8H).  $^{13}\text{C NMR}$  (126 MHz,  $\text{CDCl}_3$ ):  $\delta$  171.96, 168.66, 154.95, 151.54, 139.62, 136.07, 131.34, 130.97, 129.61, 129.47, 128.83, 128.34, 128.09, 127.56, 121.53, 80.21, 57.33, 52.65, 28.42.

**N-Boc-(4-phenylazo)-L-phenylglycine methyl ester (8):** Ammonium formate (1.1 g, 17.5 mmol, 15.8 eq.) and 10% Pd on carbon (50% water by weight, 125 mg, 5.8%) were combined with N-Boc-4-((diphenylmethylene)amino)-L-phenylglycine methyl ester (**7**, 496 mg, 1.11 mmol) under a nitrogen atmosphere. 4 mL MeOH was added and the reaction heated to 60  $^\circ\text{C}$  for 2h. The reaction was diluted with 10 mL DCM and filtered over celite, then washed with another 20 mL DCM. The organic layers were washed with 2x 30 mL  $\text{H}_2\text{O}$ , 1 x 10 mL brine, and dried over  $\text{Na}_2\text{SO}_4$ . The solvent was removed to yield 400 mg of an off-white solid. This was redissolved in 5 mL AcOH, and 167 mg (1.56 mmol, 1.4 eq) nitrosobenzene in 3 mL AcOH was added and the reaction stirred for 6 days. 50 mL DCM was added and the organic layer washed with 50 mL  $\text{H}_2\text{O}$ , 50 mL 3%  $\text{NH}_3$  and 50 mL brine. The organic layer was dried

over dried over  $\text{Na}_2\text{SO}_4$  and the solvent removed. The crude product was purified via column chromatography ( $\text{Et}_2\text{O}/\text{C}_5\text{H}_{12}$ ) to yield 303 mg of an orange solid (0.82 mmol, 74%).  $^1\text{H NMR}$  (400 MHz,  $\text{CDCl}_3$ ):  $\delta$  7.94 – 7.88 (m, 4H), 7.52 (m, 5H), 5.68 (d,  $J = 7.3$  Hz, 1H), 5.41 (d,  $J = 7.3$  Hz, 1H), 3.74 (s, 3H), 1.44 (s, 8H).  $^{13}\text{C NMR}$  (101 MHz,  $\text{CDCl}_3$ ):  $\delta$  171.29, 152.73, 152.66, 139.84, 131.33, 129.25, 128.05, 123.45, 123.05, 80.51, 57.48, 53.06, 28.45.

**N-fmoc-4-(phenylazo)-L-phenylglycine, Fmoc-APhe (10):** To N-Boc-4-(phenylazo)-L-phenylglycine methyl ester (**9**, 311 mg, 0.84 mmol) dissolved in 6 mL THF was added 1M LiOH (1.26 mL, 1.5 eq.) and the reaction stirred for 90 minutes. After cooling the reaction was combined with 50 mL DCM and 50 mL 0.5 M HCl. The layers were separated, and the organic layer washed with 50 mL  $\text{H}_2\text{O}$ , 50 mL brine and dried over  $\text{Na}_2\text{SO}_4$ . The solvent was evaporated and the intermediate was redissolved in 5 mL DCM and 5 mL TFA was added. The reaction was stirred for 2 hours, after which the intermediate was precipitated in 100 mL cold  $\text{Et}_2\text{O}:\text{C}_5\text{H}_{12}$  and collected via centrifugation at 4000 rpm for 10 minutes. The precipitate was dried under a stream of air for 5 minutes, then suspended in 150 mL 25%  $\text{H}_2\text{O}/\text{THF}$ .  $\text{NaHCO}_3$  (1.5 g) was added to neutralize the solution and Fmoc-chloride (258 mg, 1 mmol, 1.19 eq.) dissolved in 6 mL THF was added to the reaction dropwise. The solution was stirred overnight, and the next day all THF was evaporated. The reaction was combined with 60 mL DCM and 100 mL 1M HCl and separated. The Aqueous layer was extracted with 40 mL DCM, organic layers combined and washed with 100 mL  $\text{H}_2\text{O}$ , 50 mL brine and dried over  $\text{Na}_2\text{SO}_4$ . The solvent was removed and the remaining solids purified via column chromatography (DCM/MeOH with 0.5 % AcOH) to yield 254 mg of product as a bright orange powder (0.3 mmol, 63% over 3 steps).  $^1\text{H NMR}$  (600 MHz, DMSO):  $\delta$  13.11 (s, 1H), 8.44 – 8.31 (m, 1H), 7.93 – 7.87 (m, 6H), 7.77 (d,  $J = 7.5$  Hz, 2H), 7.66 (d,  $J = 8.5$  Hz, 2H), 7.64 – 7.55 (m, 3H), 7.44 – 7.39 (m, 2H), 7.32 (dt,  $J = 11.7, 7.5$  Hz, 2H), 5.32 (d,  $J = 8.2$  Hz, 1H), 4.34 – 4.22 (m, 3H).  $^{13}\text{C NMR}$  (151 MHz, DMSO):  $\delta$  171.68, 155.91, 151.92, 151.50, 143.84, 143.77, 140.74, 140.66, 131.71, 129.55, 128.99, 127.70, 127.11, 125.42, 125.42, 122.64, 120.15, 66.01, 57.78, 46.62. **LC-MS** RT = 6.65 (cis), 8.80 (trans) min,  $m/z = 178.54$  (calc  $\text{Fm}^+ = 179.09$ ), 238.71 (calc  $[\mathbf{10} + 2\text{H}^+]^{2+} = 239.59$ ), 477.28 (calc  $[\mathbf{10} + \text{H}^+]^+ = 478.17$ ), 499.46 (calc  $[\mathbf{10} + \text{Na}^+]^+ = 500.16$ ).

## 5.5 References

1. Kumita, J. R., Smart, O. S., and Woolley, G. A. (2000) Photo-control of helix content in a short peptide. *P. Natl. Acad. Sci. USA* 97, 3803-3808.
2. Wagschal, K., et al. (1999) The role of position a in determining the stability and oligomerization state of  $\alpha$ -helical coiled coils: 20 amino acid stability coefficients in the hydrophobic core of proteins. *Protein Sci.* 8, 2312-2329.
3. Tripet, B., et al. (2000) Effects of side-chain characteristics on stability and oligomerization state of a de Novo-designed model coiled-coil: 20 amino acid substitutions in position "d". *J. Mol. Biol.* 300, 377-402.
4. Acharya, A., et al. (2002) A Heterodimerizing Leucine Zipper Coiled Coil System for Examining the Specificity of a Position Interactions: Amino Acids I, V, L, N, A, and K. *Biochem.* 41, 14122-14131.
5. Acharya, A., Rishi, V., and Vinson, C. (2006) Stability of 100 Homo and Heterotypic Coiled-Coil a-a' Pairs for Ten Amino Acids (A, L, I, V, N, K, S, T, E, and R). *Biochem.* 45, 11324-11332.
6. Zhu, H., et al. (2000) The contribution of buried polar groups to the conformational stability of the GCN4 coiled coil11Edited by C. R. Matthews. *J. Mol. Bio.* 300, 1377-1387.
7. Fletcher, J. M., et al. (2017) N@a and N@d: Oligomer and Partner Specification by Asparagine in Coiled-Coil Interfaces. *ACS Chem. Biol.* 12, 528-538.
8. García-Echeverría, C. (1996) Disruption of coiled coil formation by methionine oxidation. *Bioorg. Med. Chem. Lett.* 6, 229-232.
9. Zimencov, Y., et al. (2006) Rational Design of a Reversible pH-Responsive Switch for Peptide Self-Assembly. *J. Am. Chem. Soc.* 128, 6770-6771.
10. Dublin, S. N., and Conticello, V. P. (2008) Design of a Selective Metal Ion Switch for Self-Assembly of Peptide-Based Fibrils. *J. Am. Chem. Soc.* 130, 49-51.
11. Boyle, A. L., et al. (2019) Selective coordination of three transition metal ions within a coiled-coil peptide scaffold. *Chem. Sci.* 10, 7456-7465.
12. Goodman, M., and Kossoy, A. (1966) Conformational Aspects of Polypeptide Structure. XIX. Azoaromatic Side-Chain Effects1,2. *J. Am. Chem. Soc.* 88, 5010-5015.
13. Bose, M., et al. (2006) The Incorporation of a Photoisomerizable Amino Acid into Proteins in E. coli. *J. Am. Chem. Soc.* 128, 388-389.
14. Nakayama, K., Endo, M., and Majima, T. (2005) A Hydrophilic Azobenzene-Bearing Amino Acid for Photochemical Control of a Restriction Enzyme BamHI. *Bioconjugate Chem.* 16, 1360-1366.
15. Nakayama, K., Endo, M., and Majima, T. (2004) Photochemical regulation of the activity of an endonuclease BamHI using an azobenzene moiety incorporated site-selectively into the dimer interface. *Chem. Commun.*, 2386-2387.
16. John, A. A., et al. (2015) Synthesis and Site-Specific Incorporation of Red-Shifted Azobenzene Amino Acids into Proteins. *Org. Lett.* 17, 6258-6261.

17. Luo, J., *et al.* (2018) Reversible and Tunable Photoswitching of Protein Function through Genetic Encoding of Azobenzene Amino Acids in Mammalian Cells. *Chembiochem : a European journal of chemical biology* 19, 2178-2185.
18. Kneuttinger, A. C., *et al.* (2019) Light Regulation of Enzyme Allostery through Photo-responsive Unnatural Amino Acids. *Cell. Chem. Bio.* 26, 1501-1514.e9.
19. Hoppmann, C., *et al.* (2011) Photoswitchable Click Amino Acids: Light Control of Conformation and Bioactivity. *Chembiochem : a European journal of chemical biology* 12, 2555-2559.
20. Hoppmann, C., *et al.* (2015) In Situ Formation of an Azo Bridge on Proteins Controllable by Visible Light. *J. Am. Chem. Soc.* 137, 11218-11221.
21. Wu, Y. Y., and Collier, J. H. (2017) alpha-Helical coiled-coil peptide materials for biomedical applications. *WIREs Nanomed Nanobiotechnol.* 9, e1424.
22. Utterström, J., *et al.* (2021) Coiled coil-based therapeutics and drug delivery systems. *Adv. Drug Del. Rev* 170, 26-43.
23. Szilák, L., Moitra, J., and Vinson, C. (1997) Design of a leucine zipper coiled coil stabilized 1.4 kcal mol<sup>-1</sup> by phosphorylation of a serine in the e position. *Protein Sci.* 6, 1273-83.
24. Winter, D. L., *et al.* (2020) Design of Tunable Protein Interfaces Controlled by Post-Translational Modifications. *ACS Synth. Biol.* 9, 2132-2143.
25. Robson Marsden, H., *et al.* (2009) A Reduced SNARE Model for Membrane Fusion. *Angew. Chem. Int. Edit.* 48, 2330-2333.
26. Litowski, J. R., and Hodges, R. S. (2002) Designing heterodimeric two-stranded alpha-helical coiled-coils - Effects of hydrophobicity and alpha-helical propensity on protein folding, stability, and specificity. *J. Biol. Chem.* 277, 37272-37279.
27. Rabe, M., *et al.* (2015) Determination of Oligomeric States of Peptide Complexes Using Thermal Unfolding Curves. *Biopolymers* 104, 65-72.
28. Davies, A. J., Ashwood, M. S., and Cottrell, I. F. (2000) A Facile Synthesis of Substituted Phenylglycines. *Syn. Commun.* 30, 1095-1102.
29. Lee, D.-Y., and Hartwig, J. F. (2005) Zinc Trimethylsilylamide as a Mild Ammonia Equivalent and Base for the Amination of Aryl Halides and Triflates. *Org. Lett.* 7, 1169-1172.
30. Wolfe, J. P., *et al.* (1997) An Ammonia Equivalent for the Palladium-Catalyzed Amination of Aryl Halides and Triflates. *Tetrahedron Lett.* 38, 6367-6370.
31. Asano, T., and Okada, T. (1984) Thermal Z-E isomerization of azobenzenes. The pressure, solvent, and substituent effects. *J. Org. Chem.* 49, 4387-4391.
32. Lindhout, D. A., *et al.* (2004) NMR solution structure of a highly stable de novo heterodimeric coiled-coil. *Biopolymers* 75, 367-375.
33. Zozulia, O., Dolan, M. A., and Korendovych, I. V. (2018) Catalytic peptide assemblies. *Chem. Soc. Rev.* 47, 3621-3639.
34. te Velde, G., *et al.* (2001) Chemistry with ADF. *J. Comp. Chem.* 22, 931-967.
35. Fonseca Guerra, C., *et al.* (1998) Towards an order-N DFT method. *Theor. Chem. Acc.* 99, 391-403.

36. Grimme, S., *et al.* (2010) A consistent and accurate ab initio parametrization of density functional dispersion correction (DFT-D) for the 94 elements H-Pu. *J. Chem. Phys.* 132, 154104.
37. Grimme, S., Ehrlich, S., and Goerigk, L. (2011) Effect of the damping function in dispersion corrected density functional theory. *J. Comp. Chem.* 32, 1456-1465.
38. Kollman, P., *et al.* (1997) The development/application of a 'minimalist' organic/biochemical molecular mechanic force field using a combination of ab initio calculations and experimental data, in *Computer Simulation of Biomolecular Systems: Theoretical and Experimental Applications* (van Gunsteren, W. F., Weiner, P. K., and Wilkinson, A. J., Eds.) pp 83-96, Springer Netherlands, Dordrecht.
39. Jorgensen, W. L., *et al.* (1983) Comparison of simple potential functions for simulating liquid water. *J. Chem. Phys.* 79, 926-935.
40. Abraham, M. J., *et al.* (2015) GROMACS: High performance molecular simulations through multi-level parallelism from laptops to supercomputers. *SoftwareX* 1-2, 19-25.
41. Bussi, G., Donadio, D., and Parrinello, M. (2007) Canonical sampling through velocity rescaling. *J. Chem. Phys.* 126, 014101.
42. Berendsen, H. J. C., *et al.* (1984) Molecular dynamics with coupling to an external bath. *J. Chem. Phys.* 81, 3684-3690.
43. Verlet, L. (1967) Computer "Experiments" on Classical Fluids. I. Thermodynamical Properties of Lennard-Jones Molecules. *Phys. Rev.* 159, 98-103.
44. Darden, T., York, D., and Pedersen, L. (1993) Particle mesh Ewald: An N·log(N) method for Ewald sums in large systems. *J. Chem. Phys.* 98, 10089-10092.

## Supporting information for Chapter 5

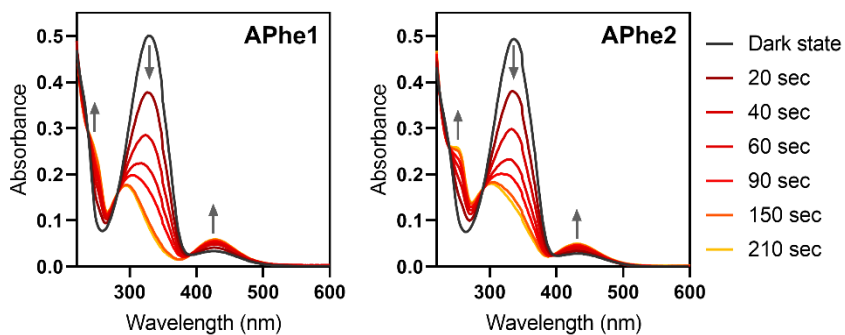


**Figure S5.1:** UV-Vis spectra of peptide K<sub>3</sub> containing either APhe1 or APhe2 at different time intervals during illumination with 340 nm light. Measurements were performed at 20 °C in PBS with [peptide] = 50 μM. Arrows indicate direction of change after illumination.

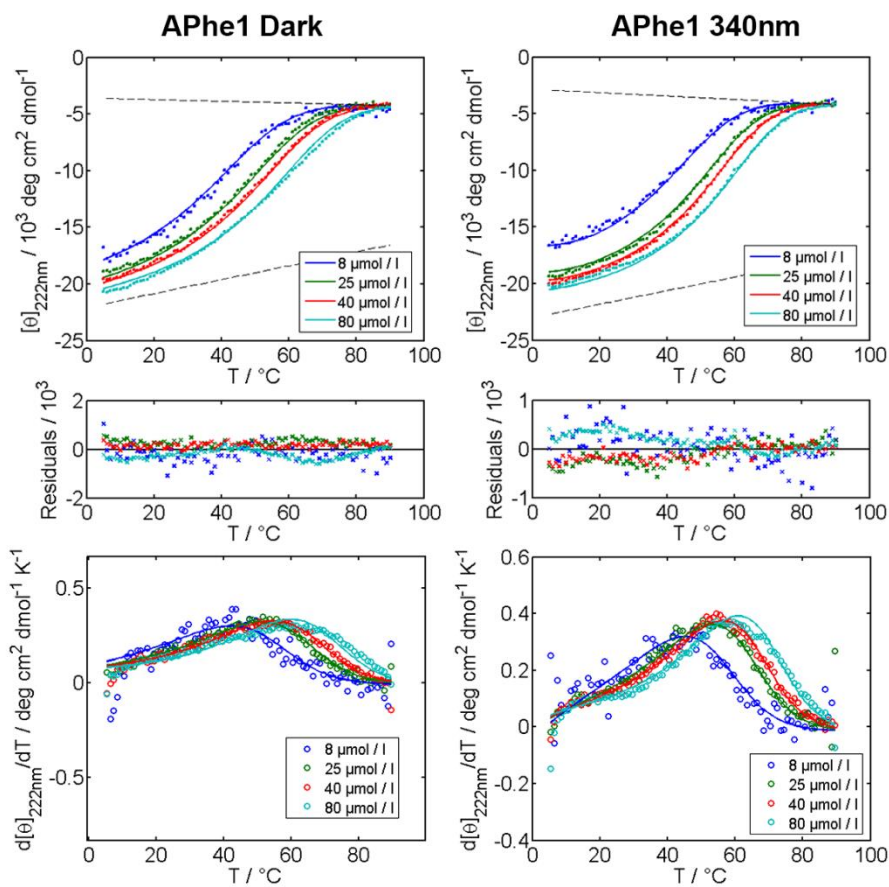


**Figure S5.2:** Fitting of CD melting curves (top) for peptide  $K_3$ -APhe1 with  $E_3GY$  in the dark adapted (left) and 340 nm irradiated (right) states performed using the Fitdis software program. Residuals (middle) and derivatives (bottom) of the best fitting (dimeric) model are shown. Measurements were performed in PBS.

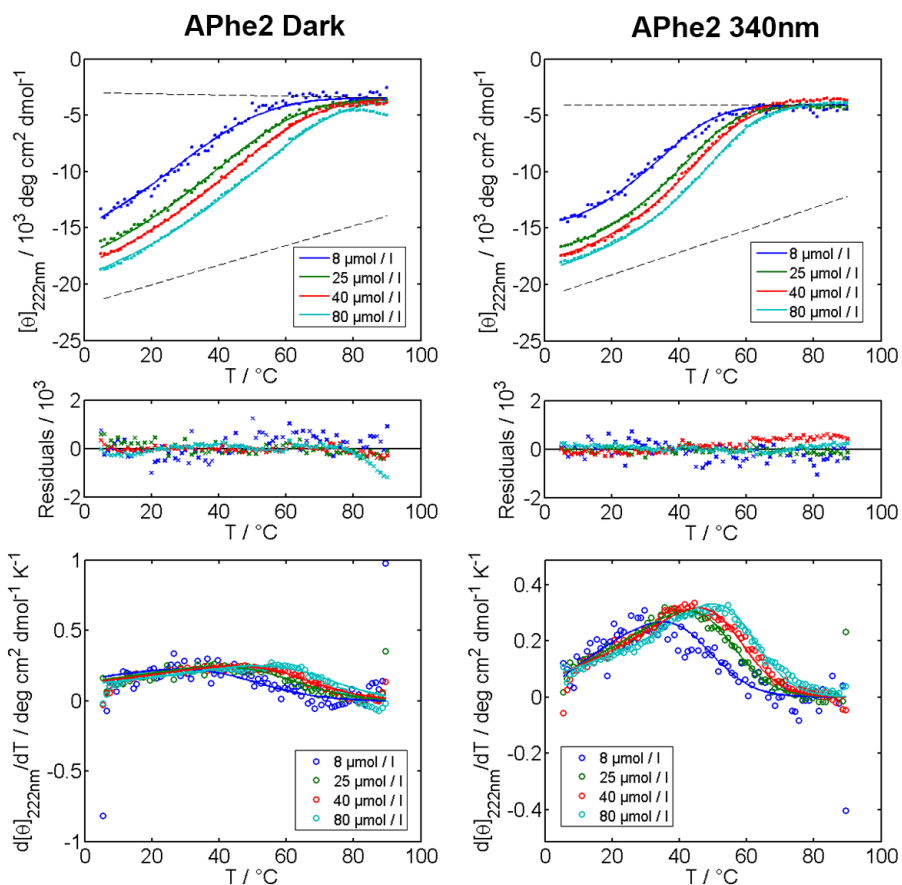


**Figure S5.3:** Fitting of CD melting curves (top) for peptide K<sub>3</sub>-APhe2 with E<sub>3</sub>GY in the dark adapted (left) and 340 nm irradiated (right) states performed by the Fitdis software program. Residuals (middle) and derivatives (bottom) of the best fitting (dimeric) model are shown. Measurements were performed in PBS.

**Table S5.1:** Fit results of thermal unfolding curves for K<sub>3</sub> peptides containing azophenylalanine amino acids with binding partner E<sub>3</sub>GY, in either the dark adapted or 340 nm irradiated state.

Coiled-coil system	K <sub>3</sub> -APhe1 Dark	K <sub>3</sub> -APhe1 340 nm	K <sub>3</sub> -APhe2 dark	K <sub>3</sub> -APhe2 340 nm
$\Delta H^{\circ a}$ (kJ mol <sup>-1</sup> )	224.7 ± 12.4	261.4 ± 7.4	175.0 ± 12.1	259.0 ± 9.7
$T^{\circ b}$ (°C)	123 ± 3.1	114.1 ± 1.5	142.5 ± 5.4	102.1 ± 2.1
$\Delta C_p$ (kJ mol <sup>-1</sup> k <sup>-1</sup> )	1.69 ± 0.22	2.46 ± 0.15	1.07 ± 0.17	2.65 ± 0.22
$\theta_F$ (deg cm <sup>2</sup> dmol <sup>-1</sup> )	-22,067 ± 413	-23,009 ± 358	-21,790 ± 548	-21,112 ± 447
$m_F$	61.3 ± 16.7	59.9 ± 14.03	87.2 ± 27.1	99.1 ± 20.6
$\theta_u$ (deg cm <sup>2</sup> dmol <sup>-1</sup> )	-3,566 ± 1062	-2,830 ± 876	-2,986 ± 887	-4,078 ± 545
$m_u$	-7.4 ± 13.0	-15.0 ± 10.7	-5.0 ± 11.0	0.0 ± 7.0
$\Delta G_{20}^c$ (kJ mol <sup>-1</sup> )	33.5	32.8	29.97	30.94
$\Delta S_{20}^c$ (J mol <sup>-1</sup> k <sup>-1</sup> )	57	-8.95	46.31	36.7
$\Delta H_{20}^c$ (kJ mol <sup>-1</sup> )	50.23	30.21	43.54	41.70
$K_f^c$ (M <sup>-1</sup> , 20 °C)	9.19 10 <sup>5</sup>	7.09 10 <sup>5</sup>	2.18 10 <sup>5</sup>	3.26 10 <sup>5</sup>
$K_u^c$ (μM, 20 °C)	<b>1.09</b>	<b>1.41</b>	<b>4.58</b>	<b>3.07</b>
Dark/340nm PSS		1.30		0.67
Adjusted R <sup>2</sup>	0.997	0.998	0.996	0.997
RMSE	300.1	248.2	298.9	248.5

<sup>a</sup>  $\Delta H^{\circ}$  and  $T^{\circ}$  are the enthalpy and the temperature where  $\Delta G = 0$  and  $K_U = K_F = 1$ . <sup>b</sup>  $\Delta C_p$  is the change in heat capacity upon unfolding. <sup>c</sup> Binding model at 20 (°C).

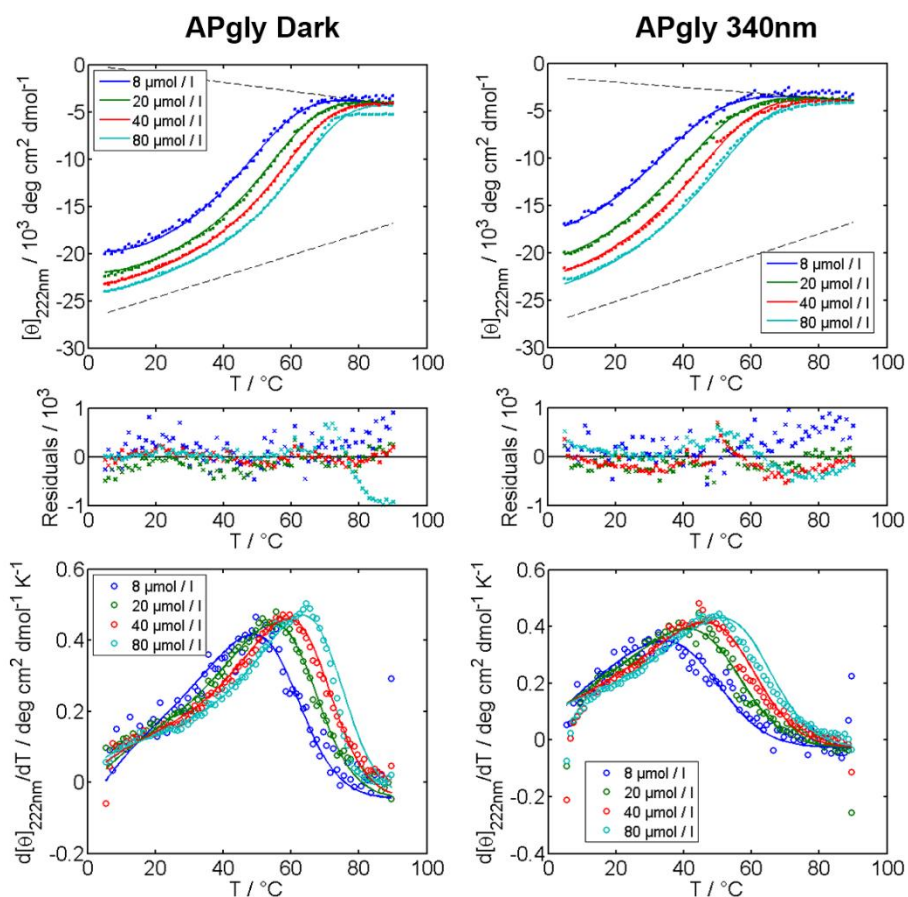


**Figure S5.4:** Fitting of CD melting curves (top) for peptide  $K_3$ -APgly with  $E_3GY$  in the dark adapted (left) and 340 nm irradiated (right) states performed by the Fitdis software program. Residuals (middle) and derivatives (bottom) of the best (dimeric) fitting model are shown. Measurements were performed in PBS.

**Table S5.2:** Fit results of thermal unfolding curves for K<sub>3</sub> peptides containing azophenylglycine with coiled-coil binding partner E<sub>3</sub>GY, in either the dark adapted or 340 nm irradiated state

Coiled-coil system	K <sub>3</sub> -APgly dark	K <sub>3</sub> -APgly 340 nm
$\Delta H^{\circ a}$ (kJ mol <sup>-1</sup> )	285.2 ± 6.5	236 ± 7.1
T <sup>o b</sup> (°C)	113 ± 1.2	110.5 ± 1.9
$\Delta C_p$ (kJ mol <sup>-1</sup> k <sup>-1</sup> )	2.8 ± 0.13	2.15 ± 0.14
$\theta_F$ (deg cm <sup>2</sup> dmol <sup>-1</sup> )	-26877 ± 353	-27513 ± 520
m <sub>F</sub>	112 ± 12.6	119 ± 23.9
$\theta_u$ (deg cm <sup>2</sup> dmol <sup>-1</sup> )	0 ± 1153	-1424 ± 687
m <sub>u</sub>	-46.6 ± 13.9	-28 ± 8.7
$\Delta G_{20}^c$ (kJ mol <sup>-1</sup> )	34.5	30.7
$\Delta S_{20}^c$ (J mol <sup>-1</sup> k <sup>-1</sup> )	-33	37.9
$\Delta H_{20}^c$ (kJ mol <sup>-1</sup> )	24.8	41.8
K <sub>f</sub> <sup>c</sup> (M <sup>-1</sup> , 20 °C)	1.38 10 <sup>6</sup>	2.97 10 <sup>5</sup>
K <sub>u</sub> <sup>c</sup> (μM, 20 °C)	<b>0.72</b>	<b>3.37</b>
Dark/340nm PSS		4.65
Adjusted R <sup>2</sup>	0.998	0.998
RMSE	274.3	288.7

<sup>a</sup>  $\Delta H^{\circ}$  and T<sup>o</sup> are the enthalpy and the temperature where  $\Delta G = 0$  and  $K_U = K_F = 1$ . <sup>b</sup>  $\Delta C_p$  is the change in heat capacity upon unfolding. <sup>c</sup> Binding model at 20 (°C).

## MD simulations

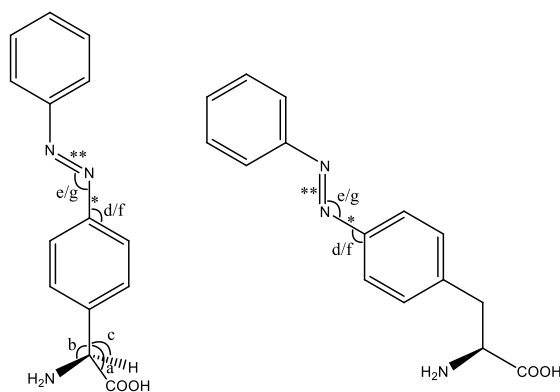


**Table S5.3:** Bond lengths, angles and dihedral angles for new atom types required for the integration of **APgly** (top left) and **APhe1** (top right) into the AMBER-96 force field for molecular dynamics simulations of azobenzene-amino acids. Bond lengths and angles as computed at BLYP-D3(BJ)/TZ2P.

	Bond type	Residue	Bond length (nm)	Force constant (kJ mol <sup>-1</sup> nm <sup>-1</sup> )	Adapted from
*	CA-NX	All	0.14398	357313.6	CA-NA
**	NX-NX	All	0.14354	357313.6	CA-NA

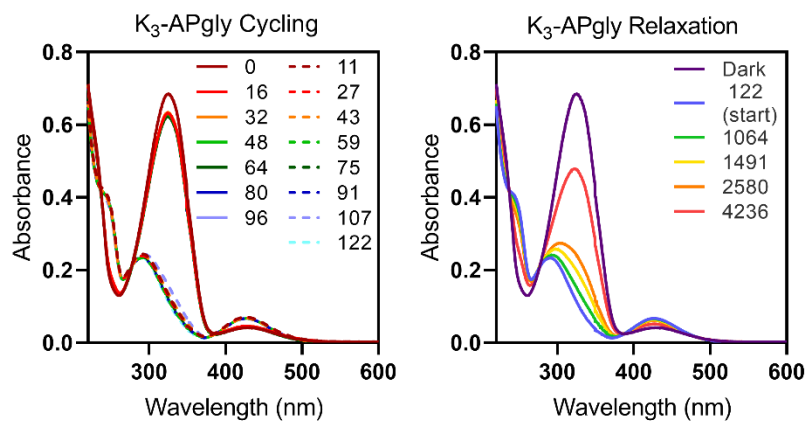
  

	Angle type	Residue	Angle (degrees)	Force constant (kJ mol <sup>-1</sup> rad <sup>-1</sup> )	Adapted from
a	CA-CT-C	Diazophenylglycine	109.139	527.184	CA-CT-CT
b	CA-CT-N	Diazophenylglycine	110.762	527.184	C-CT-N
c	CA-CT-H1	Diazophenylglycine	108.439	418.400	CA-CT-HC
d	CA-CA-NX	Cis	119.225	585.760	NA-CN-NC
e	CA-NX-NX	Cis	121.626	585.760	NA-CN-NC
f	CA-CA-NX	Trans	121.615	585.760	NA-CN-NC
g	CA-NX-NX	Trans	115.088	585.760	NA-CN-NC

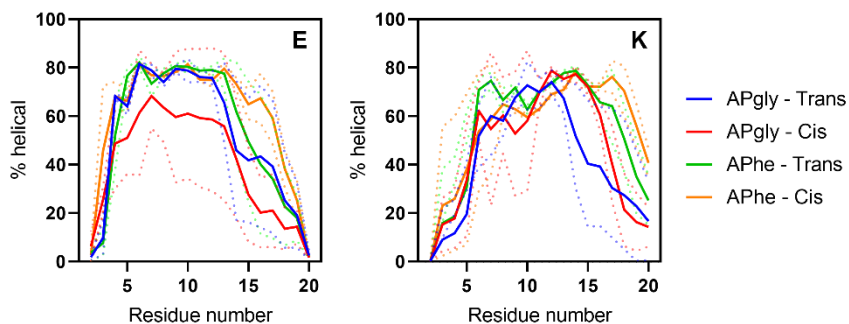
  

	Dihedral type	Residue	Dihedral angle (degrees)	Force constant (kJ mol <sup>-1</sup> rad <sup>-2</sup> )	Adapted from
	CA-CA-CA-NX	All	180.0 (improper)	4.60240	CA-CA-CA-NT
	CA-NX-NX-CA	Cis	186.5 (proper)	6.27600 <sup>†</sup>	X-CA-NA-X
	CA-NX-NX-CA	Trans	180.1 (proper)	6.27600 <sup>†</sup>	X-CA-NA-X
	CA-CA-NX-NX	Cis	227.4 (proper)	6.27600	X-CA-NA-X
	CA-CA-NX-NX	Trans	180.1 (proper)	6.27600	X-CA-NA-X

<sup>†</sup>Set to 1000 kJ mol<sup>-1</sup> rad<sup>-2</sup> for production runs

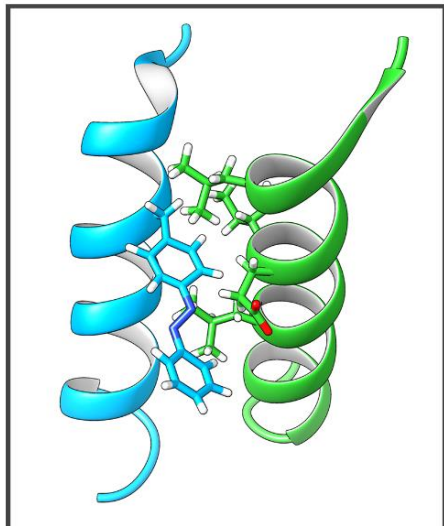


**Figure S5.5:** UV-Vis spectra of peptide  $K_3$ -APgly cycling between different photostationary states (left) and relaxing from the 340 nm PSS (right), which were used to prepare **Figure 5.5**. Spectra after illumination with 340 nm light are indicated with dotted lines (left). Graphs are numbered by time after start of the experiment. Measurements were performed at 20 °C in PBS with [peptide] = 50  $\mu$ M.

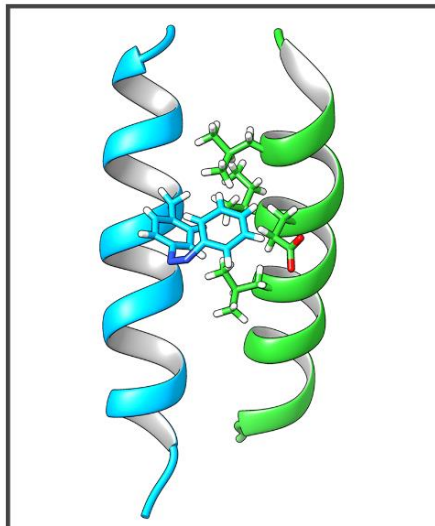


**Figure S5.6:** Percentage of amino acids classified as helical (based on GROMACS' default criteria for psi/phi dihedral angles and H-bond distances) over 500 ns of simulation time, for all amino acids in peptide E (left) and peptide K (right), averaged over 3 independent MD simulations. Standard deviations are plotted as dotted lines.

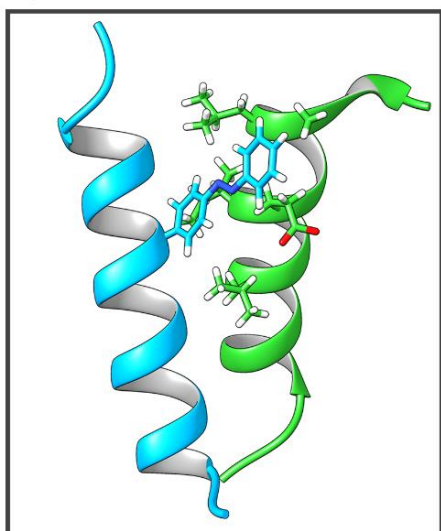
**K<sub>3</sub>-APhe1 trans**



**K<sub>3</sub>-APhe1 cis**



**K<sub>3</sub>-APgly trans**



**K<sub>3</sub>-APgly cis**

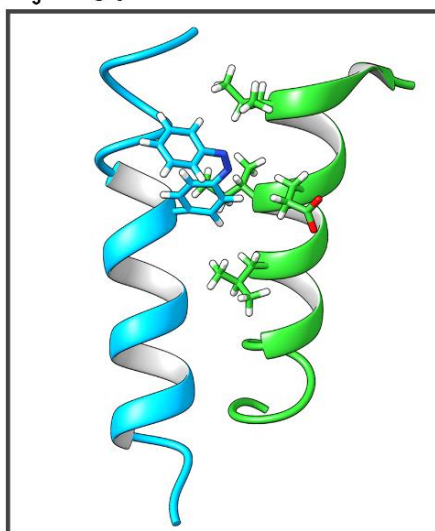


**Figure S5.7:** Snapshots from MD simulations of the coiled coil between peptide K<sub>3</sub> (blue) and E<sub>3</sub> (green), with peptide K<sub>3</sub> containing the photoswitchable amino acid **APhe1** or **APgly** at position 9 in the peptide sequence, in the *trans* or *cis* conformation. Peptides backbones are shown as a cartoon, with the photoswitch and all amino acid side chains of peptide E<sub>3</sub> within 5 Å displayed as sticks.

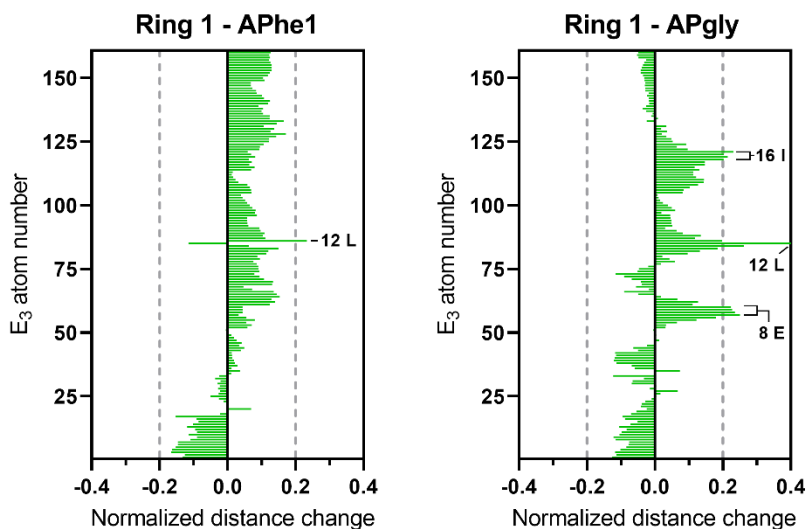
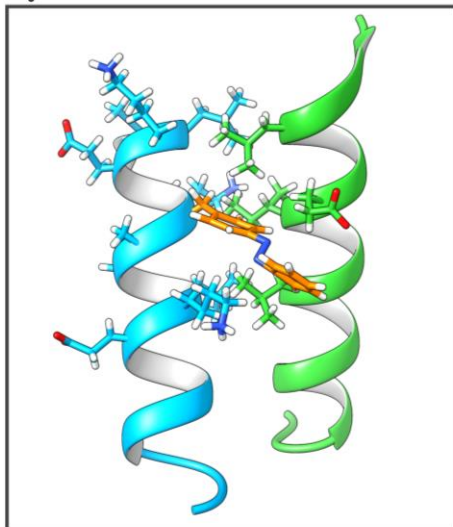
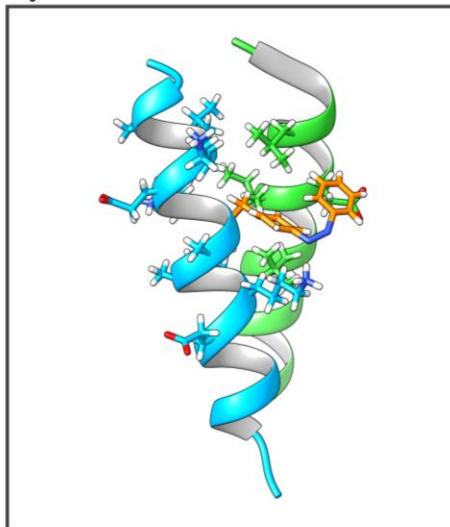


**Figure S5.8:** Normalized change in distance upon photoisomerization between the non-hydrogen atoms in peptide  $E_3$  and the azobenzene ring 1 (closest to the peptide backbone). Change in distance upon *trans* to *cis* isomerization of the azobenzene is normalized to the *trans* conformation, with positive values indicating more distance in the *cis* conformation. Distances are averaged over 3 simulations of 500 ns. Dotted lines indicate an arbitrary cut-off for significance of 0.2.

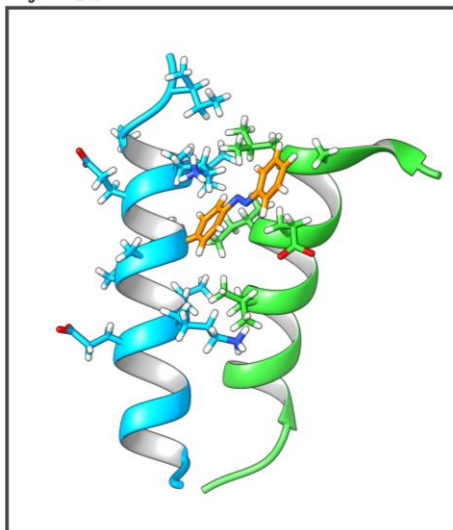
**K<sub>3</sub>-APhe1 trans**



**K<sub>3</sub>-APhe1 cis**



**K<sub>3</sub>-APgly trans**



**K<sub>3</sub>-APgly cis**

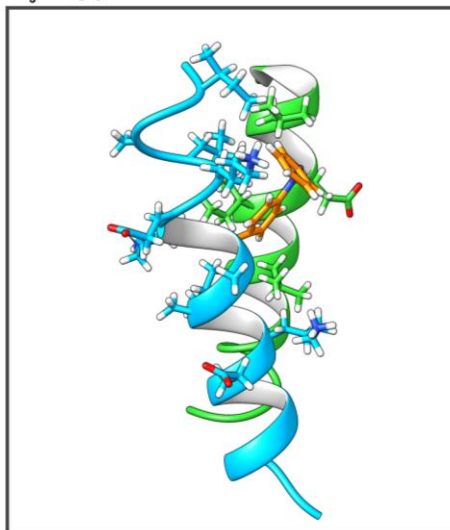


**Figure S5.9:** Snapshots from MD simulations of the coiled coil between E<sub>3</sub> (green) and K<sub>3</sub> (blue) containing APhe1 or APgly at position 9 in the peptide sequence, in either the cis or trans conformation. Photoswitchable amino acids in peptide K<sub>3</sub> have been coloured orange for clarity. Peptides backbones are shown as a cartoon, with the photoswitch and all amino acid side chains within 5 Å displayed as sticks.

*LC-MS of purified peptides***Table S5.4:** Overview of the calculated masses of all peptides used in this project, and the masses found by LCMS.

Peptide name	Calculated mass (Da)	Measured mass (Da)
E <sub>3</sub> GY	[M + 2H <sup>+</sup> ] <sup>2+</sup> 1272.69	1271.24
	[M + H <sup>+</sup> ] <sup>+</sup> 2544.39	2545.88
K <sub>3</sub> -P9-APhe1	[M + 2H <sup>+</sup> ] <sup>2+</sup> 1230.24	1228.81
K <sub>3</sub> -P9-APhe2	[M + 2H <sup>+</sup> ] <sup>2+</sup> 1252.24	1250.85
K <sub>3</sub> -P9-APgly	[M + 2H <sup>+</sup> ] <sup>2+</sup> 1223.23	1222.23





---

## Photoswitchable $\beta$ -sheet forming peptides

This chapter is in preparation as an original research paper: Niek S.A. Crone, Mousumi Samanta, Dinghao Wu, Elena Egorova, Panagiota Papadopoulou, Aimee L. Boyle, Gonen Ashkenasy, Alexander Kros, **2022**.

## Abstract

Controlling the folding of  $\beta$ -sheet peptides is of interest as a tool for the generation of responsive (bio)materials. The change in structure and polarity associated with azobenzene photoisomerization was hypothesized to disrupt  $\beta$ -sheet self-assembly when substituting other hydrophobic amino acids. To test this hypothesis, peptides were prepared based on the (EF)<sub>5</sub>EP peptide sequence which is known to form  $\beta$ -sheet fibres. Modification of a single phenylalanine to an azobenzene resulted in peptide self-assembly at lower salt concentrations. Both  $\beta$ -structure and critical aggregation concentration could be altered via photoisomerization, with the biggest effect observed with the azobenzene positioned in the peptide centre. Azobenzene-containing peptides showed self-assembly as peptide fibres, with fibre oligomerization observed when the azobenzene was positioned at the peptide terminus. Histidine containing peptide variants were subsequently prepared, and showed organocatalytic activity in ester hydrolysis that could be altered by azobenzene isomerization. Together, this study demonstrates the incorporation of amino acids carrying azobenzene moieties as a novel method for active control over  $\beta$ -structure, peptide self-assembly and activity.

## 6.1 Introduction

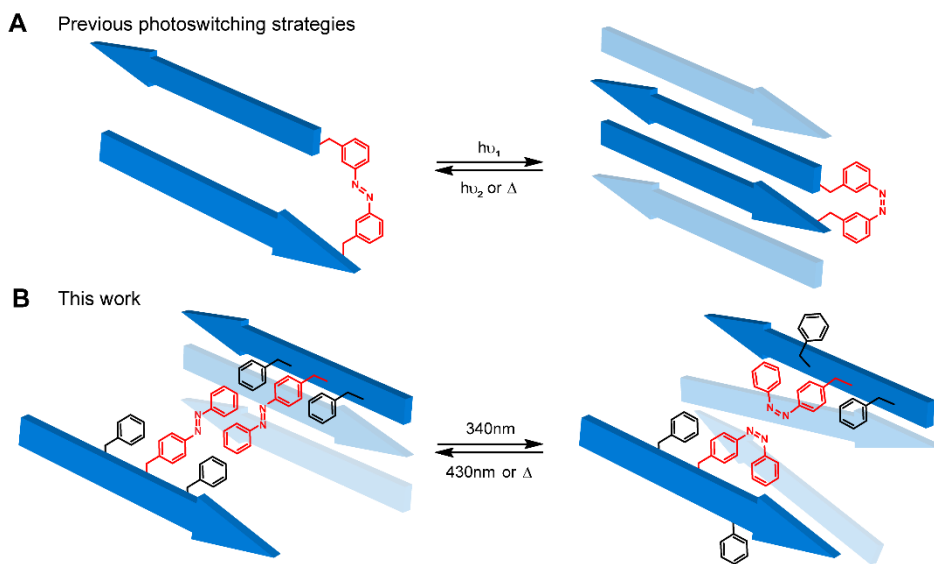
Peptides and proteins adopt three-dimensional structures in order to minimize backbone steric clashes, maximize potential hydrogen bonding interactions and facilitate favourable side-chain interactions.<sup>1</sup> One of the most dominant folds is the  $\beta$ -sheet, consisting of multiple  $\beta$ -strands connected laterally through hydrogen bonds between backbone peptide amides. Each amino acid can be defined by its tendency to fold into  $\alpha$ -helices or  $\beta$ -structures,<sup>2</sup> but the pattern in which polar and hydrophobic amino acids are repeated is what predominantly determines the type of fold.<sup>3</sup> In the previous chapters the focus has been on controlling the folding and oligomerization of  $\alpha$ -helical coiled-coil peptides, including active photocontrol via the introduction of azobenzene moieties. Active control over the folding and self-assembly of  $\beta$ -rich structures is of much interest as well, not only as a tool for the study of natural peptides and proteins, but also as a way to control assembly and (bio)activity of materials based on the  $\beta$ -strand structure.<sup>4,5</sup>

As discussed in **Chapter 4**, using light as a method of structural control has the advantage of spatial and temporal resolution in combination with biocompatibility, all of which are desirable properties for biomaterials. Photocontrol over  $\beta$ -dominant structures was first demonstrated by the groups of Hilvert and Renner, who independently worked on  $\beta$ -hairpins incorporating azobenzene turn motifs.<sup>6,7</sup> Both groups used [3-(3-aminomethyl)-phenylazo]phenylacetic acid (AMPP), an asymmetric azobenzene linker, as a photoswitchable turn motif. The *cis* isomer of AMPP is used to position two pentamer peptide sequences at an appropriate distance for hydrogen bond formation, mimicking a  $\beta$ -hairpin, where the *trans* isomer has the wrong geometry to form this structure (**Scheme 6.1A**). This initial research was focussed on gaining understanding over the structure of hairpins and to serve as a model for their folding that could be studied on an ultra-fast timescale.<sup>8-10</sup>

The use of this AMPP linker has been extended to amyloid-forming peptides, demonstrating control over intermolecular self-assembly.<sup>11</sup> The formation of amyloid structures is initiated by protein misfolding resulting in a  $\beta$ -hairpin.<sup>12</sup> This hairpin motif acts as a nucleation point for other proteins, eventually leading to formation of amyloid fibrils. Incorporation of the AMPP linker in the amyloid  $\beta$ -peptide A $\beta$ <sub>1-42</sub> yielded control over the tendency to form hairpins via

photoisomerization, with a transition to the *cis* isomer resulting in amyloid fibril nucleation and altered *in vitro* cytotoxicity.<sup>13, 14</sup> Although AMPP introduces photoswitching in  $\beta$ -hairpins, its use outside of model systems has been limited since it can only be used in small, synthetic systems with hairpin domains that are suitable for substitution with the photoactive moiety.

In **Chapter 5** of this thesis the ability of azobenzene-based amino acids to control the folding of coiled-coil peptides was demonstrated; showing that a single amino acid modification can have a significant effect on coiled-coil binding strength. The *trans* to *cis* transition of the azobenzene changes the polarity of the diazene bond, resulting in a destabilization of the hydrophobic coiled-coil interface. We hypothesize that this mechanism of action extends to  $\beta$ -sheet structures, as illustrated in **Scheme 6.1B**, if they self-assemble to form a hydrophobic domain. Specifically, the introduction of phenylazo-phenylalanine (**APhe**), a light-switchable derivative of phenylalanine, is a logical modification of phenylalanine-rich  $\beta$ -sheet domains for the introduction of photoresponsive self-assembly and activity.



**Scheme 6.1:** Previous work demonstrating light activated  $\beta$ -hairpin self-assembly (A) and the method investigated in this chapter for photocontrol of  $\beta$ -sheet self-assembly through disruption of the hydrophobic domain (B). Hairpin photocontrol makes use of an azobenzene crosslinker to connect two  $\beta$ -strand sequences, and alter their proximity by isomerization. The strategy in this chapter uses **APhe**, a light-active derivative of phenylalanine, to control self-assembly of  $\beta$ -strand hydrophobic domains.

Inspired by the work on  $\beta$ -sheet peptide assembly and self-replication in the group of G. Ashkenasy,<sup>15,16</sup> the  $\beta$ -sheet forming peptides studied in this chapter are based on the  $(EF)_n$  repeat sequence. This peptide belongs to a family with the general sequence  $(XFXF)_n$ , where  $X$  is a polar amino acid, and peptides of this family readily form  $\beta$ -structured self-assemblies.<sup>17</sup> With this alternating amino acid sequence, all hydrophobic side chains are on the same face, resulting in formation of cofacial  $\beta$ -sheet bilayers with all hydrophobic amino acids in the interior of the bilayer.<sup>18</sup> These cofacial  $\beta$ -sheets are comparable to the amyloid cross- $\beta$  structure,<sup>19,20</sup> and this class of peptides is often used as a model system for amyloid self-assembly.<sup>21,22</sup> Peptides based on the  $(XFXF)_n$  sequence have been observed to form  $\beta$ -fibres, helical ribbons or tapes and amyloid-like aggregates.<sup>18,22-24</sup> These larger structures are all based on the same cofacial  $\beta$ -sheet structure repeating in different axes, and can be selected for by alteration of amino acid composition, sequence length and amino acid chirality.<sup>22,24-26</sup> Substituting phenylalanine with large naphthalene and naphthalene diimide moieties was also well tolerated in these peptides,<sup>27,28</sup> indicating that incorporation of **APhe** is feasible. For this study, peptide 2 (**Pep2**) from the previous work of Rubinov *et. al.*<sup>16</sup> was prepared, in addition to analogues where a single phenylalanine was substituted by **APhe**. Control over peptide structure could be achieved via azobenzene photoisomerization which resulted in altered self-assembly characteristics. As a proof of concept, modified variants containing histidine residues as catalytic sites were prepared, and photoisomerization was shown to affect organocatalytic activity.

## 6.2 Results and Discussion

Fmoc-protected **APhe** (**1**, **Figure 6.1A**) based on L-phenylalanine was synthesized according to literature procedures for use in solid phase peptide synthesis (SPPS).<sup>29</sup> A detailed description of the synthesis can be found in **Chapter 5** of this thesis. Isomerization characteristics of **1** in acetonitrile were characterized via liquid chromatography (LC) and showed that in the dark **1** was over 96% in the *trans* configuration (see **Figure 6.1B** and **Figure 6.1C**). Isomerization to the *cis* isomer was performed most effectively using 340 nm light, yielding 90% conversion to *cis*, with a thermal half-life at 20 °C of 27.2h (**figure 6.1D**). Light with a higher wavelength yielded predominantly the *trans* isomer, with no difference observed using wavelengths between 375 nm and 450 nm. Illumination of samples at thermal equilibrium with 435 nm light yielded the same isomeric ratio as samples pre-illuminated with 340 nm, showing these are the photostationary states of the

azobenzene. Up to 81% of the *trans* isomer could be achieved using wavelengths of light between 385 nm and 450 nm, which is less than before illumination, and limits the effect of switching over multiple cycles to approximately 70% of what would theoretically be possible if the azobenzene could be cycled between exclusively the *cis* and *trans* isomers.

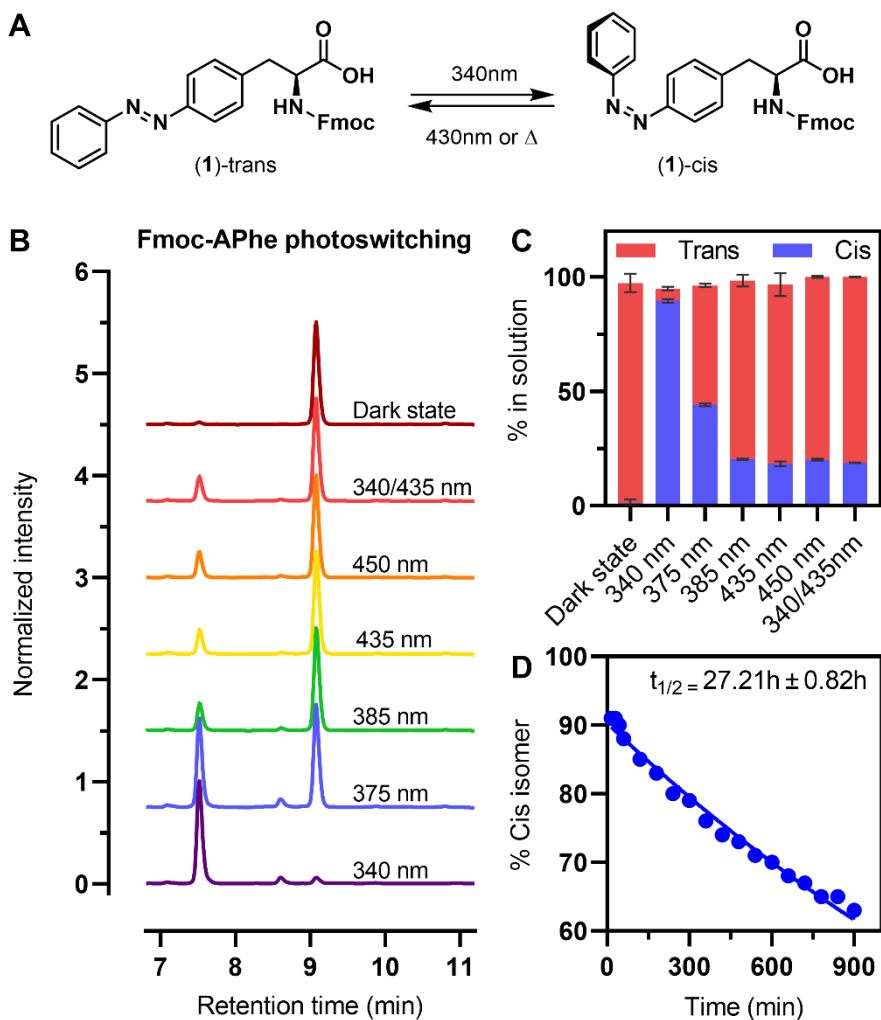


**Figure 6.1:** Structural differences between the *cis* and *trans* isomers of Fmoc-APhe (A). Liquid chromatography spectra of **1** when illuminated with different wavelengths of light (B), percentage of *cis* and *trans* isomers in solution for the different photostationary states derived from their LC Spectra (D), and thermal relaxation of the *cis* isomer of **1** (C). The isomerization and relaxation studies were performed at 20 °C [**1**]= 200 μM in MeCN. Error bars show differences for 3 repeat measurements.

*Peptide design and structural analysis*

The  $\beta$ -sheet forming peptide **Pep2** (**Figure 6.2**) was modified with **APhe** by replacing a single phenylalanine at position 2 (**P2**) or position 6 (**P6**) to probe the ability to photoswitch these peptides. Because the **APhe** moiety is larger in size than phenylalanine, any beta-sheet domain will have to change shape to allow complete incorporation of the amino acid into the hydrophobic core. This change in shape is expected to be different depending on the location of **APhe**, and should therefore result in different self-assembly dynamics.

Self-assembly of **Pep2** and its derivatives was first assayed via circular dichroism (CD) spectroscopy to observe under which conditions  $\beta$ -sheet assembly occurred. Peptides rich in  $\beta$ -structures can be classified by the alignment of adjacent strands (parallel or anti-parallel) and the presence of twist within the  $\beta$ -strand, all of which have their own distinguishable CD absorption bands.<sup>30</sup> **Pep2** showed a low CD signal when dissolved in phosphate buffer at a 100  $\mu$ M peptide concentration, with no characteristic bands for any type of  $\beta$ -structure. Because the presence of salts in solution increases the hydrophobic effect, and can aid self-assembly by the formation of salt bridges between charged amino acid side chains, the dependence of folding on salt concentration was assayed. Adding  $\text{Na}_2\text{SO}_4$  to the buffer to increase peptide-peptide interactions caused a change in structure, with two negative absorption bands appearing; a sharp band at 202 nm and a broad band with a minimum at 218 nm (**Figure 6.2, left**). Titration experiments showed a sigmoidal dependence of the CD signal on the salt concentration with a mid-point ( $f_{1/2}$ ) at 0.85 M  $\text{Na}_2\text{SO}_4$ . When the salt concentration was kept constant at 1 M  $\text{Na}_2\text{SO}_4$ , an initial linear dependence of structure on peptide concentration was observed with a maximum at approximately 150  $\mu$ M (**Figure S6.1**).

Peptide variants **P2** and **P6** showed similar spectral shapes to **Pep2**, in the absence of salt, but with more intense minima. Both variants showed signal increase upon  $\text{Na}_2\text{SO}_4$  addition, with clear differences observed between the dark and light (illuminated with 340 nm) state of the peptides. Peptide **P2** showed similar absorption peaks as **Pep2** when salt was added, with minima located at 204 and 216 nm. Lower absorption minima were observed for **P2**, indicating a higher degree of folding, but in a more irregular manner as suggested by lower separation between the peaks. The spectrum of **P6** shows a single clear absorption minimum at 225 nm, with the absorption rising sharply below that wavelength, suggesting a strong absorption maximum between 195-200 nm. This spectrum is consistent with

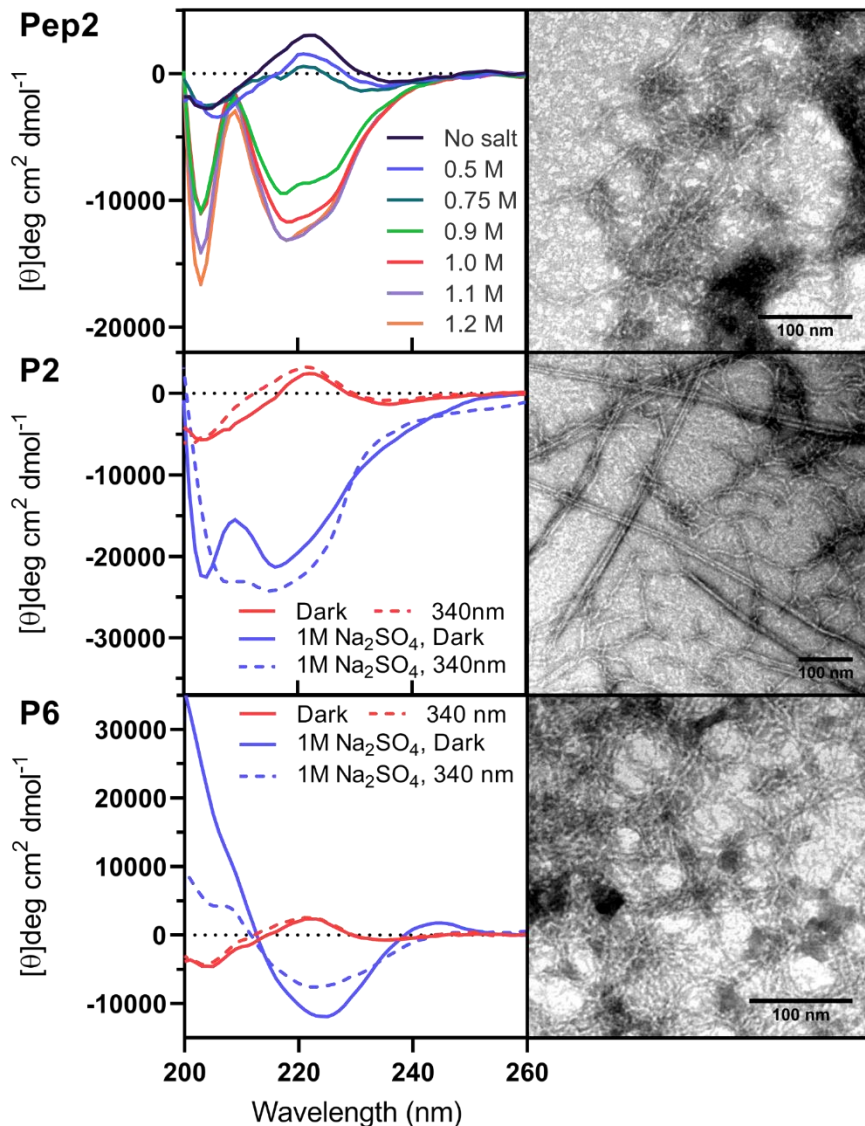
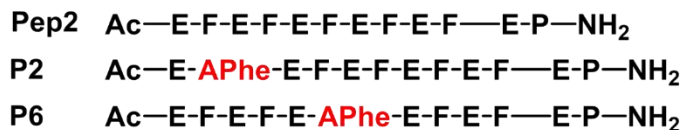


**Figure 6.2:** Schematic structure of the peptide variants prepared for photoswitching studies (top), their solution CD spectra with varying levels of Na<sub>2</sub>SO<sub>4</sub> (bottom left) and TEM images of their formed structures (bottom right). CD spectra were recorded at 100 μM peptide concentration, with 10 mM PB at pH 7.2.

that of left-twisted anti-parallel  $\beta$ -sheet peptides, with the maxima slightly blue shifted. Upon irradiation of the **APhe** containing peptides with 340 nm light, the CD spectra changed, indicative of structural rearrangement in the peptide assembly. The **P2** variant has a slightly stronger absorption minima at 216 nm, with the two absorption minima observed for the dark state broadening to the point that they are difficult to distinguish. The **P6** variant shows a general decrease in signal strength upon irradiation, with a less intense and blue shifted absorption band, and a less steep increase in signal at the lower wavelengths. Other salts were also tested for their effects on peptide folding, with the largest effect observed for  $\text{Na}_2\text{SO}_4$  (**Figure S6.2**), which was used for all further experiments.

The CD spectra show  $\beta$ -sheet structures for all three peptides when salt is present in solution, which is the main mechanism for their self-assembly into peptide fibres. To characterize their self-assembly, samples were imaged using transmission electron microscopy (TEM), revealing the presence of long fibrillar structures for all three peptides (**Figure 6.2, right**). Samples of **P6** contained fibres with a width of  $5.7 \pm 0.5$  nm, which is comparable to the thickness of fibres observed for the parent peptide **Pep2** ( $5.5 \pm 0.4$  nm). Thicker and less uniform ( $7.2 \pm 1.0$  nm) fibres were observed for **P2**, which additionally showed larger, linear assemblies that appear to consist of 2 (double) or more (multiple) fibres bundled together. Analysis of the larger assemblies in the **P2** sample (representative image shown in **Figure S6.3**) shows a repeating pattern with spacing of the same size as single fibres. An overview of fibre thickness is given in **Figure S6.4** and **Table S6.1**. These results suggest that peptide **P2** is capable of forming peptide fibres, similar to the other two peptides, although with a different overall structure since the CD signal of the peptide is quite different and fibre oligomerization is observed. This polymerization of **P2** peptide fibres suggests that the ends of the  $\beta$ -sheet, where the peptide termini are located, are not as stable as for the other two variants. The **APhe** moiety is relatively large and more hydrophobic compared to phenylalanine, and when placed at the termini such as in peptide **P2** likely results in rearrangement of the fibre structure to minimize interactions between the azobenzene and the aqueous environment. Aggregation of multiple fibres at the terminal ends would allow the azobenzene to be shielded from the environment by the neighbouring fibre, resulting in a more classical  $\beta$ -sheet structure.

Because a characteristic dependence of peptide folding on the concentration of dissolved salts was observed for peptide **Pep2**, titrations were performed with its **APhe** substituted derivatives. The light irradiated (*cis* dominant) and thermally

equilibrated (*trans* dominant) states of **P2** at 100  $\mu\text{M}$  showed different behaviours, with the *trans* dominant sample folding at a lower salt concentration ( $f_{1/2} = 0.66 \text{ M}$  vs 0.79 M, **Figure 6.3** and **Figure S6.5**) but the irradiated state shows a stronger signal at 218 nm. A different behaviour was observed for **P6**, where the dark state showed both a lower midpoint ( $f_{1/2} = 0.45 \text{ M}$  vs 0.58 M, **Figure 6.3** and **Figure S6.6**) and a higher degree of overall folding. Comparing the response to changes in  $\text{Na}_2\text{SO}_4$  concentration for all three peptides shows that **APhe** modifications at position 6 has the largest effect on self-assembly, lowering the transition point for folding by 47% with respect to **Pep2**. Modification at the terminus, as seen in **P2**, also reduced this transition point by 22%, showing that the **APhe** amino acid has a favourable effect on peptide self-assembly. The transition point for salt-dependent

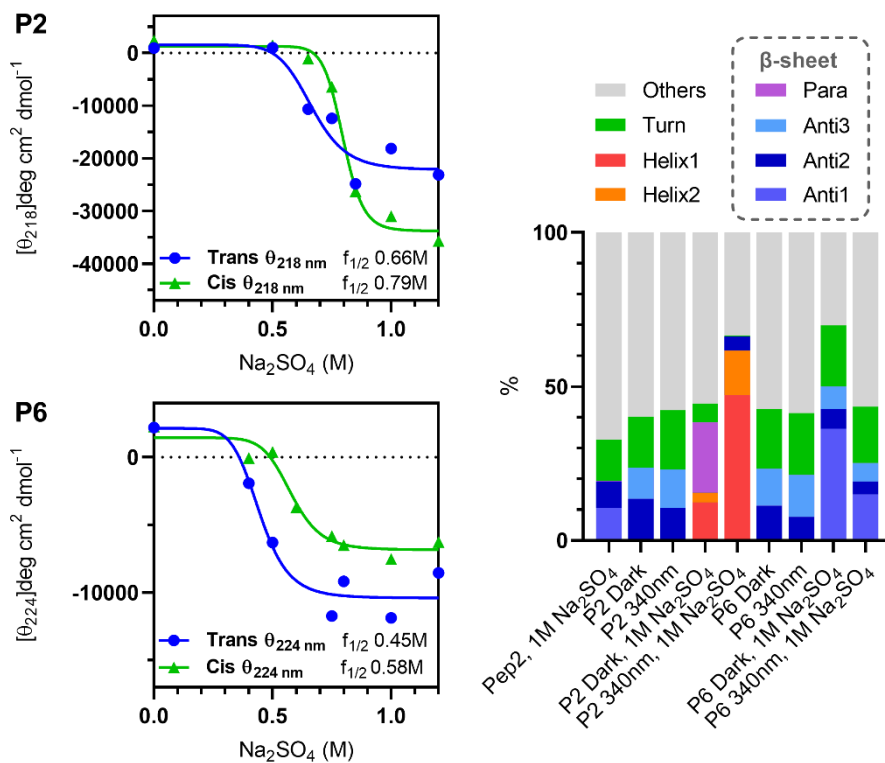


**Figure 6.3:** Structural dependence of peptides **P2** and **P6** on the concentration of sodium sulphate demonstrated via CD titrations (left), and structural deconvolution of CD spectra discussed in this chapter using the BeSTSel web server (right).<sup>31</sup> CD titrations were performed at 100  $\mu\text{M}$  peptide in 10 mM PB, complete spectra can be found in **Figure S6.5** and **Figure S6.6**. Figure legend: Anti1 = left-twisted  $\beta$ -strand; Anti2 = relaxed  $\beta$ -strand; Anti3 = right-twisted  $\beta$ -strand; Helix1 = regular  $\alpha$ -helix; Helix2 = distorted  $\alpha$ -helix; Para = Parallel  $\beta$ -strand.

self-assembly was different between the *cis* and *trans* state for both novel peptides, showing that these isomers have distinct self-assembly behaviours.

To better understand the structural components of the  $\beta$ -sheet forming peptides discussed in this chapter, the CD spectra in **Figure 6.2** were analysed using the BeStSel web server, which was specifically designed to deconvolute CD spectra of  $\beta$ -structure rich proteins.<sup>30, 31</sup> The results of this analysis are shown in **Figure 6.3** (right) and **Table S6.2**. Both **P2** and **P6** show a mixed structure, consisting of relaxed and left-twisted  $\beta$ -strands, and turn motifs when no salt is present. With 1 M  $\text{Na}_2\text{SO}_4$  **P6** shows increased folding (70% folded structures over 43% with no salt), dominated by right-twisted  $\beta$ -strand motif. Upon *trans* to *cis* isomerization of **P6**, the amount of folded structures is reduced by 26%, predominantly via loss of the right-twisted  $\beta$ -strand motifs (21% less). Analysis of peptide **P2** with salt shows a structure dominated by parallel  $\beta$ -strand motifs in the dark state, combined with some  $\alpha$ -helical structures. Upon light irradiation of **P2**, helical structures become recognized as the dominant structural fold. This originates from the two observed absorption minima at 218 nm and 202 nm and an apparent absorption maximum below 200 nm, which is similar but blue shifted from what one would expect for a helical peptide. However, the amino acid sequence should not be predisposed to form helical structures,<sup>2</sup> and the peptide is based on a known  $\beta$ -sheet forming sequence. Since the sequence of **P2** is not encountered in nature, it can adopt structures unfamiliar to the BeStSel algorithm, which was trained on solved protein structures. This is also supported by the lack of  $\beta$ -sheet structure attributed to **Pep2**, a known anti-parallel  $\beta$ -sheet forming peptide, by the BeStSel algorithm. Furthermore, the absorption peaks observed for **P2** resemble previously reported spectra for  $\beta$ -sheet forming peptides with the  $(\text{KFKE})_n$  repeat sequence.<sup>24, 32</sup> Because of this similarity in the CD spectra of **P2** to previously reported  $\beta$ -sheet peptides and its ability to form fibres in solution with a similar dimension to those of **Pep2** and **P6**; it most likely forms peptide fibres dominated by  $\beta$ -sheet structures.

#### *Characteristics of fibre formation*

The structural analysis via CD spectroscopy shows the dependence of peptide folding on concentration and solutes, which is related to the self-assembly of peptides into larger structures, but does not provide any insight into self-assembly. To further investigate the self-assembly into  $\beta$ -sheet fibres the critical aggregation concentration (CAC) was determined using dynamic light scattering (DLS). Plotting the observed count rate in DLS versus the peptide concentration shows two distinct

domains; one at lower concentration where the count rate did not increase significantly, and a domain at higher concentration where the count rate increased rapidly (**Figure 6.4A**). The intersect of these two domains is defined as the CAC for that condition (CAC data for all peptides and conditions can be found in **Table S6.3**). Peptide **P2** and **P6** both showed a low CAC with 1 M  $\text{Na}_2\text{SO}_4$  in solution, of 6 and 11  $\mu\text{M}$  respectively, which increased when samples were irradiated with 340 nm light. The CAC of **P2** increased 4.8 times after irradiation (**Figure 6.4A left**) and the CAC of **P6** increased by 1.8 times (**Figure S6.7**). The lower difference between the light and dark state was assumed to relate to the difference between the salt

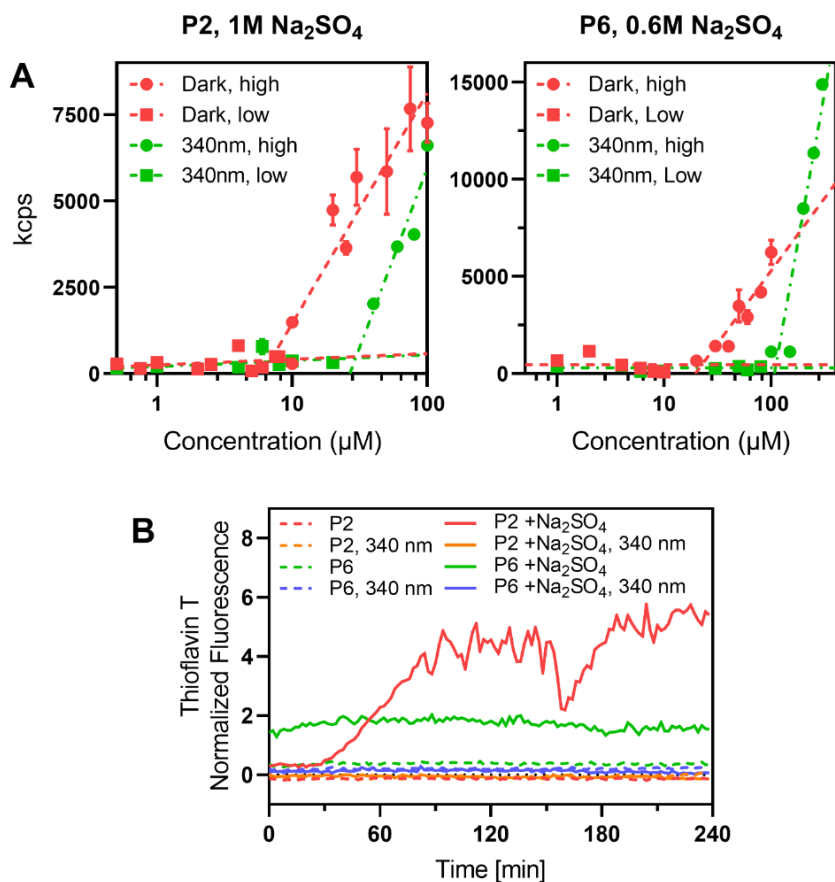


**Figure 6.4:** Light scattering count rate dependence on the concentration of peptides **P2** and **P6** for determination of CAC (A) and thioflavin T fluorescence used to observe the kinetics of beta-sheet fibre assembly at [peptide] = 100  $\mu\text{M}$  (B). Fluorescence was recorded at 490 nm and normalized to the fluorescence of Thioflavin T with no peptides in solution, which is set to 0. Fluorescence samples contained [ThT] = 100  $\mu\text{M}$  and [ $\text{Na}_2\text{SO}_4$ ] = 1 M if present.

dependence observed via CD spectroscopy. Therefore, the experiment was repeated for **P6** at a reduced concentration of 0.6 M Na<sub>2</sub>SO<sub>4</sub>, resulting in a 5-fold increase in CAC from 22 to 109 μM (**Figure 6.4A**, right). This indicates that the CD titration experiments relate well to formation of self-assembled aggregates.

To investigate the type and kinetics of self-assemblies formed by the peptides, Thioflavin T (ThT) was used as a fluorescent probe. The fluorescence behaviour of ThT is dependent on its environment; it is specifically known to bind to β-sheet rich protein domains, resulting in a large increase in fluorescence intensity and a shift in emission wavelength.<sup>33, 34</sup> Because of this property, it has been used in the study of amyloid fibres and plaques.<sup>35</sup> Kinetic experiments were performed with peptides **P2** and **P6** at 100 μM adapted to dark conditions or irradiated with 340 nm light, in PB with and without 1 M Na<sub>2</sub>SO<sub>4</sub>. Only the samples prepared with dark adapted peptides and containing 1 M Na<sub>2</sub>SO<sub>4</sub> showed a significant increase in ThT fluorescence. Peptide **P2** initially shows no fluorescence increase, but after 30 minutes a steady rise in the signal observed, which evens out at 5-fold more fluorescence after 4 hours. In contrast, **P6** showed an immediate increase, stabilizing around a 2-fold increase in fluorescence during the remainder of the experiment.

Overall, we observed different assembly kinetics for the two azobenzene containing peptide variants; fast assembly for **P6** and nucleated self-assembly for **P2**. The fluorescence of **P6** is increased from the start of the experiment (about 30 seconds after mixing) and quickly reaches a plateau where ThT fluorescence intensity does not change. In contrast, a lag phase is observed at the start of the experiment for **P2**, followed by an increase in fluorescence that keeps going through the remainder of the experiment. This suggests the requirement for a nucleation point or β-sheet seed that initiates the self-assembly process. This nucleated assembly is very similar to what has been observed for amyloid-like aggregates of insulin, a known model system for amyloidogenic proteins.<sup>35</sup> This comparable kinetic mechanism strengthens the idea that the fibres formed by **P2** form β-sheet dominated structures similar to amyloids. With no salt in solution both peptides were unable to form these larger structures, mirroring the observed effect of salt on β-sheet structure observed in CD experiments. No increase in signal was observed if peptide samples were pre-irradiated with 340 nm light, showing that the effect of **APhe** isomerization observed in CD and CAC experiments is large enough to control intermolecular self-assembly.

### *Cryo-EM analysis of P6*

The solution-based experiments show that peptide self-assembly is dependent on both peptide concentration and dissolved solutes. This raises the question; how well do the peptide fibres observed with TEM in **Figure 6.2** represent the structure of the peptides observed in solution? The TEM samples of these peptides are prepared from high-concentration peptide stock solutions containing no added  $\text{Na}_2\text{SO}_4$ , which seems essential for self-assembly. Furthermore, the drying of the sample and negative staining with uranyl acetate might influence their morphology in a manner which is difficult to predict. Therefore, peptide **P6** was also investigated via cryogenic electron microscopy (cryo-EM), shown in **Figure 6.5**. Long (>100 nm) fibres were observed with a diameter of  $4.5 \pm 0.9$  nm, which is comparable in size to those observed in TEM ( $5.7 \pm 0.5$  nm). The slight (not significant) difference in average size can be explained by the drying and staining procedures discussed above.

Previous use of peptides with  $(\text{EF})_x$  repeat motifs showed formation of self-assembled structures in MD simulations consisting of two antiparallel  $\beta$ -sheet monolayers oriented antiparallel to each other,<sup>36</sup> similar to the previously discussed cross- $\beta$  structure. A model of **P6** was prepared assuming this structure, and is shown in **Figure 6.6**. A cross-section of this structure has a width of 4.6 nm (**Figure S6.8**), which reflects the observed fibre width in TEM and cryo-EM. Therefore, we conclude that the structure of **P6** is likely the discussed double antiparallel  $\beta$ -sheet, with the width of the fibre equalling the length of a single peptide chain.

### *Introduction of catalytic activity*

The light-controlled self-assembly of beta-sheet fibres of peptides **P6** and **P2** might enable control over structure-related activity of these peptides. variants of **P6** were synthesized containing a histidine (His) in its sequence. Histidine has a nucleophilic nitrogen with a  $\text{pK}_a$  between 6 and 7 depending on its environment,<sup>37</sup> allowing it to function both as a proton transfer group as well as a nucleophilic catalyst. In various self-assembled systems, introduction of His moieties has been shown to result in organocatalytic activity of self-assembled materials.<sup>38-40</sup> Peptide **P6** was chosen over **P2** because it self-assembles at a lower salt concentration, and has only been observed to self-assemble into one structure which is highly folded as an antiparallel  $\beta$ -sheet.

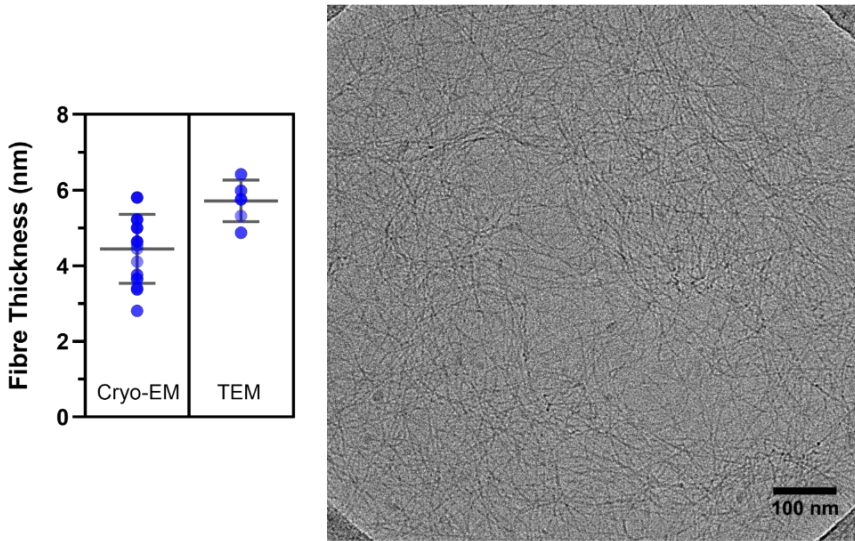


**Figure 6.5:** Cryo-EM images of fibres formed by peptide **P6** in solution (right), and distribution plot of the measured fibre width in nm (left) for both cryo-electron microscopy and transmission electron microscopy. Scale bar indicates 100 nm, and the image was recorded at 36K magnification, yielding a nominal pixel size of 2.8 ångström (Å).

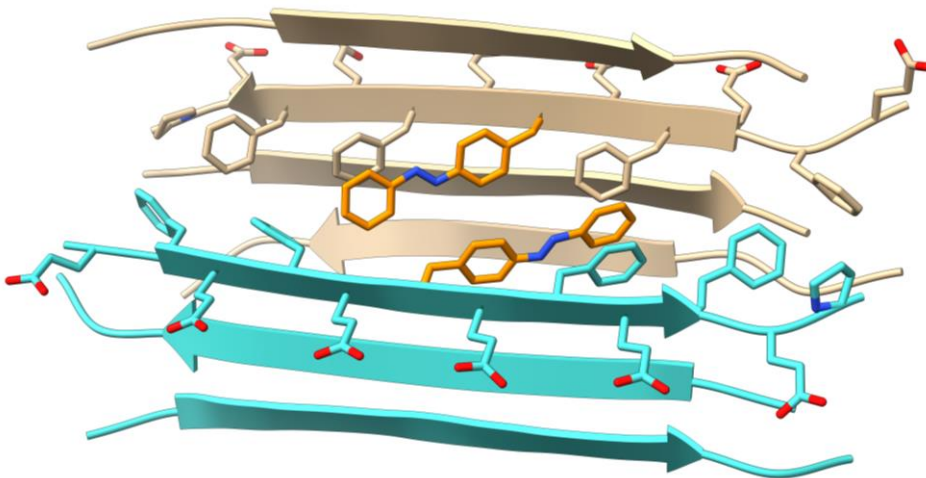


**Figure 6.6:** Model showing **P6** assembled into a double antiparallel  $\beta$ -sheet structure, which is the hypothesized structure for the peptide fibres observed under TEM and Cryo-EM. Two opposing strands are coloured separately for clarity and have their side chains displayed, with the **Aphe** moiety coloured orange. The remaining strands are displayed as a cartoon, showing the direction of the  $\beta$ -sheet fibre. Fibre model was prepared using the UCSF chimera and chimeraX software package.<sup>41, 42</sup>

Two histidine containing variants were prepared, one where a single phenylalanine was replaced by His and a second where a single glutamic acid was replaced by His. These two variants were synthesized to observe the difference in self-assembly and catalysis when the His was placed in a hydrophobic or hydrophilic environment. The resulting peptides were named **P5H-P6** and **P6-P8H**, and are shown in **Figure 6.7**. His substitution was performed close to the azobenzene moiety, as this was expected to maximize the effect of photoswitching on catalysis.

CD spectra of dark-adapted **P5H-P6** show a strong minimum at 206 nm, with a shoulder at 218 nm, indicative of a mixed irregular and right-twisted  $\beta$ -sheet

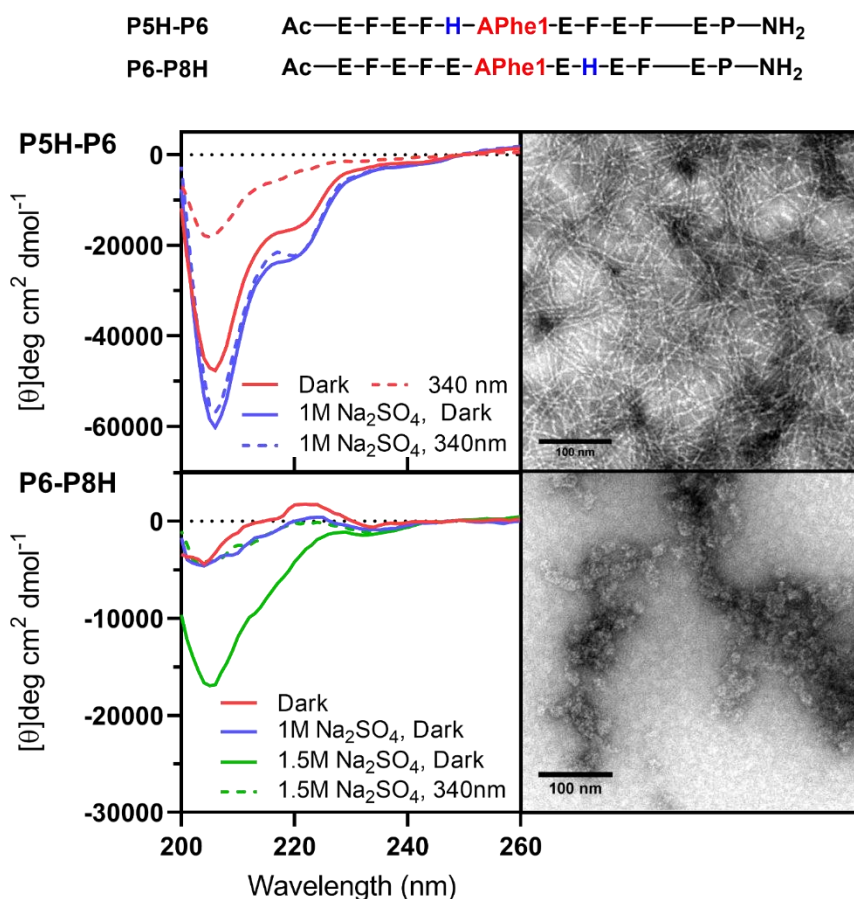


**Figure 6.7:** Peptide sequences (top), CD spectra (left) and TEM images (right) of histidine-containing peptides. CD spectra were recorded with [peptide] = 100  $\mu$ M and 10 mM PB. TEM samples were treated with uranyl acetate as a negative stain before imaging, with scale bars indicating 100 nm.

structure. Peak intensity at 206 nm is higher than one would expect for a combination of these two, suggesting the structure might differ from both of these.<sup>30</sup> Isomerization of the sample with 340 nm light results in a decrease in overall folding, with a 60% reduction of the signal at 206 nm and 70% reduction of the signal at 218 nm. CD spectra of **P5H-P6** containing added Na<sub>2</sub>SO<sub>4</sub> showed an overall increase in signal strength at both wavelengths, but only marginal differences between the dark adapted and 340 nm photostationary state. From 200 mM Na<sub>2</sub>SO<sub>4</sub> and higher, no differences between the two states could be observed (**Figure S6.9**). Although the CD spectra and response to added salt are very different from the **P6** parent peptide, TEM imaging still shows fibre formation, with a similar fibre width ( $6.35 \pm 0.39$  nm, **Figure S6.4**) to **P6**. The opposite is observed for substitution of a phenylalanine with histidine in peptide **P6-P8H**, which did not assemble into fibres (**Figure 6.7**). Instead, spherical aggregates were observed with no apparent (internal) structure. In CD spectroscopy, **P6-P8H** shows a weakly folded signal until the salt concentration has been increased to 1.5 M Na<sub>2</sub>SO<sub>4</sub>, which displays a broad absorption peak with a minimum at 205 nm. At the high salt concentration there is a clear difference between the spectra of the dark adapted and 340 nm irradiated samples, with the irradiated sample again showing weak folding. An exact secondary structure cannot be assigned to this absorption peak in isolation, and the broadness of the peak suggests that it there might be some flexibility in its structure. Both histidine-containing peptides show different CD spectra from **P6**, but they are comparable in shape to previous reported CD spectra on peptides with the repeat sequence (FKFE)<sub>n</sub>, which self-assemble as antiparallel cofacial  $\beta$ -sheet fibres.<sup>22, 24</sup>

The two histidine-containing peptides were tested for catalytic activity in the ester hydrolysis of *para*-nitrophenylacetate (*p*NPA), a common marker for hydrolysis because of the strong absorbance of the *para*-nitrophenol product.<sup>43, 44</sup> Peptides were tested for catalytic behaviour at a concentration of 300  $\mu$ M to increase signal (self-assembly characteristics as studied by CD were comparable between 100 and 300  $\mu$ M, **Figure S6.10**). Both peptides showed an increase in hydrolysis, with **P6-P8H** showing the largest substrate conversion (**Figure 6.8A**). The rate of hydrolysis with **P6-P8H** was dependent on the peptide concentration, demonstrating its function as a catalyst, and similar catalytic turn-over frequencies were found at 100  $\mu$ M ( $0.068 \text{ h}^{-1}$ ) as at 300  $\mu$ M ( $0.078 \text{ h}^{-1}$ ) of peptide. Isomerization of **P6-P8H** with 340 nm light resulted in a 34% reduced reaction rate, showing the catalysis can be influenced by the **APhe** photoswitch adjacent to the histidine. Because the histidine

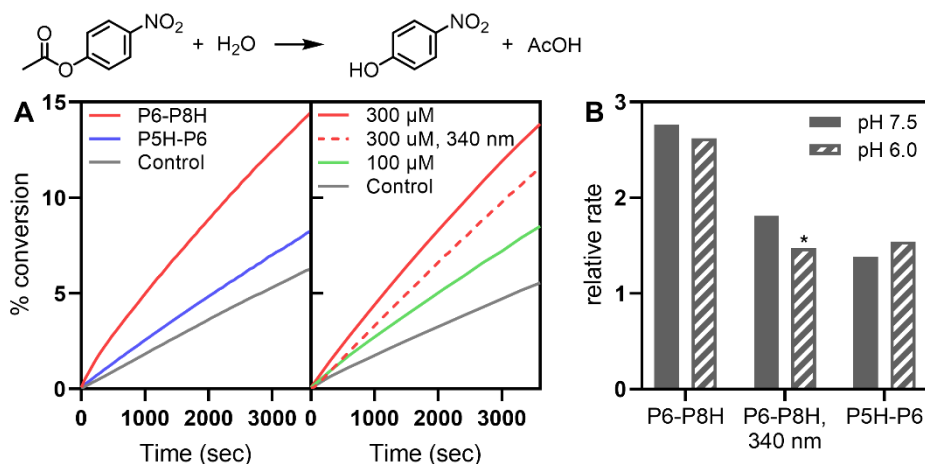


**Figure 6.8:** Catalytic effect of His-containing peptides on the rate of *p*-nitrophenylacetate hydrolysis. Kinetic experiments comparing the two catalytic peptides (A, left) and the effect of concentration and 340 nm illumination on peptide **P6-P8H** (A, right). Initial rate of hydrolysis relative to background rate (B), asterisk indicates the rate was calculated over the entire experiment. [pNPA] = 200 μM, [peptide] = 300 μM at 25 °C and in pH 7.5 phosphate buffer unless noted otherwise. Kinetic experiments for pH 6.0 can be found in **Figure S6.11**.

protonation state was theorized to affect catalytic rates, the experiments were repeated at pH 6.0, with no effect on the relative rate of ester hydrolysis (**Figure 6.8B**). Peptide **P6-P8H** showed the best catalytic activity for the hydrolysis of pNPA, and its activity could be controlled by **APhe** isomerization, reducing its TOF by 54% by irradiation with 340 nm light. The mechanism through which catalytic activity is affected is not yet clear, since it does not show characteristic  $\beta$ -sheet assembly as the other peptides do.

### 6.3 Conclusions and outlook

The photoswitchable amino acid **APhe** was successfully incorporated in phenylalanine-based  $\beta$ -sheet forming peptides in the centre of the sequence or close to the terminus. Both modified positions resulted in peptides that self-assembled as  $\beta$ -sheet dominant structures in the presence of  $\text{Na}_2\text{SO}_4$ . Both peptide structure and CAC are dependent on the salt concentration, and effect of salt on folding was related to the effect on CAC. TEM images showed peptide fibres for both variants, with peptide **P2** also showing fibrillar structures multiple times the fibre width. Soluble fibres were observed for peptide **P6** via cryo-TEM, and showed a fibre width consistent with self-assembly of the peptide as a cofacial  $\beta$ -sheet structure. Irradiation with 340 nm light resulted in isomerization of the azobenzene

to dominantly *cis*, and resulted in a loss of structure as observed via CD, and a 5-fold reduction in the observed CAC. Kinetic experiments using Thioflavin T showed an initial lag period for **P2**, suggesting a cooperative assembly mechanism, and both switchable variants did not show increased signal when isomerized to the *cis* conformation. From this we conclude that **APhe** can be used to control the self-assembly of  $\beta$ -sheet peptides, with the most effective control occurring if it is placed in the centre of the  $\beta$ -sheet domain. Positioning of **APhe** at the termini of the peptide does allow for photocontrol, but also leads to oligomerization of the peptide fibres in solution.

Histidine containing variants of **P6** were prepared and tested as a catalyst for ester hydrolysis. The histidine significantly altered the self-assembly of the peptides, which no longer adhered to the salt-induced self-assembly observed for the parent peptide **P6**, and resulted in non-fibrous structures when substituting a phenylalanine in the case of **P6-P8H**. Both peptides showed a rate of ester hydrolysis above background, with the largest increase in rate observed for **P6-P8H**. The reaction rate could be reduced via isomerization with 340 nm light, showing **APhe** isomerization can be used to control the catalytic activity.

## 6.4 Methods

Fmoc-protected amino acids were purchased from Novabiochem (Amsterdam, The Netherlands). Acetic anhydride ( $\text{Ac}_2\text{O}$ ), acetonitrile (MeCN), dimethylformamide (DMF), piperidine, pyridine, trifluoroacetic acid (TFA) and tetrahydrofuran (THF) were purchased from Biosolve (Valkenswaard, The Netherlands). Oxyma was purchased from Carl Roth (Karlsruhe, Germany). *N,N'*-Diisopropylcarbodiimide (DIC), 1,2-Bis(2-mercaptoethoxy)-ethane (EODT), 1-[Bis(dimethylamino)methylene]-1H-1,2,3-triazolo[4,5-b]pyridinium 3-Oxide Hexafluorophosphate (HATU), and Thioflavin T were purchased from Sigma Aldrich (Zwijndrecht, The Netherlands). Chloroform, dichloromethane (DCM), ethyl acetate (EtOAc), ethanol, diethyl ether ( $\text{Et}_2\text{O}$ ) and pentane were supplied by Honeywell (Meppel, The Netherlands). All reagents were used as purchased. Ultrapure water was purified using a Milli-Q™ purification system from Millipore (Amsterdam, The Netherlands). A detailed description of the synthesis of **1** can be found in **chapter 5** of this thesis.

**Peptide synthesis** was performed via Fmoc-based SPPS, on a CEM liberty blue microwave-accelerated peptide synthesizer. Peptides were prepared on a 0.05 or 0.1 mmol scale using Tentagel HL resin (0.39 mmol/g), using 5 equivalents each of

amino acid, Oxyma pure and DIC as coupling reagents at 90 °C for 4 minutes. Deprotection was achieved with 20% piperidine in DMF heated to 90 °C for 1 minute. Between deprotection and peptide coupling 3 DMF washes were performed, with a single washing step between the coupling and deprotection steps. Amino-acid **1** was coupled manually to reduce the required equivalents, using 2.5 equivalents of **1**, 2.5 equivalents of HATU, and 5 equivalents DIPEA in DMF for 2-3 hours. After the last Fmoc deprotection, the N-terminus was acylated using 5 mL/mmol each of Ac<sub>2</sub>O and pyridine in DMF, for 5 minutes. To eliminate potential light absorption, the N-terminus of **pep2** and derivatives was acetylated instead of capping with 4-acetaminobenzoic acid as previously reported.<sup>16</sup> The resin was washed 3 times with DMF, MeOH and DCM followed by drying under a continuous air flow. Cleavage of peptide was achieved with TFA (5 mL) containing 2.5% water and 2.5% TIS for 1 hour, followed by precipitation in 1:1 C<sub>5</sub>H<sub>12</sub>/Et<sub>2</sub>O. The precipitate was collected via centrifugation (4000 rpm, 10 minutes), the organic layer removed and the product resuspended in water for purification or lyophilization.

Peptides were purified using reverse-phase HPLC on a Shimadzu system consisting of two KC-20AR pumps and an SPD-20A or SPD-M20A detector fitted with a Phenomenex Kinetix Evo C18 column. A linear gradient from 2-35% MeCN in water containing 0.1% NH<sub>3</sub> as buffer in both phases, at a flow rate of 12 ml/min. Collected fractions were checked via analytical HPLC, pooled and lyophilized. LC-MS analysis was performed with a Thermo Scientific TSQ quantum access MAX mass detector connected to an Ultimate 3000 liquid chromatography system fitted with a 50x4.6 mm Phenomenex Gemini 3 μm C18 column.

**Analytical HPLC** was performed using a Shimadzu Prominence-*i* LC-2030C 3D system fitted with a Phenomenex Kinetix Evo C18 column. For quantification of **1** photoswitching, a linear gradient of 10-90% MeCN in water containing 0.1% TFA. Peptide purity was confirmed with analytical HPLC using a gradient of 5-50% MeCN in water and containing with 10 mM NH<sub>3</sub> as buffer.

**CD** spectra were recorded on a Jasco J-815 CD spectrometer fitted with a Peltier temperature controller. Spectra were recorded in a 1 mm quartz cuvette at 20 °C, unless otherwise specified. Spectra were recorded between 190 and 280 nm with 1 nm intervals, at a scan rate of 100 nm/min with 5 subsequent spectra averaged for accuracy. The mean residue molar ellipticity ( $\theta$ , deg cm<sup>2</sup> dmol.res<sup>-1</sup>), was calculated using equation 1:

$$[\theta] = (100 * [\theta]_{obs}) / (c * n * l) \quad (1)$$

Where  $[\theta]_{obs}$  represents the observed ellipticity in mdeg,  $c$  represents the peptide concentration in mM,  $n$  the number of peptide bonds and  $l$  the path length of the cuvette in cm.

**TEM** samples were prepared on carbon/formvar coated 200 mesh copper grids by the addition of a drop of 0.5 mM peptide solution (containing 10 mM phosphate buffer). After 30 seconds, excess solution was blotted and the grid stained with uranyl acetate (0.25 mg/ml) for less than 10 seconds, and excess liquid removed. The grids were left to air dry completely for at least 2 hours. Measurements were performed on a JEM1400 plus transmission electron microscope operating at 80 kV and fitted with a CCD camera.

**Cryo-TEM** samples of **P6** (3  $\mu$ L, 300  $\mu$ M total concentration) were applied to a freshly glow-discharged Lacey carbon film 200 mesh Cu grid from Electron Microscopy Sciences (Wageningen, The Netherlands). Grids were blotted for 3 s after a 10 s wait at 99% humidity in a Thermo Fisher FEI Vitrobot<sup>TM</sup> Mark III (Landsmeer, The Netherlands). Cryo-EM images were collected on a Talos L120C (NeCEN, Leiden University) operating at 120 kV. Images were recorded manually at a nominal magnification of 36000x yielding a pixel size at the specimen of 2.8  $\text{\AA}$ . Images were analyzed using the Fiji software program.<sup>45</sup>

**DLS** measurements were performed on a Malvern Zetasizer Nano S, using plastic micro-cuvettes. The attenuator was fixed manually at 10, with each experiment consisting of 10 scans of 20 seconds duration. The measurement was repeated 3 times. For each peptide and condition a set of samples was prepared in amber Eppendorf tubes, and left to incubate for a minimum of 2 hours before measurement. The samples were agitated with a pipette just before transferring to the cuvettes. For experiments requiring the *cis* isomer, samples were prepared from stock solutions irradiated with 340 nm, and irradiated again for 3 minutes before the start of the measurement.

**UV-Vis** spectra were recorded on an Agilent Cary-300 UV-Vis spectrophotometer, at a scanning speed of 200 nm/min with a switchover between the visible and ultraviolet lamp at 350 nm. Samples were measured in quartz cuvettes with a path length of 10 mm, and baseline corrected using a blank sample of the same solvent used for sample preparation. During the measurements, samples were kept at room temperature (20 °C) using an Agilent Cary temperature controller.

**Kinetic hydrolysis experiments** were carried out on an Agilent Technologies, Cary 60 UV-Vis spectrophotometer. The substrate, pNPA was dissolved in acetonitrile (10mM) and the peptide catalysts were dissolved in phosphate buffer (0.1 mM, pH 6.0 or pH 7.5). The experiments were performed with 200  $\mu$ L samples containing 100 or 300  $\mu$ M peptide and all solutions were equilibrated at 25 °C for 20 minutes. Reactions were performed in QS quartz cuvettes with a 1 cm path length and equipped with Teflon stoppers (3.5 mL; Starna Analytics). Experiments were performed at 25°C and started by addition of the pNPA stock solution (2 v%), with substrate hydrolysis monitored for 1-4h. As a control, water was added instead of the peptide solutions. The following extinction coefficients at 400 nm were used:  $\epsilon = 1700 \text{ M}^{-1} \text{ cm}^{-1}$  (pH 6.0, 25 °C, 4-nitrophenolate),  $\epsilon = 16400 \text{ M}^{-1} \text{ cm}^{-1}$  (pH 7.5, 25 °C, 4-nitrophenolate).

**Fluorescence** experiments were performed in 96-well plates using a TECAN Infinite M1000 Pro microplate reader. For Thioflavin T experiments, fluorescence was recorded every minute, with excitation set at 450nm ( $\pm 5$ nm) and emission at 490nm ( $\pm 10$ nm). All numbers were normalized to the fluorescence of Thioflavin T under the same buffered conditions.

**Sample illumination** Sample illumination at 340 nm was achieved using a Thorlabs M340F3 Fiber-coupled LED powered by a T-Cube driver at 1000 mA. For all other wavelengths, high-power single chip LEDs were purchased from Roithner Laser (Vienna, Austria) from the H2A1 series. LEDs from Roithner Laser were mounted on an aluminum back plate for heat dissipation, and powered at 350 mA current using a driver built in-house. For illumination the LED was placed parallel to the side of the cuvette at a distance of 5 mm, and centered to the width and height of the sample.

## 6.5 Acknowledgments

This work benefited from access to the Netherlands Centre for Electron Nanoscopy (NeCEN) at Leiden University, an Instruct-ERIC centre, with technical assistance from Ludovic Renault, Willem Noteborn, Wen Yang and Jamie Depelteau.

## 6.6 References

1. Rose, G. D., *et al.* (2006) A backbone-based theory of protein folding. *P. Natl. Acad. Sci. USA* 103, 16623-16633.
2. Nick Pace, C., and Martin Scholtz, J. (1998) A Helix Propensity Scale Based on Experimental Studies of Peptides and Proteins. *Biophys. J.* 75, 422-427.

3. Xiong, H., *et al.* (1995) Periodicity of polar and nonpolar amino acids is the major determinant of secondary structure in self-assembling oligomeric peptides. *P. Natl. Acad. Sci. USA* 92, 6349-6353.
4. Levin, A., *et al.* (2020) Biomimetic peptide self-assembly for functional materials. *Nat. Rev. Chem* 4, 615-634.
5. Hauser, C. A. E., and Zhang, S. (2010) Designer self-assembling peptide nanofiber biological materials. *Chem. Soc. Rev.* 39, 2780-2790.
6. Aemissegger, A., *et al.* (2005) A Photoinducible  $\beta$ -Hairpin. *J. Am. Chem. Soc.* 127, 2929-2936.
7. Dong, S.-L., *et al.* (2006) A Photocontrolled  $\beta$ -Hairpin Peptide. *Chem. Eur. J.* 12, 1114-1120.
8. Schrader, T. E., *et al.* (2007) Light-triggered  $\beta$ -hairpin folding and unfolding. *P. Natl. Acad. Sci. USA* 104, 15729-15734.
9. Schrader, T. E., *et al.* (2011) Folding and Unfolding of Light-Triggered  $\beta$ -Hairpin Model Peptides. *J. Phys. Chem. B* 115, 5219-5226.
10. Hofmann, S. M., *et al.* (2020) Folding and Unfolding of the Short Light-Triggered  $\beta$ -Hairpin Peptide AzoChignolin Occurs within 100 ns. *J. Phys. Chem. B* 124, 5113-5121.
11. Deeg, A. A., *et al.* (2011) Light-Triggered Aggregation and Disassembly of Amyloid-Like Structures. *ChemPhysChem* 12, 559-562.
12. Chen, G. F., *et al.* (2017) Amyloid beta: structure, biology and structure-based therapeutic development. *Acta pharmacologica Sinica* 38, 1205-1235.
13. Hoppmann, C., *et al.* (2012) Light-Controlled Toxicity of Engineered Amyloid  $\beta$ -Peptides. *Chembiochem : a European journal of chemical biology* 13, 2657-2660.
14. Doran, T. M., *et al.* (2012) An Azobenzene Photoswitch Sheds Light on Turn Nucleation in Amyloid- $\beta$  Self-Assembly. *ACS Chem. Neurosci.* 3, 211-220.
15. Nanda, J., *et al.* (2017) Emergence of native peptide sequences in prebiotic replication networks. *Nat. Commun.* 8, 434.
16. Rubinov, B., *et al.* (2009) Self-Replicating Amphiphilic  $\beta$ -Sheet Peptides. *Angew. Chem. Int. Edit.* 48, 6683-6686.
17. Bowerman, C. J., and Nilsson, B. L. (2012) Review self-assembly of amphipathic  $\beta$ -sheet peptides: Insights and applications. *Peptide Science* 98, 169-184.
18. Marini, D. M., *et al.* (2002) Left-Handed Helical Ribbon Intermediates in the Self-Assembly of a  $\beta$ -Sheet Peptide. *Nano Lett.* 2, 295-299.
19. Fitzpatrick, A. W. P., *et al.* (2013) Atomic structure and hierarchical assembly of a cross- $\beta$  amyloid fibril. *P. Natl. Acad. Sci. USA* 110, 5468-5473.
20. Nelson, R., *et al.* (2005) Structure of the cross-beta spine of amyloid-like fibrils. *Nature* 435, 773-778.
21. Caplan, M. R., *et al.* (2000) Self-Assembly of a  $\beta$ -Sheet Protein Governed by Relief of Electrostatic Repulsion Relative to van der Waals Attraction. *Biomacromolecules* 1, 627-631.
22. Swanekamp, R. J., *et al.* (2012) Coassembly of Enantiomeric Amphipathic Peptides into Amyloid-Inspired Rippled  $\beta$ -Sheet Fibrils. *J. Am. Chem. Soc.* 134, 5556-5559.

23. Hwang, W., *et al.* (2003) Supramolecular structure of helical ribbons self-assembled from a  $\beta$ -sheet peptide. *J. Chem. Phys.* 118, 389-397.
24. Clover, T. M., *et al.* (2020) Self-Assembly of Block Heterochiral Peptides into Helical Tapes. *J. Am. Chem. Soc.* 142, 19809-19813.
25. Lee, N. R., Bowerman, C. J., and Nilsson, B. L. (2013) Effects of Varied Sequence Pattern on the Self-Assembly of Amphipathic Peptides. *Biomacromolecules* 14, 3267-3277.
26. Lee, N. R., Bowerman, C. J., and Nilsson, B. L. (2013) Sequence length determinants for self-assembly of amphipathic  $\beta$ -sheet peptides. *Peptide Science* 100, 738-750.
27. Betush, R. J., Urban, J. M., and Nilsson, B. L. (2018) Balancing hydrophobicity and sequence pattern to influence self-assembly of amphipathic peptides. *Peptide Science* 110, e23099.
28. Ivnitski, D., *et al.* (2014) Introducing charge transfer functionality into prebiotically relevant  $\beta$ -sheet peptide fibrils. *Chem. Commun.* 50, 6733-6736.
29. Nakayama, K., Endo, M., and Majima, T. (2005) A Hydrophilic Azobenzene-Bearing Amino Acid for Photochemical Control of a Restriction Enzyme BamHI. *Bioconjugate Chem.* 16, 1360-1366.
30. Micsonai, A., *et al.* (2015) Accurate secondary structure prediction and fold recognition for circular dichroism spectroscopy. *P. Natl. Acad. Sci. USA* 112, E3095-E3103.
31. Micsonai, A., *et al.* (2018) BeStSel: a web server for accurate protein secondary structure prediction and fold recognition from the circular dichroism spectra. *Nucleic Acids Res.* 46, W315-W322.
32. Easterhoff, D., *et al.* (2011) Enhancement of HIV-1 Infectivity by Simple, Self-Assembling Modular Peptides. *Biophys. J.* 100, 1325-1334.
33. Voropai, E. S., *et al.* (2003) Spectral Properties of Thioflavin T and Its Complexes with Amyloid Fibrils. *J. App. Spec.* 70, 868-874.
34. Biancalana, M., *et al.* (2009) Molecular Mechanism of Thioflavin-T Binding to the Surface of  $\beta$ -Rich Peptide Self-Assemblies. *J. Mol. Bio.* 385, 1052-1063.
35. Gade Malmos, K., *et al.* (2017) ThT 101: a primer on the use of thioflavin T to investigate amyloid formation. *Amyloid* 24, 1-16.
36. Raz, Y., *et al.* (2013) Effects of mutations in de novo designed synthetic amphiphilic  $\beta$ -sheet peptides on self-assembly of fibrils. *Chem. Commun.* 49, 6561-6563.
37. Hansen, A. L., and Kay, L. E. (2014) Measurement of histidine pKa values and tautomer populations in invisible protein states. *P. Natl. Acad. Sci. USA* 111, E1705-E1712.
38. Zhang, C., *et al.* (2017) Switchable Hydrolase Based on Reversible Formation of Supramolecular Catalytic Site Using a Self-Assembling Peptide. *Angew. Chem. Int. Edit.* 56, 14511-14515.
39. Huang, Z., *et al.* (2013) Self-assembly of amphiphilic peptides into bio-functionalized nanotubes: a novel hydrolase model. *J. Mat. Chem. B* 1, 2297-2304.
40. Guler, M. O., and Stupp, S. I. (2007) A Self-Assembled Nanofiber Catalyst for Ester Hydrolysis. *J. Am. Chem. Soc.* 129, 12082-12083.
41. Pettersen, E. F., *et al.* (2021) UCSF ChimeraX: Structure visualization for researchers, educators, and developers. *Protein Sci.* 30, 70-82.

42. Pettersen, E. F., *et al.* (2004) UCSF Chimera—A visualization system for exploratory research and analysis. *J. Comp. Chem.* 25, 1605-1612.
43. Hamley, I. W. (2021) Biocatalysts Based on Peptide and Peptide Conjugate Nanostructures. *Biomacromolecules* 22, 1835-1855.
44. Zozulia, O., Dolan, M. A., and Korendovych, I. V. (2018) Catalytic peptide assemblies. *Chem. Soc. Rev.* 47, 3621-3639.
45. Schindelin, J., *et al.* (2012) Fiji: an open-source platform for biological-image analysis. *Nat. Methods* 9, 676-682.

## Supporting Information for Chapter 6

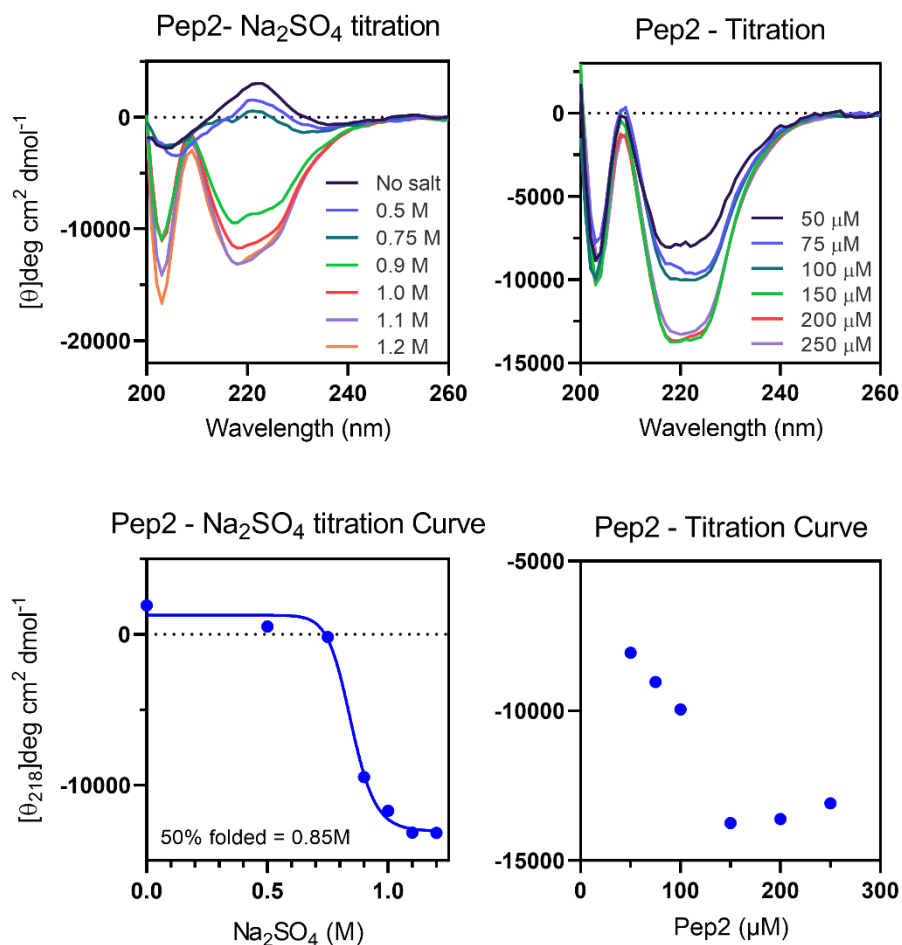


**Figure S6.1:** CD titrations of **Pep2**, showing the effect of salt (left) and peptide (right) concentration on self-assembly. Salt titrations were performed at a fixed peptide concentration of 100 μM, and peptide titrations with a fixed salt concentration of 1 M Na<sub>2</sub>SO<sub>4</sub>. Top figures show the entire CD spectra, with bottom figures showing the normalized absorption at 218 nm plotted against concentration. All samples contained 10 mM phosphate buffer at pH 7.4 and were measured at 20 °C.

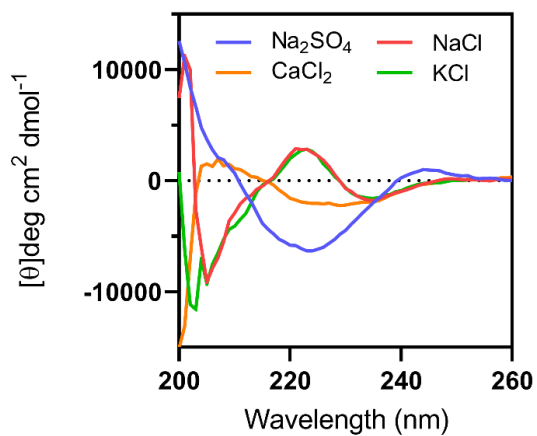


**Figure S6.2:** CD spectra of peptide P6 in the presence of different salts. The peptide was thermally equilibrated and [peptide] = 100  $\mu$ M. Salt concentration was 0.5 M, with 10 mM phosphate as buffer (pH 7.4) and were measured at 20 °C.

## TEM image analysis

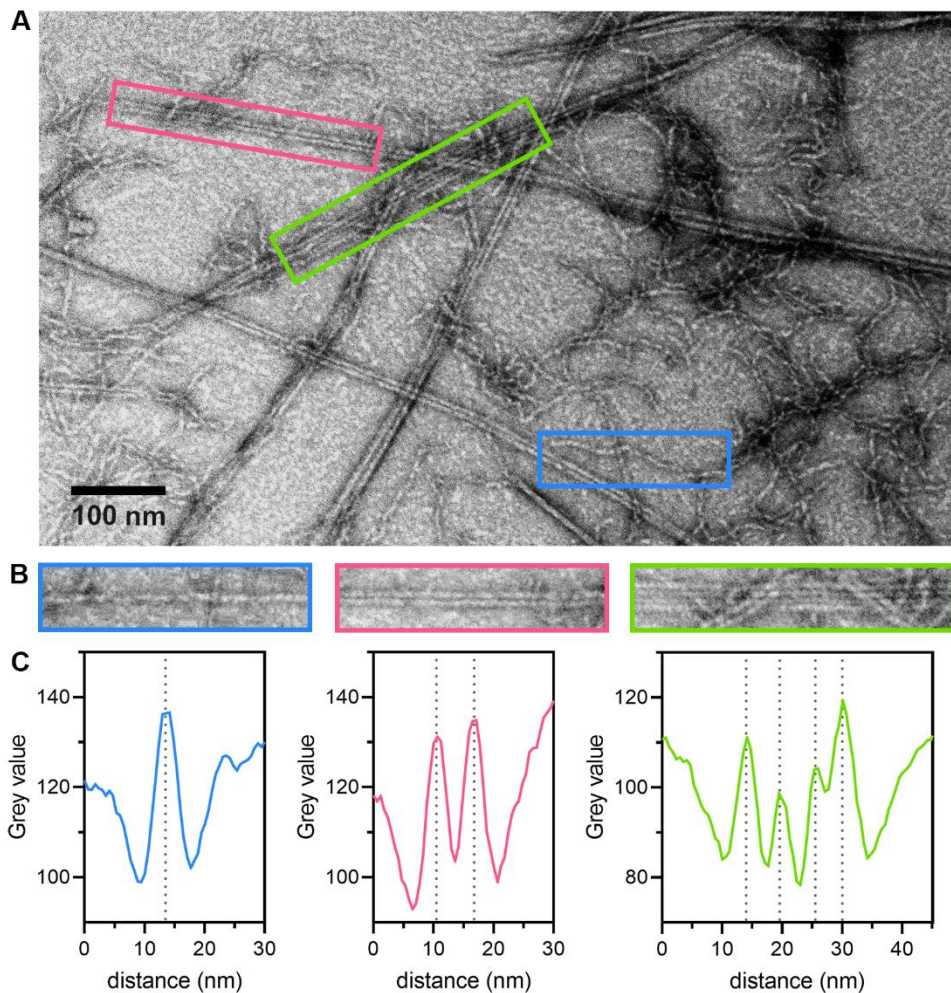


**Figure S6.3:** Representative TEM image showing the different types of structures observed for peptide **P2** (A). Structures are divided into 3 groups; single fibres (blue), double fibres (magenta) and structures comprised of multiple fibres (green). Straightened images (B) and derived profile plots (C) of selected fibres were prepared using Fiji. Dotted lines in the profile plots mark the center of peptide fibres.

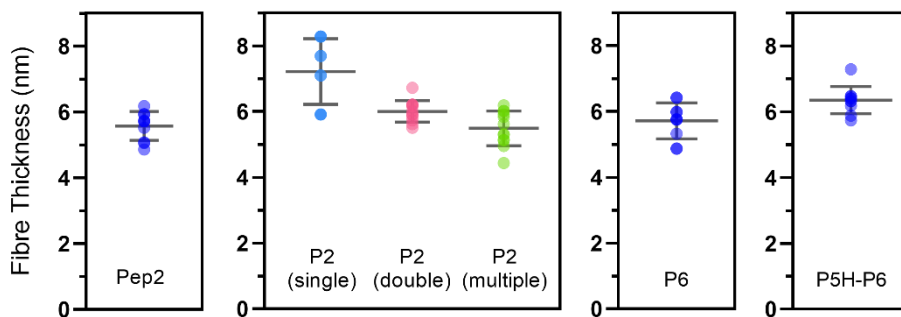


**Figure S6.4:** Size distribution of peptide fibres observed with TEM, with peptide **P2** divided in the three distinguishable groups of single, double, and multiple fibres as shown in **Figure S6.3**. Size distributions are also summarized in **Table S6.1**.

**Table S6.1:** Thickness and deviation of peptide fibres as observed via TEM (**Figure 6.2** and **Figure 6.7**) and Cryo-EM (**Figure 6.5**) and displayed graphically in **Figure S6.4**.

	<b>Avg. Size (nm)</b>	<b>Std. Dev. (nm)</b>	<b>N fibres</b>
Pep2	5.57	0.42	10
P2 (Single)	7.22	0.95	10
P2 (Double)	6.01	0.31	12
P2 (Multiple)	5.49	0.51	12
P6	5.71	0.52	10
P6 (Cryo-EM)	4.45	0.91	30
P5H-P6	6.35	0.39	10

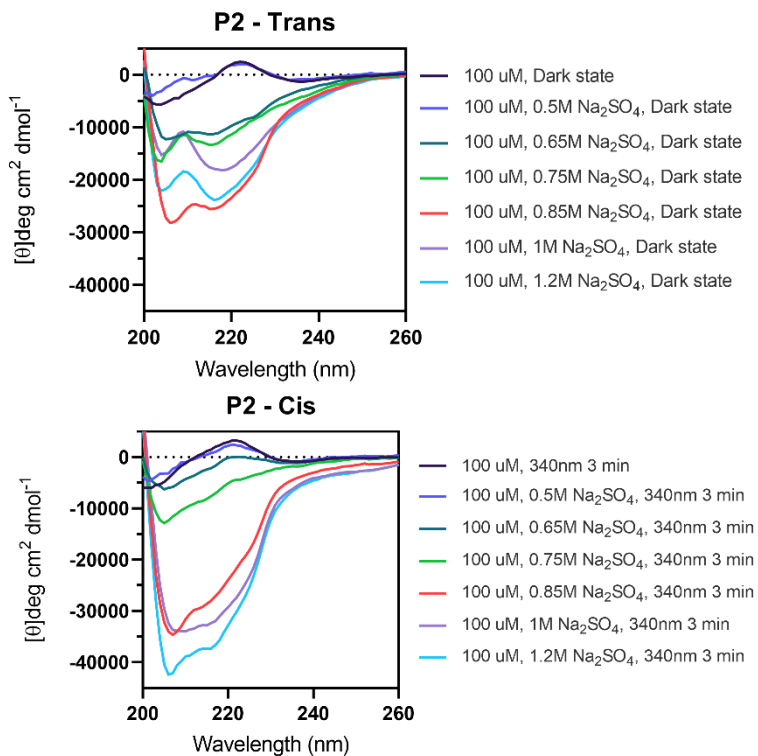


**Figure S6.5:** CD titration experiments to determine the effect of added salts on the structure of P2 in the *trans* (dark, top) or *cis* (light, bottom) conformations. Measurements were performed at a 100  $\mu\text{M}$  peptide concentration in 10 mM PB and were measured at 20  $^{\circ}\text{C}$ .

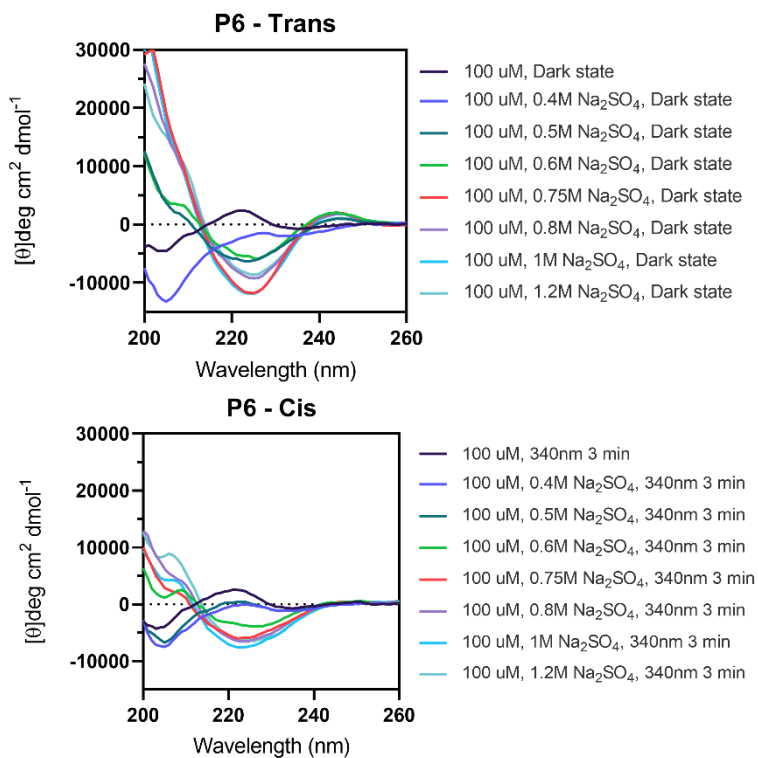


**Figure S6.6:** CD titration experiments to determine the effect of added salts on the structure of **P6** in the *trans* (dark, top) or *cis* (light, bottom) conformations. Measurements were performed at a 100  $\mu\text{M}$  peptide concentration in 10 mM PB and were measured at 20 °C.

**Table S6.2:** Structural components (%) computed by the *BeStSel* web server from measured CD spectra in **Figure 6.2**. Legend: Anti1 = left-twisted  $\beta$ -strand; Anti2 = relaxed  $\beta$ -strand; Anti3 = right-twisted  $\beta$ -strand; Helix1 = regular  $\alpha$ -helix; Helix2 = distorted  $\alpha$ -helix; Para = Parallel  $\beta$ -strand. NRMMSD = Normalised residual mean square deviation.

	Helix1	Helix2	Anti1	Anti2	Anti3	Para	Turn	Others	NRMMSD
<b>P6 340nm, 1M Na<sub>2</sub>SO<sub>4</sub></b>	0	0	14.96	4.14	6.06	0	18.33	56.51	0.049
<b>P6 Dark, 1M Na<sub>2</sub>SO<sub>4</sub></b>	0	0	36.33	6.34	7.36	0	19.85	30.12	0.0182
<b>P6 340nm</b>	0	0	0	7.68	13.64	0	20.02	58.66	0.0794
<b>P6 Dark</b>	0	0	0	11.29	11.98	0	19.49	57.24	0.0754
<b>P2 340nm, 1M Na<sub>2</sub>SO<sub>4</sub></b>	47.21	14.52	0	4.59	0	0	0.23	33.45	0.0467
<b>P2 Dark, 1M Na<sub>2</sub>SO<sub>4</sub></b>	12.32	3.2	0	0	0	22.83	6.09	55.56	0.0585
<b>P2 340nm</b>	0	0	0	10.47	12.62	0	19.18	57.74	0.0719
<b>P2 Dark</b>	0	0	0	13.53	10.09	0	16.57	59.81	0.0733
<b>Pepp2, 1M Na<sub>2</sub>SO<sub>4</sub></b>	0	0	10.59	8.58	0	0.18	13.43	67.22	0.1262

**Table S6.3:** CAC values determined using DLS for peptides in thermal equilibrium (dark) and 340 nm irradiated state. Ratio indicates the fold increase in CAC for samples after irradiation.

	Dark ( $\mu\text{M}$ )	340nm ( $\mu\text{M}$ )	Ratio
<b>P2</b> , 1 M $\text{Na}_2\text{SO}_4$	6	29	4.8
<b>P6</b> , 0.6 M $\text{Na}_2\text{SO}_4$	22	109	5
<b>P6</b> , 1 M $\text{Na}_2\text{SO}_4$	11	20	1.8

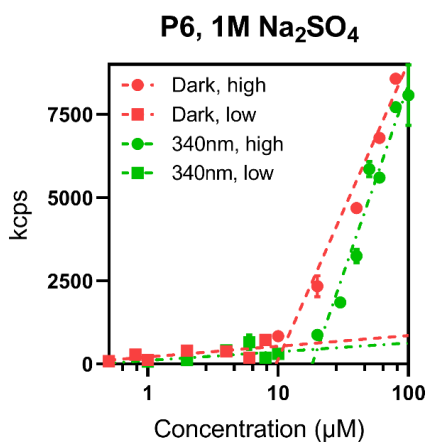


**Figure S6.7:** DLS determination of CAC of peptide **P6** with 1M  $\text{Na}_2\text{SO}_4$ , measured at 20 °C.

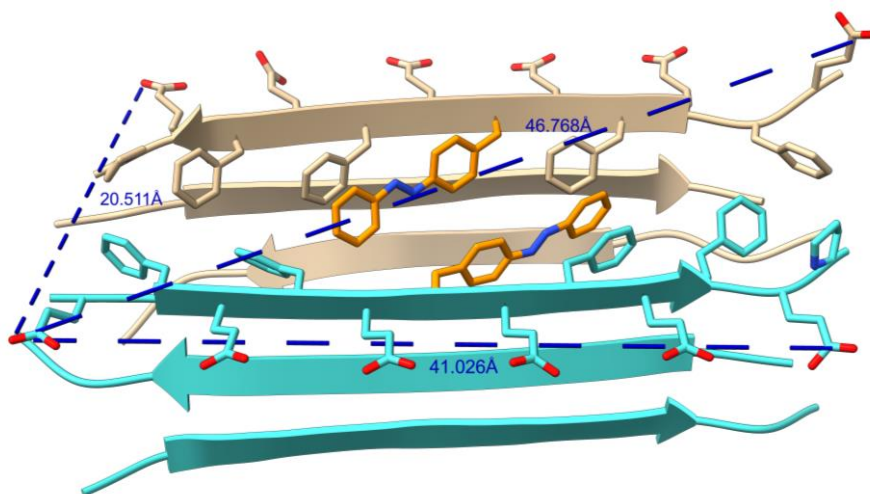


**Figure S6.8:** Image showing the calculated distances in a structural model of **P6** fibres assuming self-assembly into a double antiparallel  $\beta$ -sheet structure.

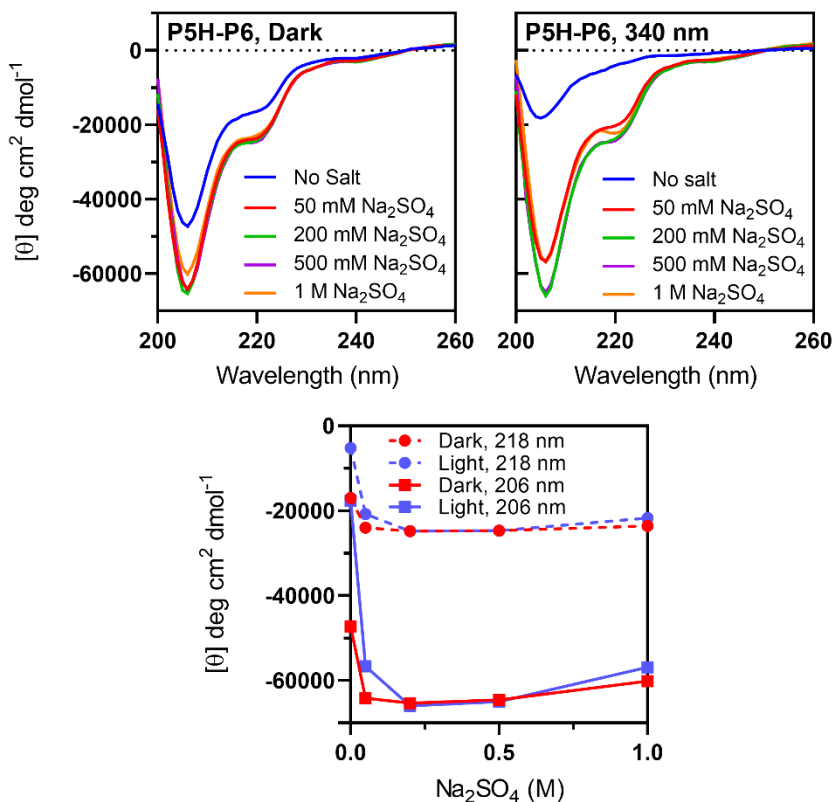


**Figure S6.9:** CD spectra of 100 μM P5H-P6 in 10 mM phosphate buffer, with varying concentrations of Na<sub>2</sub>SO<sub>4</sub> (top) and CD absorption at 218 or 206 nm versus the Na<sub>2</sub>SO<sub>4</sub> concentration (bottom). Samples were measured at 20 °C and were either equilibrated in the dark or irradiated with 340 nm light to achieve PSS.

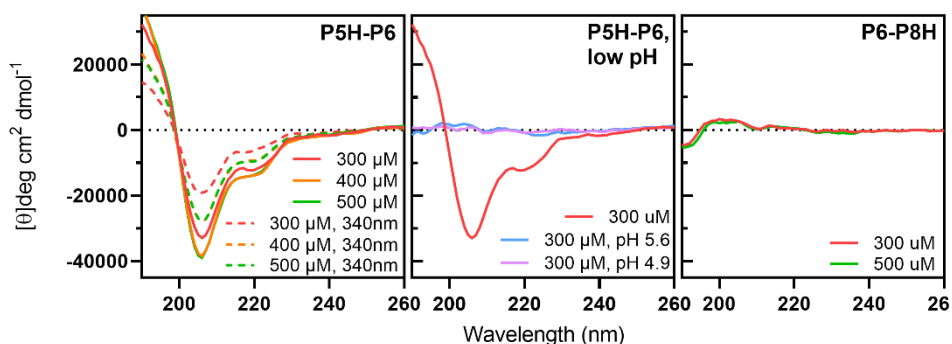


**Figure S6.10:** CD Spectra of peptides P5H-P6 and P6-P8H at higher concentrations. Measured samples were equilibrated in the dark or irradiated with 340 nm light to achieve PSS. Samples contained 10 mM phosphate buffer and were measured at 20 °C.

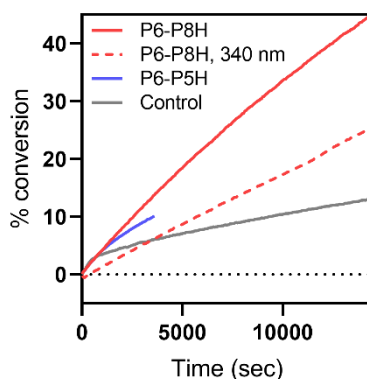


**Figure S6.11:** Kinetic hydrolysis curves of pNPA with different peptides as catalysts, performed at pH 6.0. The sample at 340 nm was illuminated before the start of the experiment, but not during the experiment.

**Table S6.4:** Overview of the catalytic parameters calculated from the kinetic hydrolysis experiments shown in **Figure 6.8** and **Figure S6.11**. Relative  $K_i$  is in comparison to the control samples of the same condition, with no peptide present. Turn over frequency (TOF) and  $K_i$  are calculated for the first 15 minutes of the experiment, unless noted otherwise.

Catalyst	Peptide (uM)	Dominant isomer	pH	$K_i$ ( $s^{-1}$ )	TOF ( $h^{-1}$ )	Rel. $K_i$
No Peptide			7.5	1.80E-05		
P5H-P6	300	<i>Trans</i>	7.5	2.47E-05	0.016	1.38
P6-P8H	300	<i>Trans</i>	7.5	4.96E-05	0.076	2.76
P6-P8H	300	<i>Cis</i>	7.5	3.26E-05	0.035	1.81
P6-P8H	100	<i>Trans</i>	7.5	2.68E-05	0.068	1.49
No Peptide			6	2.72E-05		
P5H-P6	300	<i>Trans</i>	6	4.17E-05	0.035	1.54
P6-P8H	300	<i>Trans</i>	6	7.12E-05	0.105	2.62
No Peptide			6	1.76E-05 <sup>a</sup>		
P6-P8H	300	<i>Trans</i>	6	3.11E-05 <sup>a</sup>	0.053 <sup>a</sup>	1.77
P6-P8H	300	<i>Cis</i>	6	2.59E-05 <sup>a</sup>	0.021 <sup>a</sup>	1.47

<sup>a</sup> Values were calculated as the average over a 4-hour experiment.

### LC-MS of purified peptides

**Table S6.5:** Overview of the calculated masses of all peptides used in this project, and the masses observed by LCMS.

Peptide name	Calculated mass (Da)	Measured mass (Da)
Pep2	[M - H <sup>-</sup> ] <sup>-</sup> 1664.68	1665.10
P2	[M - H <sup>-</sup> ] <sup>-</sup> 1779.71	1769.51
P6	[M - H <sup>-</sup> ] <sup>-</sup> 1779.71	1686.85
P5H-P6	[M + H <sup>+</sup> ] <sup>+</sup> 1779.75	1778.50
P6-P8H	[M + H <sup>+</sup> ] <sup>+</sup> 1760.38	1761.72

## Summary and Perspectives

Coiled coil peptides have found applications in synthetic biology because of their biocompatibility, high binding strength and selectivity for their binding partner. In this thesis, a synthetic membrane fusion system based on the heterodimeric coiled coil peptides 'E' and 'K' is investigated. Structural variants of these peptides are prepared and tested in fusion assays, to uncover the mechanism behind coiled-coil based membrane fusion. To improve upon the functionality of the system, the introduction of a photoactive azobenzene moiety is investigated. Coupling photoisomerization to coiled coil activity should allow for precise spatiotemporal control of biomolecules and nanomaterials containing coiled-coil peptides.

As a mimic of naturally occurring side-chain palmitoylation, in **Chapter 2** peptide derivatives were prepared with the lipid anchor positioned in the center of the peptide sequence (**fCPK** and **fCPE**), in contrast to attachment at the N-terminus. Liposomes containing these novel peptides showed reduced efficiency in fusion assays and liposomes with **fCPE** were unstable. These findings were attributed to homomeric peptide interactions between different lipopeptide containing liposomes. Homomeric interactions of peptide E were previously assumed to have either no effect, or a negative effect, on fusion efficiency. The observed instability demonstrates the role of homomeric peptide interactions in stabilizing the lipopeptide on the liposome surface before fusion can take place. Furthermore the conclusion can be drawn that terminally anchored coiled-coil peptides are more effective at inducing membrane fusion than peptides anchored in the center of the sequence.

Previously, the membrane interactions of peptide K were considered one of the key features that allows for high fusion efficiency of the coiled-coil system. In **Chapter 3** this theory is further investigated via the preparation of intramolecular crosslinked (stapled) derivatives of peptide K. These stapled peptides are structural isomers that differ in the location and ring size of the macrocycle, achieved by the use of different dibromoxylene crosslinkers. This strategy was effective in increasing peptide  $\alpha$ -helicity, coiled-coil binding strength and stability to denaturation, with calorimetric experiments revealing that this occurs through a preorganization mechanism. Liposomal fusion studies with stapled lipopeptides

demonstrated a large increase in content mixing, which was directly related to the increase in coiled-coil binding strength. This provides the conclusion that the previously proposed theory was incorrect for this peptide system and coiled-coil binding is the major driving force behind membrane fusion. The lipid membrane interactions might still be beneficial to the process, but for further optimization of this system they should not be the main focus.

Because membrane fusion efficiency was strongly dependent on coiled-coil binding strength, active control over coiled-coil peptides was hypothesized as a novel strategy for controlling fusion efficiency. To test this hypothesis, in **Chapter 4** stapled peptides were prepared with the dibromoxylene crosslinker substituted by a photoactive azobenzene moiety. Photocontrol over peptide structure was shown for peptide K, and three-heptad coiled coils could also be switched between different folded states using light illumination. These results were promising, but the crosslinking strategy was very low yielding, therefore a different intramolecular crosslinking strategy is suggested for further investigation of this hypothesis.

An alternative coiled coil photomodulation strategy was investigated in **Chapter 5**, not relying on crosslinking, but on the incorporation of azobenzene-based amino acids. Three azobenzene amino acids were prepared, two literature examples based on phenylalanine and one novel amino acid based on phenylglycine (**APgly**). Derivatives of peptide K containing these amino acids were easy to prepare, and showed effective photoisomerization. Out of the three photoactive amino acids, **APgly** showed both the highest overall coiled-coil binding and the largest difference in structure and binding between the two different isomers. This difference was hypothesized to originate from the methylene group present in phenylalanine, which positions the diazo group outside of the hydrophobic core. Molecular dynamics simulations support this theory and also displayed less distance changes between the two isomers of **APgly**. Together, these data show the novel **APgly** as an effective amino acid for coiled-coil photocontrol, acting through the disruption of the hydrophobic core by changing polarity after photoisomerization.

This mechanism of photocontrol was hypothesized to extend to other peptides that self-assemble by forming a hydrophobic domain. In **Chapter 6** we tested the ability of a phenylalanine-based azobenzene amino acid (**APhe**) to control folding and self-assembly of a  $\beta$ -structured peptide known to form self-assembled peptide fibers. Both peptide structure and self-assembly characteristics could be controlled through **APhe** isomerization, with its position in the peptide also observed to affect

peptide fiber oligomerization. To test if this change in self-assembly could be used to change peptide activity, catalytic histidine residues were introduced in the peptide sequence. In ester hydrolysis experiments, photoisomerization was observed to affect the organocatalytic reaction rates of the peptides, but the exact mechanism through which this occurs is not yet clear. This chapter confirms the initial hypothesis, that the photoisomerization of azobenzene-based amino acids can be used to control self-assembly of  $\beta$ -structured peptides, in addition to  $\alpha$ -helical peptides.

The work presented in this thesis directly impacts the development of synthetic membrane fusion systems. Peptide stapling was shown to be an effective technique to increase coiled-coil binding, which, in turn was shown to be the major contributor to the effectiveness of the E/K coiled-coil membrane fusion system. It also provides a new hypothesis; that regulation of synthetic membrane fusion can be achieved through active control over coiled-coil formation. Furthermore, the presented work on peptide photocontrol of both  $\alpha$ -helical coiled-coils and  $\beta$ -structured peptides provides a mechanistic background, and a novel amino acid, that can be used to introduce photo-responsive activity in many other peptide or protein systems. These techniques function as tools for the generation of active materials in synthetic biology, and might help shine a light on the complex protein interactions observed in the natural world.

## Nederlandse Samenvatting

Coiled coil peptiden hebben een sterke en selectieve binding die verenigbaar is met biologische systemen. Deze eigenschappen maken coiled coil peptiden de ideale bouwsteen in de synthetische biologie. In deze thesis wordt een synthetisch membraanfusie systeem onderzocht, gebaseerd op de peptiden 'E' en 'K', die in combinatie een dimerische coiled coil vormen. Verschillende structurele varianten van deze peptiden zijn geprepareerd en getest op hun eigenschappen in fusie-experimenten, met als doel het achterliggende mechanisme op te helderen. Om de functionaliteit van dit coiled-coil systeem te vergroten is de introductie van een licht-actieve azobenzeen groep onderzocht. Het koppelen van de licht-gedreven isomerisatie van de azobenzeen met de structuur van de coiled-coil introduceert een schakel-functie in de activiteit van deze peptiden. Deze schakel functie leidt tot controle over de activiteit van biomoleculen en nano-materialen gebaseerd op deze coiled coil peptiden.

Een vaak voorkomende modificatie van aminozuur zijketens in de natuur is het bevestigen van een palmitinezuur, of andere vetstaart. In **hoofdstuk 2** wordt onderzocht hoe de plaatsing van vetstaarten op de zijketens van aminozuren, in plaats van op de N-terminus, effect heeft op de efficiëntie van membraanfusie. Liposomen gemodificeerd met deze nieuwe peptiden (**fCPK** en **fcPE**) lieten een vergelijkbare of verminderde fusogeniciteit zien, waarbij in het geval van **fcPE** waren deze liposomen niet stabiel. Deze veranderingen zijn toegekend aan de homomerische interacties tussen liposomen gemodificeerd met deze peptide. In eerdere studies zijn de homomerische interacties van peptide E altijd als niet belangrijk beschouwd. De instabiliteit die in deze studie is geobserveerd laat zien dat de homomerische interacties toch een belangrijke rol spelen; ze stabiliseren de peptiden op het oppervlakte van liposomen, nog voordat fusie plaats kan vinden. Daarnaast kan de algemene conclusie getrokken worden dat peptide die terminaal verankert zijn aan het membraan een gelijke of hogere efficiëntie van fusie vertonen.

Eerdere studies naar de interacties van peptide K hebben aangetoond dat deze peptide een affiniteit heeft voor lipidenmembranen, wat is voorgesteld als één van de redenen voor de efficiëntie van het E/K fusiesysteem. In **hoofdstuk 3** wordt deze

theorie verder onderzocht via de preparatie van cyclisch varianten (ook wel bekend als 'stapled peptides') van peptide K. Deze cyclische varianten zijn structurele isomeren van elkaar, welke alleen verschillen in de locatie van de modificatie en de grootte van de ring. Dit is gerealiseerd door het verbinden van twee cysteïnes met verschillende dibromoxyleen linkers. Deze cyclisatie strategie resulteerde in meer gevouwen peptiden, sterkere binding en meer stabiliteit van de respectievelijke coiled-coils, wat verklaard wordt door een pre-organisatie mechanisme. Fusie-experimenten met cyclische peptide die een lipide anker bevatten resulteerden in een zeer efficiënte menging van de inhoud van liposomen, welke direct gerelateerd is aan de toename in bindingssterkte van de peptide. Deze resultaten leiden tot de verwerping van de vorige hypothese en stelt dat de bindingssterkte van de coiled coil peptiden de grootste drijfveer is achter de fusie van membranen. Een positief effect op fusie door de interacties van peptide K met lipiden membranen is hiermee niet uitgesloten, maar verdient niet de focus in de optimalisatie van dit systeem.

Omdat de fusie-activiteit sterk afhankelijk was van de bindingsterkte van de coiled-coil, zou het theoretisch mogelijk moeten zijn om deze fusie-activiteit aan of uit te zetten door een actieve component in te bouwen in de binding van de coiled coil peptiden. Deze hypothese wordt onderzocht in **hoofdstuk 4**, waar opnieuw stapled peptides worden gemaakt, maar in dit project is de xyleen linker vervangen door een licht-actieve azobenzeen. Deze azobenzeen heeft twee verschillende isomeren, 'cis' en 'trans', en isomerisatie tussen deze twee conformaties is mogelijk met behulp van licht. Deze strategie is toegepast op peptide K en resulteerde in controle over zijn structuur met behulp van licht. Coiled-coils met een lengte van 21 aminozuren konden ook tussen verschillende structuren wisselen met behulp van licht. Deze resultaten tonen aan dat deze strategie in principe toepasbaar is, maar synthese van deze varianten met een azobenzeen linker was erg inefficiënt. Voor praktische toepassingen is dus andere methode vereist.

In **hoofdstuk 5** wordt een nieuwe strategie onderzocht voor controle over de self-assemblage van coiled coil peptiden met behulp van licht. Deze strategie maakt gebruik van aminozuren die een azobenzeen groep bevatten, en plaatst deze azobenzeen in het hydrofobe domein van de coiled-coil. Drie verschillende aminozuren met een azobenzeen groep zijn getest; twee daarvan zijn gebaseerd op eerder onderzoek met de structuur van fenylalanine als basis. Het derde aminozuur is een nieuw ontwerp op basis van fenylglycine (genaamd **APgly**). De synthese van peptide K varianten met deze aminozuren was eenvoudig en de azobenzeen

groepen vertoonden na de synthese nog steeds goede isomerisatie eigenschappen. Van de drie varianten vertoonde peptide K met **APgly** het grootste verschil in binding tussen de twee isomeren van de azobenzeen, en de sterkste coiled coil binding in het algemeen. Dit verschil komt waarschijnlijk door de extra methyleen groep in de phenylalanine-derivaten, welke de azobenzeen buiten het hydrofobe domein van de coiled-coil plaatst. Moleculaire simulaties ondersteunen dit idee en lieten ook kleinere structuurveranderingen zien in de positie van de azobenzeen in **APgly** in vergelijking met dezelfde phenylalanine variant. Deze resultaten laten dit zien dat het nieuwe aminozuur **APgly** effectief de binding tussen coiled coil peptiden kan beïnvloeden, wat veroorzaakt wordt door verstoring van het centrale hydrofobe domein in de coiled-coil na foto-isomerisatie van de azobenzeen.

Ditzelfde mechanisme zou in principe toepasbaar moeten zijn op andere peptiden-structuren met een hydrofoob domein. In **hoofdstuk 6** wordt getest of azobenzeen-gemodificeerd phenylalanine (**APhe**) in staat is de structuur en zelf-assemblage van peptiden met een  $\beta$ -structuur te beïnvloeden. Hiervoor zijn peptiden gebruikt die bekend zijn om te assembleren als ' $\beta$ -sheet' vezels, waarbij de binnenkant van de vezels bestaat uit hydrofobe aminozuren. Zowel de  $\beta$ -sheet structuur als de self-assemblage van deze peptiden kon met licht beïnvloed worden wanneer één van de aminozuren was veranderd tot **APhe**, met de positie in de sequentie van invloed op de oligomerisatie van peptiden vezels. Om te onderzoeken of de structurele veranderingen veroorzaakt door **APhe** isomerisatie leidt tot verschillen in de activiteit van de peptiden, is er een katalytische histidine in de sequentie geïntroduceerd. De hydrolyse van esters, gekatalyseerd door deze peptiden, kon beïnvloed worden door isomerisatie van de azobenzeen, hoewel hier nog geen duidelijk verband tussen de  $\beta$ -structuur en de hydrolyse snelheid geobserveerd is. Dit hoofdstuk bevestigt de hypothese; dat de foto-isomerisatie van azobenzeen bevattende aminozuren ook gebruikt kan worden voor het verstoren van hydrofobe domeinen in  $\beta$ -sheet peptiden.

In deze thesis worden verschillende onderzoeken gepresenteerd met als doel het ontwikkelen van een ideaal synthetisch membraanfusie-systeem. Het aanbrengen van peptiden staples resulteerde in een hogere coiled coil binding, wat direct gerelateerd kan worden met de fusie-efficiëntie van het systeem. Dit onderzoek heeft ook tot de nieuwe hypothese geleid; dat membraanfusie gecontroleerd plaats kan vinden door actieve controle over de bindingsterkte van de coiled-coil. De tweede helft van deze thesis introduceert een nieuwe strategie om zowel coiled

coil peptiden met een  $\alpha$ -helix structuur, als die van  $\beta$ -sheet vormende peptide te beïnvloeden met licht. Deze strategie berust op aminozuren met een licht-actieve azobenzeen groep, die de hydrofobe domeinen van deze geassembleerde peptiden verstoort. De  $\alpha$ -helix en  $\beta$ -structuur zijn de twee meest voorkomende structuren in eiwitten, en suggereren daarmee dat deze strategie algemeen toepasbaar is in andere peptiden en eiwitten. Deze nieuwe methode gaat hopelijk een brede applicatie vinden in de synthetische biologie, en daarmee een licht schijnen op de complexe eiwit-interacties die voorkomen in de natuur.

## Curriculum Vitae

Niek Crone was born on the 10<sup>th</sup> of July 1992, in Almere, the Netherlands. After obtaining a VWO diploma from the Baken Park Lyceum in Almere, he started the study 'Molecular Science and Technology' at Leiden University and Delft University of Technology. During this study he investigated copper coordination complexes for chemical sensing purposes under the supervision of Dr. Tom v. Dijkman and Prof.dr. Lies Bouwman. After finishing his Bachelor studies, in the summer of 2013 he joined an exchange program with Williams college (Massachusetts, USA) where he worked under the supervision of Prof.dr. Sarah Goh. During this internship he worked on the synthesis of block copolymers through RAFT polymerization for the preparation of polymer nanomaterials. At the end of this project he returned to Leiden to continue his studies in the field of chemistry, with the specialization 'design and synthesis'. During this master he took part in two research projects, with the main project investigating the coating of gold nanorods for bioimaging applications in the supramolecular and biomaterials chemistry (SBC) group, under the supervision of Dr. Aimee Boyle. A second research project was performed at the Radboud University, Nijmegen, and investigated the mechanism behind cell-penetrating peptides together with Dr. Dennis Löwik. He finished his MSc. studies in 2016, with the honorarium *cum laude*.

Soon afterwards he started in his doctoral research at the SBC group, working together with Prof.dr. Alexander Kros and Dr. Aimee Boyle on the synthetic modification of fusogenic coiled-coil peptides. The research performed during these studies has been presented at multiple conferences:

- 2021 Designing functional biomolecular assemblies: Beyond Biology (Poster)
- 2020 GRC conference on the Chemistry and Biology of Peptides, USA (Poster)
- 2019 CHAINS chemistry conference, NL (Poster)
- 2018 CHAINS chemistry conference, NL (Oral presentation and poster)
- 2018 Dutch Peptide Symposium, NL (Poster)
- 2018 Reedijk Symposium, NL (Poster)
- 2017 DutchBiophysics conference, NL (Poster)
- 2017 Alpbach Coiled-coil workshop, CH (Oral presentation and poster)
- 2017 Reedijk Symposium, NL (Poster)

## List of publications

1. Niek S. A. Crone, Dirk Minnee, Alexander Kros, Aimee L. Boyle; Peptide-mediated liposome fusion: The effect of anchor positioning, *International journal of Molecular Sciences*, **2018**, 19(1), 211.
2. Aimee L. Boyle, Martin Rabe, Niek S. A. Crone, Guto G. Rhys, Nicolas Soler, Patrick Voskamp, Navraj S. Pannua, Alexander Kros; Selective coordination of three transition ion metals within a coiled-coil peptide scaffold, *Chemical Science*, **2019**, 10, 7456.
3. Niek S. A. Crone, Alexander Kros, Aimee L. Boyle; Modulation of coiled-coil binding strength and fusogenicity through peptide stapling, *Bioconjugate chemistry*, **2020**, 31, 3, 834-843.
4. Niek S.A. Crone, Niek v. Hilten, Alex v.d. Ham, Aimee L. Boyle, Alexander Kros; Azobenzene-based amino acids for photocontrol of coiled coil peptides. *Manuscript in preparation*.
5. Niek S.A. Crone, Mousumi Samanta, Dinghao Wu, Elena Egorova, Panagiota Papadopoulou, Aimee L. Boyle, Gonen Ashkenasy, Alexander Kros; Photocontrol of peptides self-assembling as  $\beta$ -sheet fibers. *Manuscript in preparation*.
6. Mengjie J. Shen, Ye Zeng, Ankhush Singhal, Niek S. A. Crone, Agur Sevink, Aimee L. Boyle, Alexander Kros; Enhanced liposomal drug delivery via membrane fusion triggered by dimeric coiled-coil peptides. *Manuscript in preparation*.
7. Fernando Lozano Vigarío, Inés Simó Vesperinas, Marie A.C. Depuydt, Niek S.A. Crone, George M.C. Janssen, Peter van Veelen, Alexander Kros, Joke A. Bouwstra, Johan Kuiper, Wim Jiskoot, Bram Slütter; Identification of ApoB100-derived peptides as targets of CD4 T cell responses in human atherosclerosis. *Manuscript in preparation*.

## Acknowledgements

Promoveren doe je niet alleen. Er zijn heel veel mensen die bij hebben gedragen aan het succesvol afronden van dit traject en hen wil ik hier hartelijk bedanken.

**Alexander**, bedankt voor deze positie en de mogelijkheid om mijzelf te ontwikkelen binnen SBC. Je gaf me veel vrijheid in het ontwikkelen van ideeën en het uitvoeren van het onderzoek, en ik heb hier ontzettend van geleerd. In het voortzetten van mijn (wetenschappelijke) carrière denk ik dit goed te kunnen gebruiken.

**Aimee**, als er één reden is waarom dit boek er nu ligt dan ben jij dat wel. Als ‘peptide queen’ was je er altijd om ons te helpen met problemen. De bank in je kantoor was een goeie plek om rond te hangen en te discussiëren over peptide-problemen, maar ook over de wetenschap in het algemeen. Jouw continue vertrouwen en vermogen een positieve kant te vinden leverde de motivatie wanneer die bij mij even ontbrak.

Het werk in deze thesis was niet mogelijk zonder de grote hoeveelheid slimme en gepassioneerde wetenschappers waar ik de afgelopen jaren mee samen heb mogen werken. **Niek** en **Alex** bedankt voor de hulp met computersimulaties, en sorry dat jij nu bekend staat als Niek<sub>2</sub>. **Gonen** and **Mousumi**, it was a lot of fun working together with you on the last project in this thesis, and in our conversations to hear about the different perspectives of the pandemic. Also, my appreciation goes out to **Elena**, **Panagiota**, **Mengjie** and **Dinghao** for helping me with experiments, even if the outcome was uncertain. Daarnaast ook mijn dank aan **Viorica**, **Hans** van Biosyn, **Loli** from the IBL en **Robert** in het LUMC voor hun hulp met het vergaren van data; en aan **Hessel** voor discussies over organische synthese.

Niet te vergeten zijn de studenten die de afgelopen jaren mee hebben geholpen aan dit onderzoek. **Dirk** en **Andy**; Jullie waren allebei harde werkers die bij mij synthese hebben leren kennen en daar nu verder in willen ontwikkelen. **Frank**, je was niet mijn student, maar dat zou niemand weten met de hoeveelheid tijd dat je met mij peptiden aan het maken was. **Jenna**, it was a lot of fun to show you ‘real’ chemistry, your views and stories about Hawaii always put an interesting perspective on life here in Leiden. **Wessel**, de figuren in hoofdstuk 4 doen geen recht aan de hoeveelheid werk die jij in de synthese van *ortho*-pyrrolidinyll

azobenzeens hebt gestopt. Het doorzettingsvermogen dat je daar getoond hebt gaat je vast veel helpen in je promotieonderzoek. Wanneer de pyridine's je de neus uitkomen, denk dan af en toe nog terug aan het gemak van een 50-staps peptidensynthese. Ik wens jullie allemaal heel veel succes met de rest van jullie studies en carrière.

Een goede sfeer is belangrijk voor het doen van goed onderzoek, en daarom wil ik heel SBC bedanken voor de leuke tijd die ik er gehad heb. Of het nou ging om gezamenlijk lunchen, wetenschappelijke problemen bespreken, Science-club (of flip-cup) en Lemmy's in de avond, of gewoon zeuren over het koffiezetapparaat; gezelligheid was altijd wel te vinden. Daarvoor heel veel bedankt: **Roy, Jolinde, Willem, Victorio, Lia, Amadeo, Gabriela, Fred, Max, Pauline, Erik, Tingxian, Ciqing, Ying, Ye, Batuhan, Jeroen, Rianne, David, Indigo, Jasper, Jorn, Dennis, Renzo, Thomas**, en alle andere groepsleden van SBC.

Daarnaast wil ik **Guido, Charlotte, Siebren, Paul, Martijn en Sven** bedanken voor alle discussies, het is heel fijn om frustraties over werktijden, reacties en andere chemische zaken te kunnen delen; evenals alle discussies over politiek, de huizenmarkt, bier en lekker eten. Ook ben ik dankbaar voor het hebben van een leuke vriendengroep die niets met scheikunde te maken heeft. **Carlo, Franck, Niels, Rens, Floyd, Patrick** en alle ander apekoppen heel erg bedankt voor de gezelligheid en vooral ook een plek waar ik niet met de universiteit bezig hoeft te zijn. Daarnaast waren de avondwandelingen met **Jonas** discussiërend over politiek en de maatschappij altijd heel fijn, en de bergvakantie elke zomer met **Sander** voor mij even het moment om alles los te laten.

Ook mijn familie mag in dit lijstje niet ontbreken, zij hebben me altijd ondersteunt in het doen van mijn PhD, ook al was het soms lastig te begrijpen waar ik mee bezig was of waarom weekend dagen in het lab juist zo effectief waren. **Herma, Esther** en **Schelto** bedankt voor jullie continue support. Ook de andere **Crone's, Nauta's, Snoeken**, van **Lindentollen**, en recentelijk de **Renderings**; heel erg bedankt voor de altijd aanwezige gezelligheid en de warme onthalen bij jullie thuis.

En **Bart**, wat is het fijn dat ik dit allemaal met jou heb kunnen delen. Alle lange dagen in het lab en late uurtjes achter de computer nam jij voor lief. Het thuis werken werd een stuk fijner met jou om de hoek om mij op te vrolijken en het eten klaar te zetten als ik nog even iets langer bezig was. Jij begrijpt me als geen ander, en ik kijk er naar uit samen te ervaren wat het leven na promoveren gaat brengen.